BUREAU D'ENQUETES ET D'ANALYSES POUR LA SECURITE DE L'AVIATION CIVILE

Scientific Report from the Drift Group

Michel OLLITRAULT – IFREMER/Brest
Bruno BLANKE – CNRS/Brest
Changsheng CHEN – UMass/ Dartmouth
Nicolai DIANSKY – INM RAS/ Moscow
Marie DREVILLON – Mercator-Océan/Toulouse
Eric GREINER – CLS/ Toulouse
Fabien LEFEVRE – CLS/ Toulouse
Richard LIMEBURNER – WHOI/ Woods Hole
Pascal LEZAUD – IMT/ Toulouse
Stéphanie LOUAZEL – SHOM/ Brest
George NURSER – NOC/ Southampton
Denis PARADIS – Météo-France/ Toulouse
Robert SCOTT – NOC/ Southampton

ESTIMATING THE WRECKAGE LOCATION OF THE RIO-PARIS AF447

Coordination: BEA

June 30 2010

Contents

Introduction

During the night of June 1 2009, the A330 Airbus plane (registered F-GZCP) on the AF447 flight from Rio de Janeiro to Paris met significant turbulent atmospheric activity associated with the Intertropical convergence zone (ITCZ) near 3°N, 30°30'W. The plane last known position (LKP), 2°58.8'N 30°35.4'W, was transmitted at 2h10 UTC[1] on June 1 2009 by the Aircraft Communication Addressing and Reporting System (ACARS). This position and time may be referred also as the ACARS point. An analysis of the messages[2] sent through ACARS before and after 2h10 indicates that the impact at sea surface occurred most likely before 2h15 and the plane wreck should be located within a 40 nautical miles (or 75 km) radius circle centred on LKP (called ACARS circle in the following).

The first debris, possibly from the Airbus remains, were sighted on June 5 2009 at 16h10 by a Singaporean merchant ship near 3°38'N 30°26.8'W, and by the Brazilian Navy near 3°33.6'N 30°26.4'W at about 21h. One day later (on June 6 2009) the first two human bodies were recovered near 11h55 and at 3°34.2'N 30°27.6'W by a Brazilian ship just arrived in the area (situated some 36 nautical miles north of LKP) which was soon confirmed to contain several aircraft debris and bodies still floating at the surface.

Actually several ships crisscrossed this zone afterwards, sighting and recovering, as far as possible, the bodies and debris from the plane. After June 7 all the floating remains were entrained to the North by an approximate 1 knot (or 0.5 m s^{-1}) current.

Since there is about a four and a half day interval between the time of the accident and the time of discover of the drifting debris, the BEA decided to rely on a working group (called the "Comité de dérive") to estimate a possible crash zone within the ACARS circle, with the help of ocean general circulation numerical models (OGCMs in the following) and available in-situ surface current measurements. First results from the different OGCMs were frustrating because they disagreed with each other (order of 100 km differences on the particle positions after one week of integration) and did not reproduce satisfactorily the sixteen 12h surface drifts recovered from 8 Argo

---

[1] All times in this report will be given in Universal Time Coordinated (UTC).

[2] See BEA interim reports n°1 and n°2

floats cycling near the ACARS region. Thus, with the models and data at hand two weeks or so after the accident, it was not possible to define any research zone with confidence.

Nevertheless, searches for the flight recorders in June 2009, sampled several locations within the ACARS circle (and even one location outside), unfortunately without hearing their acoustic signals.

Obviously, without new data and in particular directly measured surface currents near or within the ACARS circle and for the period June 1 to June 6 (at least), no sensible progress would be possible. And even so, methods should be developed or adapted to estimate as accurately as possible the space and time velocity field over the zone of interest, whether by combining models and data or by using efficiently (in-situ or remote) data alone.

After the unfruitful results of phases 1 & 2, and in preparation for phase 3, a working group was formed with experts from over the world, and with complementary skills. This international group was organised in two task forces: one the so-called "drift group", in charge of estimating the possible wreck location and defining the search zone, the other in charge of selecting the required means.

In this report, we present the scientific work done by the drift group, which worked intensively over about six months.

The document is organised as follows:

- In the first chapter, the observation data collected and used in this study,
- In the second chapter, an estimation of the current field and the particle tracking done with in-situ data (whence a determination of the wreckage area using observed currents),
- The third chapter is dedicated to similar estimations with numerical ocean models run with and without data assimilation[3] (whence several determinations of the wreckage area using OGCMs),
- finally, we propose a region to be searched in the light of the results obtained so far.

[3] i.e. constraining the model solution, using also information on model and data errors.

I Observation data

Figure 1 shows the surface current data available shortly after the accident.

Eight Argo floats happened to cycle twice within 300 km distance of the ACARS point between May 25 and June 14. Two surface drifters from the Atlantic Oceanographic and Meteorological Laboratory (AOML) also drifted in the region during the same period.

Later, on June 15 2009, four drifters were launched by the Brazilian Navy along 30.5W approximately spaced by 1° in latitude (between roughly 1.5N and 4.5N). We shall not use these trajectories in our analysis because they came too late (although this would have been a great idea to launch two or three such drifters around LKP just after the accident).

Ship-borne Acoustic Doppler Current profiler (ADCP) measurements were done from the IFREMER R/V Pourquoi-Pas beginning June 10 in the afternoon near 6°N 28.5°W and ending near 4°N 30°W on June 14 2009. These data were also a bit too late to be of much use in our analysis. However they can serve as a comparison for model currents and will be inter-compared with the float and drifter currents.

We have been fortunate enough to be provided during last autumn with a large data base of surface buoy trajectories acquired by the BEA from European, African and American fishermen. These new current measurements (in addition to the ones already available in June) will reveal crucial to improve the surface velocity field estimation.

Figure 2 shows the previous Argo float 12h surface displacements and the two AOML drifter trajectories, together with 17 new trajectories from the fisheries buoys. Two of these fisheries buoys passed inside the ACARS circle during the week following the crash[4] and a third one went westward (with a large inertial oscillation) just north of 4°N during the same period.

Remotely sensed data were also recovered, such as the altimetric measure of dynamic topography, the sea surface temperature (SST) and the color of the sea.

---

[4] Crash or accident are used interchangeably in the following

Various winds (or surface stresses), measured by scatterometers on board satellites or calculated by atmospheric models (ECMWF, NCEP or Météo-France) or given as a blend between remotely sensed and model products (WRF, Cersat HR Blended) were used in this study.

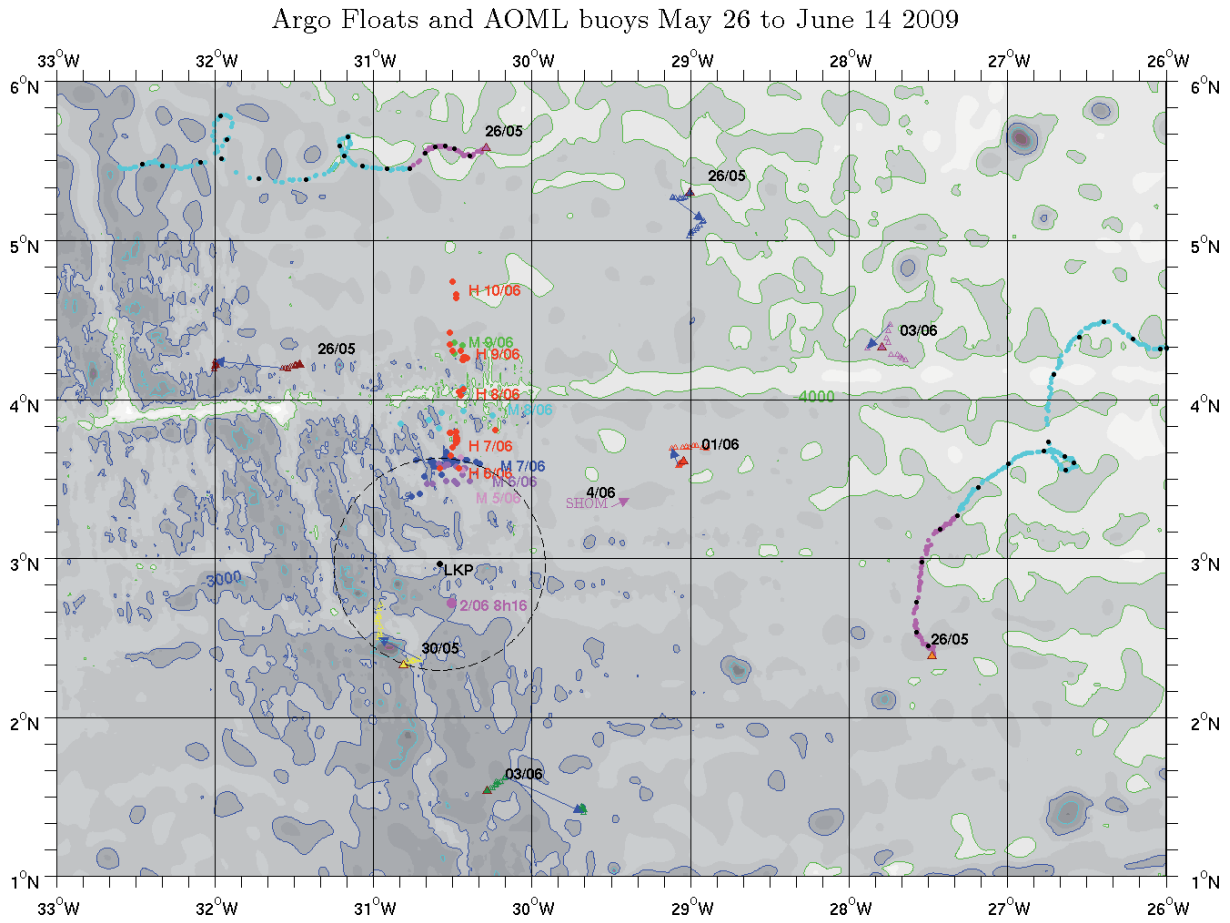

Figure 1 Argo float surface locations are given by triangles while 10-day deep displacements (generally near 1000 m depth) are given as blue arrows. Only the date of first surfacing is given. Argo floats stay at surface for order of 12h only. Two surface drifters from AOML (drogued near 15m depth) were available in real time. Their trajectories are coloured magenta and cyan respectively before and after June 1 2009 at 0h (recall crash time is 2h15). Bathymetry is from SRTM[5] file with a 0.5' resolution (grey shading is every 500 m and contouring every 1000 m). A few plane parts (M) and human bodies (H) are positioned in the Figure where they were sighted or recovered. AF447 last known position (LKP) is at the centre of ACARS circle (dashed). A possible pollution spot (magenta dot) was sighted by a synthetic aperture radar (SAR) on June 2 at 8h16.

[5] available at http://topex.ucsd.edu/WWW_html/srtm30_plus.html

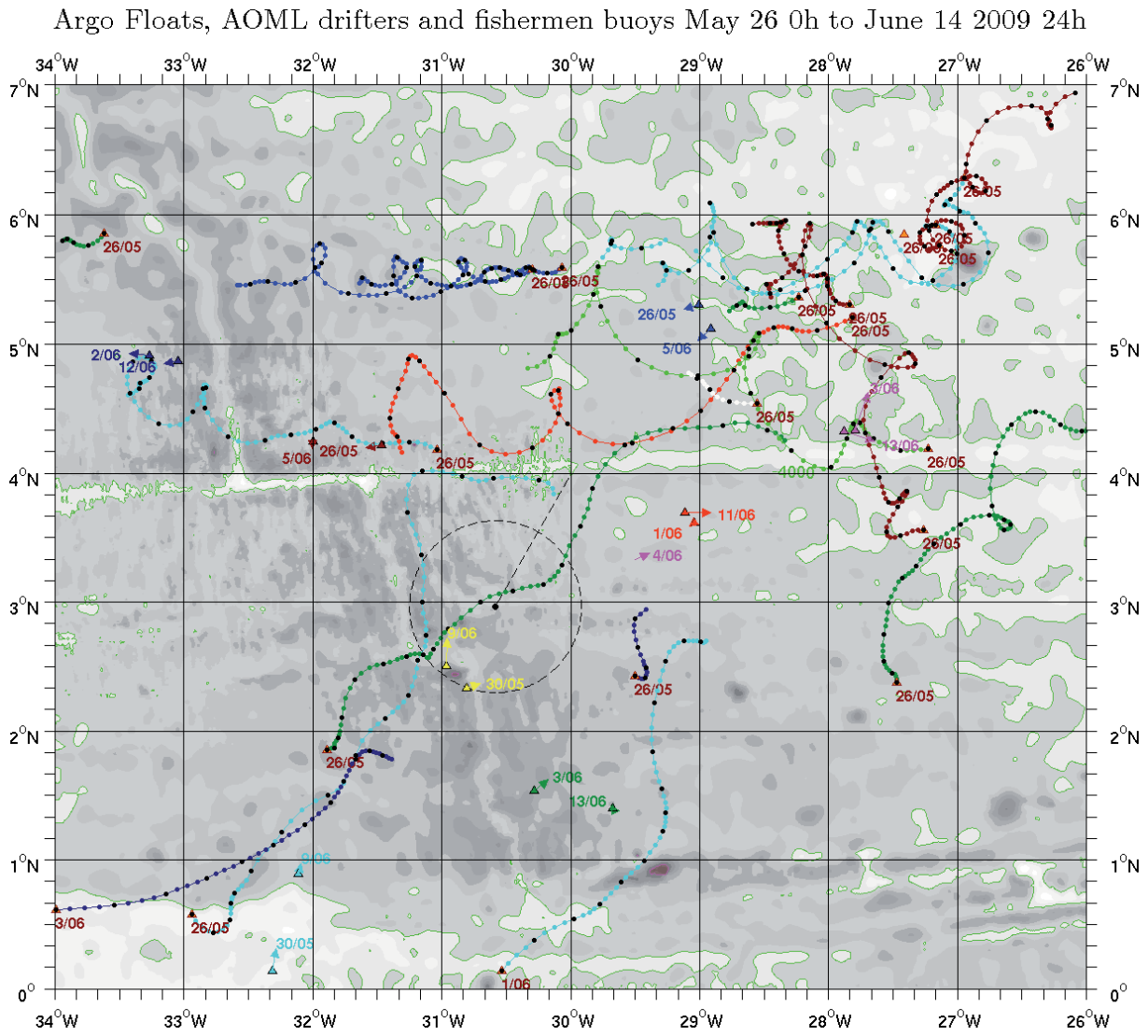

Figure 2 Trajectories of 17 fisheries surface buoys drogued probably near 10 or 15m depth. The trajectories of the two AOML drifters are also shown (see Figure 1) as well as the overall 12h displacements of the Argo floats while they are at the sea surface (Argo floats are not drogued and drift near 1m depth). The drifter and buoy trajectories raw positions were slightly smoothed and then sampled every 6h (the small coloured dots in the Figure). The small black dots are daily positions at 0h. Slanted dashed line shows the flight track the AF447 plane should have followed after the LKP.

The Argo floats

These instruments are derived from the multi-cycle subsurface Lagrangian floats first developed by Davis (1992) and Ollitrault et al. (1994) for the World Ocean Circulation Experiment (WOCE) during the late 90s.

Basically the standard Argo float cycles a great number of times (order of 100 or more) between the surface and a prescribed depth (generally 1000 m deep) every 10 days, staying at depth most of the time, and only order of 12h at the surface, to transmit its data via the Argos system (do not confuse Argo and Argos!). This float needs a few hours to dive to 1000m or to rise from that depth to the surface. The big difference with earlier floats cited above is that it acquires P, T and S measurements continuously while ascending (Figure 3 gives an example).

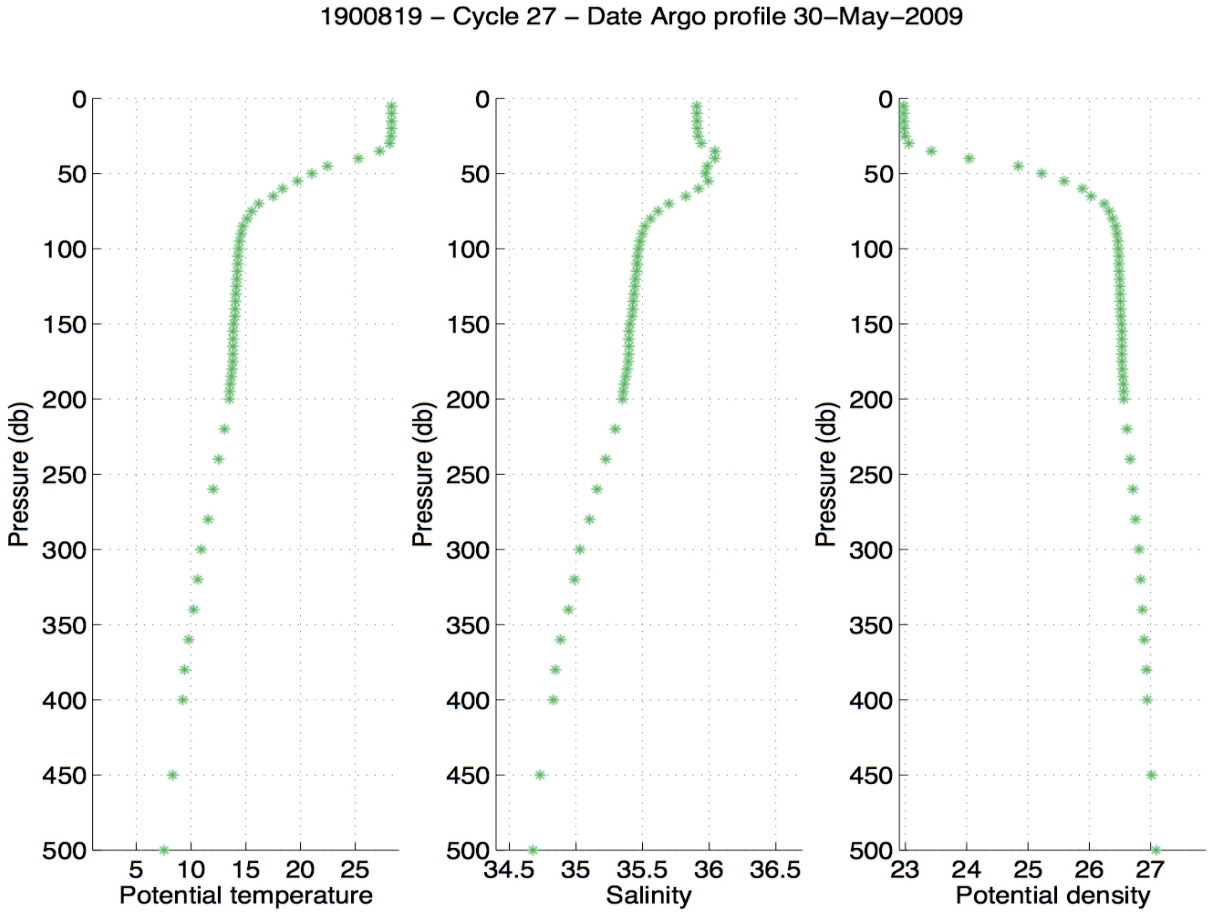

Figure 3 Temperature (C), salinity (PSU[6]) and density (kg m^{-3}) versus pressure (only the upper 500 m or so are shown). There is a well-mixed surface layer down to 40 m.

[6] PSU means Practical salinity unit and represents the mass of dissolved salts (in kg) in 10^3 kg of sea-water.

Generally Argo floats are not positioned when they are drifting in deep water, contrary to the SOFAR (Rossby and Webb, 1970) or RAFOS (Rossby et al., 1986) subsurface floats, but since they are frequently (every hour or so) Doppler located by the Argos satellites during their 12h surface drift at the end of each 10 day cycle, it is simple to estimate a deep drift from the first Argos location at surface just after surfacing and the last Argos location just before diving at the end of the previous cycle.

Argos surface fixes are generally obtained with an error of order 1 km. Due to the current shear between the drifting depth and the surface and to the delay between surfacing time and first Argos fix time (which can be several hours), resulting position accuracy at drifting depth is of the order of a few km. Davis and Zenk (2001) give a general account of the induced error on deep velocity estimates (less than 1 cm s^{-1} with 10-day means).

Only the T and S measurements from Argo profiles are currently assimilated in operational models like PSY2V3 or HYCOM (the deep 10-day mean or the surface 12h mean velocity vectors are not). FVCOM however does also assimilate the surface current data (More details on that in chapter III).

Argo floats are aluminium cylinders 1 or 2 m long and order of 15 cm diameter. They have been developed by several manufacturers and do have some differences in their functioning but for our study this is not important since when they are at the surface they are almost completely immerged near 1m depth and are passively advected (by the current, whatever it is). Data were processed at IFREMER directly from the raw data received at the French GDAC[7] Coriolis in Brest by Jean Philippe Rannou (ALTRAN)

Of the eight Argo floats selected, 6 drifted near 1000 m (wmo# 1900712, 1900713, 1900819, 1901078, 3900692, and 3900693), one near 1500 m (wmo# 6900522) and the last one (wmo# 1900656) near 200 m depth.

Figure 4 gives the example of Argo float #3900692 cycle#42 surface displacement.

[7] GDAC processed data can now be recovered from public NetCDF files found on either of the two websites: http://www.coriolis.eu.org/ or http://www.usgodae.org/argo/.

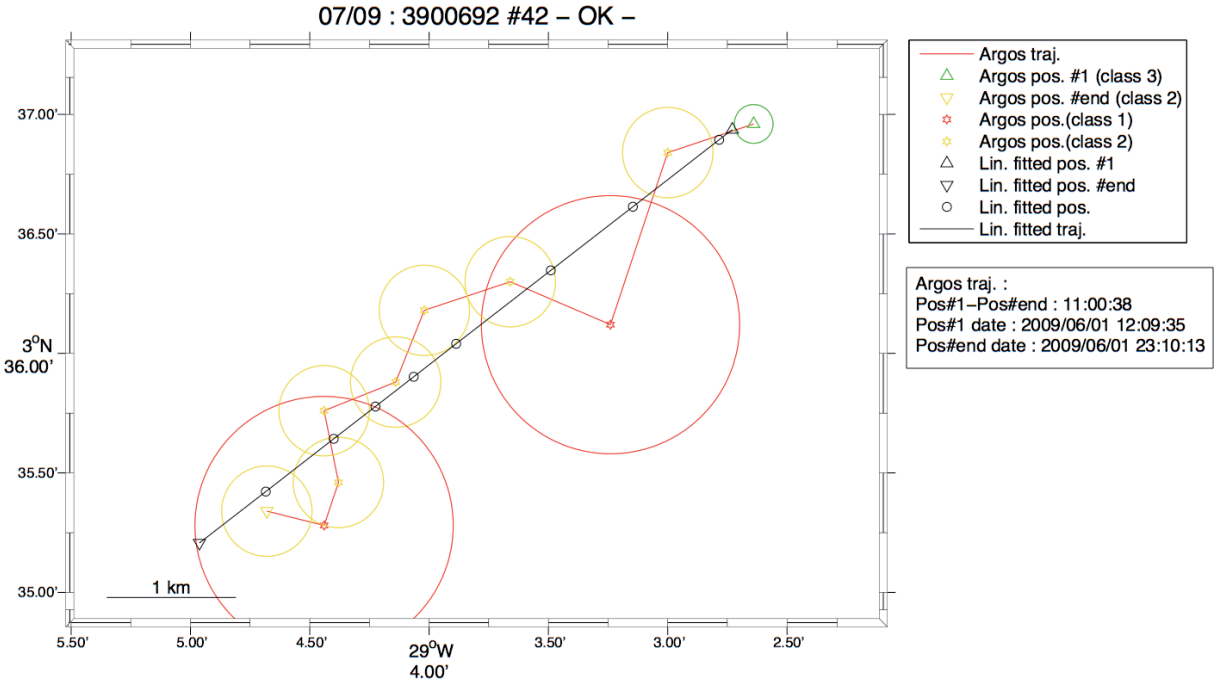

Figure 4 The surface current is southwest during June 1 afternoon, near 3.6°N 29°W. The red circle (1 km radius) gives the Argos class 1 position accuracy, while the green circle (150 m radius) is for class 3 positions (class 2 positions have a 350 m uncertainty). The blue curve is a least square fit of a constant velocity vector.

Over 12h and except for one or two floats, the surface motions were not too different from being quasi rectilinear (account taken of the various location accuracies). That is why in the following mean velocity vectors calculated over the time at the surface (order of 12h) will be used without further comments.

If a refined study were to be done however in the future, it could be rewarding to use a better approximation, even if it is not always clear that a linear plus inertial fit as proposed for example by Park et al. (2005) would work. Figure 5 shows possibly part of an inertial curve.

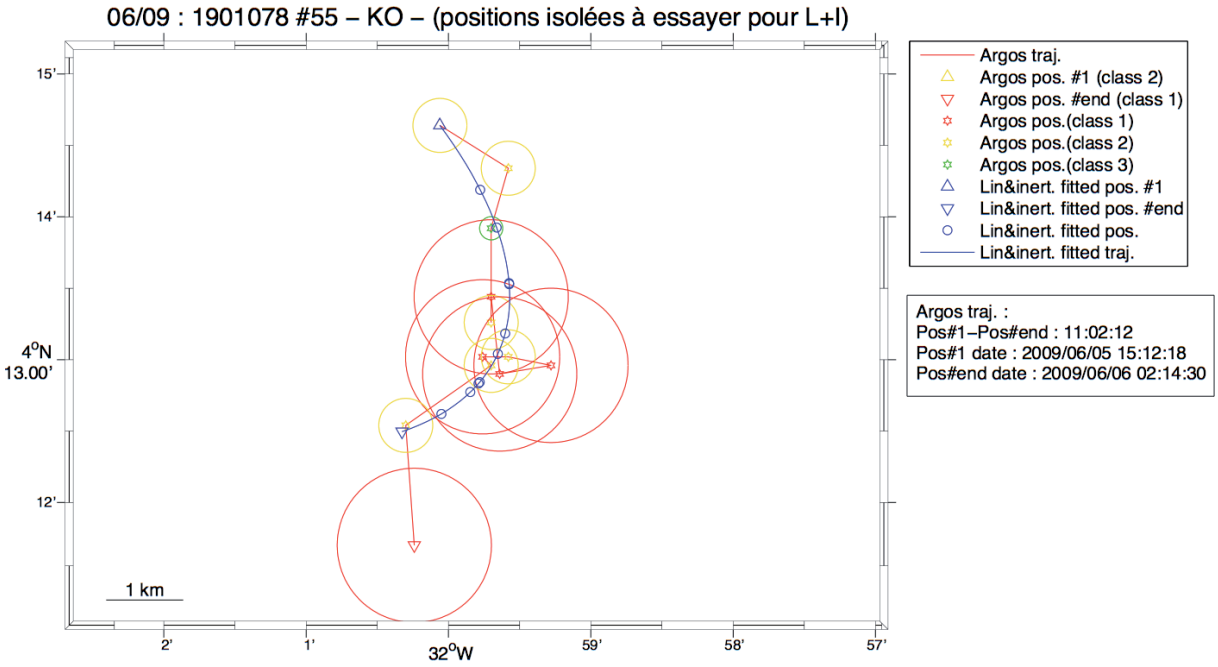

Figure 5 Flow is southward but veers to Southwest probably as part of an inertial oscillation (at 4°N, the inertial period is 7 days).

The Surface Drifters

The two surface drifters from AOML (wmo#31526 and 31919) are of the standard Surface Velocity Programme (SVP) design: a small (38 cm diameter) spherical surface float, a wire tether and a drogue in the shape of a cloth cylinder with circular holes on its sides (Niiler, 2001). The drogue mid-depth is around 15m. To minimise the 'slip' of the drogue through the water, the ratio of the drag area of the drogue and the sum of the drag areas of the float and the tether is over 40.

Niiler et al. (1995) have shown the wind-induced slip of such drifters was less than 1 cm s^{-1} in winds of 10 m s^{-1}.

Over our region of interest, there is a well-mixed surface layer, roughly 35 m thick (see Figure 3) and we can presume the current is approximately constant over this layer (this will be supported by ADCP measurements presented below). Thus if the drogue was still attached the buoy motion would be hopefully close to that of a true surface particle), if we neglect any Stokes drift. It can be lost sometimes, which would be better for our problem, but that information was not available for the two buoys.

Comparison with Argo float surface displacements did convince us that these buoy trajectories were, at least over the period concerned (June 1 to June 7 2009), not unlike the 1 m surface layer water motion. Remember we need to estimate the motion of human bodies and plane debris, which generally were not immerged deeper than order of a few metres (see section below about bodies and debris).

The 17 fisheries buoy tracks shown in Figure 2 are extracted from a much larger data set of almost 600 buoys found between 60°W and 10°E and between 20°S and 20°N over May and June 2009 (see the report by F. Lefèvre). We have retained for our analysis the 34 buoys found in [40°W 20°W], [0°N 10°N] within the period from May 26 0h to June 14 at 24h. It is fortunate that half of these buoys were found around the ACARS zone.

Although they may seem tinkered compared to the well-studied SVP buoys, we assumed they were good surface current followers (note they generally have some kind of drogue down to order of 10 m) and do not depart appreciably from the SVP drifter behaviour. Trajectory of buoy#30299 for example is seen to be very consistent with that of AOML drifter#31919 (in Figure 2 the two blue trajectories going westward near 5° 30'N west of 30°W).

All 34 fisheries buoys were GPS positioned every 12h or 24h (occasionally every hour or so). A filtered data set was also provided by CLS, with two positions per day (at 6h and 18h). The filter used is a Gaussian (with a standard deviation σ of 8 h). However some gaps (less than 2 days but greater that the original sampling interval) in the raw time series may be filled slightly erroneously, due to a linear interpolation on the latitudes and longitudes prior to the filtering proper. For those floats, it was decided to use a cubic spline fit (and calculate the velocity component as the derivative of the polynomial at the time concerned). We have also sampled all the trajectories every 6h, thus at 0h, 6h, 12h and 18h, in order to have a greater time resolution for the velocity field estimation to come later. Figure 6 below gives the velocity components for the fisheries buoy #30299 and reveal one or two spikes in the initial filtered data that have been eliminated by the above procedure.

On a few occasions, an Argo float happened to surface close to a drifting buoy, which permitted comparison of the measured velocity. Figures 7a, 7b and 7c show such encounters. Although the Argo float #1900713 (Figure 7b) was not well positioned (5 fixes of Argos localisation class 1) the relative velocity variation is only of the order of 10%. In general, the current direction compares very well, if not always the speed, as in this example. For the two other encounters the agreement is better (error of the order of 5%). Examination of the spatial structure of the surface currents revealed by these 10-15 m drogued buoys, together with the Argo and SVP floats leads us to assume that the near surface currents so measured were probably reliable surface particle tracers.

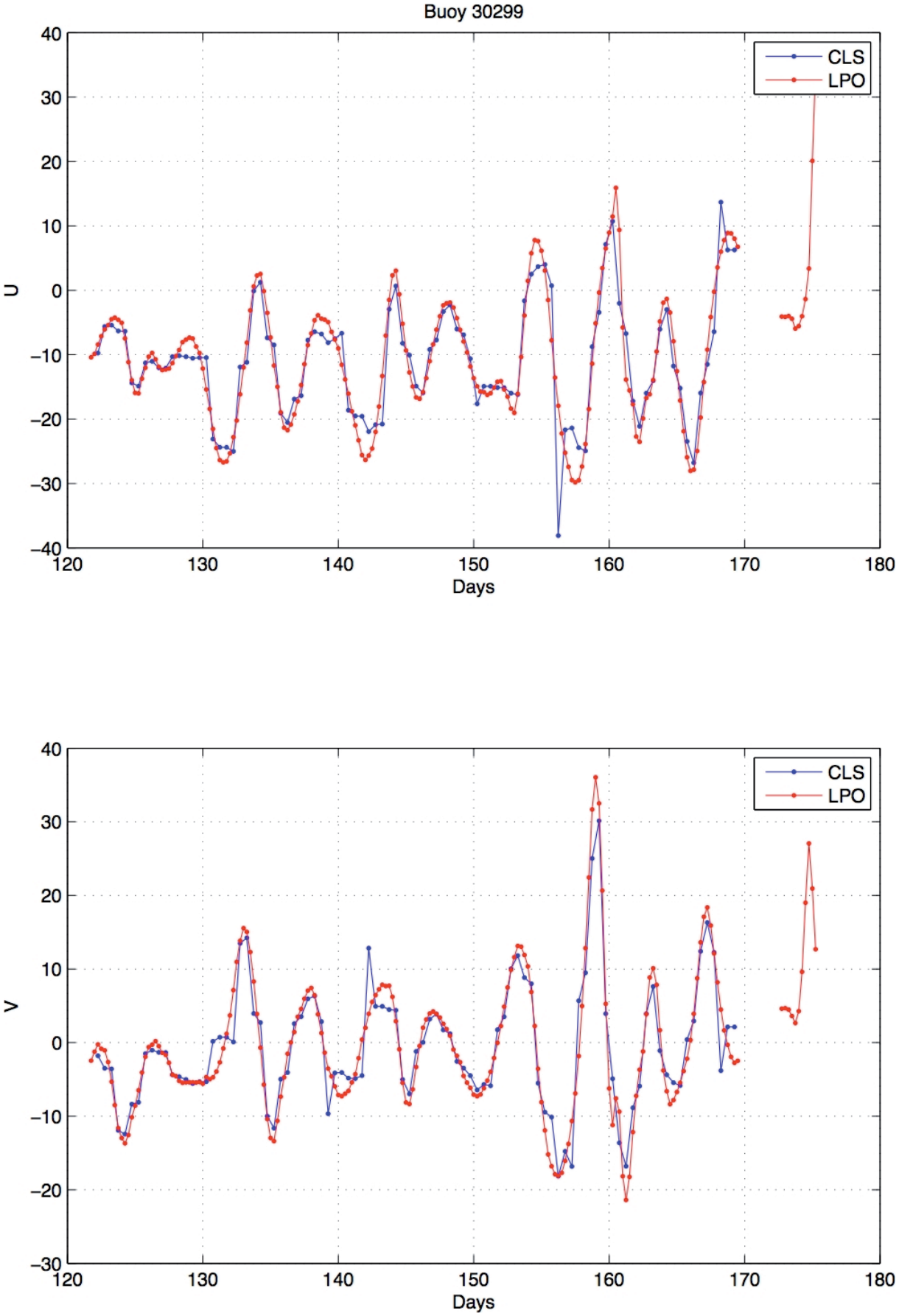

Figure 6 In red the 6 hourly velocity components as given by the derivative of the cubic spline fit trough the raw time series of longitudes and latitudes. In blue the 12 hourly components from the Gaussian filtered time series. Day 151 corresponds to June 1 2009.

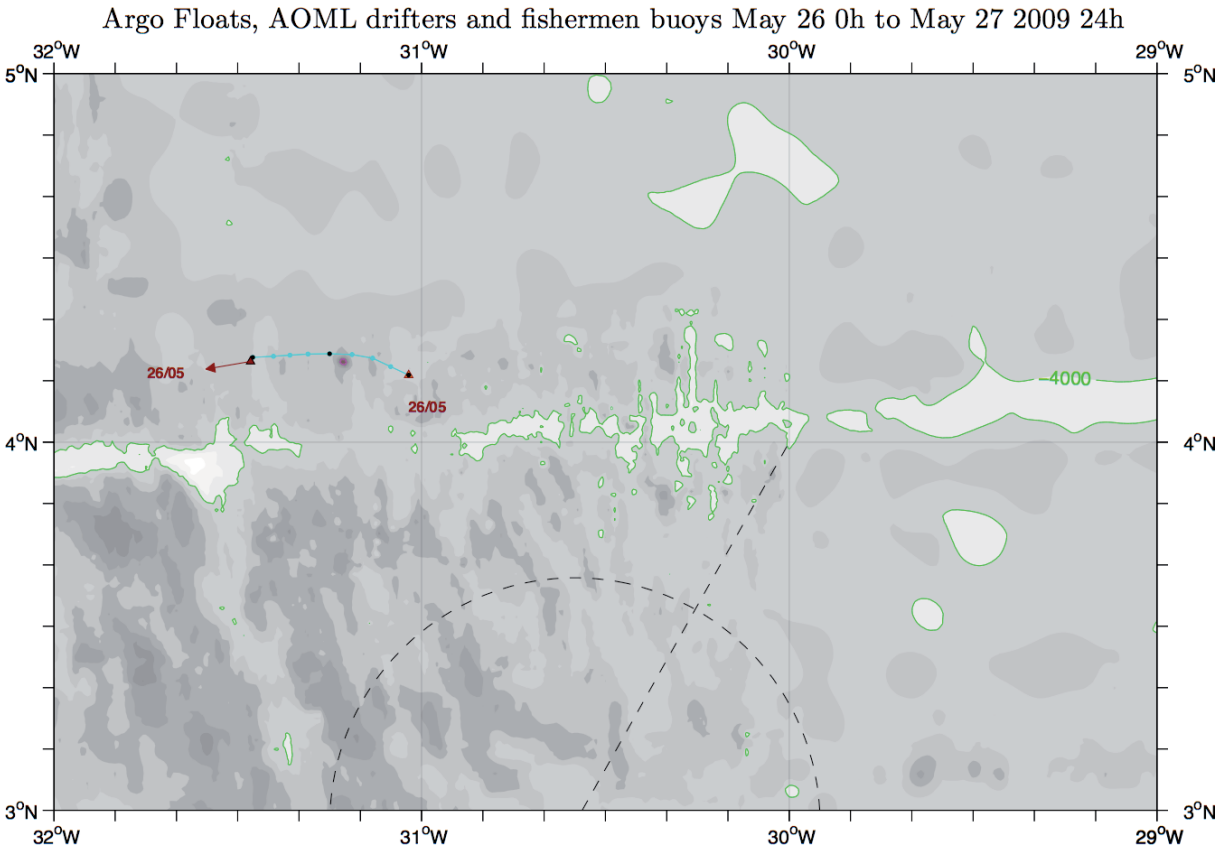

Figure 7a Argo float #1901078 first surface Argos fix occurred on May 26 2009 at 15h20 and last fix on May 27 at 3h20. Its 12h linear displacement (the brown arrow) compares well with the trajectory of buoy #92 (cyan). There is a 6h interval between points on the trajectory.

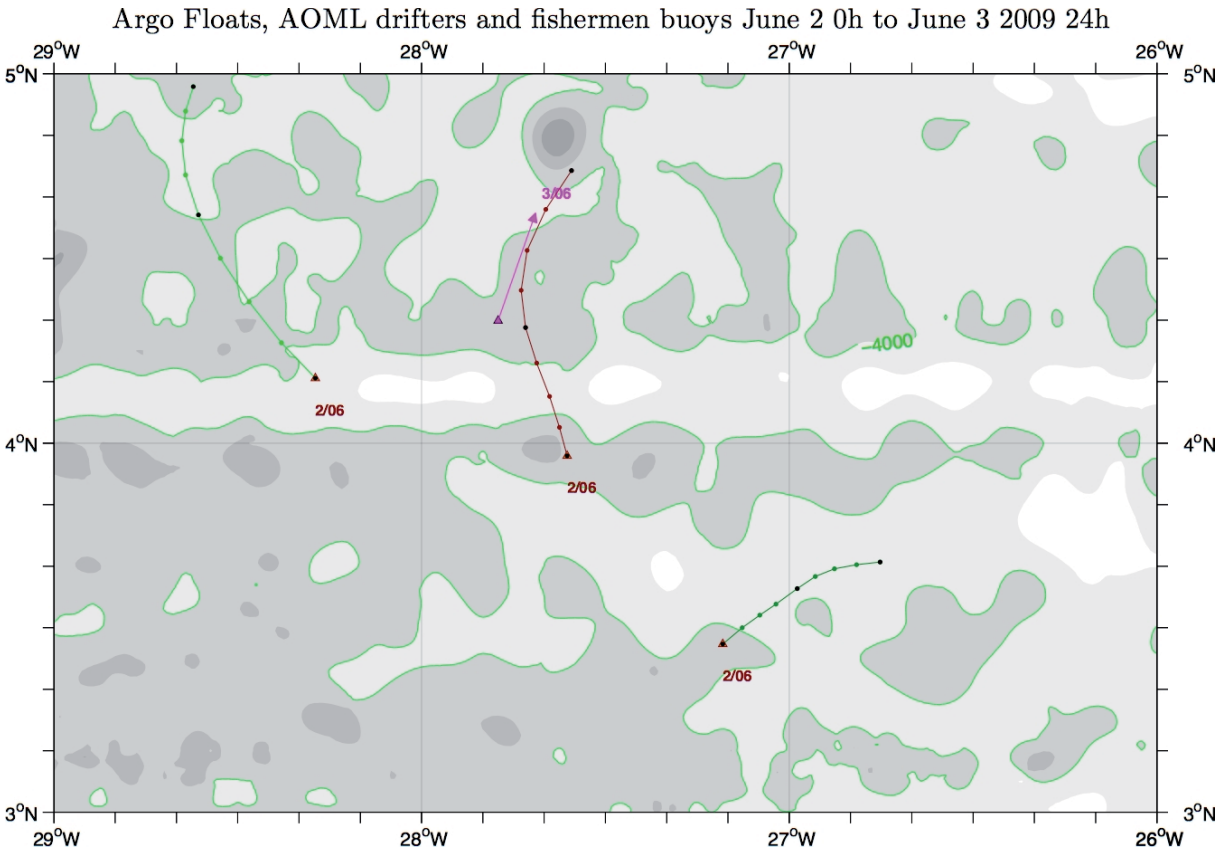

Figure 7b (on previous page) Argo float #1900713 first surface Argos fix occurred on June 3 2009 at 18h20 and last fix on June 4 at 0h05. Although it was positioned five times only, its equivalent 12h linear displacement (the magenta arrow) is compared favourably with the same 12h displacement of nearby fisheries buoy #31754 (brown). There is a 6h interval between points on trajectories (the two other buoy trajectories show the coherency of the surface motions over 100 km).

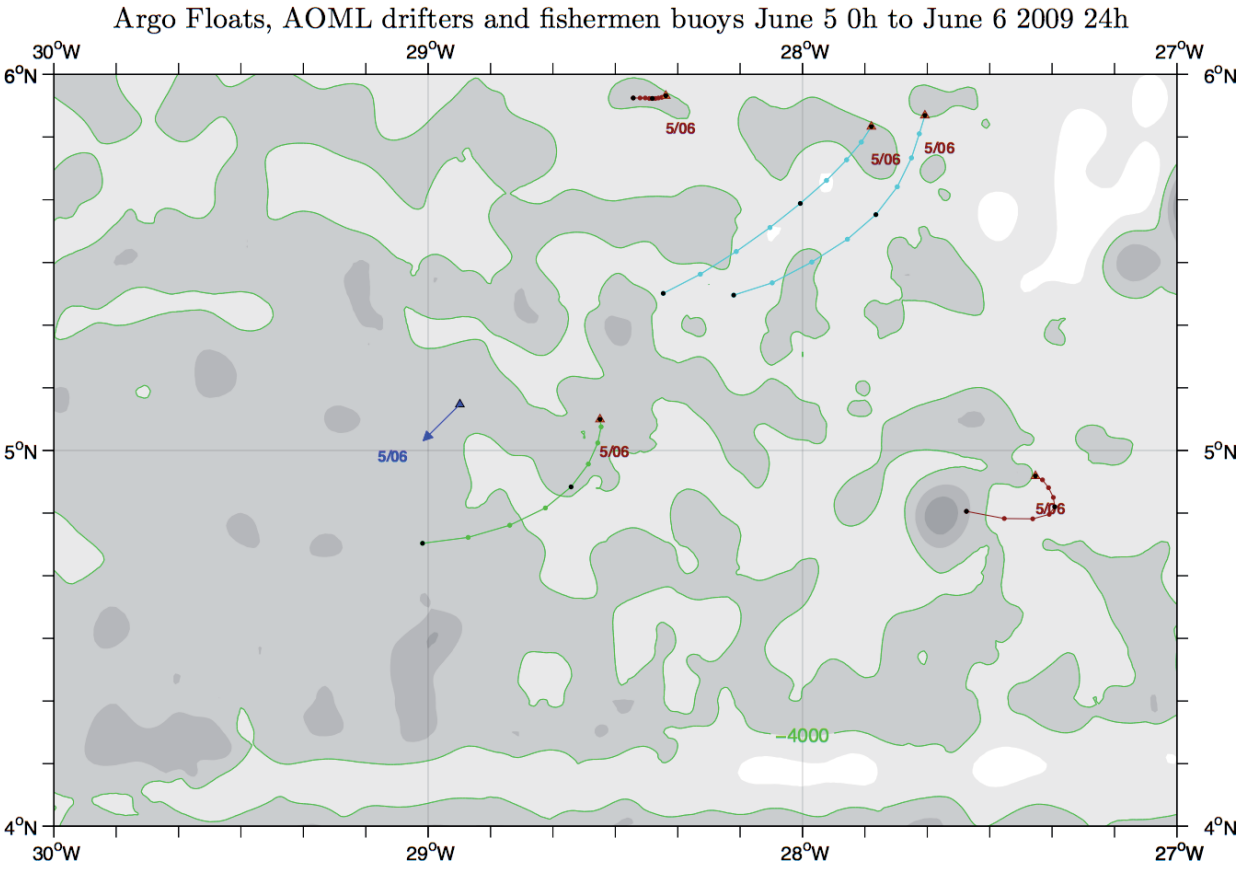

Figure 7c Argo float #3900693 first surface Argos fix occurred on June 5 2009 at 12h and last fix on June 5 at 24h. Its 12h linear displacement (the blue arrow) also compares well with the same 12h displacement of nearby fisheries buoy #29317 (green). There is a 6h interval between points on trajectories. The two cyan buoy trajectories show the longitudinal (as opposed to transversal) coherency of the surface motions over 100 km. But the two brown buoy trajectories reveal that currents can rapidly change in the transversal direction.

Ship-borne ADCP data

Between June 3 2009 and July 8 2009, the R/V Pourquoi-Pas made current measurements with a 150 kHz four-beam acoustic Doppler current profiler (ADCP).

However, because the ship was trying to hear the flight recorders (with the ADCP shut down), most of the ADCP measurements done are well north of the area of interest.

Only the period from June 9 14h to July 8 4h is covered by the ADCP data, corresponding to the ship track being south of 12°N. The ship track (after June 9 2009 14h) together with the 19 m depth (actually averaged between 15m and 23m) ADCP horizontal currents are given in Figure 8. Data processing was done by C. Kermabon (details in Appendix 1).

A latitude dependent vertical section showing the zonal and meridional velocity components is given in Figure 9.

Figure 10 gives an example of the vertical current structure at 29.92°W 3.92°N on June 12 2009 at 8h. Currents measured at the same time by buoy #246 at 4.35°N 29.08°W and 14h earlier by Argo float #3900692 at 3.69°N 29.00°W fall close to the two shallowest ADCP currents, giving support in this case, to intensified near surface currents almost constant above 30 m. These two floats are some 100 km ahead (i.e. to the east) of the ADCP data and it is surprising to find such an agreement, which may be fortuitous. Actually, buoy #42, found (on June 12 at 8h) at the same latitude but 95 km west of the ADCP measurement gives only a 33 cm s^{-1} eastward flow. This doesn't contradict necessarily the idea of a uniformly flowing mixed layer but may show the finiteness of zonal length scales.

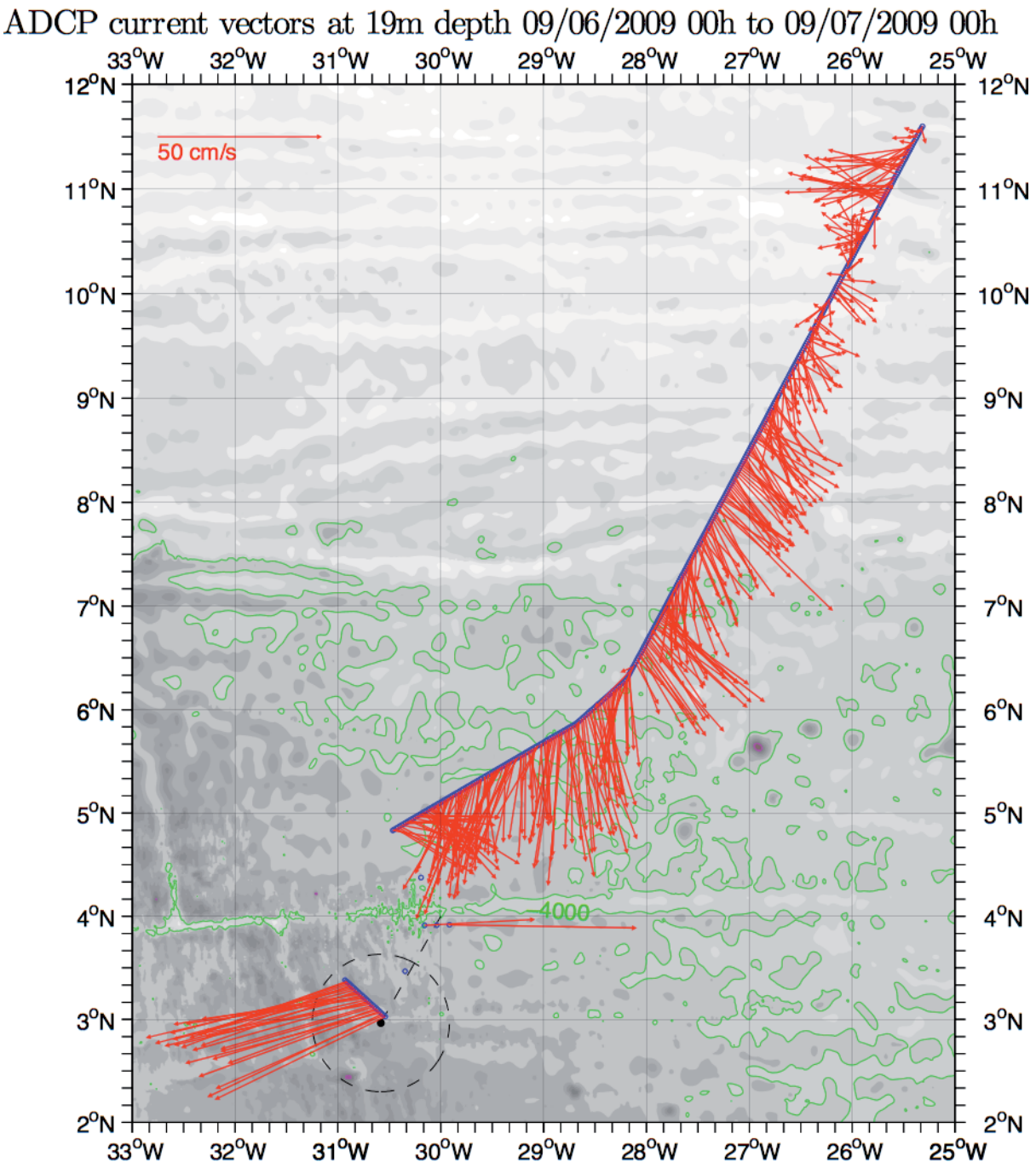

Figure 8 Pourquoi-Pas ADCP 19m depth velocity vectors, between June 9 2009 14h26 and July 8 2009 4h33. There is no measurement between June 14 8h18 and July 8 1h54. One arrow every 2 km. Spatial structures seem larger south of 8°N than in the northern part of the record. The currents measured near LKP on July 8 are completely different from those occurring one month before (the ocean is turbulent with a few days near surface decorrelation time scale)

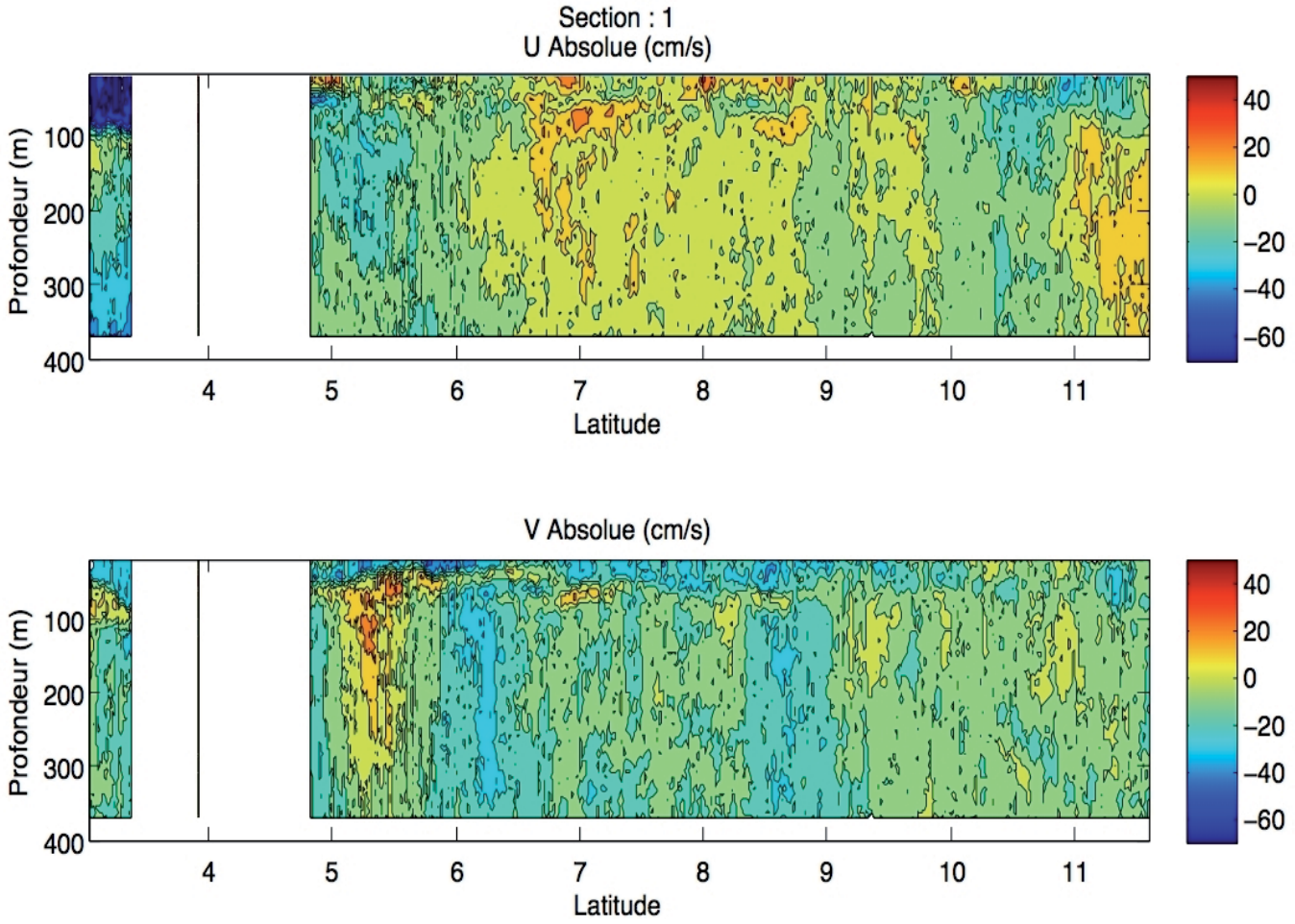

Figure 9 Vertical section showing zonal and meridional ADCP velocity components versus latitude. Note the mixed surface layer roughly 40 m thick between 5°N and 6°N (corresponding dates are June 10 and June 11 2009).

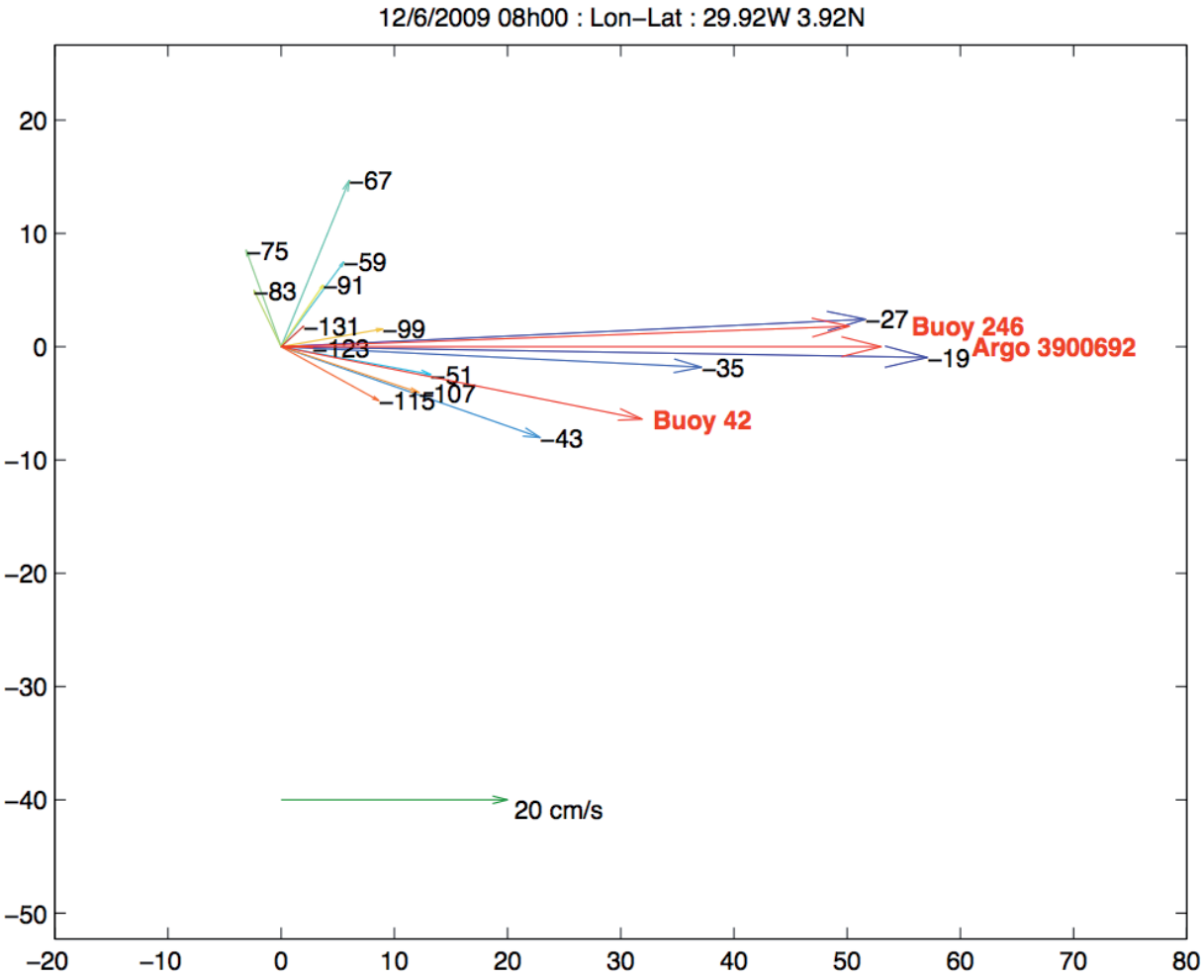

Figure 10 ADCP velocity vectors versus the first 15 depth levels (–19 m, –27 m, –35 m, ...) for station # 388 (near 4°N 30°W). Buoys #246 and #42 velocities on June 12 at 8h. Argo float #3900692 velocity on June 11 at 18h. Buoy #42 is 95 km to the west, while Argo float and buoy # 246 are 100 km to the East and East northeast respectively (see also Figures A2_5 in Appendix 2 or A3_4 in Appendix 3).

Sea surface height

Satellite altimetry is used (since the launching of Topex/Poséidon in 1992) to map the shape of the sea surface. Actually, present altimeters (flying on Jason 1 or Jason 2 for example) can reach a 2-3 cm accuracy on sea level measurement over a distance of 6 km (made within approximately 1 s flight time). However such a sea level is relative to a given ellipsoid and does not give the sea surface height (SSH) relative to the Geoid (which is the potential surface in the earth gravity field which would correspond to the sea surface of a hypothetical motionless ocean). Unfortunately the Geoid is only known accurately enough for the large wavelengths (under 1000 km wavelength Geoid errors are larger than those for sea level).

If we are only interested in sea level variations over time, under a repeat track, we can use directly the sea level anomaly (SLA), which is the difference between the sea level (relative to a given ellipsoid) and the average sea level (obtained from many sea level measurements done at the same position but during many repeat tracks).

Once a barometric pressure correction has been done (roughly, 1 mb increase corresponding to 1 cm decrease) it is simple to get the surface current variations under the quasi-geostrophic[8] approximation. The latter approximation is well verified (within 10%) in the middle and high latitudes. However as one tends toward the equator, it degrades to become a nonsense right at the equator (even though an equatorial approximation exists for the zonal component of the current). Fortunately, the quasi-geostrophic approximation works well even at a few degrees latitude (3° is the practical limit). But this is not the whole story, because we need also the part of the surface current which is directly driven by the momentum imparted by the wind.

If we want the absolute quasi-geostrophic current we must rely on SSH (relative to the Geoid) instead of SLA. To circumvent the uncertain knowledge of the Geoid, a mean “dynamic” topography (MDT) is estimated using in situ data or OGCM velocity field (see Rio & Hernandez, 2004). Then we assume that this MDT is a good approximation of the true mean SSH, whence SSH = MDT + SLA.

Besides Jason1 and Jason2 which fly at a 1336 km altitude and cover the Earth surface (between 66°S and 66°N) in 10 days, EnviSat also does altimetric measurements but covers the earth surface

[8] Or geostrophic (depending on authors). Quasi here is for approximate.

(between 81°S and 81°N) in 35 days instead (it flies at 800 km altitude and the inter-track distance on the equator is 80 km (compared to 315 km for the Jasons). Only one ascending track of Jason1 and one descending track from Jason2 fall close to LKP (within 40 km) respectively on June 1 at 16h 18 and June 3 at 3h 48.

Figure 11 shows the cross track component of the quasi-geostrophic current given by: $v = \frac{g}{f}\frac{\partial SSH}{\partial y}$, where y is the along track distance, g the earth gravity (9.8 ms^{-2}) and $f \equiv 2\Omega \sin\varphi$ the Coriolis parameter (Ω is the earth rotation rate, and at the latitude $\varphi = 4°$ N, $f \approx 10^{-5}$ (rd) s^{-1}).

One could then use the superposition of the quasi-geostrophic velocity field (estimated by SSH = MDT + SLA) and a model of the wind generated surface current (like the simple slab model for the well mixed layer as seen on Argo profiles) to follow particle motions on the sea surface (see Gill, 1982 e.g.). A related approach combining equatorial and off-equatorial geostrophic estimations, with steady state wind generated surface currents (Lagerloef et al., 1999) is described in Appendix 6. This is the Surcouf model run at CLS.

However the present MDT is accurate enough only for wave-length of the order of 300 km or greater. In this near equatorial region, meridional scales for the mean circulation are of the order of 100 km, and even if we knew the (absolute) mean circulation perfectly, the inter-track distance (~ 300 km for the Jasons) would preclude the precise estimation of the actual velocity field over the O(100 km by 100 km) region concerned by our problem.

Nevertheless SLA data is very important when assimilated in OGCMs, whether the MDT is independently determined (an example is Rio & Hernandez, 2004) or it is estimated within the model itself (or via a lower resolution model). Actually, SLA allows constrain changes in elevation due to large-scale currents and changes due to local density variations. Multivariate data assimilation methods calculate corresponding changes in temperature and salinity that are used by the model to correct its currents (more on that in chapter III).

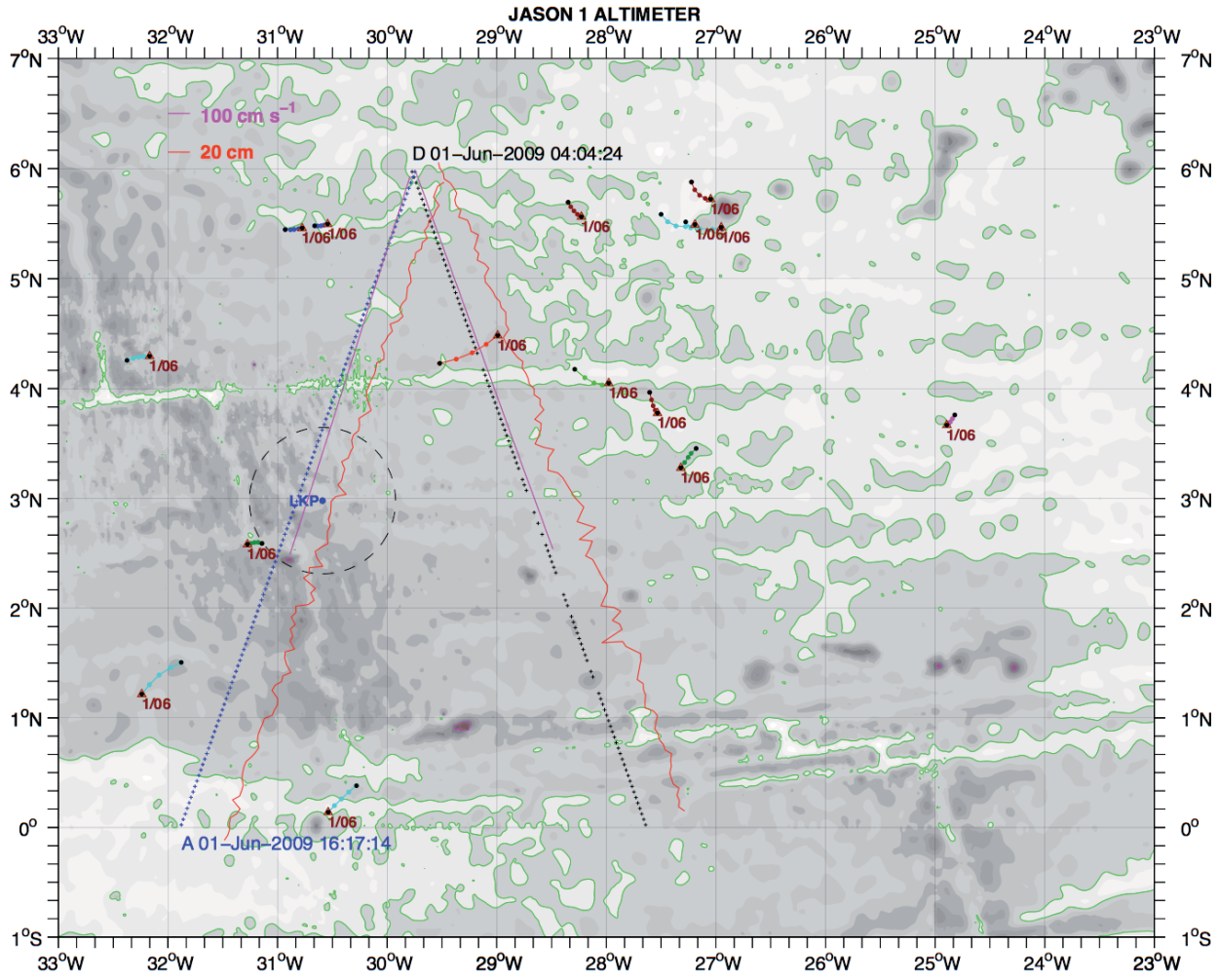

Figure 11 Jason 1 altimeter tracks on June 1 2009. The ascending (A) track falls close to LKP, but only the very large-scale quasi-geostrophic cross-track current below the mixed surface layer can be estimated (possibly eastward at 30 cm s^{-1}). Obviously, the variable surface currents (shown by the 24h buoy displacements) are not quasi-geostrophic and not directly related to these lower-frequency underneath currents. The plot using SLA instead gives almost the same quasi-geostrophic current estimates. SSH is plotted (red) to the right of the satellite tracks, and the quasi-geostrophic current component normal to the track is given by the magenta smooth curve, whose distance to the track is proportional to the velocity.

Sea surface temperature and colour of the sea

Sea surface temperature (SST) can be deduced from passive radiometers (on board satellite) measuring microwave or infrared radiations emitted by the sea surface. Figure 12 shows such SST estimates from different instruments and methods (we do not detail, but see for example Stewart, 1985 for the physics involved).

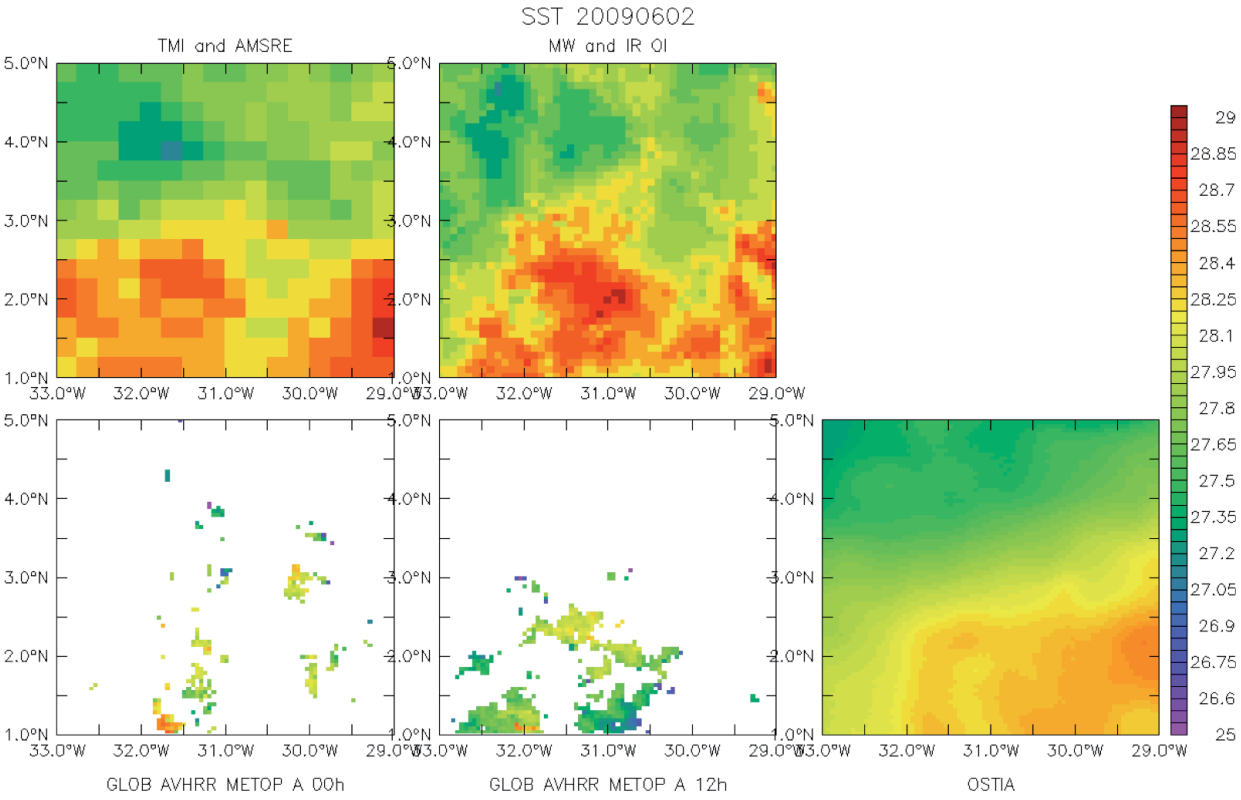

Figure 12 TMI and AMSR-E are μ-wave radiometers and AVHRR a multi channel IR radiometer. The Objective interpolation (OI) and OSTIA are reconstructed SST fields from REMSS and UK Met office respectively.

Infrared (IR) radiations do not pass through the clouds, which is why there are so few data with the IR radiometer on board METOP. Note also the biases between the IR and μ-wave instruments. Obviously OSTIA is a low passed SST field. There are nevertheless similarities in the different SST fields, and the REMSS Optimal Interpolation does show some structure that can be related to the current field to be shown later (for instance, the two relatively cold patches centered at 32°W 2°N and 30°W 3°N are associated with cyclonic motion, i.e. “contra solem”). It is however difficult to be more precise and the evolution of SST is not easily related to the particle motions. Some SST structures can also correspond to the fresh water of the rainfalls.

In the region and over the period concerned, Chlorophyll content (which gives its colour to the sea) as remotely sensed by satellite is difficult to interpret because of the rainfalls and because of the complexity of the dynamics. Actually the links between the thermodynamics and the biogeochemistry is very complex.

Winds

A good knowledge of the near surface winds is requested since the momentum imparted to the sea is one of the main forcing which drives the ocean circulation (other forcing are the heat fluxes through the air-sea interface, the precipitation and evaporation together with the river runoffs and the tidal forces).

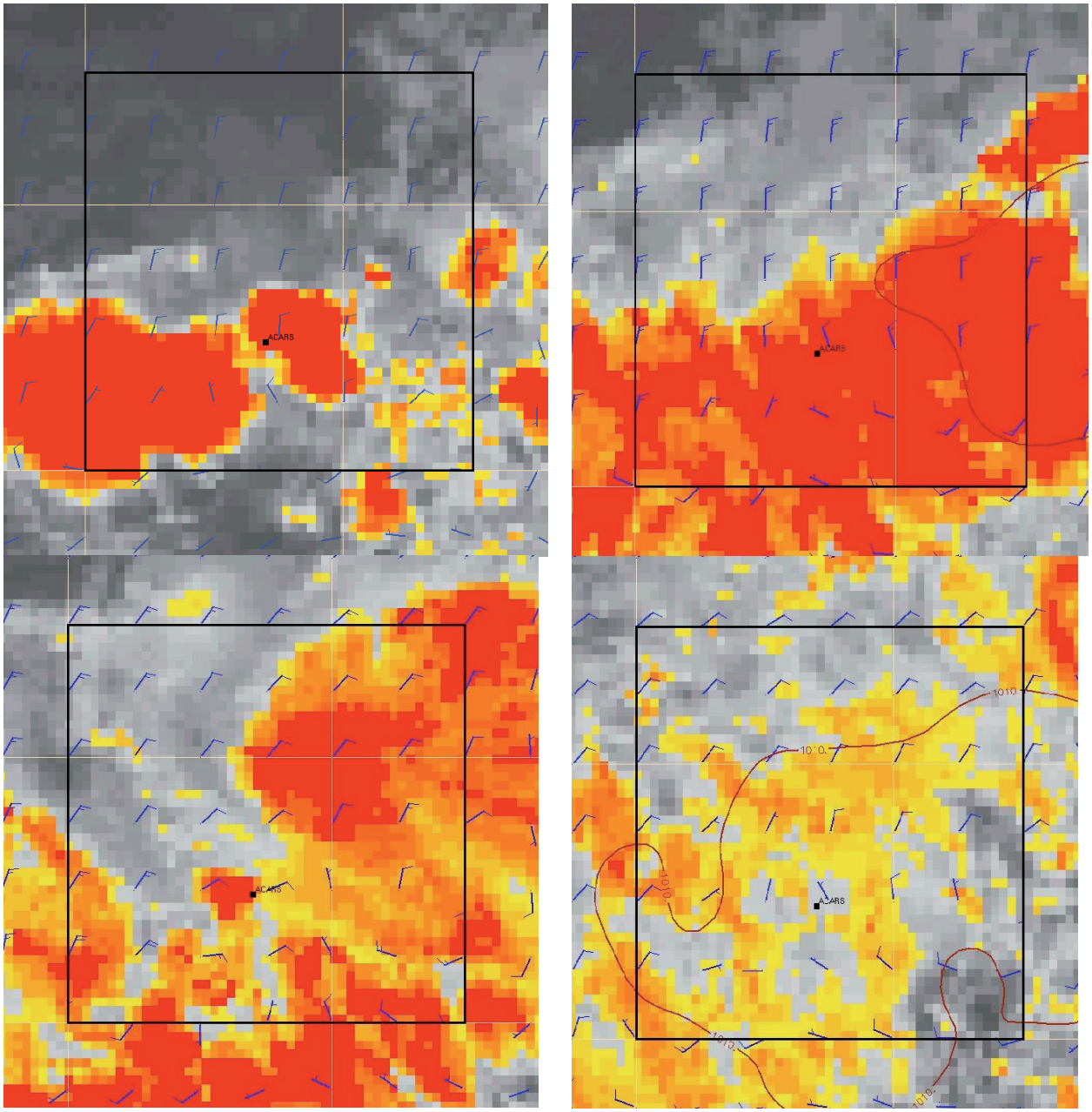

Figure 13 June 1 2009 ECMWF winds and sea-level pressure, cloud temperature less than -40°C are shown orange and red. Top left 0h, top right 6h, bottom left 12h and bottom right 18h. Limits of the 3°x3° black square are 2°N and 5°N in latitude, 29°W and 32°W in longitude. Similar plots for the following days are given in Météo-France (2010) report.

Several wind products are available for our study area and period. All come from numerical weather prediction (NWP) models assimilating a large amount of meteorological data (measured in-situ or remotely).

Three global (i.e. world covering) wind fields have been used: NCEP (named after the National Centers for Environmental Prediction), ECMWF (named after the European Center for Medium-range Weather forecast) and an experimental version of ARPEGE from Météo-France. Actually, both the operational products and their reanalysis (NRA-2, ERA Interim) were used. A reanalysis is a new run of the model but with assimilation of more and fully validated past data (thus it is not a forecast but a "hindcast"). Time resolution is four times daily (0h, 6h, 12h and 18h) and the spatial grid is a 0.5° regular one in longitude and latitude over the ACARS zone. However, the ARPEGE version has a finer 0.18° mesh size and 1 hourly wind outputs (see C. Payan report for details).

Figure 13 shows the ECMWF winds (at 10 m above the sea surface) and cumulonimbus clusters on June 1 every 6h. Southward winds are prevailing north of LKP, and there is a strong convective activity (with heavy rains) over the zone except in the Northwest. During the following days winds slackened and veered to easterly trades, while the convective activity decreased drastically.

Figure 14 gives the (equivalent 10 m height) wind field as obtained from QuikScat over the 6-day period (June 1 to 6 2009) during which debris and bodies drifted before being sighted and recovered. QuikScat is a sun-synchronous satellite (flying at 800 km altitude and with a 99° inclination angle on equator) with an onboard scatterometer which can measure wind stress vectors on the sea surface. Actually it is the wind stress $\boldsymbol{\tau}$ which matters physically and consequently these measurements are fundamental to assess the quality of the NWP wind fields.

Wind velocity vector $\mathbf{W}_{10\mathrm{m}}$ is related to $\boldsymbol{\tau}$ by the relation:

$\boldsymbol{\tau} = \rho_{air} \cdot C_{drag} \cdot \left\|\mathbf{W}_{10m}\right\| \cdot \mathbf{W}_{10m}$ with C_{drag} a slowly varying function of $\left\|\mathbf{W}_{10m}\right\|$ and air stratification (or stability).

Unfortunately, backscatter from surface capillary ripple waves of the 13.4 GHz EM pulse scatterometer signal, from which the wind speed component along the radar antenna direction[9] is estimated, is

[9] QuikScat antenna was revolving, thus allowing to obtain the exact wind direction

highly corrupted by rain. That is why there is a large blank zone on June 1 at 7h 40 min in Figure 14 upper left panel.

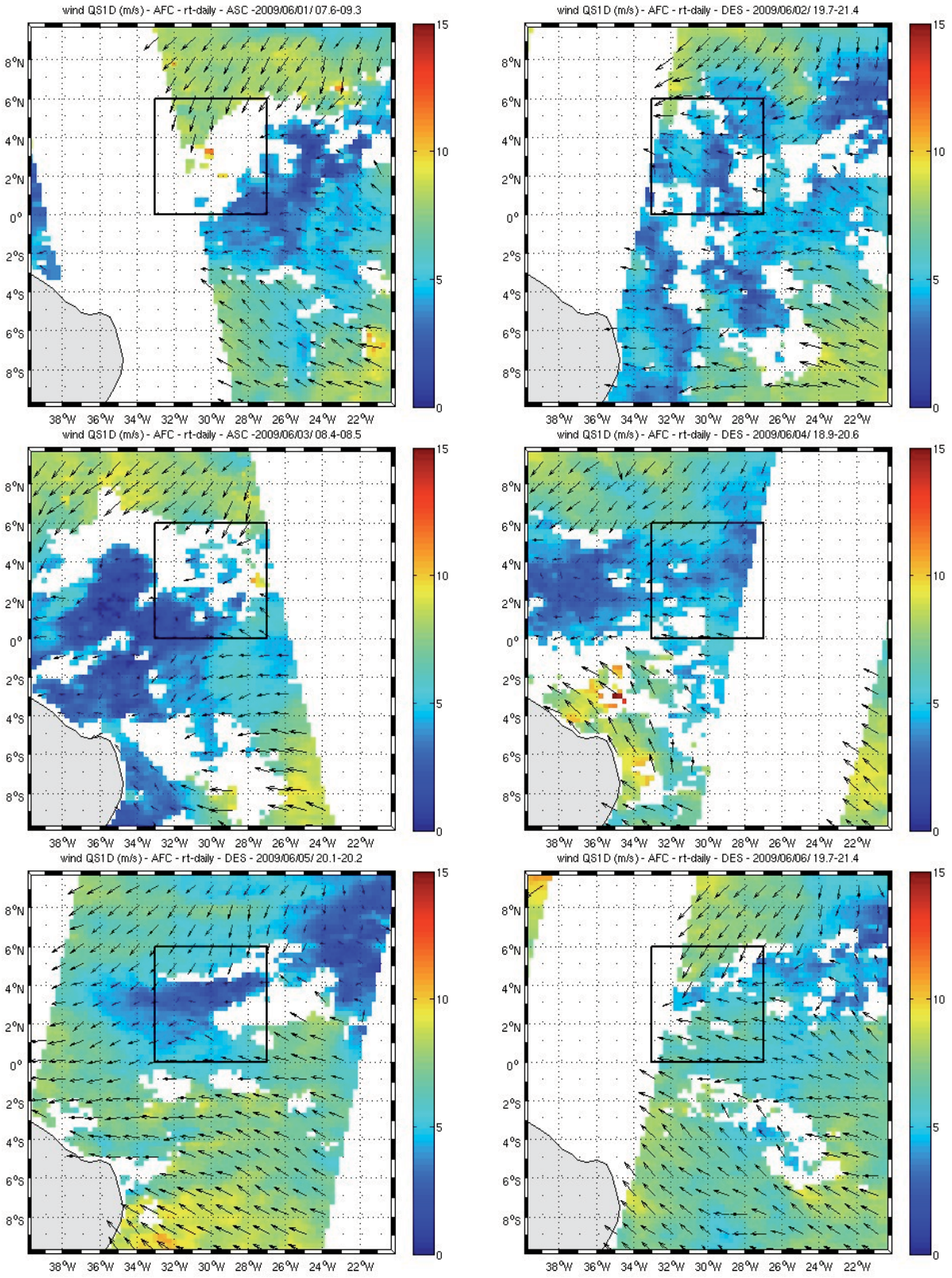

Figure 14 QuikScat wind measurements over June 1 to 6 2009. Units are m s^{-1}. ASC and DES means ascending and descending tracks (around 8h and 20h respectively). Only a few of the wind vectors are plotted for the Figure clarity.

By and large, QuikScat data validates the ECMWF wind field, at least north of LKP. However at a few places, there can be large deviations for the ECMWF directions.

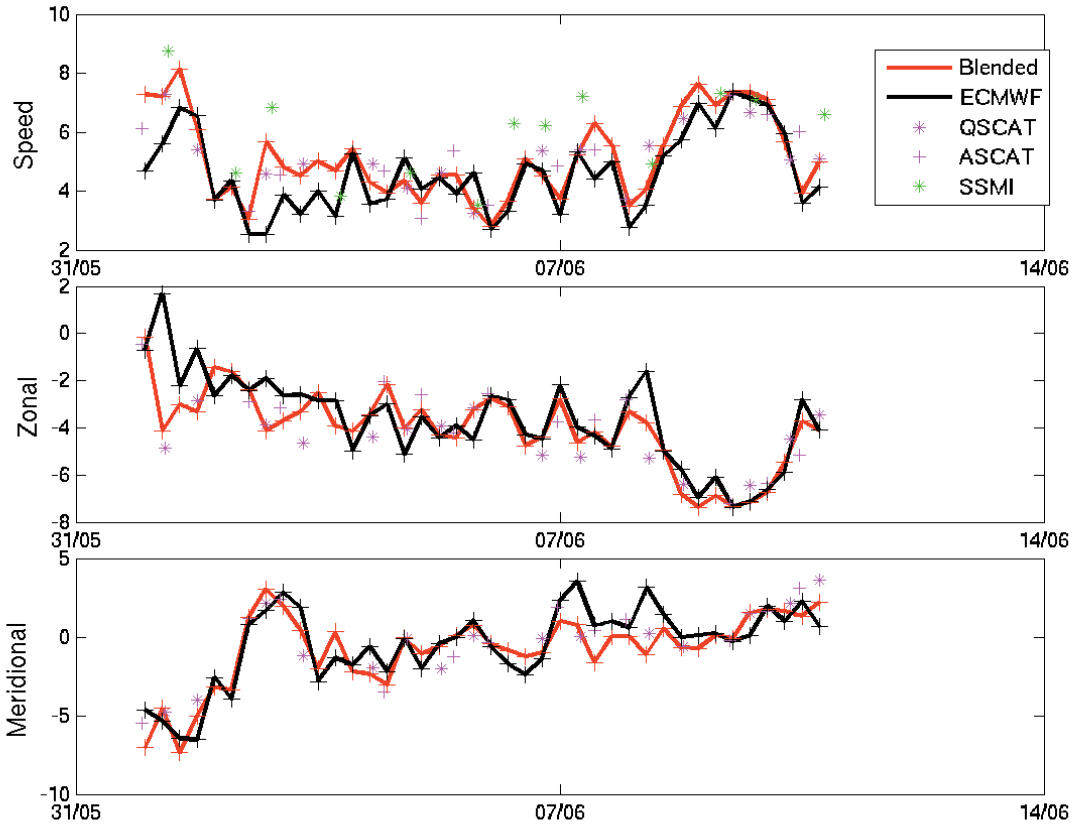

Figure 15 Time series of 10 m height wind velocity at 31°W, 3°N, as seen by ECMWF and Cersat HR blended product. Measurements from QuikScat, Ascat and SSMI. Units are m s^{-1}.

That is why refinements of the wind fields have been proposed for use in this study, based on a full use of all scatterometer (AScat, QuickScat) and μ-wave radiometer (SSMI, AMSR-E) data, blended with reanalysed NWP outputs.

Two such products will be used: the 1/8° Cersat[10] HR (for high resolution) blended fields and the 1/4° NOAA blend fields. Figure 15 shows the comparison between ECMWF and Cersat HR blended at 31°W, 3°N together with satellite sensed data (Complementary details can be found in A. Bentamy & D. Croizé-Fillon report). Figure 16 shows an example of various wind estimates available over the region.

[10] Centre d'exploitation et de recherche satellitaire (in Brest)

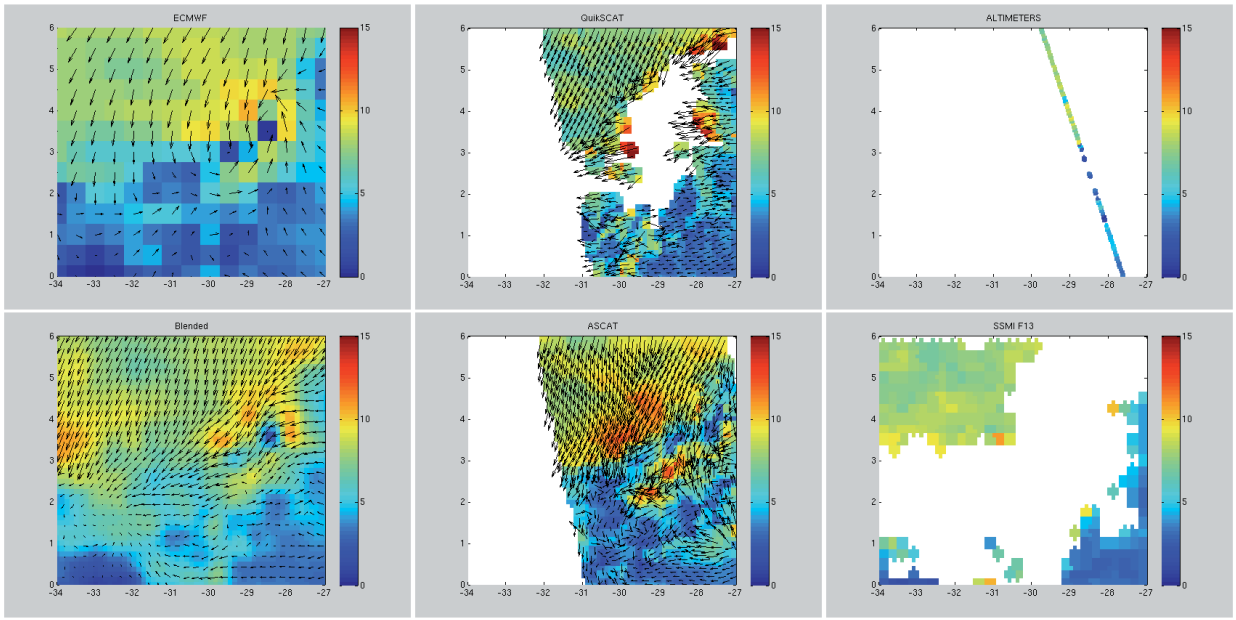

Figure 16 Wind fields for June 1 2009 near 6h (± 3 h) as estimated from ECMWF, Cersat HR Blended, and measured by QuikScat, AScat and Jason1 altimeter and SSMI onboard F13 satellite (only the wind speed can be obtained with the latter two). Actually AScat pass occurred on May 31 at 23h50.

ARPEGE winds have also been compared with scatterometer winds, but generally the agreement seems inferior to that of ECMWF. Full details are given in Météo-France (2009) report. See also Figure 26.

Finally, a local HR (1/12°) wind field named WRF (Wind Research Forecast) has been obtained as the output of a nested model, driven by the global NCEP reanalysis NRA-2.

There are other valuable wind products such as NOGAPS for example, which is used as the forcing wind field for the HYCOM and NCOM OGCMs (only HYCOM has been used in our study).

Bodies and debris

It is important to recall that one of the basic assumptions for the estimation of the search zone is that the debris sighted and retrieved after June 5 split apart when the aircraft collided with the sea and, therefore, that their displacements and relative scatter the days following the crash are only due to the effects of currents and winds. This assumption results from the examination of the debris, as detailed in the first two interim reports issued by the BEA.

Two kinds of difficulties were met when trying to compute the backward drift of these debris and bodies, namely getting validated data regarding their retrieval dates and positions on the one hand and estimating their behaviour in the water on the other hand[11].

The reported positions of recovery were validated for most of the objects and bodies by using data such as the records from the AWACS airplane deployed on site by the French army, or from recorded positions of the ship Ventôse. These data were made available to the group by the French Ministry of Defence.

As for the behaviour of the debris and bodies in the water, under the action of currents, waves and wind, it is difficult to be very precise. The wind and current drag will depend of the immersion rate and the geometry of the debris considered. Generally the slippage velocity (that is the object velocity relative to the surface current) is estimated as a few percent of the wind vector. Actually the drag force due to the wind on an object at rest is given by $\rho_a C_a S_a \|\mathbf{W}\|\mathbf{W}$, where ρ_a is air density, S_a the object area normal to the wind vector $\mathbf{W}$. C_a is a non dimensional number called the drag coefficient, of the order of one, but whose exact value depends on the body geometry and the wind turbulent character. A similar expression can be given for the sea current ($\rho_w C_w S_w \|\mathbf{U}\|\mathbf{U}$, where $\mathbf{U}$ is the current vector and the index w is for water). The action of the waves is generally included in the surface current. If there is no acceleration of the object, it is easy to obtain the slippage velocity as $\mathbf{v}_{slip} \approx \left(\frac{\rho_a S_a C_a}{\rho_w S_w C_w}\right)^{1/2} \cdot \mathbf{W} = \alpha \cdot \mathbf{W}$. We do not know C_a and C_w, and it is unfortunate that no experimental data exist for most of the objects recovered. However, we generally assume $C_w \approx C_a = 1$, $\rho_w/\rho_a \approx 800$, but we still do not know the immersion rates. A notable exception concerns a case (43x28x16 cm^3, 11.6 kg) found 3 km away from the Galley G2 one hour later (16h10 on June 6), which means they may have drifted close together. Its immersion rate $I = S_w/(S_w+S_a)$ is known ($I \approx 0.6$), which allows to estimate $\alpha^2 = (1-I)\rho_a/\rho_w I$, thus $\alpha \approx 0.0285$ (or 2.85% of the wind velocity). This value should also apply to G2.

In the following two chapters we shall generally use α values constant over time, explaining how we can gain confidence in the

---

[11] We do not speak here of the ocean surface velocity estimation (the main subject of the next two chapters) nor of the wind estimation (already discussed).

values retained. We shall also explore the possibility of a crosswind component (see the section on MOTHY, chapter III).

Regarding the bodies proper, it was possible to estimate the density of some of them by using the results of the autopsy report and the Boyd (1935) as well as the Sendroy and Collison (1966) formulae. Then, considering the Henssge (1988) formula, it was possible to approximate the time needed for the body to reach the equilibrium temperature with the environment (including the surface waters)[12]. For these bodies (the first ones recovered and entire) it could be inferred they most likely reached the equilibrium temperature during the first three hours after the crash and that the colliquative putrefaction started during the first 24 h, and developed over a short time duration as compared to 24 h (water temperature was about 27-28°C for many days). From the body examinations, it is assumed that entire bodies did not loose any significant amount of mass during the first 24 h. At the same time their volumes increased, as a consequence of the creation of putrefaction gas.

Thus, the evolution in time of an entire body density can perhaps be modelled simply as follows:

- during the first 24 h, the state of the body did not evolve significantly and its density remained close to that of the surface water,
- shortly after and on the following days (till the recovery) the body volume was inflated on the order of 50% (compared to the initial volume) implying a 2/3 immersion rate). Thus 24 h after the crash a body density is of the order of 0.7 kg dm^{-3}.

Note that the crew of the Ventôse reported that the bodies recovered on June 7 were floating with approximately 60% immersion rate. This information is consistent with the above-mentioned estimate.

Table 1 below gives a short list (positions and dates) of debris and bodies sighted or recovered on June 5, 6, 7, 8 and 9. Those which are highlighted by their initials were mainly used for the computation of forward and backward drifts presented in the next two chapters.

---

[12] Corrective factors must be applied to account for the fact that bodies were wearing clothes and were in non-stagnant water because of the waves. Other factors such as the exposure to sunlight can further influence the result.

Table 1

Ursulla sighting	U	June 5 2009 at 16h10	3.63N	30.45W
Brazilian sighting 1	S1	June 5 2009 at 21h02	3.56N	30.44W
3m part sighting 2	S2	June 6 2009 at 10h59	3.47N	30.47W
Galley G2[13] (sighted)	G2	June 6 2009 at 11h06	3.47N	30.66W
First two bodies	BB	June 6 2009 at 11h55	3.57N	30.46W
Galley G2 (recover.)		June 6 2009 at 15h00	3.47N	30.66W
Case		June 6 2009 at 16h10	3.46N	30.63W
Body E1 (sighted)	E1	June 7 2009 at 9h11	3.65N	30.51W
Vertical fin(sighted)	VTP	June 7 2009 at 13h38	3.61N	30.62W
Body 2Z (recover.)		June 7 2009 at 16h39	3.70N	30.50W
Body 3Z (recover.)	3Z	June 7 2009 at 17h17	3.73N	30.48W
Body 6Z (recover.)		June 7 2009 at 17h29	3.74N	30.48W
Body 4Z (recover.)		June 7 2009 at 17h41	3.75N	30.47W
Vertical fin(recover.)		June 7 2009 at 18h35	3.47N	30.68W
Body 5Z (recover.)		June 7 2009 at 18h55	3.73N	30.47W
Body 7Z (recover.)		June 7 2009 at 20h35	3.75N	30.47W
Body 8Z (recover.)		June 8 2009 at 16h58	4.04N	30.46W
Body 9Z (recover.)		June 8 2009 at 17h25	4.03N	30.45W
Body 10Z (recover.)		June 8 2009 at 17h50	4.06N	30.44W
Body (recover.)		June 8 2009 at 18h34	4.06N	30.43W
Body (recover.)		June 8 2009 at 19h25	4.08N	30.43W
Body (recover.)		June 8 2009 at 19h56	4.09N	30.43W
Body 11Z (recover.)		June 9 2009 at 9h45	4.25N	30.44W
Body 12Z (recover.)		June 9 2009 at 10h16	4.25N	30.43W
Body 13Z (recover.)		June 9 2009 at 11h02	4.25N	30.41W
Body 14Z (recover.)		June 9 2009 at 12h29	4.27N	30.42W
Body 15Z (recover.)		June 9 2009 at 12h56	4.27N	30.43W
Body 16Z (recover.)		June 9 2009 at 13h29	4.31N	30.45W
Body 17Z (recover.)		June 9 2009 at 14h21	4.31N	30.51W
Body 18Z (recover.)		June 9 2009 at 15h45	4.35N	30.52W
Body 19Z (recover.)		June 9 2009 at 15h45	4.35N	30.52W
Body 20Z (recover.)		June 9 2009 at 16h24	4.41N	30.52W

[13] Not fully confirmed

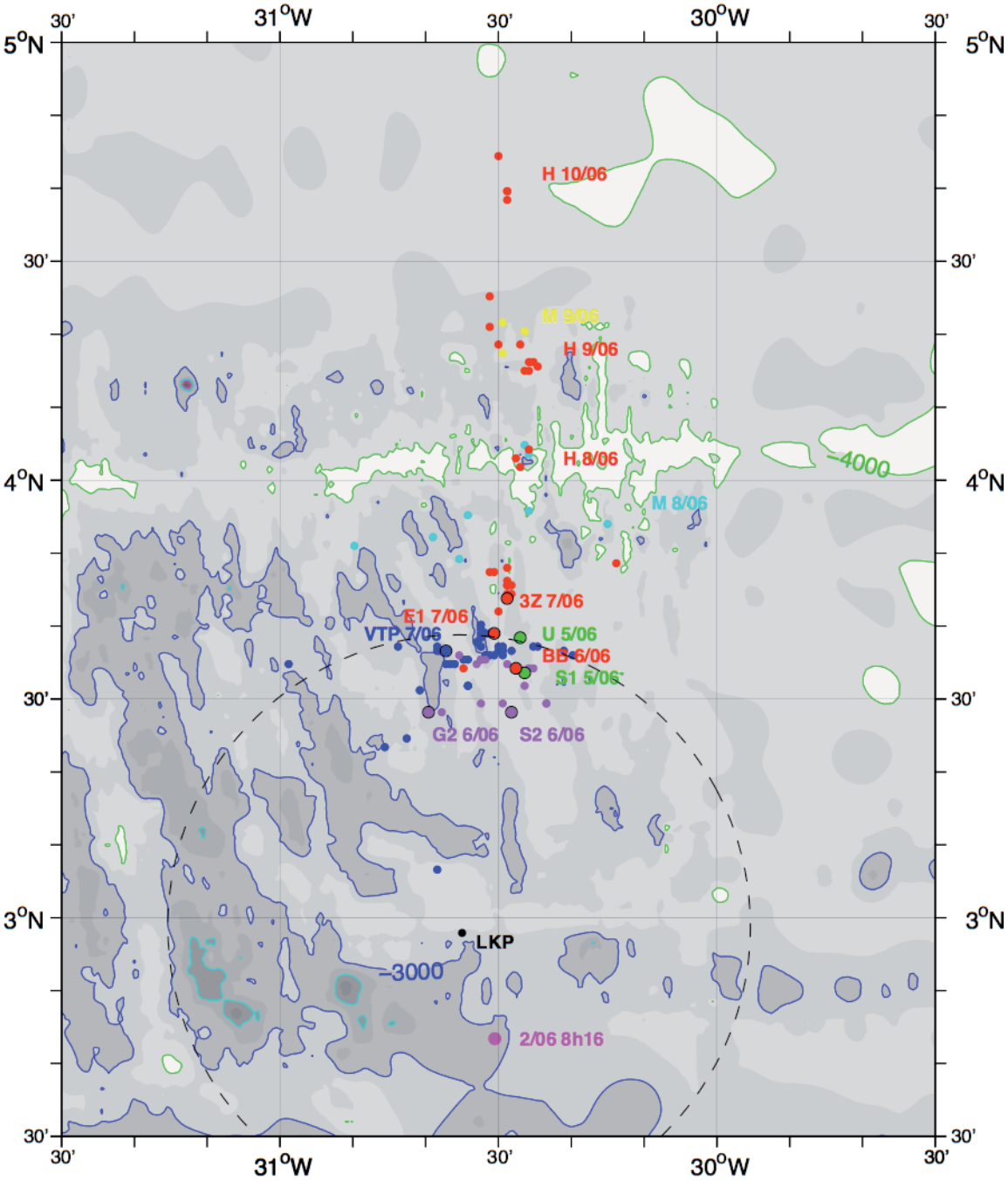

Figure 17 Distribution of the bodies (red dots) and debris (color coded: green on the 5th, purple on the 6th, blue on the 7th, cyan on the 8th and yellow on the 9th of June). Bigger dots refer to the eight particles identified by their initials in Table 1. The pink dot south of LKP is a possible pollution spot SAR detected on June 2 at 8h16 (see Appendix 7 for details). Many more material parts were sighted or recovered on June 8 and later on, than shown here. But we have not used them in our study. M means material, H human remains in the Figure. The two red dots positioned at 3.57N 30.58W and 3.81N 30.23W were only sighted as probable bodies (thus they are not given in Table 1).

II Determination of the wreckage area using in situ observations

Optimal estimation of the velocity field

We have shown in the preceding section that all in-situ measurements were generally consistent, and we can now estimate the current field in the ACARS zone.

To determine the spatial and time structure of the surface velocity field, to be used later for tracking particles (either backward or forward), we have used a linear combination of all the available measured current data (from surface drifters, Argo floats and marginally ADCP) minimising the mean square error of the sought after estimate (Bretherton et al., 1976). Currents derived from sea surface height are not included in this analysis.

Briefly, given N velocity vector observations $\mathbf{u}(\mathbf{x}_i)$, i=1,…,N at a given time, and assuming they are sampled from a turbulent 2D velocity field, the minimal mean square error linear estimate of $\mathbf{u}(\mathbf{x})$ is obtained as $\mathbf{u}(\mathbf{x}) = \mathbf{C}_\mathbf{x}\mathbf{A}^{-1}\varphi$, where $\varphi^t = [u_1(\mathbf{x}_1), u_1(\mathbf{x}_2), \ldots u_1(\mathbf{x}_N), u_2(\mathbf{x}_1), u_2(\mathbf{x}_2), \ldots, u_2(\mathbf{x}_N)]$ is the row vector of observations, and $\mathbf{C}_\mathbf{x}$ the 2×2N covariance matrix between observations and the velocity vector to be estimated (indexes 1 and 2 refer to zonal and meridional components):

$\mathbf{C}_\mathbf{x}^{(1)}=E[u_1(\mathbf{x})\bullet u_1(\mathbf{x}_1),\ldots,u_1(\mathbf{x})\bullet u_1(\mathbf{x}_N),u_1(\mathbf{x})\bullet u_2(\mathbf{x}_1),\ldots,u_1(\mathbf{x})\bullet u_2(\mathbf{x}_N)]$

for the zonal component (similarly for the meridional one).

A is the 2N×2N covariance matrix between all pairs of observations:

$$A_{r,s} = E[u_1(\mathbf{x}_r)\bullet u_1(\mathbf{x}_s)] + \varepsilon\delta_{rs}$$
$$A_{s+N,r} = A_{r,s+N} = E[u_1(\mathbf{x}_r)\bullet u_2(\mathbf{x}_s)]$$
$$A_{N+r,N+s} = E[u_2(\mathbf{x}_r)\bullet u_2(\mathbf{x}_s)] + \varepsilon\delta_{rs}$$

ε is the assumed measurement error (instrumental or local sampling error).

Mean square error (mse) on the zonal component is given as:

mse $(u_1(\mathbf{x})) = E[u_1(\mathbf{x})\bullet u_1(\mathbf{x})] - \mathbf{C}_\mathbf{x}^{(1)}\,\mathbf{A}^{-1}\,\mathbf{C}_\mathbf{x}^{(1),t}$ and similarly for the meridional component.

With an assumed 2D homogeneous and isotropic turbulent field, the velocity covariances can be derived from two scalar functions f(r) and g(r), the longitudinal and tranversal covariance functions (see Davidson, 2004 e.g.) with

$$E[u_i(\mathbf{x})\bullet u_j(\mathbf{x}+\mathbf{r})] = \cos\theta_i\bullet\cos\theta_j\bullet(f(r) - g(r)) + g(r)\delta_{ij}$$

(θ_i being the angle between **r** and the i axis)

If we further assume the velocity field is non divergent, there exists a stream function ψ such that u =-∂ψ/∂y v =∂ψ/∂x. Then f and g can be derived from the stream function covariance F(r)= E[ψ(**x**)ψ(**x**+**r**)] as rf = -dF/dr, and g = d(rf)/dr.

We have done such a non divergent analysis for the period May 30 to June 14, every 6h, with ε = 0.025·EKE (EKE meaning eddy kinetic energy) and we have used the analytical formulation for F (whence f[14] and g) given in (Colin de Verdière, 1986). The longitudinal and transversal covariance functions were estimated from the surface current data (Figure 18) and the needed spatial scale factor of F, f and g estimated from the data fit. It is no surprise to find a zero crossing of the order of 200 km for the transversal function in this near equatorial region (Internal Rossby radius is of the same order).

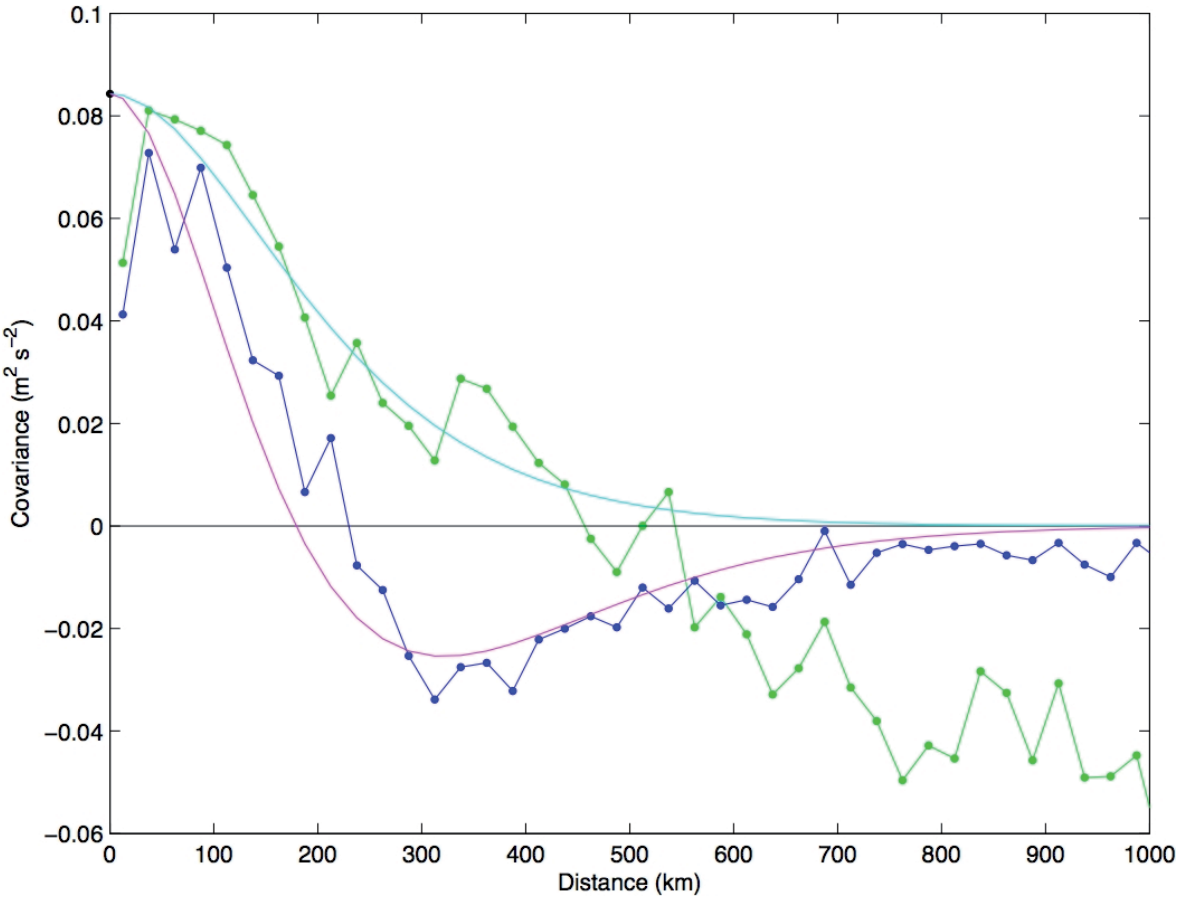

Figure 18 Longitudinal and transversal function analytical forms (after Colin de Verdière, 1986) fitted to the available Drifter and Argo float data within the region 40°W 20°W, 2°N 10°N and for the months of May and June 2009.

[14] $f = \mathrm{EKE} \cdot \exp(-\frac{r}{r_0}) \cdot \left(1 + \frac{r}{r_0} + \frac{1}{3}\left(\frac{r}{r_0}\right)^2\right)^2$

For the optimal estimation[15], we have selected all the observed currents within the rectangle 40°W 20°W, 0°N 8°N, but we have estimated the surface current field in the smaller zone 33°W 27°W 1°N 6°N. Figure 19 shows the optimal interpolated field for June 4 at 12h as an example.

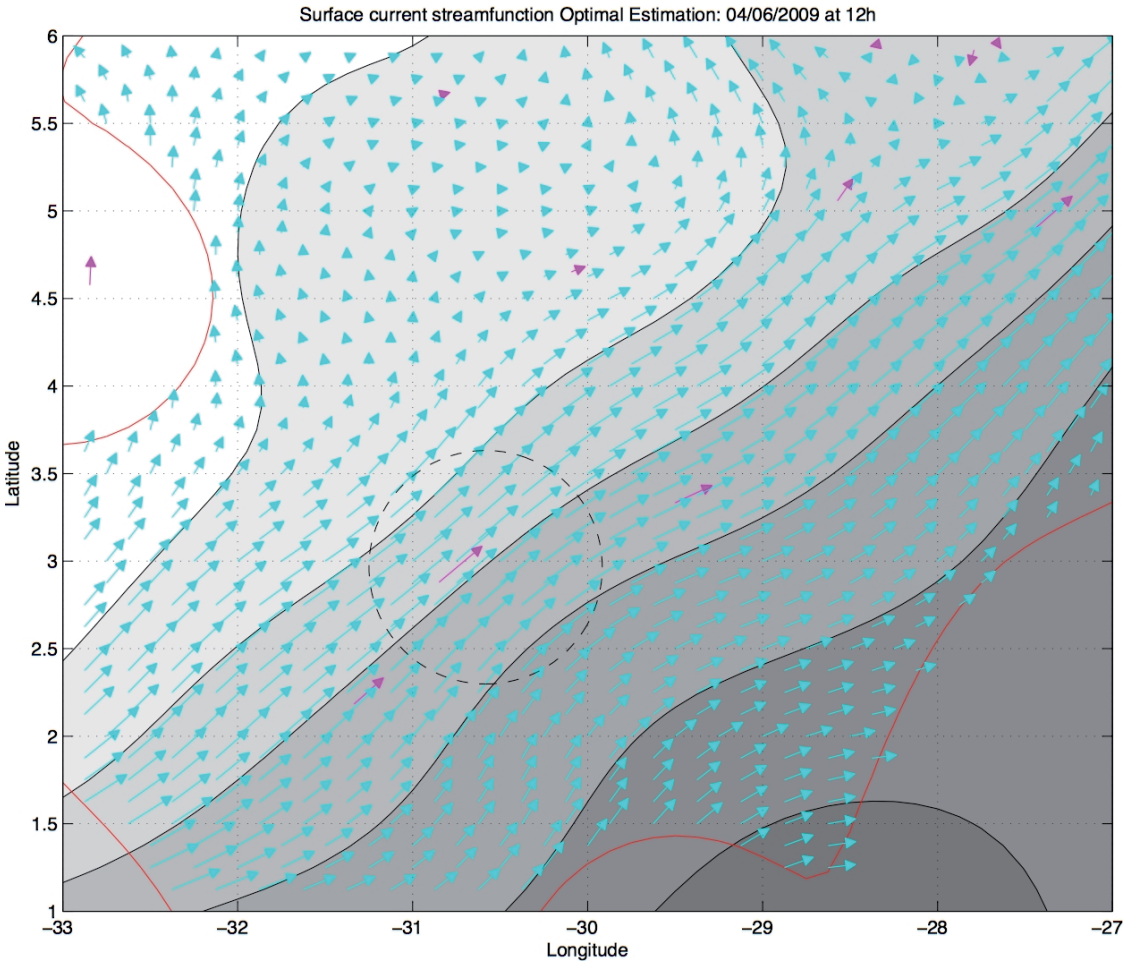

Figure 19 The optimally estimated velocity field on June 4 at 12h. Magenta vectors give the observed currents and cyan vectors the reconstructed velocity vectors within the region (limited by the red curve) where the (normalised) mse is less than 0.4. Dotted circle is the ACARS circle. Vectors are shown as daily displacements.

The ψ, f and g covariance functions depend on only one parameter r_0 (homogeneous to a distance). r_0 = 85 km from the fitted f and g in Figure 18. A smaller value (r_0 = 50 km) has also been tried to resolve slightly smaller scales, but with less statistical confidence (greater mse).

[15] Also called optimal interpolation or objective analysis, or objective mapping. We shall use interchangeably these terms, which may not satisfy the purist.

Figures 20 and 21 give the situation on June 1 at 12h with r_0 = 85 km and r_0 = 50 km respectively. Both reconstructions give very similar results, but with slightly stronger currents for r_0 = 85 km. Note that in both estimations there is a west southwest flow near the northern part of ACARS circle, contrary to most OGCM, even with data fitted (see the following chapter on models). In our case this west-southwest flow is due to the presence of a strong current near 4.5°N 29°W and to the longitudinal correlation at a 150km distance.

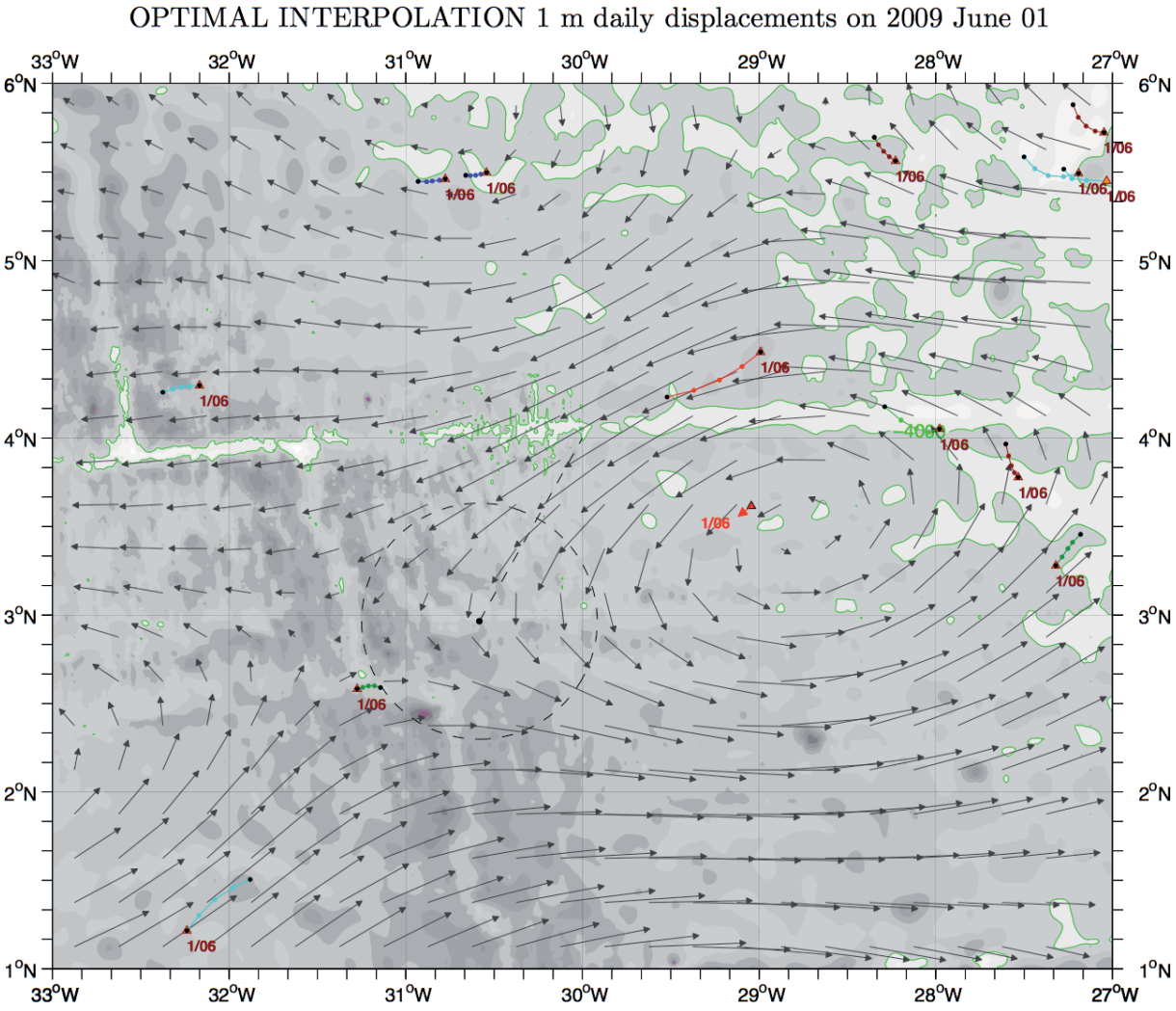

Figure 20 Estimated surface circulation on June 1 around 12h, with r_0 = 85 km. Vectors are shown as daily displacements. Surface buoys trajectories over 24h on June 1 2009 with positions every 6h, starting at the triangle symbol. Although the agreement is very good close to the data, there may be small scale structures not resolved in this kind of analysis.

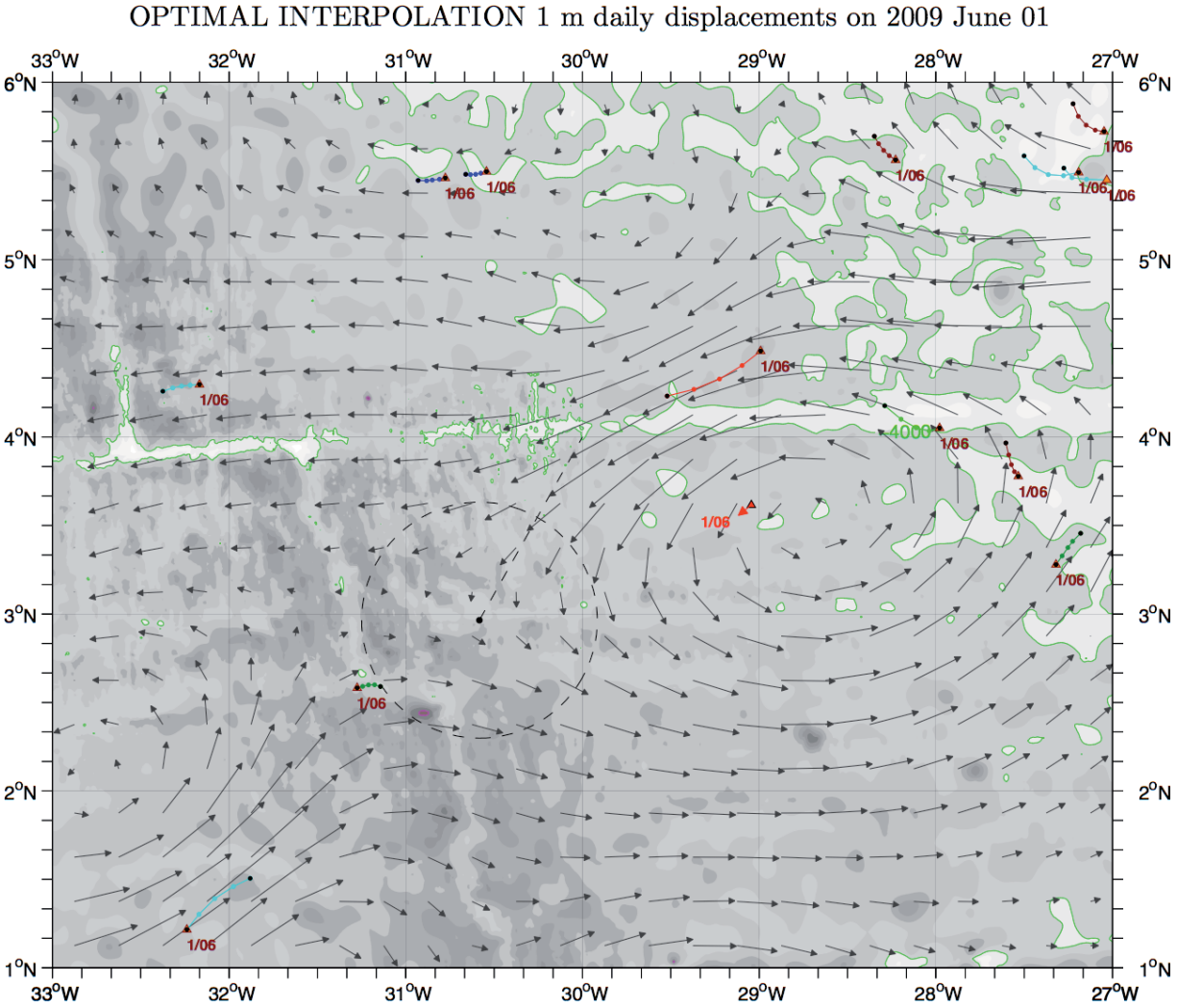

Figure 21 Estimated surface circulation on June 1 around 12h with r_0 = 50 km. Vectors are shown as daily displacements. Surface buoys trajectories over 24h on June 1 2009 with positions every 6h. Near the north of ACARS circle, currents are smaller than in the reconstruction with r_0 = 85 km.

Which reconstruction (r_0 = 50km, 85 km or an intermediate value?) is best for our problem will be discussed later. From now on we present the analysis with r_0 = 85 km.

Figure 22 gives an overview of the variation of the currents over the ACARS zone from June 1 until June 6, when the first debris and bodies were recovered. Only the situations around 12h are given (recall however the estimations are available every 6h). There is a westward propagation of the current structure, (whether a turbulent eddy or a tropical instability wave) apparent until June 4. On June 5 and 6 there is a saddle point (weak currents) near the north of ACARS.

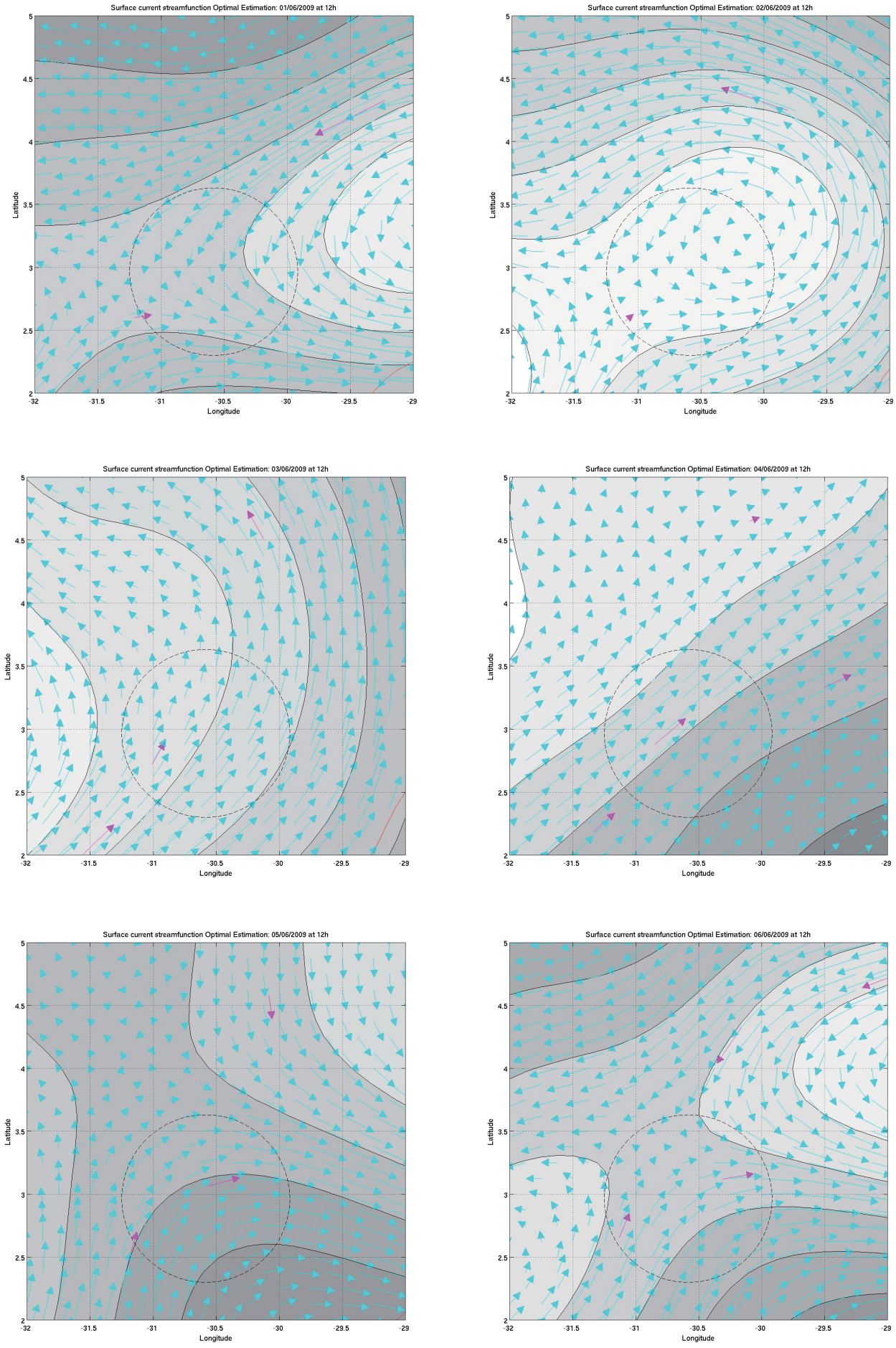

Figure 22 Velocity field around 12h between June 1 and June 6 2009, shown as daily displacements.

Particle trajectories

From the surface velocity field optimally estimated every 6h, particle trajectories are calculated using an Euler scheme (accurate enough, see page 82).

To test the method, we can start particles on June 1 at 0h and at the corresponding positions of the various drifters. Figure 23 gives the trajectories so obtained together with the original drifter trajectories (buoys #42, #246, #27045, #92).

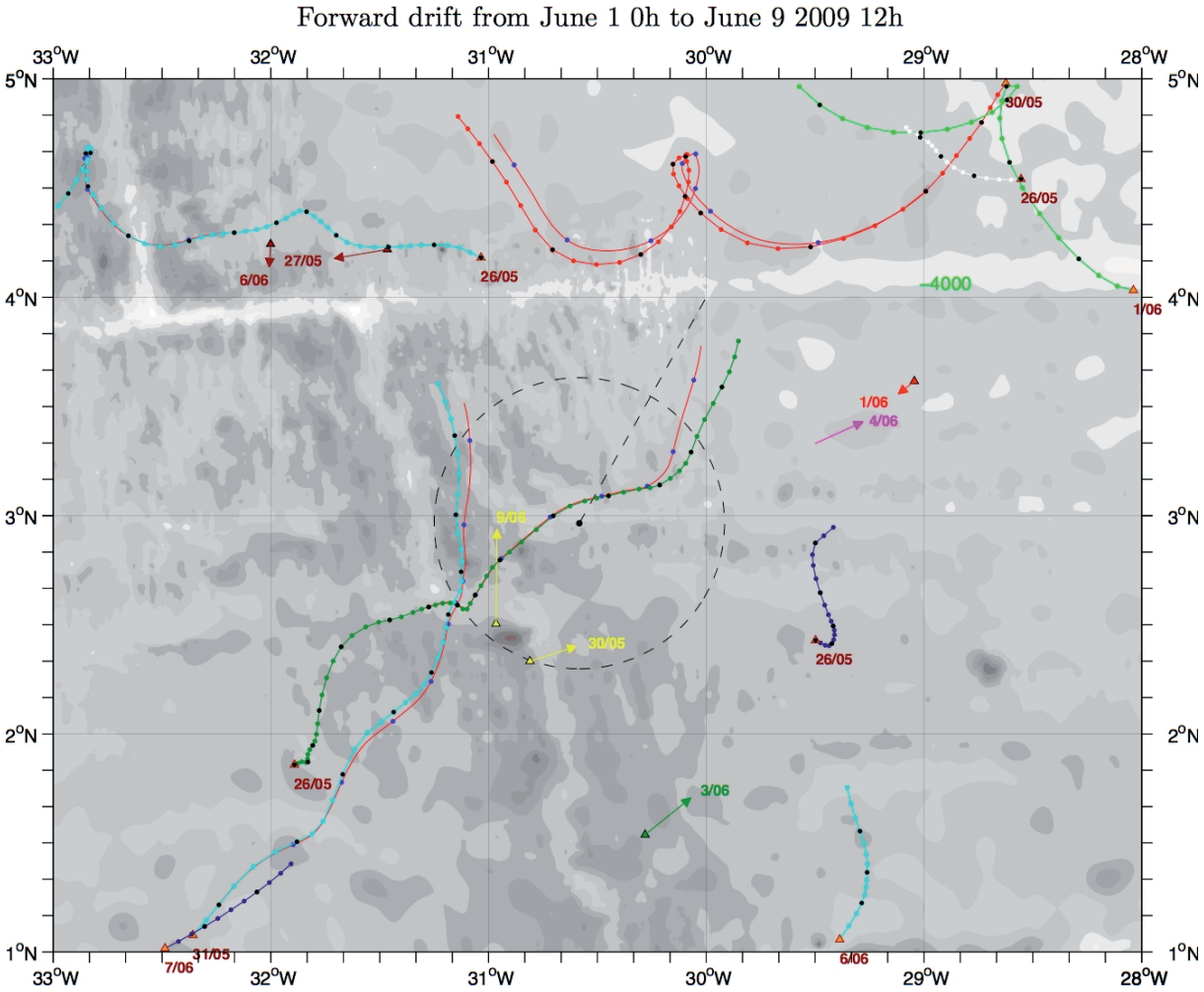

Figure 23 Red curves give the simulated trajectories (from June 1 0h to June 9 12h) of buoys #42 (cyan), #92 (cyan, flowing westward), #246 (green) and #27045 (red). Small blue dots every day at 0h. 24h equivalent Argo displacements are also given.

Until June 7 at 0h, the comparison between the true trajectories and the simulated ones is good, degrading thereafter. The distance between true and estimated positions increases with time more or less steadily however, reaching 5 km on June 6 at 0h, 5 days later (Figure 24).

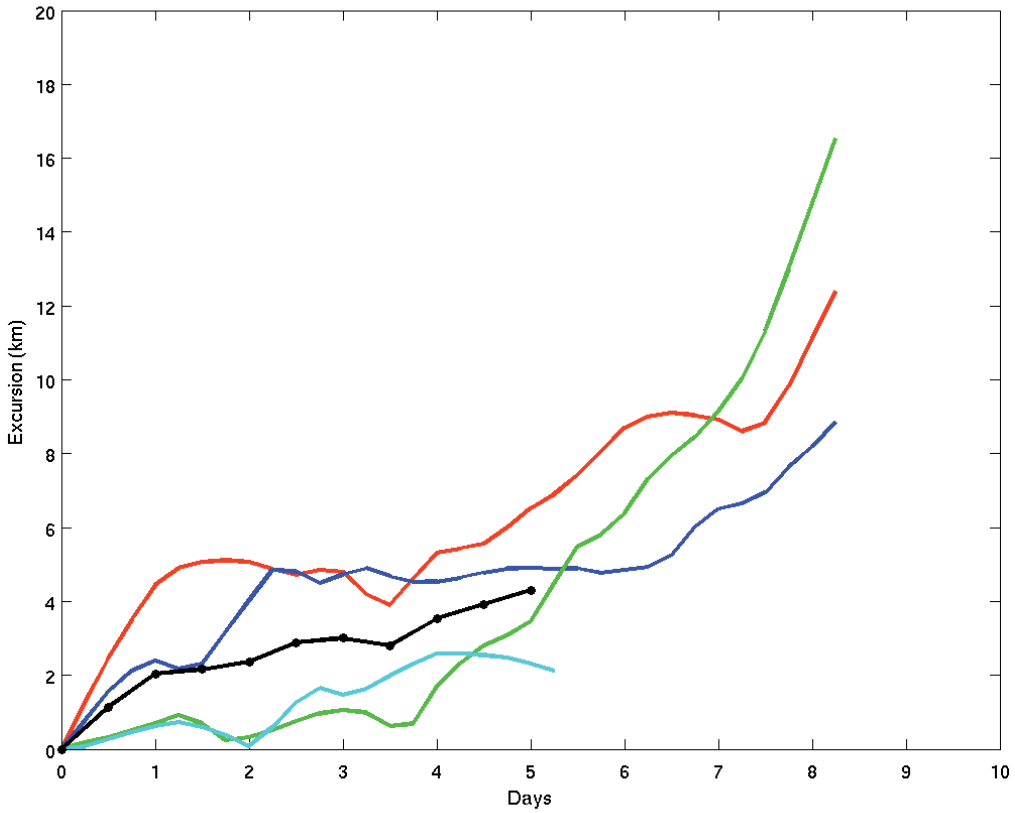

Figure 24 Distance between true and simulated trajectories of buoys #42 (blue), #246 (green), #92 (cyan) and #27045 (red). Black curve gives the mean distance versus time.

We cannot assume that such a small error occurs everywhere in the region, because the mean square error (mse) grows further, away from the drifters. An estimate of a realistic error, away from data locations, is given in Appendix 6.

We note that after June 7, the blue (#42) and green (#246) drifters are diverging compared to their simulated trajectories. This may well signal a possible divergence in the true velocity field at that date. Actually, it is difficult to get an agreement between the simulated currents north of the ACARS circle after the 7th and the apparent motion of the human bodies recovered (10 miles ahead of simulated particles). That is why we focus first on the period June 1 to June 6.

Figure 25 shows the backward trajectories for the first five bodies or debris given in Table 1. Integration is done from the initial positions and dates (see Table 1) back to June 1 at 2h15 (corresponding positions are the big orange dots). No windage is considered on the particles, for the moment.

The 2 green curves give the estimated backward trajectories from the first two sightings of the plane debris, from June 5 in the afternoon, back to June 1 at 2h.

The yellow dot in Figure 25, south of the last know position of the plane, is the possible pollution spot discovered on a synthetic aperture radar (SAR) image on June 2 at 8h16. The exact nature of this pollution spot is presently unknown, and its forward tracking (shown as a red curve in Figure 25) does not match the positions of the debris and bodies found. However it is interesting to note that backtracking from this pollution spot leads to a point roughly below the plane track, one minute or so before it reached its last known position. We have presently no explanation for this coincidence (but see appendix 7).

Similarly, the possibility of a crash at LKP seems here unlikely on examination of the forward tracking of a particle initially launched there on June 1 at 2h10 (not shown in the Figure, but similar to the pollution spot trajectory).

We find that the two bodies recovered by the Brazilian on June 6 at noon would be coming (red curve) from 3.60N 30.59W, while the two material parts found on the 6th would be coming from crash positions much farther to the south west (the Galley G2 position being the farthest). This is no surprise since G2 was seen floating partly immerged on recovery and should have experienced an important wind drag (estimated 2.85% in chapter I, section on debris and bodies). Thus we can make no progress if we do not take due account of the wind.

This may prove difficult since we do not know how the various parts floating around will respond to the wind. However, if we can assume that during the first 24h the body submergence due to gases had not begun, then the bodies were totally immerged or so (see section on bodies and debris). Since the wind appears to have weakened after the 2nd we can make the bold assumption that until the 6th even if the bodies were then only 2/3 immerged, there may be only a negligible windage on the bodies, the wind having been weak over that 4-day period.

So doing, leads us to consider the point circled in blue in Figure 25 as a possible candidate for the crash position (CP).

Distributing 8 particles regularly on the circumference of this 5km radius circle centred on CP, they are found after five and a half days (that is on June 6 at 18h) zonally distributed (the blue open circles in Figure 25) and not unlike the few northernmost debris found the same day.

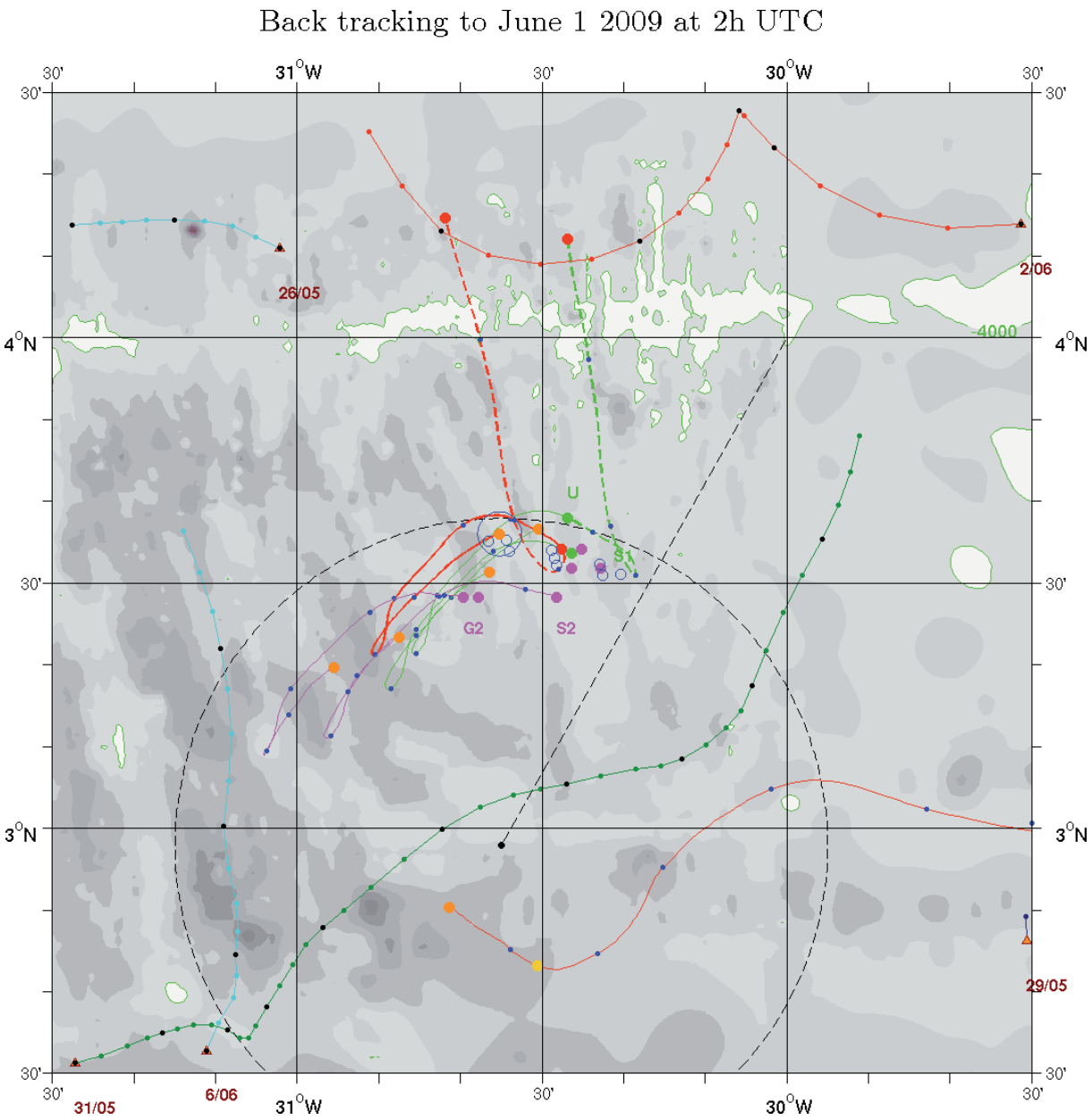

Figure 25 Backward trajectories from the first 5 initial positions and dates (Table 1), without any windage. Orange dots correspond to June 1 at 2h. The two bodies recovered on June 6 at noon are found at the orange dot with a blue 5km radius circle around. Particles seeded on this circle at the crash date (and forward integrated) are found five and a half days later at the blue open circles. Forward integration (until June 9 at 18h) from Ursulla (U) and the first two bodies are dashed green and red respectively.

Let us now introduce some windage.

Figure 26 shows the wind stress (in N m^{-2}) around the location of the first derelicts found and over the period May 30 to June 10 2009. Three different wind products are displayed: ECMWF generally used as atmospheric forcing for the OGCMs, ARPEGE 1/6° product and the Cersat HR blended 1/8° product, the latter combining ECMWF winds,

scatterometer measurements and radiometer data (see chapter I, section on wind data).

Although it is the wind velocity which is used to estimate the slippage of objects or bodies partly emerged, we show the stress in Figure 26, because it reveals more clearly stronger and weaker wind events (for instance, the calm period between June 2 and June 6).

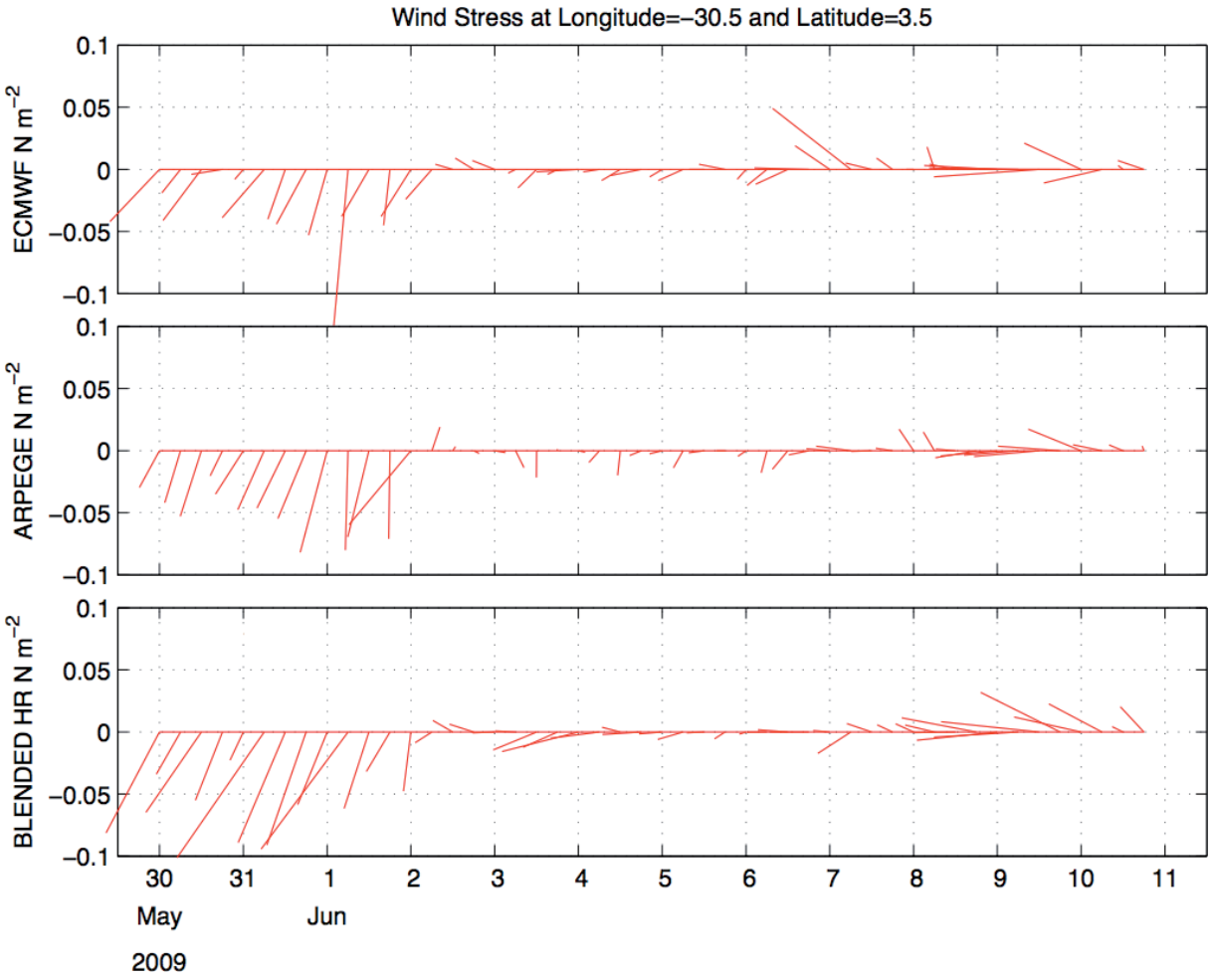

Figure 26 Wind stress at 3.50N 30.50W as given by three different wind products. Between June 2 and June 6 or 7 the wind stress is weak.

In the following we use only Cersat HR Blended winds.

Of course, we do not know which percentage of the wind velocity we must use with a particular object or body. We only know the slippage is proportional to the wind approximately: $\mathbf{v}_{slip} = \alpha \cdot \mathbf{W}$, where $\mathbf{W}$ is the wind velocity vector (see chapter I, section on bodies and debris).

Let us assume α is constant over time (for a given object). We have several objects (let say n) with various (but still unknown) α_i , i=1,…, n. If we can select for each object a α value, such that all the backtracks converge to a single point (or in a small zone, on practical grounds) at impact time, we may with some confidence consider the α values so selected as reasonable ones.

Doing so for the first five objects or bodies of Table 1, and assuming also there is no windage on the two human bodies recovered on June 6 (they were immerged for 24h and thereafter the wind was very light, as explained before), we find that $\alpha \approx 2.5\%$ for galley G2, and 1% and 2% for sightings S1 and S2 respectively. We have not considered any windage on Ursulla because we do not know exactly what the Singaporean sailors saw. Figure 27 shows the possible impact points so deduced (all 5 points fit into a 15 km diameter circle).

It is very satisfying to recover by an independent method a 2.5% value for G2, close to the 2.85% estimated in Chapter I (see Appendix 5 for a further discussion).

Forward integration until June 9 at 18h, from the Ursulla and first two bodies positions, does show a strong northward flow after June 7, but too weak on the 7th if we rely on the bodies found that day by the French navy ship Ventôse (more details on that later).

Given a distance error of 25 km on one back integrated trajectory after 5 days or so (see discussion below and Appendix 6), that is a marginal standard error σ of 20 km with an isotropic distribution[16], we would obtain with the 5 backtracked trajectories (if we could consider them as independent, not evident!) a standard error of 20/2 = 10 km on the average estimated crash position CP_{85} (the index indicates this is estimated with the r_0 = 85 km analysis). It is probably safer to keep a standard error of 20 km even for the mean:

CP_{85} = 3° 35'N 30° 32'W ± 20 km (1σ)

This means that within a 40 km diameter circle centred on CP_{85}, there is roughly a 0.39 probability to find the wreck (and within a 80 km diameter a 0.86 probability) with a Gaussian distribution (Bomford, 1972).

---

[16] If the position error has a 2D isotropic Gaussian distribution, the distance is Rayleigh distributed and the expected distance is given as $\sqrt{\frac{\pi}{2}}\sigma$ = 1.25 σ (Feller, 1972).

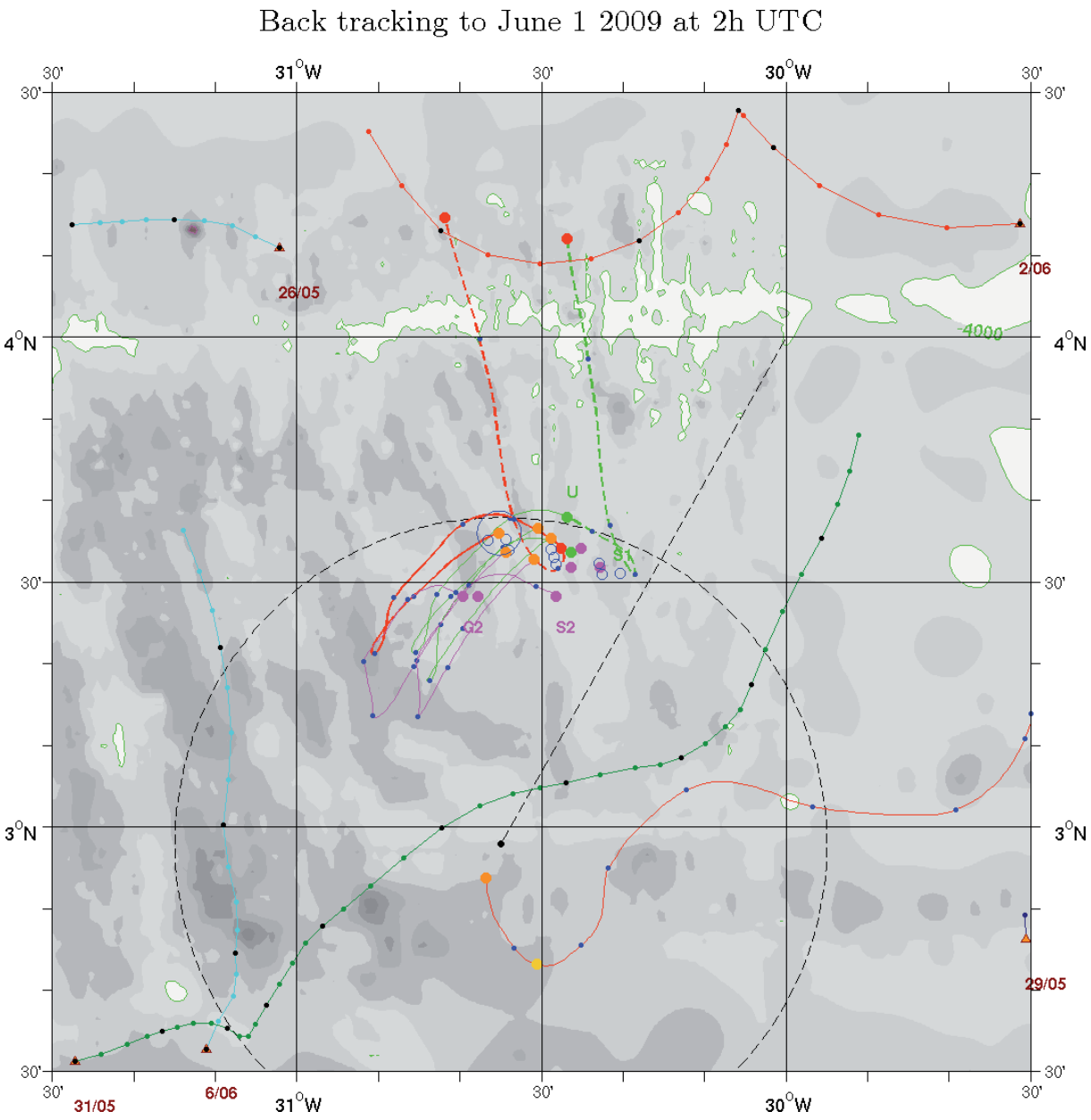

Figure 27 Backward trajectories from the first 5 initial positions and dates given in Table 1, with windage. The first two bodies recovered on June 6 at noon are found (on June 1 at 2h) at the orange dot with a blue 5km radius circle around. The 5 possible crash positions are within a 15 km diameter circle. This possible wreck zone is obtained through estimation of the windage coefficients α_i. Particles seeded on this circle circumference at the crash date (and forward integrated) are found five and a half days later at the blue open circles (without windage). A 2% windage is assumed for the back tracking of the pollution spot (3 to 4% are assumed generally for oil spill, see appendix 7).

Discussion

Several assumptions used in this approach can be challenged:

- Is r_0 = 85 km the best choice? Why not a shorter correlation parameter?
- Is the surface flow non-divergent?
- Is isotropy acceptable in this near-equatorial region?
- Can we obtain a realistic estimation of the position error?
- Should we use time correlation in the optimal estimation?

Analysis with r_0 = 50 km

We noticed in Figure 21 that the south westward flow (estimated with a r_0 = 50 km) found near 3.5N 30.5W on June 1 is weaker than the corresponding one in Figure 20 (estimated with a r_0 = 85 km). This flow is clearly induced through the optimal estimation by the buoy #27045 0.5 ms^{-1} southwestward flow. Since this buoy is at a 180 km distance, such a strong current in the north of ACARS circle may be questionable. One may thus consider the r_0 = 50 km reconstruction there as equally plausible.

On June 5 around 18h, a French Navy buoy measured current (unavailable when the optimal interpolation was done), can be used as a check on the two r_0 fields for that date. Figures 28 and 29 compare the buoy current to the estimated velocities of the 50 km and 85 km reconstructions respectively. Here too the 50 km velocity is weaker than its 85 km counterpart and furthermore compares more favourably with the independent data.

This gives some credit to an analysis with a scale parameter smaller than the one fitted statistically to the data. The backtracked trajectories integrated through the r_0 = 50 km velocity field still converge rather satisfactorily (with windage considered on G2, S1 and S2) but about 25 km west of CP_{85}:

CP_{50} = 3° 33'N 30° 45'W ± 20 km (1σ)

This shows that there is some uncertainty in the longitude of the crash zone (full results for the r_0 = 50 km are given in M. Ollitrault's report).

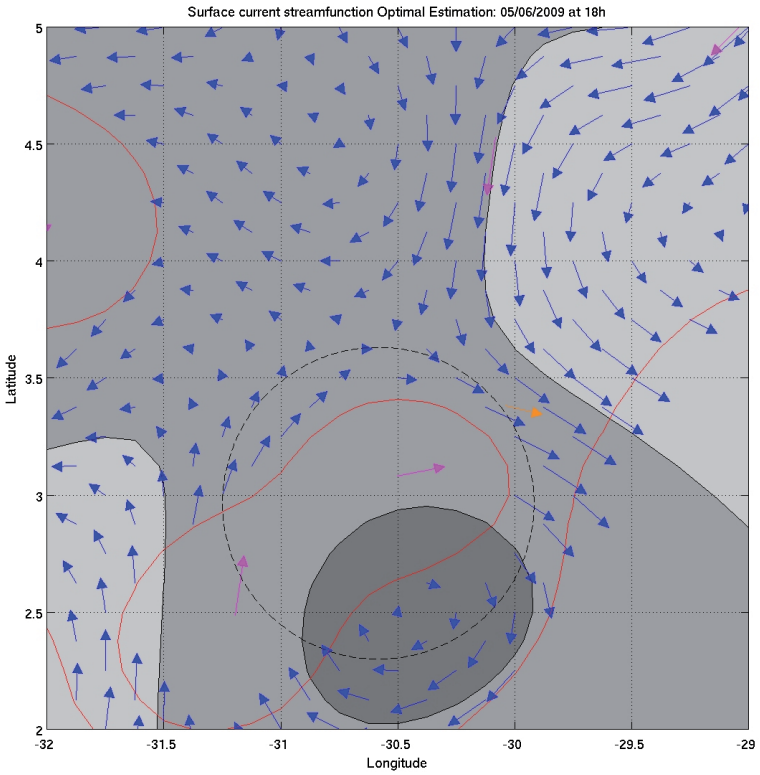

Figure 28 Orange vector (24h equivalent displacement) gives Navy current measured between 16h and 18h40 on June 5. r_0=50 km reconstruction (mse < 0.5).

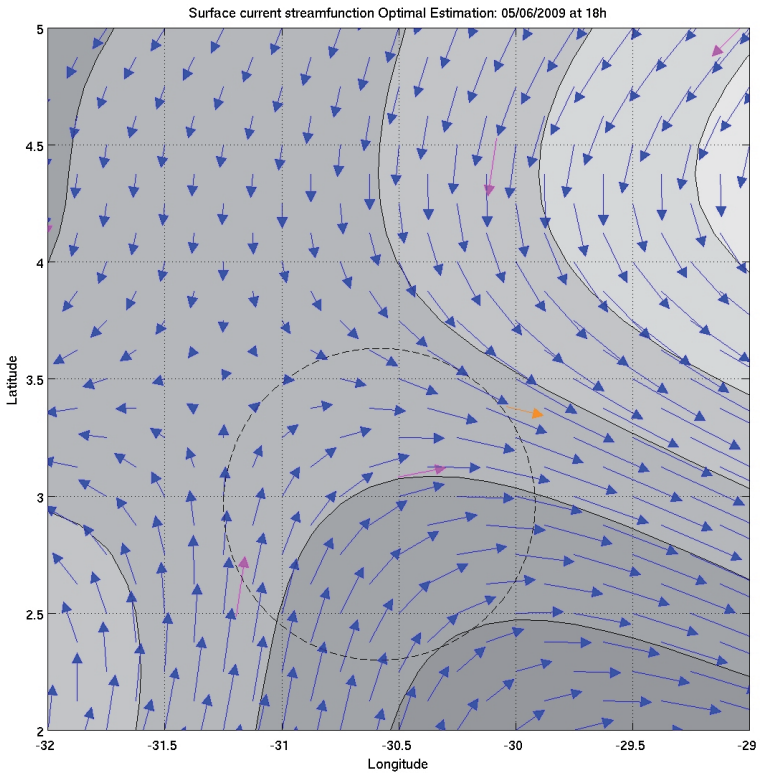

Figure 29 r_0=85 km reconstruction. The estimated current (shown as a 24h displacement) is almost twice as strong as the measured one.

Figure 30 displays the distribution of the debris and bodies found as a function of time, both in latitude and longitude. The northward flow estimated by the apparent body motion (red dots) is reproduced by the analysis but with a time lag of about 12h. Thus the present analysis should not be trust after June 7.

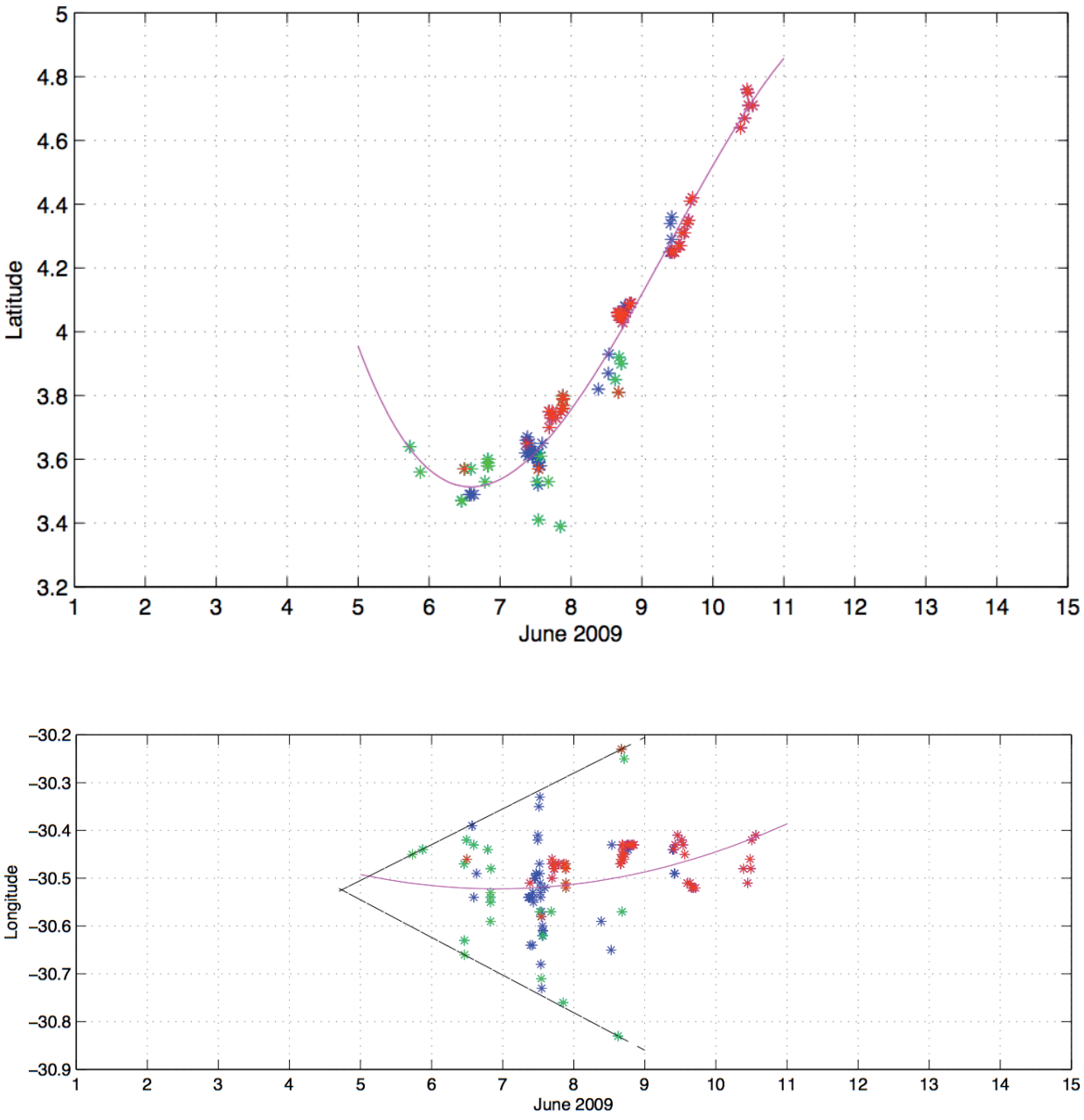

Figure 30 Positions of debris and bodies found by the Brazilian and French ships, as a function of time. The northward motion is 0.5 m s^{-1} between June 8 and June 10. Debris found by Brazil (green), by French (blue). Bodies (red). Cubic curves are fitted to the data. The body near 3.80°N 30.23°W is suspicious because it is far from all the other recovered bodies and was only sighted on June 8 2009.

It is interesting to note that the upper and lower envelopes of the longitudes of debris and bodies (bottom panel of Figure 30) are two straight lines crossing themselves near June 5 0h and near 30.53°W. This corresponds rather well to the saddle point already mentioned. It is also possible to reproduce approximately this zonal dispersion via forward integration (without or with windage), but it is not shown here (Figures 25 or 27 show only the dispersion on June 6 at 18h).

Non divergence assumption

We have seen that the f and g related functions under the horizontal non divergence assumption, fit reasonably well the data base at hand (see Figure 18). This is not a proof of the non divergence but at least this does not reject it. Of course that does not tell us that for the period considered and over the given region the velocity field is always and everywhere non divergent, but at least on a statistical basis this is correct.

Divergence and convergence in the well-mixed surface (order of 40m thick) layer are directly correlated to variations of this layer thickness, via the continuity equation:

$$\frac{\partial \mathrm{H}}{\partial t} + \nabla_{2\mathrm{D}} \cdot \left(\mathbf{u}\mathrm{H}\right) = 0$$

Here H is the instantaneous thickness of the well-mixed layer, and **u** is the average over the thickness of the surface layer. If **u** is independent of depth we have $\frac{1}{\mathrm{H}}\frac{D\mathrm{H}}{Dt} + \nabla_{2\mathrm{D}} \cdot \mathbf{u} = 0$

Let us do a scaling of this equation: if L, U and T are characteristic length, velocity and time scales (with T= L/U), there comes $\frac{\delta \mathrm{H}}{\mathrm{H}}\frac{\mathrm{U}}{\mathrm{L}}$ and $\frac{\mathrm{U}}{\mathrm{L}}$ for the two terms of the continuity equation. If we can prove that $\delta H/H << 1$, then the non divergence hypothesis is justified.

We can presume the strong stratification at the base of the surface mixed layer may damp vertical motion. Neglecting the influence of rotation (f= 8.9 10^{-6} s^{-1} at 3.5°N), a scaling of the momentum equation $\frac{\partial \mathbf{u}}{\partial t} + \mathbf{u} \cdot \nabla_{2\mathrm{D}}\mathbf{u} + f\mathbf{k} \times \mathbf{u} = -\mathrm{g}'\nabla_{2\mathrm{D}}\mathrm{H}$ where g' is the reduced gravity ($g'=g(\rho_2-\rho_1)/\rho_2$), gives $\delta H = U^2/g'$.

Thus $\delta H/H = U^2/(g'H)$ which is of the order of 0.07 with the values obtained from the data: $u_{rms} = 0.3\ ms^{-1}$, $g' = 3.5\ 10^{-2} ms^{-2}$ ($\rho_1 = 1023\ kg\ m^{-3}$, $\rho_2 = 1026.5\ kg\ m^{-3}$) and H = 40m. However we cannot neglect rotation because it implies a $\delta H/H$ of 0.4 (This approach is due to A. Colin de Verdière).

Using Helmholtz decomposition theorem (Chorin and Marsden, 1983), we can also estimate the divergent and rotational parts in an OGCM field and see if that divergent part induces a negligible particle excursion after a few days or not. This decomposition has been calculated with the June 5 velocity field of the Mercator PSY2V3 model giving divergent velocities of order 1/20 of the total velocities.

Conclusion: the non-divergence seems to be an acceptable assumption (maybe the scaling was too pessimistic).

Isotropy

Concerning isotropy, we could simply test a non isotropic ψ covariance function (for example like $\exp[-(x^2/a^2 + y^2/b^2)]$) and see if the results fit better to real data (see appendix in Rio and Hernandez, 2005). This has not been done.

Error on the integrated trajectories

To estimate the accuracy of the objective analysis we cannot compare the actual buoy trajectories to the integrated ones since, by construction, they will be close (if the velocity field is compatible with the assumptions done). But one can use the currents from a given OGCM (e.g. Mercator PSY2V3) at a few selected times and positions to reconstruct the complete velocity field by optimal estimation. The comparison then of the model trajectories with the trajectories estimated by integration through the reconstructed velocity field will give a reliable estimate of the absolute error. Appendix 6 details the results and show that we can assume a 25 km distance error after 5 days for the trajectories integrated in the optimally estimated velocity field.

Time correlation and data addition

To possibly obtain a better fit between data and reconstructed buoy trajectories, a temporal correlation was added in the stream function covariance function (now given by $F^*(r, t) = F(r) \exp(t^2/\tau^2)$). Results were not much different however (final choices are τ= 24h and data only within 12h of the current date are considered).

A much greater improvement came from addition of a few current measurements estimated on board the Ventôse (trimmed a bit because their date and place are not known precisely) and confirmed by apparent body motions on June 8 and after (see Figure 30). The Navy measured current on June 5 at 18h and a null current on June 6 at 12h at galley G2 position (galley G2 was sighted at 11h and recovered 4h later at the same location[17]) were also taken in the analysis.

Now, for r_0 comprised between 55 and 100 km, the backtracked positions of the two bodies E1 and 3Z converge satisfactorily with the other objects considered (whereas previously they were backtracked well outside the ACARS circle). Best fits with the buoy trajectories however are obtained with r_0= 70, 75, 80 or 85 km. Figure 31 shows such a fit for r_0= 70 km. The present analysis (with time correlation and complementary data) will be referred to as the new (objective) analysis, in the following. The differences between buoy and reconstructed trajectories are now of the order of 1 km after 6 days (for 70 km $\leq r_0 \leq$ 85 km) whereas our primary analysis gave a 5 km difference (see Figure 24).

The fact that changing the r_0 parameter does change the crash position, even if backtracked trajectories still converge satisfactorily, and even if the fit with actual buoy trajectories is excellent, clearly shows the sensitiveness of the method: with many current measurements over a mesoscale area (e.g. 100 km by 100 km), let us say every 25 km, we would recover well the velocity field, because there would be no latitude for the estimated velocity field to drift from the current data.

---

[17] The galley G2 null motion during 4h (same positions on sighting and recovery) could also indicate that current and wind effects cancel each other. Since the wind was very weak at noon on June 6, we assume the current was also very weak at that time and G2 position.

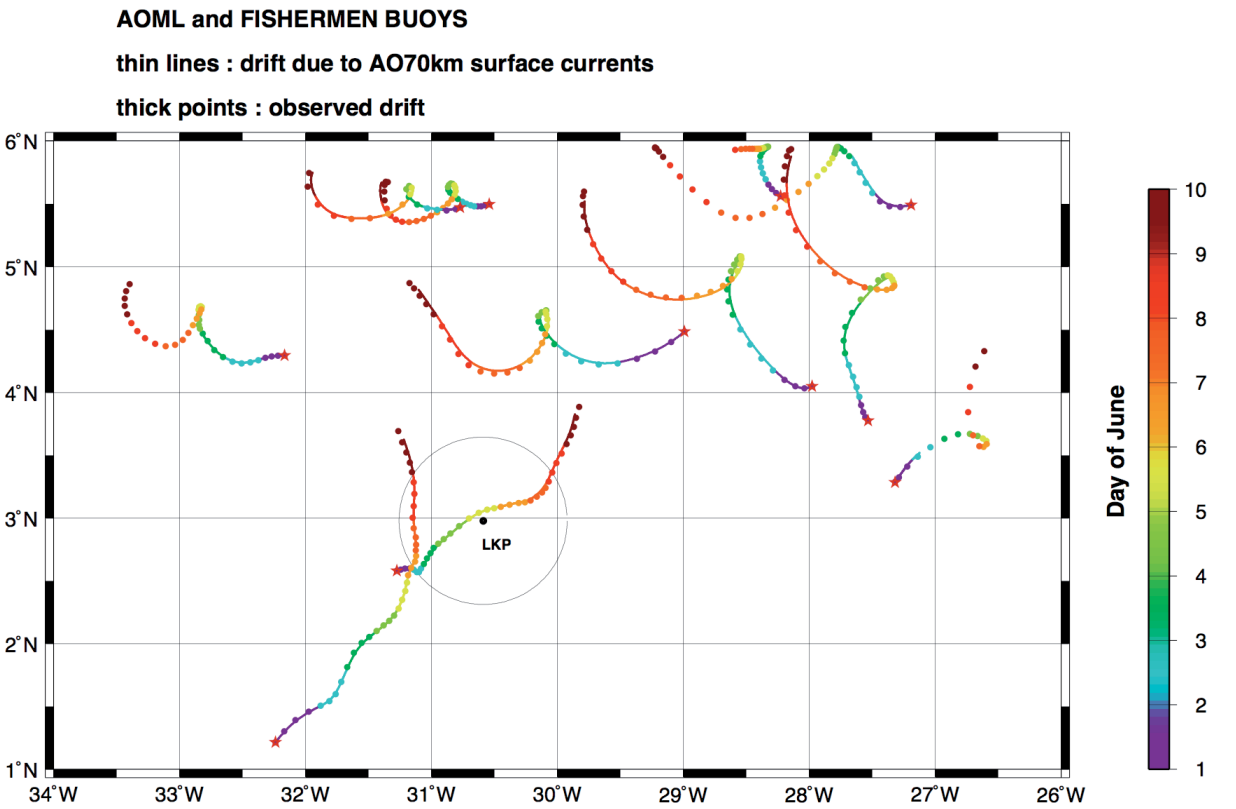

Figure 31 Objective (new) analysis (with $r_0 = 70$ km) model trajectories (forward) compared with real trajectories (one dot every 6h). Had we an independent buoy trajectory (with its data not used in the objective analysis), the reconstructed trajectory would certainly not fit so well. Similar plots done with r_0= 75 km or r_0= 80 km show almost no detectable difference.

Figure 32 below gives the backtracked positions with r_0= 75 km. All six selected particles (see Table 1 for initial positions and dates) are backtracked within a 15 km diameter circle centred on the average CP. The dotted circle (40 km diameter) gives the absolute 1σ uncertainty on one CP (but as said before, this is also used for the average CP). The vertical fin or vertical tail plane (VTP) sighted on June 7 at 13h38 is also backtracked within 7.5 km of the average CP, if a 2.5% windage is applied (not shown in the Figure). Without any windage applied, its backtracked position would be found much to the west (near 3° 21'N 30°57'W at a 42 km distance from average CP). Note that the VTP behaviour under the combined action of wind, waves and currents is largely unknown, and it may have experienced some crosswind (i.e. perpendicular to the wind direction) force. This point will be addressed in chapter III (a leeway statistical approach).

Note that in the next chapter, model results will be given (to be easily compared with the present analysis), using the same presentation as given in the Figures 31 and 32.

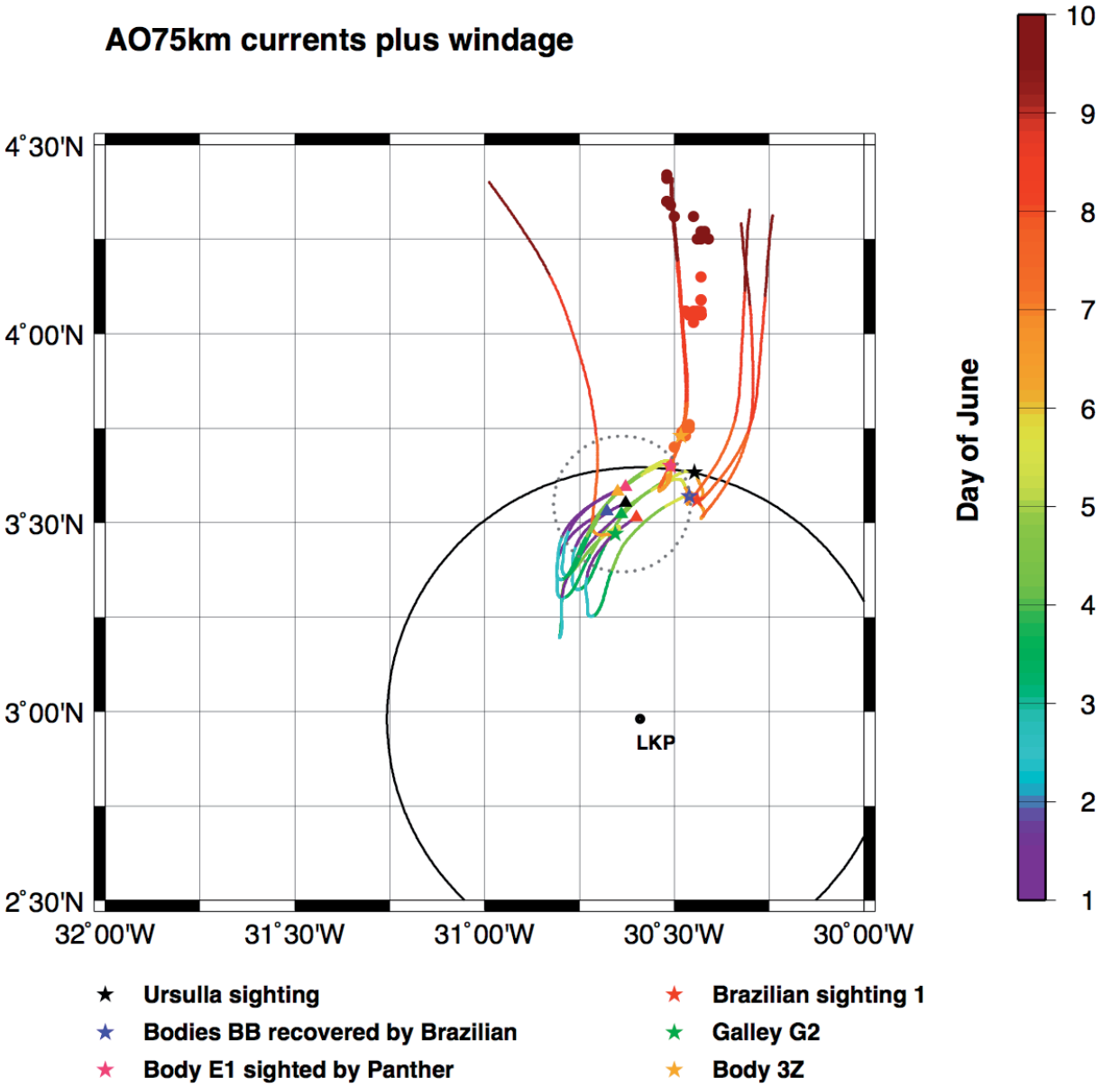

Figure 32 Backward trajectories (new analysis, r_0= 75 km) from the six initial particles listed (initial positions and dates in Table 1). There is no windage on U, BB, E1 and 3Z, 1% and 2.5% on sighting 1 and Galley G2 respectively. All six backtracked positions fall inside a 15 km diameter circle. The 20 km radius dotted circle gives the standard error on a backtracked point for June 1 at 2h15.

Provisory search zone

With the latter updated (or new) analysis, we have estimated several possible crash points, according to the correlation scale used in the reconstruction:

$$\mathbf{CP_{70}^{*} = 3° 33'N \;\; 30° 40'W \pm 20\ km\ (1\sigma)}$$

CP_{75}^{*} = 3° 32'N 30° 38'W ± 20 km (1σ)
CP_{80}^{*} = 3° 32'N 30° 36'W ± 20 km (1σ)
CP_{85}^{*} = 3° 32'N 30° 35'W ± 20 km (1σ)

Crash positions obtained with r_0= 55 km (respectively 100 km) are to the west (respectively to the east) of CP_{70}^{*} and CP_{85}^{*}, but fit less well the trajectory data.

We could thus propose to consider the following zone:

30°27'W to 30°47'W & 3°27'N to 3°37'N

This zone spans a 10' latitude extent only, due to the quasi-constancy of the latitude of the different CP^{*}, whence an error on the average latitude of order 10 km (or 5' approximately).

This approach is independent of any wind forcing (contrary to models), since the surface currents as given by Argo float displacements (the wind drag on Argo float antenna is assumed negligible) for example are assumed to be quasi-perfect tracers for bodies totally immerged near 0.5 m depth.

Any Stokes drift is assumed to be contained in the surface current observed by Argo floats.

We have assumed the surface currents are approximated by the drogued drifters or buoys motions, and this may have introduced some error (possibly of a few cm s^{-1}): at 10-15 m depth, the Stokes drift is only of the order of one fourth of its surface value, and even with a flat sea, there can be a vertical shear in the horizontal current (see the discussion on the Stokes drift, at the end of chapter III).

Using a different analytical form for the covariance function (e.g. Arhan & Colin de Verdière, 1985) does not make any detectable difference in the estimated velocity field (and thus on the crash zone).

However, small-scale structures (such as filaments), not seen in this kind of analysis, may invalidate the solution. This is seen after June 7: after adding a few current measurement in the analysis, backtracked trajectories for the bodies E1 and 3Z became consistent with the others. We definitively lack data on June 1 and 2, to be sure of these results.

III Determination of the wreckage area using numerical ocean models

Principles of numerical ocean modelling

Introduction

Like the atmosphere, the ocean is a fluid whose evolution can be predicted by a computer model that steps forward the equations of motion. Fluid is accelerated by the 'Coriolis force'—an apparent force resulting from the earth's rotation that is directed to the right of the motion (in the northern hemisphere)—as well as by wind and by pressure forces arising from variations in the sea surface height and density. These changes in density are linked by the 'equation of state' to changes in temperature and salinity that are caused by advection by ocean currents, surface forcing (solar heating, heat exchange with the atmosphere, long wave radiation, rainfall and evaporation) and diffusion.

Discretization

Even the most powerful computers have finite power, so it is necessary to approximate the continuous nature of space by a discrete grid with finite spatial resolution. The models discussed here typically operate at 1/12° (~9 km) horizontal resolution, and with vertical resolution ranging from about a meter near the surface, becoming coarser with increasing depth, with typically 50 vertical levels covering the total ocean depth (~4 km).

However many processes operate at small scales that are not sampled by such numerical models. Viscous dissipation and diffusive mixing operate on centimetre scales. The Kelvin-Helmholtz billows that extract energy from vertical shear have cm-m scales, while convection cells that develop where denser water overlies less dense waters have scales O(1cm)-O(100 m). Frontogenesis and filamentation operate at scales ≤1 km. All of these processes therefore need to be 'parameterized'—that is, the turbulent momentum and tracer fluxes they generate must be related to the fields that the model can resolve.

Approximations

The equations of motion are then couched in a coordinate system involving longitude, latitude and geopotential height, and then approximated (Gill, 1982) by assuming (i) that the metric factors have the same form as if the geopotentials were spheres, so the equations

have the same form as they would have in spherical coordinates with gravity aligned radially and (ii) that where the Earth's radius appears in a metric factor it can be considered as a constant—the 'thin shell approximation'.

Additionally the horizontal resolution of the models described here is too coarse for vertical accelerations to be significant compared to buoyancy forces or vertical pressure gradients, and so hydrostasy is assumed, whereby the vertical momentum equation is reduced to a balance between the vertical pressure gradient and the buoyancy force. The vertical velocity is no longer stepped forward from the vertical acceleration, but is instead diagnosed.

Although not essential, most ocean models (cf. Griffies 2004) make the Boussinesq approximation whereby density is assumed constant everywhere, except in the gravitational acceleration (buoyancy) term. Flow is therefore assumed to be non-divergent, and density changes modify the mass of a fluid parcel rather than its volume.

Splitting into depth-integrated and depth-varying flow

Ocean models step forward in time u and v (the eastward and northward velocities), together with temperature and salinity. Since variations in density are much smaller than the air-sea density difference, the external (surface) waves that transmit changes in sea surface height (SSH) travel much faster than the internal waves that affect the depth-varying flow (Gill, 1982). It is thus convenient to treat the depth-integrated flow separately from the depth-varying component of the flow.

Most current models (cf. Griffies 2004) therefore step forward the SSH together with the depth-integrated flow, using a small time step to resolve the fast surface waves. A longer time step is adequate to advance temperature, salinity and the depth-varying part of the velocity. Another approach involves filtering the surface waves by stepping forward the SSH and depth-integrated flow implicitly (Campin et al, 2004) or by including an explicit filter (Madec 2010), so that the longer time step can also be used for the depth-integrated flow. Previous models (Bryan 1969) assumed the 'rigid lid' approximation whereby SSH did not change. In this case the depth integrated flow is found diagnostically.

Vertical coordinates

Different models use different vertical model coordinates. The most popular choice is simply geopotential height, or z-levels, as employed

by MOM4 (Griffies et al., 2004), MITGCM (Marshall et al, 1997), POP (Smith and Gent, 2004) and NEMO (Madec, 2010). The Mercator PSY2V3 system used here (see Drévillon et al, 2008 and Hernandez, 2009 for discussion of earlier, lower resolution versions) is based on NEMO. Terrain following, or sigma coordinates (where the ocean floor and surface are both surfaces of constant sigma) are frequently employed in coastal models such as ROMS (Haidvogel et al. 2008), and are employed by the INMOM (Marchuk et al., 2005) model used here. FVCOM uses generalized sigma coordinates (Pietrzak et al., 2002), which allow the upper levels to be horizontal. MICOM (Bleck et al., 1992) and HIM (Hallberg, 2009) use isopycnic coordinates, whereby the vertical coordinate is potential density. The HYCOM model (Bleck, 2002) is based on MICOM, but uses hybrid coordinates, with *z*-levels within the surface ocean boundary layer, sigma coordinates near coasts and potential density throughout the rest of the ocean.

Forcing

Momentum is supplied to the ocean by wind, and lost by viscous stresses and form (pressure) drag on the ocean floor. Tidal forcing also generates flow. However tidal flows are weak in the deep ocean and produce negligible displacements because of their oscillatory nature. Therefore many basin- and global-scale models (though not coastal models) neglect the tides.

Heat is input by solar heating and exchange of sensible heat with the atmosphere, and lost by evaporation (latent heat) and long wave radiation. Freshwater is supplied by rainfall and lost by evaporation[18].

Unfortunately many of these forcing fields are poorly known, because of the lack of observational data. Generally they are calculated from bulk formulae using satellite or ocean model SST and fields of atmospheric temperature, wind speed, cloudiness etc from numerical atmospheric models. However, the wind stress on the ocean may now be found from satellites using scatterometery (e.g QuikScat).

Obviously ocean forecasts, as produced by ocean forecasting systems, can only use forecast atmospheric fields. However a so called 'hindcast'—a numerical simulation of the ocean at an earlier time, as required here—can make use of satellite data, and of 'reanalyzed' fields (i.e. with observations merged in) from the atmospheric weather forecast models.

---

[18] River discharges are also considered

Limitations

The predictive skill of models is limited by various factors:

- Inaccuracy resulting from the discretization
- Inadequate parameterization of small-scale (sub-grid size) processes
- Inadequate knowledge of the initial state
- Inadequate knowledge of surface forcing
- The inherent chaotic nature of nonlinear fluid dynamics that causes small errors to grow in scale and magnitude.

For these reasons, a purely predictive model will not produce a very accurate 'ocean forecast'. These difficulties are evident in the results of a (state of the art) prognostic model such as INMOM which has no data assimilation (it simply relaxes to observed SST). Similar difficulties limit weather forecasting: the predictive weather forecast loses accuracy after 5 days or so, and so must be rerun each day from a new initial state derived from merging observations with model output.

Usefulness of data assimilation

Assimilative models can give improved hindcasts by continuously adjusting fields of the model variables (SSH, u, v, temperature and salinity) towards their observed values: 'assimilating' the observations into the model. This approach is possible in a hindcast since observations from the past are available. Unfortunately, observations of the ocean are still sparse compared with the atmosphere, although the data provided by the Argo floats is invaluable (but does not extend below 2000m). Therefore it is a challenge, even for assimilative models, to produce accurate hindcasts, on the small scales O(10 km) and short timescales (days) over which we need to know the flow over our region of interest.

INMOM

The Institute of Numerical Mathematics Ocean Model (INMOM) developed at the Russian academy of sciences is a sigma (terrain-following) coordinate ocean model. It splits 3D advective processes into a sequence of 1D operations (Marchuk 1968, 1988). This technique improves the numerical discretization of the pressure gradient in the σ-coordinate system, generally (Shchepetkin and McWilliams, 2003) a weakness of such models.

The model simulation considered here is of the North Atlantic between 10°S and 60°N and a part of the Mediterranean Sea, run at 1/6°×1/12° (in longitude and latitude resp.) horizontal eddy-resolving resolution. It was initialized from climatology, spun up for ten years using the CORE 'normal year' forcing, and then run from January 1 through to June 25 2009 forced by ERA-interim surface fluxes reanalyzed from the ECMWF numerical model. No formal assimilation was performed, but the top level (3.5m thick) of the model was strongly relaxed to the ERA-interim SST on a timescale of 3 days.

Validation of the model was performed by comparing actual tracks of AOML drifters and fishermen's buoys in the region around the LKP. Agreement is poor in the southern part of this region (everywhere south of 4°N), but better towards the north (see Figure 33, and the full report by N. Diansky et al.). As explained more fully in the paragraph (to be found later in the text) about the limits of predictability, we cannot expect much better than that from an OGCM that does not assimilate observation data.

A corrected model was therefore devised, INMOMC, in which the flows were brought towards those predicted by the optimal interpolation method. This is discussed separately, below.

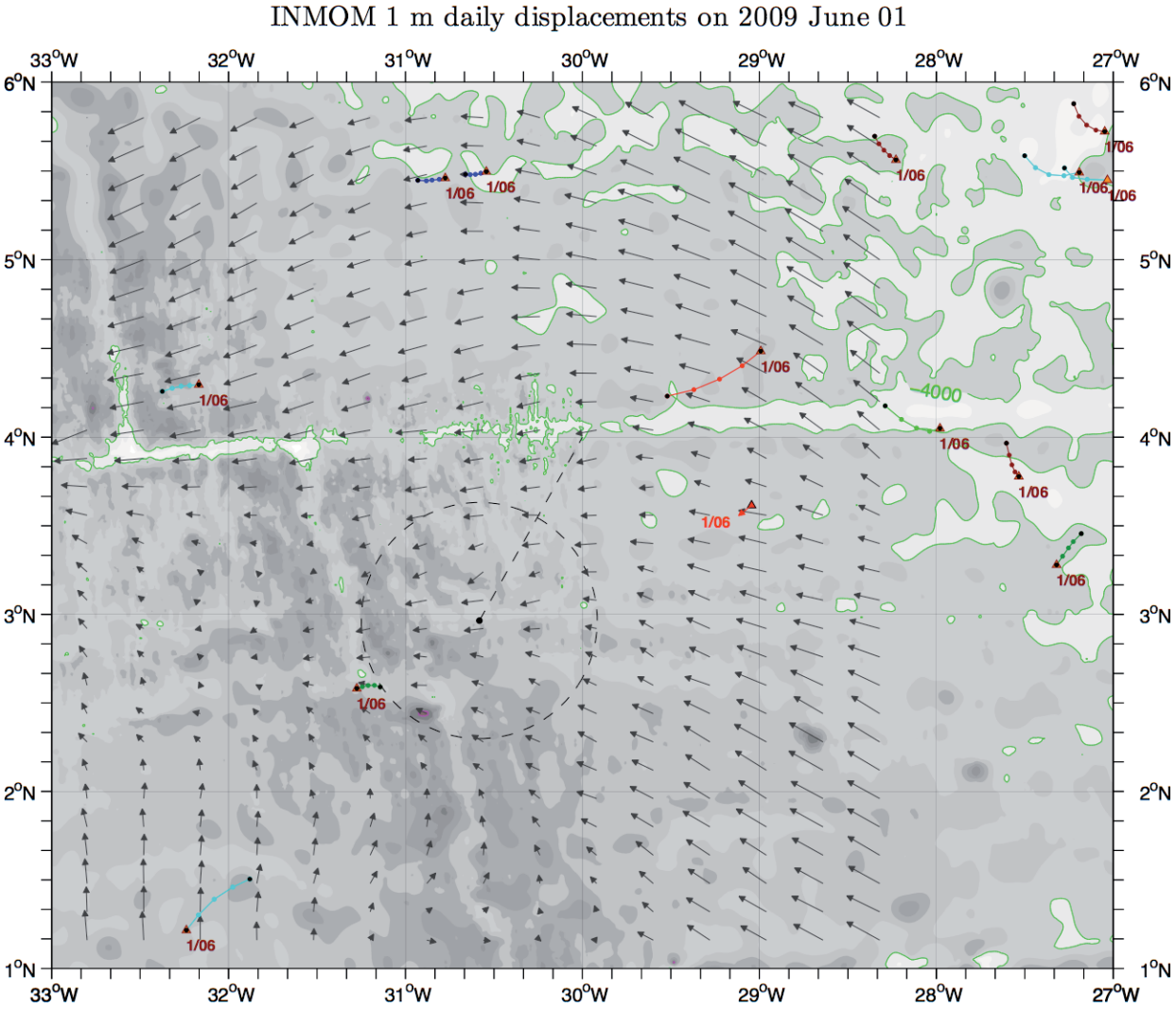

Figure 33 The daily velocity field of INMOM on June 1 2009. Vectors give equivalent 24h displacements and buoy trajectories are shown over the 24h period between 0h and 24h on June 1 2009.

Standard assimilative models

We now present results from Operational Oceanography systems based on NEMO (Mercator PSY2V3, Dombrowsky et al., 2009) and HYCOM (HYCOM/NCODA: Chassignet et al., 2007, 2009) that assimilate sea surface temperature (SST) and SSH from satellite observations (available globally), as well as temperature and salinity profiles (where available). Mercator PSY2V3 is a version of NEMO run at 1/12° horizontal resolution over the North Atlantic Ocean (20°S to 80°N) and Mediterranean. It is forced by daily ECMWF analyses. HYCOM/NCODA is run globally at 1/12° horizontal resolution, and forced by 3-hourly fields from the US Navy NOGAPS atmospheric analysis.

Both models can be either run in forecast mode, from a merged initial state, or in hindcast mode, continuously assimilating ocean data and calculating surface fluxes from atmospheric model analyses (or reanalyses), or possibly from satellite data. Here we evaluate and use these models in hindcast mode. Further details of these models and the procedures used to assimilate SST, SSH and density (T and S function of P) profiles are in Appendix 2.

A comparison of many historical drifter trajectories over the equatorial Atlantic to their backtracked simulated trajectories as predicted by HYCOM/NCODA and PSY2V3 (in hindcast mode) is also presented in Appendix 2. The root mean square (rms) error in position grows by about 15-20 km per day of integration, so that trajectories backtracked for 5 days (about the length of time between the crash of AF447 and the discovery of the first debris) have rms errors of about 100 km for both models. Given that AF447 is thought to have impacted the sea within 75 km of the LKP, this result suggests that these models may not be very useful in estimating the crash position. Given the limitations of the models discussed above, and the sparseness of the data that may be assimilated, this may not be too surprising.

Nevertheless, for purposes of comparison, let us show now the modelled velocity field and backtracked trajectories of the debris found between June 5 and 7 for both the PSY2V3 and HYCOM/NCODA. We also show in Appendix 3 the velocity field and trajectories for an improved version of the Mercator model (termed PSY2-REANA) that assimilates higher quality (delayed mode) in situ and satellite data as well as extra in situ data.

Velocity field and backtracks from Mercator PSY2V3

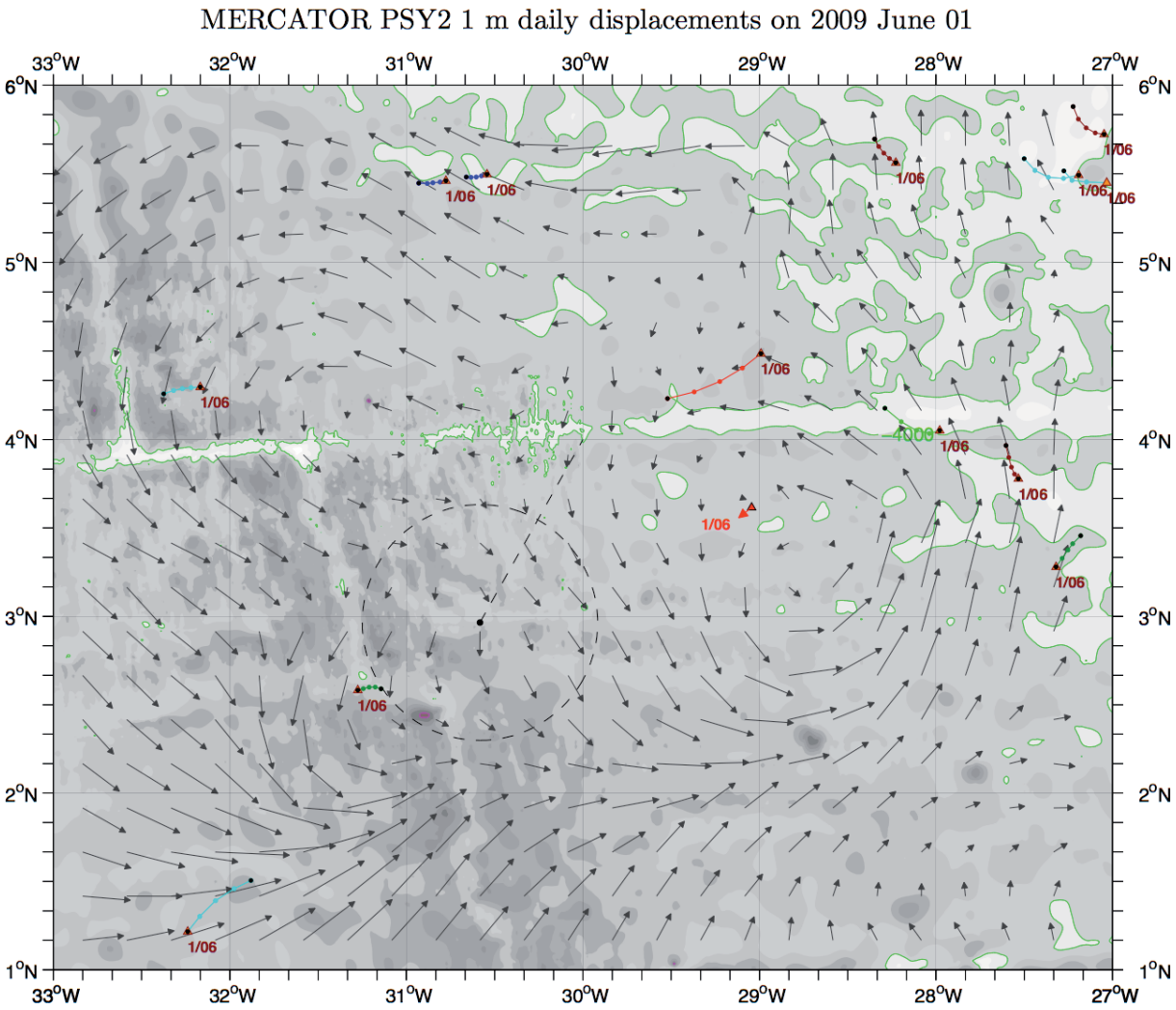

Figure 34 The daily velocity field given by Mercator PSY2V3 model on June 1 2009. Vectors give equivalent 24h displacements and buoy trajectories are shown over the 24h period between 0h and 24h on June 1 2009.

The PSY2V3 surface currents do not reproduce well the buoy measured currents (Figure 34). The backtracked particles are found within a 45 km diameter area, slightly west of LKP (Figure 45).

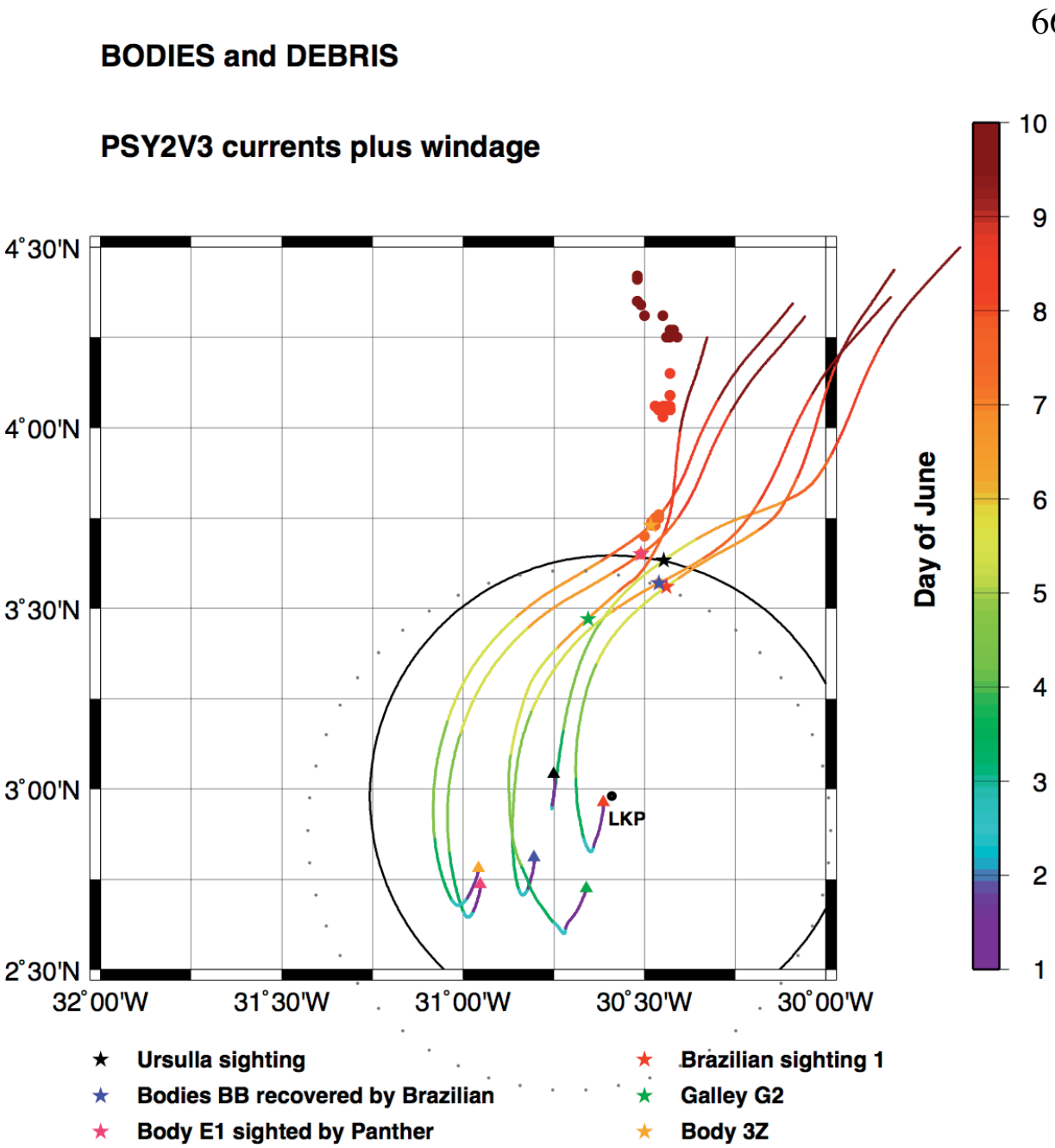

Figure 35 Backtracked positions (using Mercator PSY2V3 model) for six debris or bodies found over the period June 5 to June 7 2009 (Ursulla and S1 on June 5, BB and G2 on June 6, E1 and 3Z on June 7). No windage on Ursulla and the bodies, 1% and 2.5% on sighting 1 and Galley G2 respectively. The 85 km radius dotted circle gives the standard error on a backtracked point for June 1 at 2h.

Velocity fields and backtracks from HYCOM/NCODA

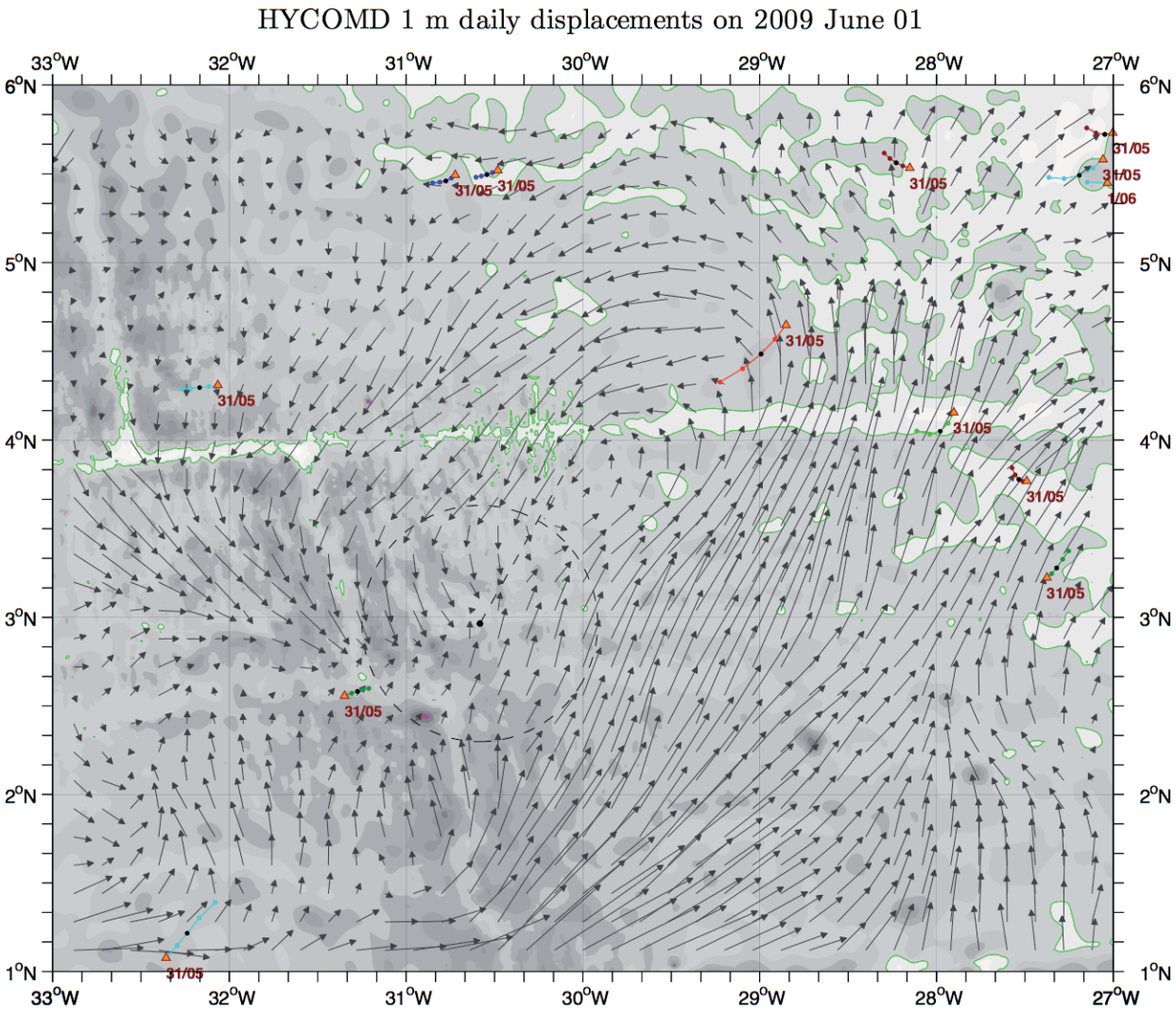

Figure 36 The (snapshot) velocity field given by HYCOM model on June 1 2009 at 0h. Vectors give equivalent 24h displacements and buoy trajectories are shown over the 24h period between 12h on May 31 and 12h on June 1 2009.

HYCOM apparently does not reproduce better than PSY2V3 the observed currents, but the quantitative comparison with the buoy trajectories, shown in Appendix 6, gives a standard error of 65 km versus 85 km (for PSY2V3). On another hand, the backtracked particles are scattered over 93 km, twice as much as for PSY2V3 (Figure 37).

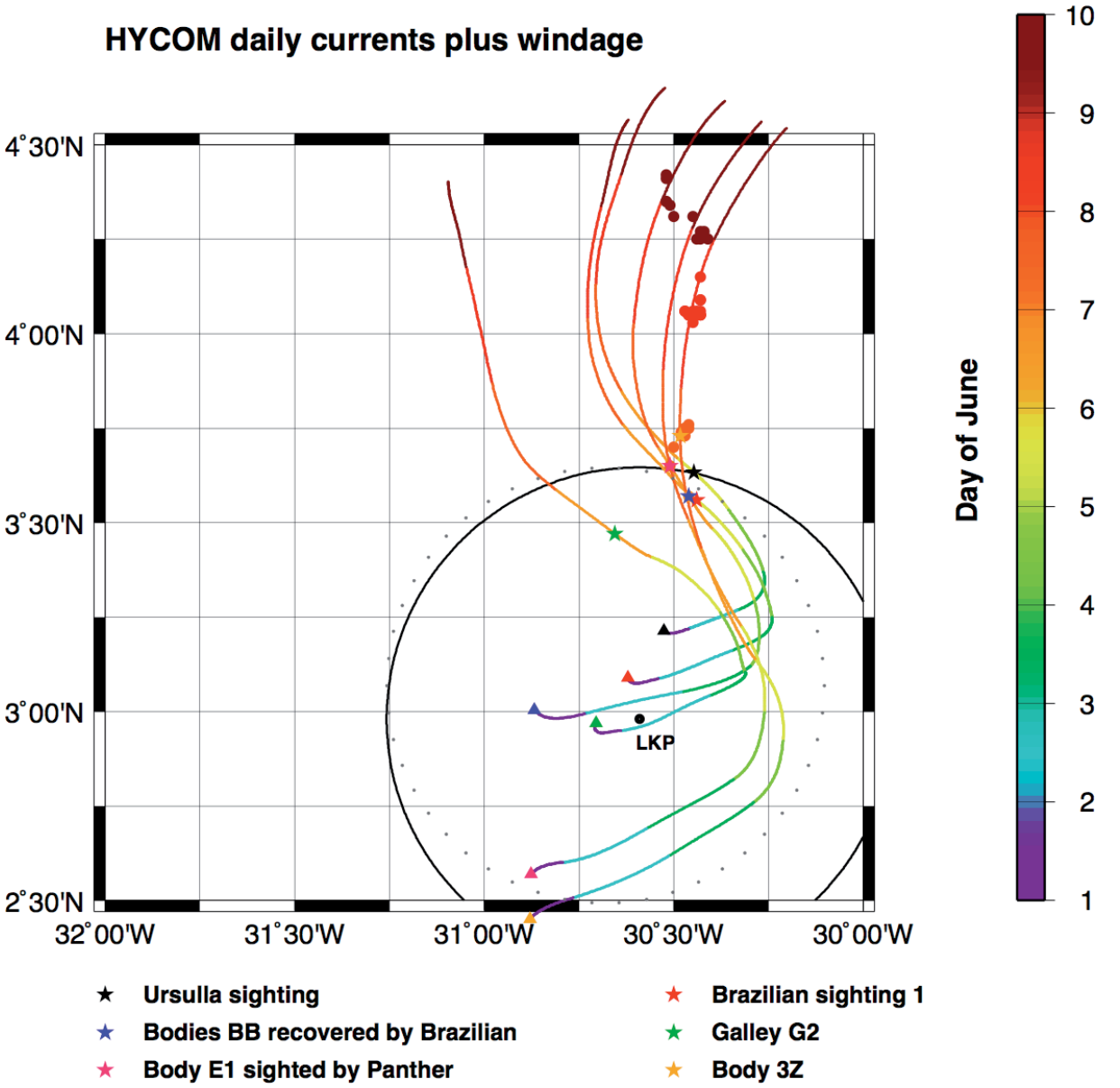

Figure 37 Backtracked positions (using HYCOM model) for six debris or bodies found over the period June 5 to June 7 2009 (Ursulla and S1 on June 5, BB and G2 on June 6, E1 and 3Z on June 7). No windage on Ursulla and the bodies, 1% and 2.5% on sighting 1 and Galley G2 respectively. The 65 km radius dotted circle gives the standard error on a backtracked point for June 1 at 2h.

ZOOM1 and ZOOM2

In the ZOOM1 and ZOOM2 runs a small 12°x8° (36°W-24°W and 1°N-9°N) configuration of NEMO (but with the same spatial resolution) over the region of the crash was embedded into the reanalysis solution (i.e. took its boundary conditions from the PSY2-REANA fields). The mixed layer and advection schemes were modified, and a non-linear free surface was employed. In order to avoid temporal jumps in the solution, data assimilation was not performed over the 'zoom' domain. See M. Drévillon's report for more details.

Additionally, the boundary conditions used time-smoothed PSY2-REANA fields, to prevent propagation of jumps into the 'zoom' domain. The ZOOM1 model was driven by 3 hourly ECMWF winds while the ZOOM2 used 1 hourly ARPEGE ones, over the period 26th May to 16th June. Solar radiation and long-wave heat fluxes were estimated from daily-mean cloud cover (with an analytic solar diurnal cycle), and latent and sensible heat fluxes were calculated from bulk formulae using daily-mean temperature and relative humidity with the high-frequency winds.

Figure 38 shows the ZOOM2 surface velocity field on June 1 2009 at noon. Although still far for reproducing well the observed currents, the general circulation pattern is better mimicked than with PSY2V3 or HYCOM. Moreover, the convergence of the six backtracked particles chosen for estimating the wreckage area, is quite convincing, since they are found inside a 18 km diameter circle (Figure 39). The standard error on a backtracked point is 48 km.

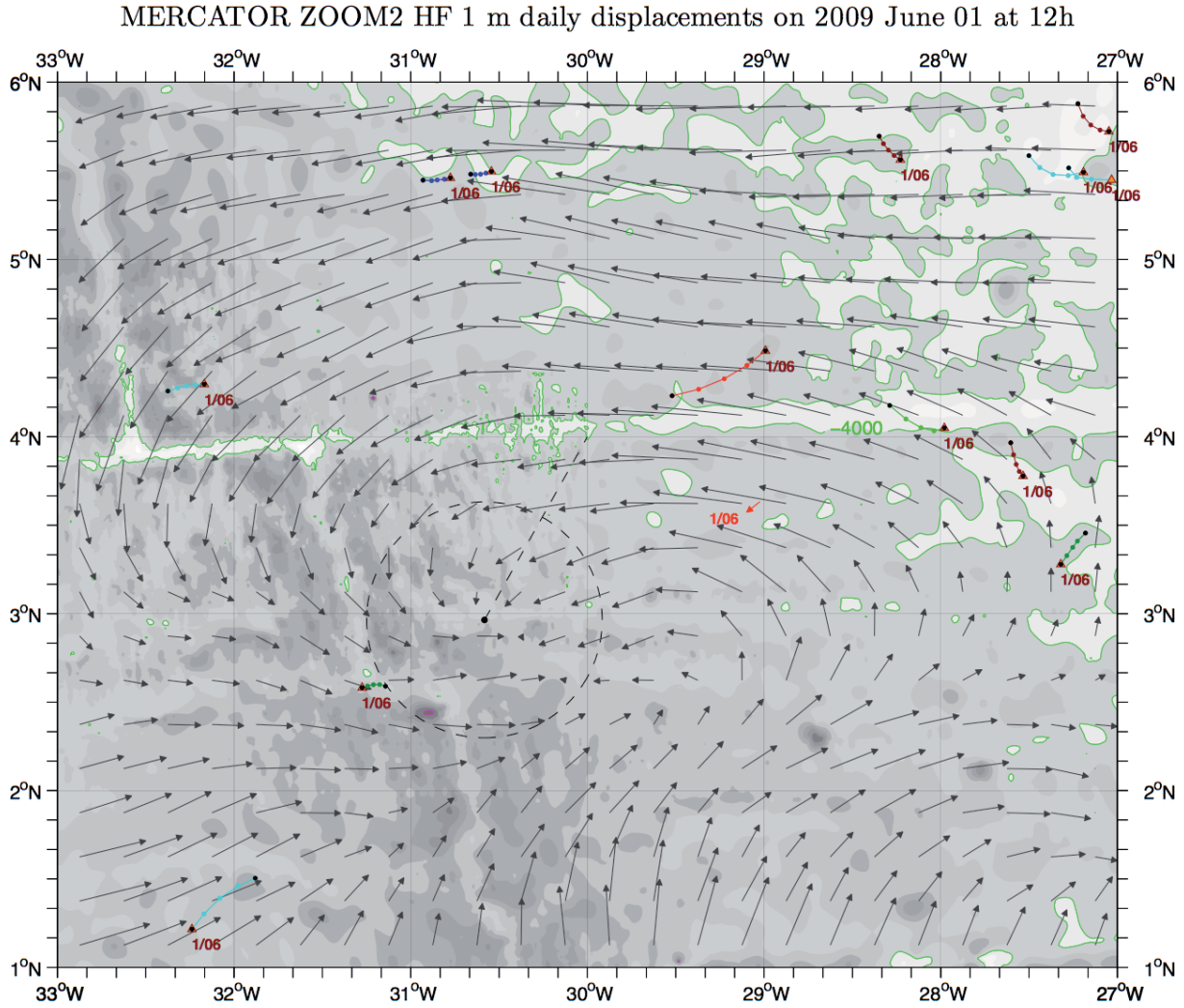

Figure 38 The hourly velocity field given by Mercator ZOOM2 model on June 1 at 12h. Vectors give equivalent 24h displacements and buoy trajectories are shown over the 24h period centred at the time of the velocity field estimation (here June 1 2009 at 12 h).

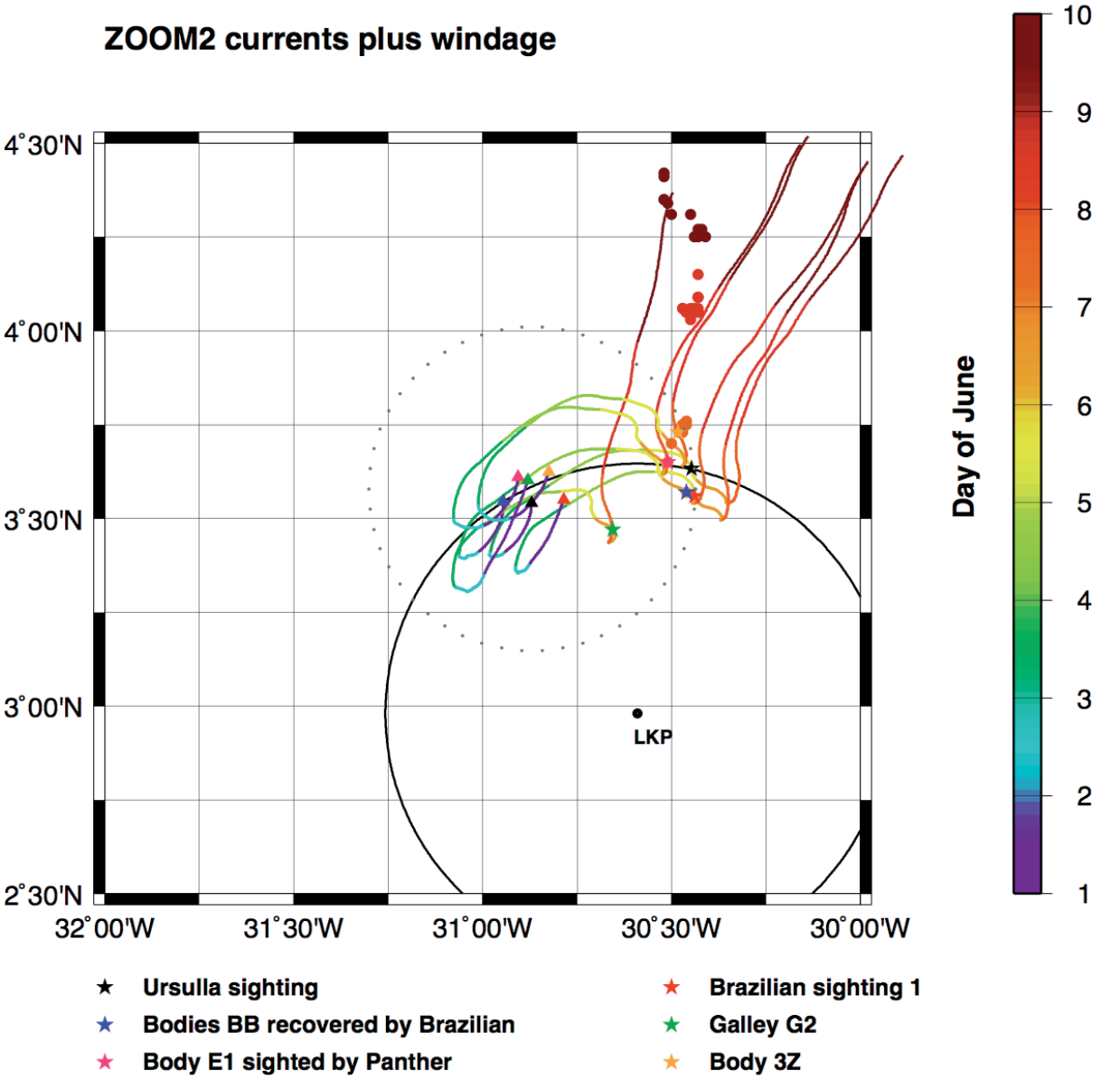

Figure 39 Backtracked positions (using Mercator ZOOM2 model) for six debris or bodies found over the period June 5 to June 7 2009 (Ursulla and S1 on June 5, BB and G2 on June 6, E1 and 3Z on June 7). No windage on Ursulla and the bodies, 1% and 2.5% on sighting 1 and Galley G2 respectively. The 48 km radius dotted circle gives the standard error on a backtracked point for June 1 at 2h.

INMOMC

The original velocity field from INMOM did not fit well the observations, south of 4°N (as we saw above). A specific correction was implemented to improve the fit with the measured buoy currents over the period June 1-7: the temporal mean model velocity field over

these first seven days was replaced by the corresponding mean from the (first) objective analysis (with r_0= 85 km). That is $u_{Corr} = u_{Model} - \langle u_{Model} \rangle_t + \langle u_{OA85} \rangle_t$, the brackets denoting the temporal mean over June 1-7.

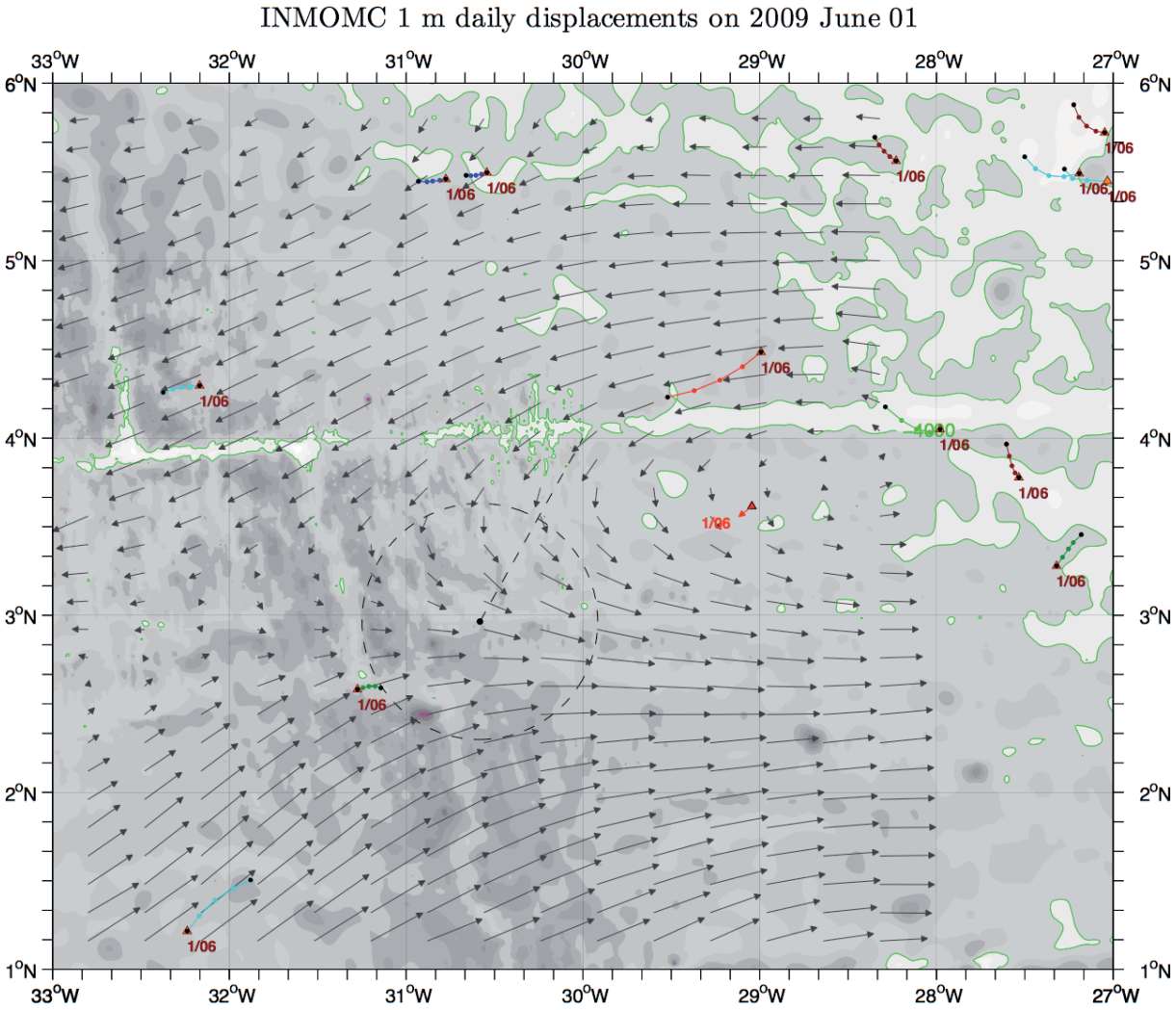

Figure 40 The daily velocity field given by INMOMC model on June 1 2009. Vectors give equivalent 24h displacements and buoy trajectories are shown over the 24h period between 0h and 24h on June 1 2009.

With this temporal mean replacement, the model (now named INMOMC for Corrected) velocity field agrees better with the observations, as is exemplified on Figure 40 (compare with Figure 33).

The backtracking of the six particles (U, S1, BB, G2, E1, 3Z) also gives a coherent area near 3°30'W, 30°30'W (backtracked positions inside a 40 km diameter circle). But do not consider forward trajectories after June 7 in Figure 41, since the correction applies only for the June 1-7 period.

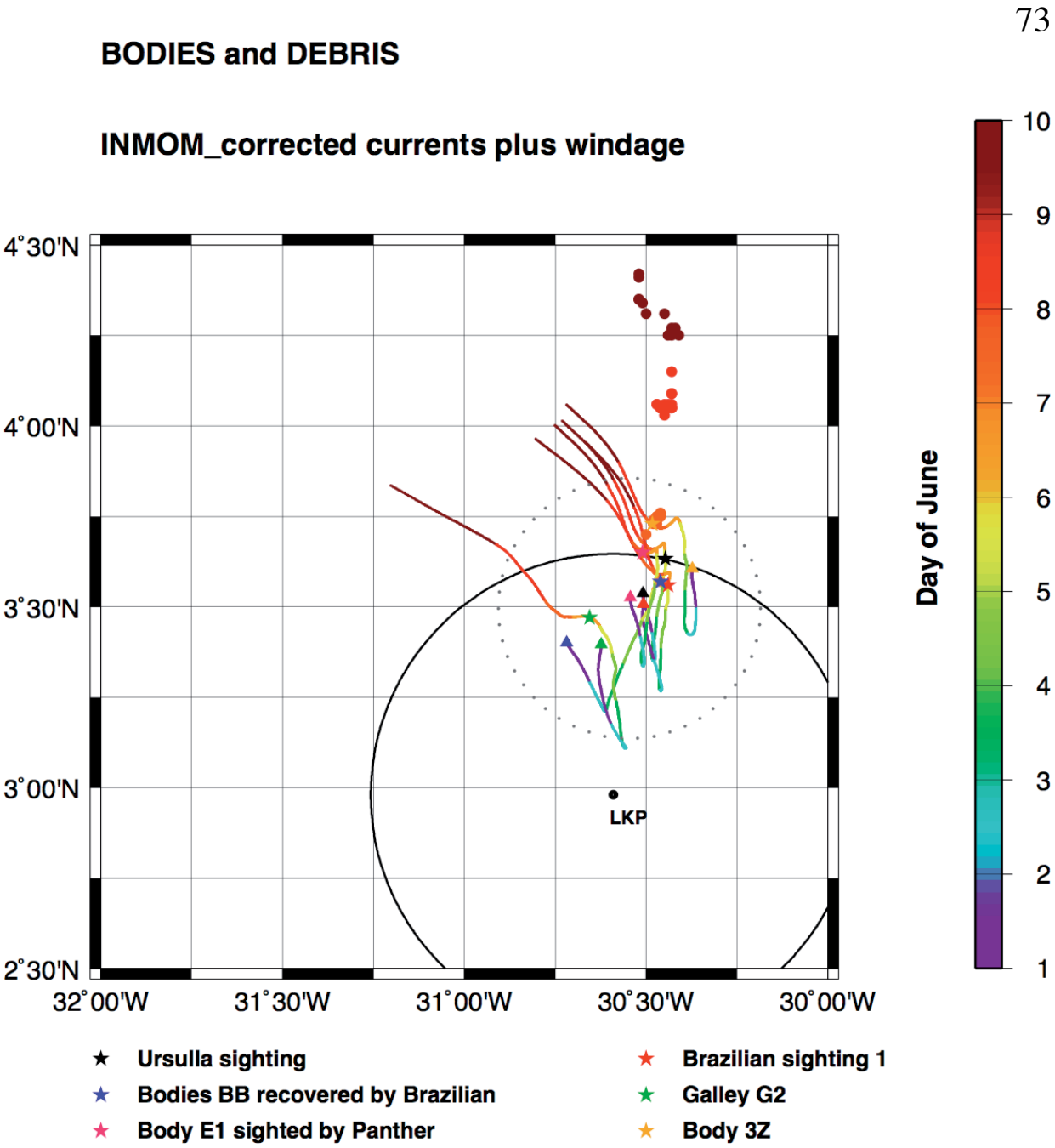

Figure 41 Backtracked positions (using INMOMC model) for six debris or bodies found over the period June 5 to June 7 2009 (Ursulla and S1 on June 5, BB and G2 on June 6, E1 and 3Z on June 7). No windage on Ursulla and the bodies, 1% and 2.5% on sighting 1 and Galley G2 respectively. The 40 km radius dotted circle gives the standard error on a backtracked point for June 1 at 2h.

We have not tried to justify on theoretical grounds the replacement of the temporal mean but at least the resulting standard error of 40 km on a backtracked point would plead for considering this model. However the six backtracked particles are scattered over 45 km (like PSY2V3), which is not so satisfying.

Models with assimilation of drifter data

FVCOM

This model was run under three different wind fields: the NCDC Blended product (which uses satellite data and NCEP reanalysis), ECMWF and WRF (see description in the data section). Nudging[19] is used for the assimilation of SST and SSH, optimal interpolation (OI) for currents derived from drifters. However not all the buoy data have been assimilated.

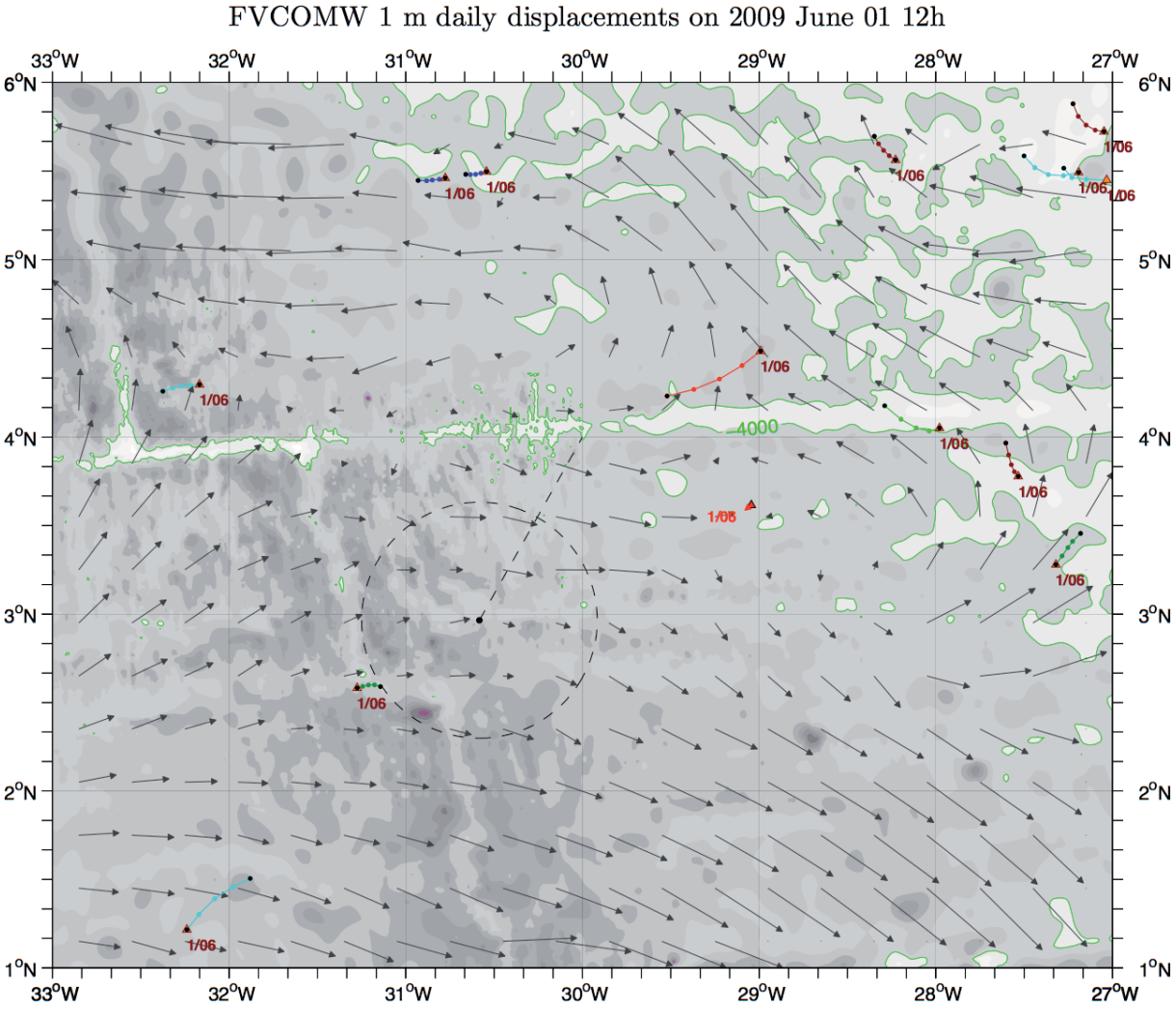

Figure 42 The hourly velocity field given by FVCOMW model on June 1 at 12h. Vectors give equivalent 24h displacements and buoy trajectories are shown over the 24h period centred at the time of the velocity field estimation (here June 1 2009 at 12 h).

[19] Nudging introduces a relaxation term (towards the data) in the model equations. OI linearly combines data and model variables (using known statistics) at a given time, then step forward (in time) the model equations from these initial conditions, until new data are available.

Furthermore wave-current interactions have been included in a refined version named FVCOMW (for Wave). This implies the Stokes drift is included in FVCOMW velocity field.

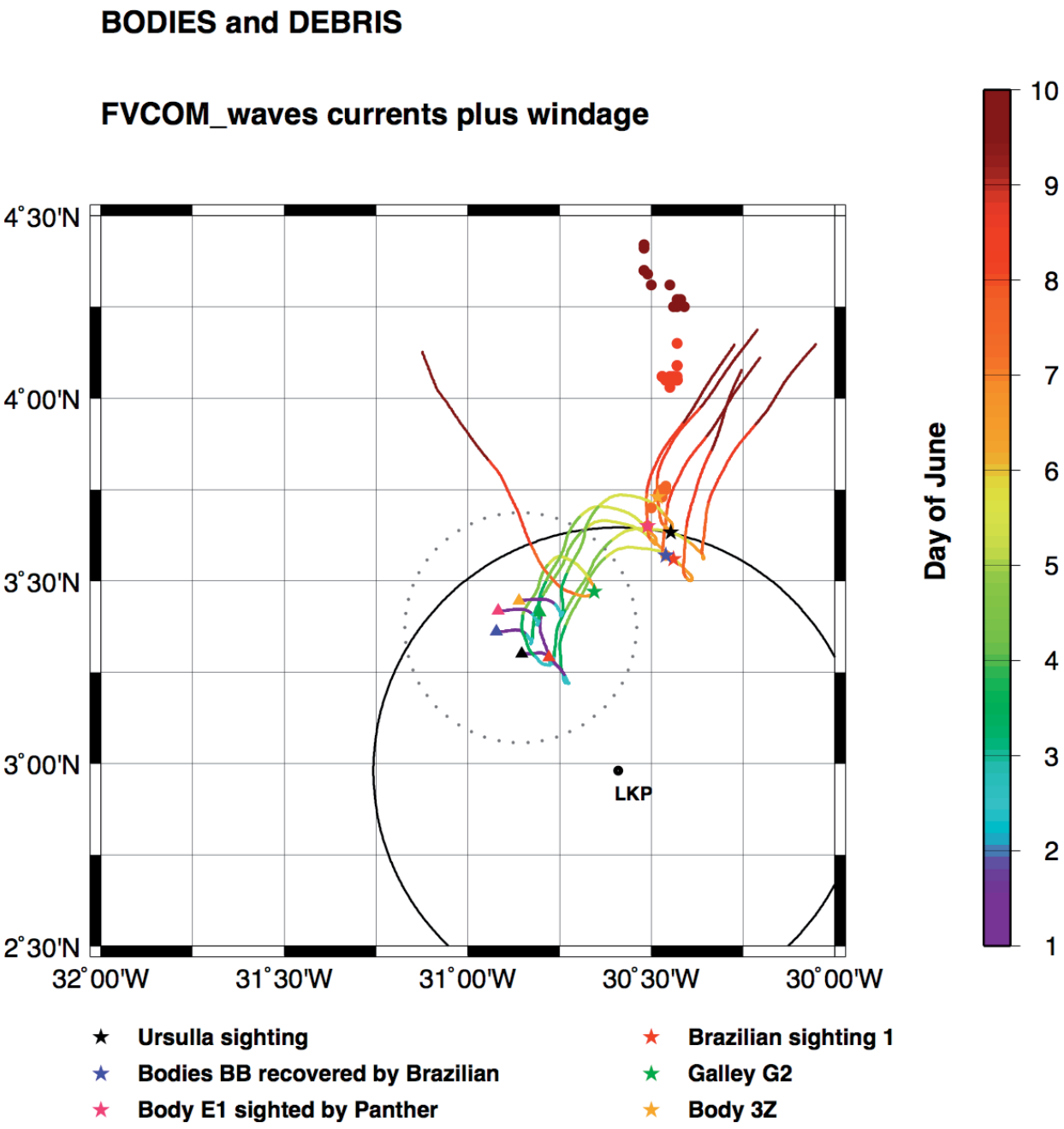

Figure 43 Backtracked positions (using FVCOMW with WRF winds) for six debris or bodies found over the period June 5 to June 7 2009 (Ursulla and S1 on June 5, BB and G2 on June 6, E1 and 3Z on June 7). No windage on Ursulla and the bodies, 1% and 2.5% on sighting 1 and Galley G2 respectively. The 35 km radius dotted circle gives the standard error on a backtracked point for June 1 at 2h.

Figure 42 shows a good agreement, with buoy displacements except notably near 29°10'W 4°20'N since the motion of buoy #27045

(in red) is not reproduced by far. But this particular buoy current data is not assimilated in the model. This reduces the relevance of this model since this buoy may have constrained strongly the velocity field near the crash zone. However backtracking of the six particles (U, S1, BB, G2, E1 and 3Z) does show a satisfying convergence (all points are within a 20 km diameter circle, see Figure 43).

Only results from FVCOMW with WRF winds are shown since they were judged better than those using other combinations (see report by C. Chen & R. Limeburner for full results and details).

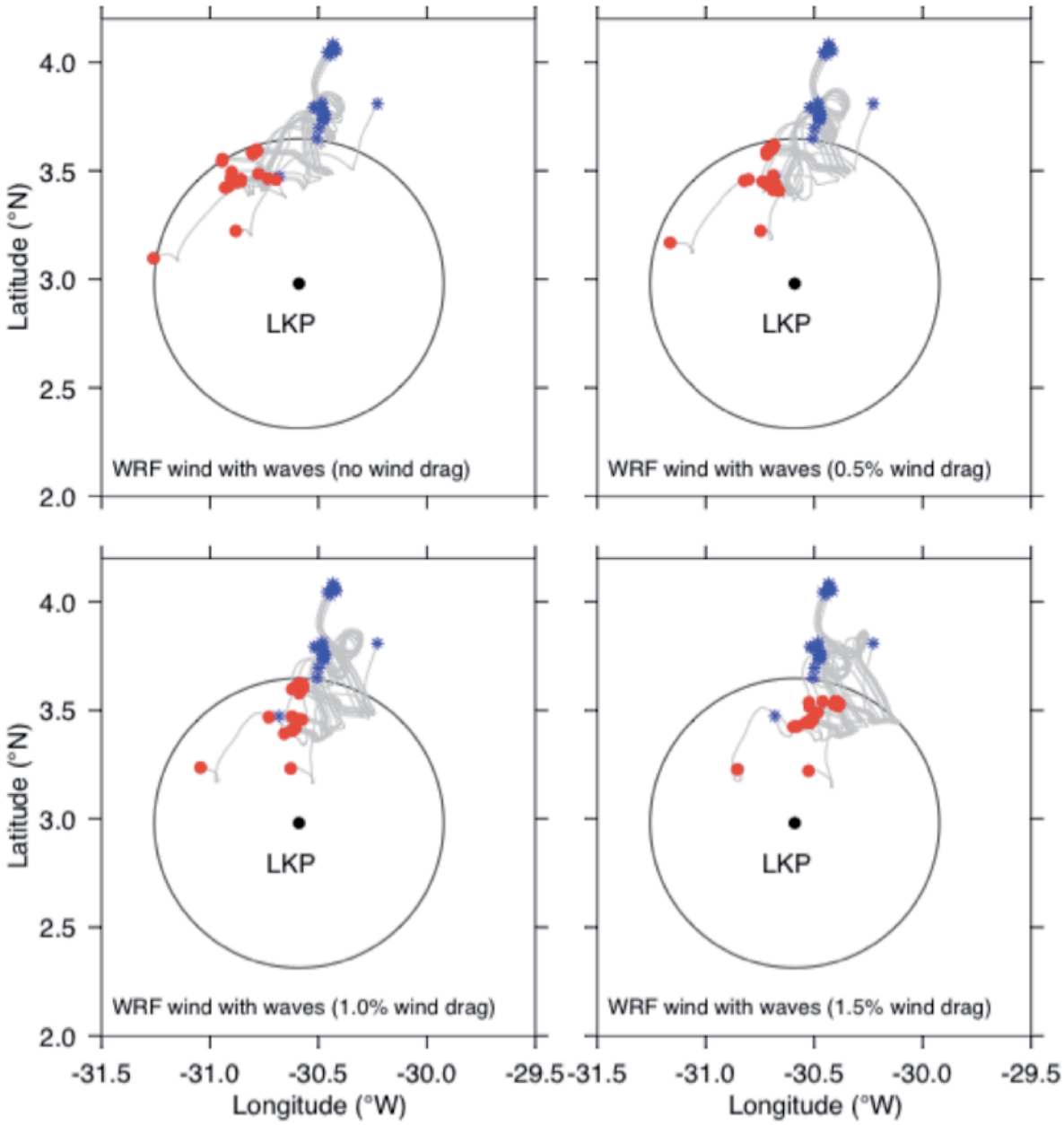

Figure 44 Original locations (red) of bodies found (at the blue locations) in the period of June 7-8, predicted by backtracking with FVCOMW and WRF winds. Drags (or windages) on bodies are 0%, 0.5%, 1% and 1.5%.

It has already been argued that before June 7, bodies recovered had possibly only been weakly dragged by wind (which was low between June 2 and June 6). This is no longer true on June 8 and afterwards. That is why windages between 0% and 1.5% were tried (not excluding bodies recovered on the 7th). For a given windage (see Figure 44), the backtracked bodies do converge satisfactorily (if we exclude the two isolated bodies, whose exact recovered locations are questionable, see caption of Figure 17). It is thus difficult to choose a preferred α value: 1% would give a possible crash zone (between 27 and 37 nautical miles) north of LKP.

If we consider all the predicted backtracked positions for bodies found on June 6-8 (Figure 45), under different wind drag conditions, we obtain an interesting clustering (if we exclude of course the two outliers in the south, already discussed). The right panel is the preferred solution since it includes the Stokes drift. It may be remarked however that the difference between the two approaches (without and with wave current interaction) is not so large as the difference implied by the Stokes drift alone, estimated with Wave Watch III (see discussion on Stokes drift later).

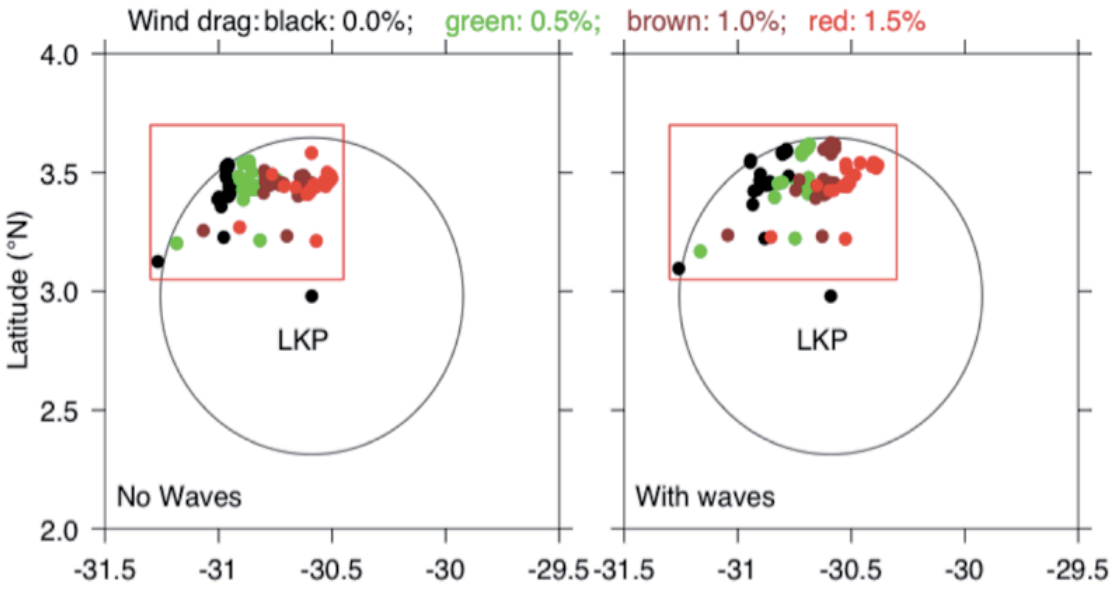

Figure 45 The ensemble original locations of bodies (found in the period of June 7-8) predicted by FVCOM under WRF wind condition for the case without (left panel) and with (right panel) the inclusion of the current-wave interaction.

Data Fitting

We have seen previously that the different model velocity fields were not in good agreement with the in situ velocity data. An idea to cope with this problem is to adjust the model velocity field to match the data locally, or in other words to deform the velocity field so that it conforms better to the data. It is a kind of primitive assimilation because as we'll see below it does not preserve the dynamical equations (contrary to the assimilation procedure used in FVCOM, even if nudging is creating kind of discontinuity near the data position and date).

Basically data fitting is performed as follows. Given a model velocity field at some time, we look for observed current data within a few hours of this time. Model velocity vectors, which are given on a regular grid in space (every 1/10° or 1/12° with the models used in our study), are first interpolated (generally using a bilinear interpolation) to observation positions. Then the observation increments (i.e. observed minus interpolated model values), scaled by exp $[-(\delta t/\tau)^2]$ (with τ= 3 days) are spread back to the surrounding four grid points (using the adjoint of the interpolation operator). Now the resulting field of increments is low pass filtered with a 2D Gaussian (with 90 km and 45 km marginal standard deviation in the zonal and meridional directions respectively). Finally the original velocity field is corrected by this filtered increment field (possibly scaled by a factor less than one). This is one iteration.

Generally between 5 and 10 iterations are performed.

Figure 46 shows the current field on June 1 resulting from such a data fitting to the velocity field of PSY2AVG. Actually PSY2AVG velocity field is the average from three different simulations: PSY2V3, ZOOM2 and ZOOM1. Such an ensemble average is chosen because it seems to give better results, statistically (see appendix 2). Obviously the agreement of PSY2AVG data fitted with the buoy trajectories is good (and much better than for OGCM without data fitting).

Such an approach is also interesting, because it can be applied to different models (except those already using the current data, like FVCOM and the objective analysis) and the results compared (see E. Greiner's report).

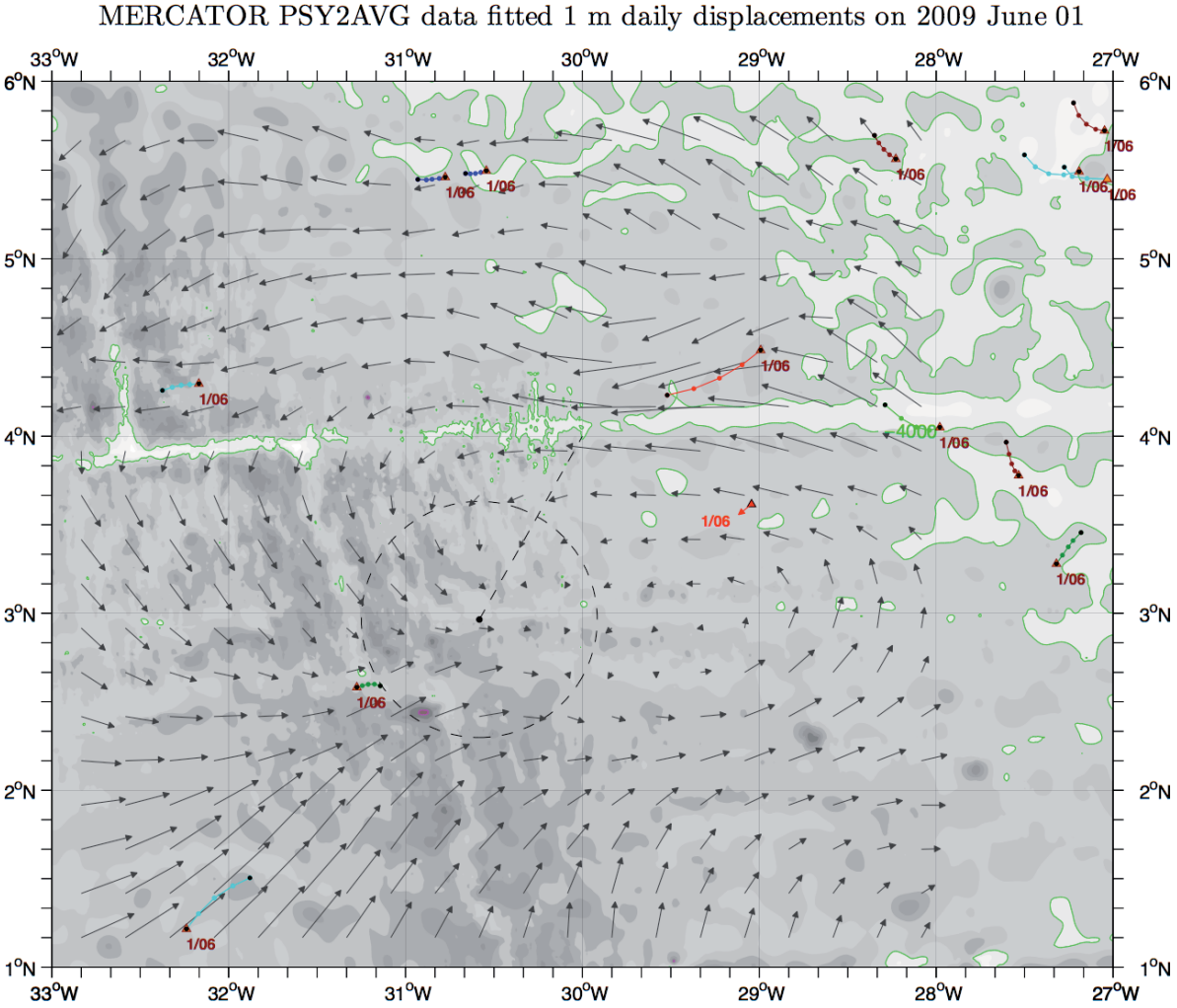

Figure 46 The daily velocity field given by Mercator PSY2AVG data fitted model on June 1 2009. Vectors give equivalent 24h displacements and buoy trajectories are shown over the 24h period between 0h and 24h on June 1 2009. There is a good agreement between the model data fitted and the buoy velocities (except perhaps for the Argo displacement near 29°W, 3°40'N).

An ensemble method to define a search zone

Given a model velocity field, data fitted or not, several (actually eleven) particles can be seeded at every grid point, on June 1 at 2h15mn and advected forward (with various windages, between 0% and 10%). Then a mean distance to the observation positions (e.g. all the body recovered locations, or all the debris sighted positions, or whatever choice) is calculated and the trajectory that minimises the mean distance is kept as the "best one".

The mean distance for a particle trajectory is obtained as follows: At the times of the selected observations, distances between the particle and the observation positions are computed. Then the one third of the smallest distances are averaged and the mean distance so obtained is

allocated to the initial point of the trajectory considered. It is possible also to vary the model velocity field by a constant factor (between 0.7 and 1.4) when looking for the minimum distance trajectory: this in some sense can cope partly with model uncertain velocity field. A few more details can be found in E. Greiner's report.

Let us apply this technique to the positions of bodies recovered before June 11: with ZOOM2 (i.e. the PSY2 zoom forced by ARPEGE winds) the best trajectory is found for 19 km (and a velocity scale of 0.85) without data fitting. With data fitting the minimal distance to the bodies is 18 km (and a scale of 0.9). Figure 47 shows the results.

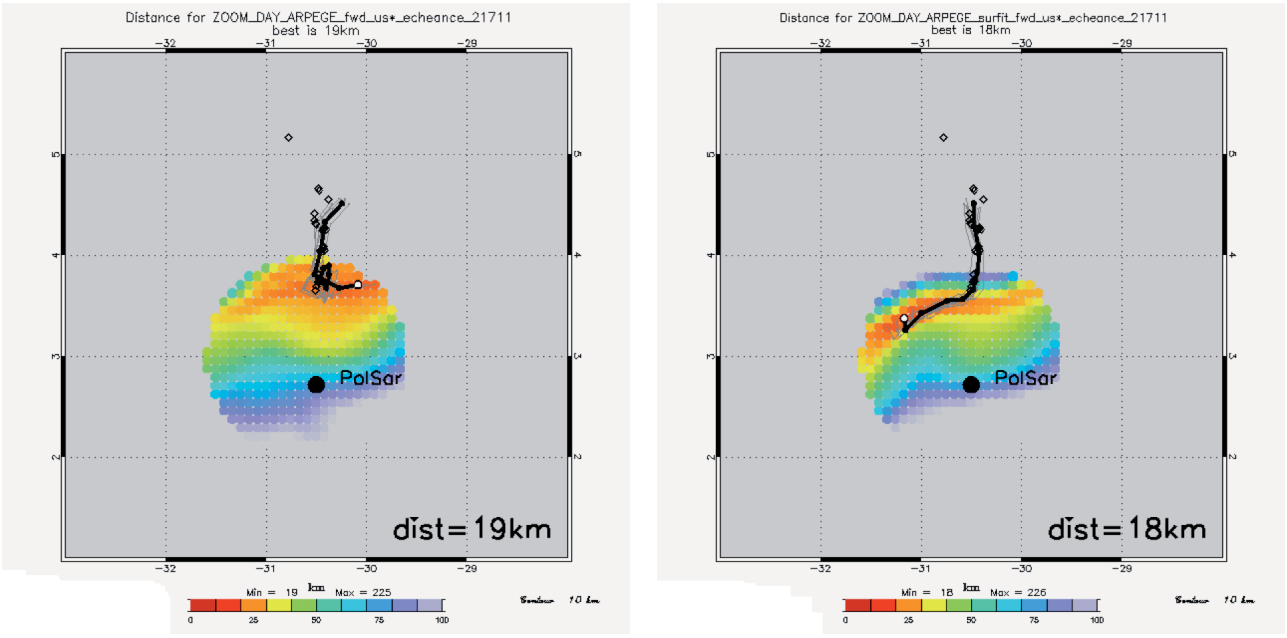

Figure 47 Mean distance repartition for ZOOM2 (with a 0.85 velocity scale) on the left, for ZOOM2 data fitted (with a 0.9 velocity scale) on the right. The black trajectory realizes the minimum distance. Particles are seeded within a 55 nm circle around LKP. The black dot denotes the pollution spot sighted by SAR.

With ZOOM1 (i.e. the PSY2 zoom forced by ECMWF winds) the best solution is obtained without data fitting (minimal distance is 17 km versus 18 km), see Figure 48. It is difficult however, to conclude which solution is best.

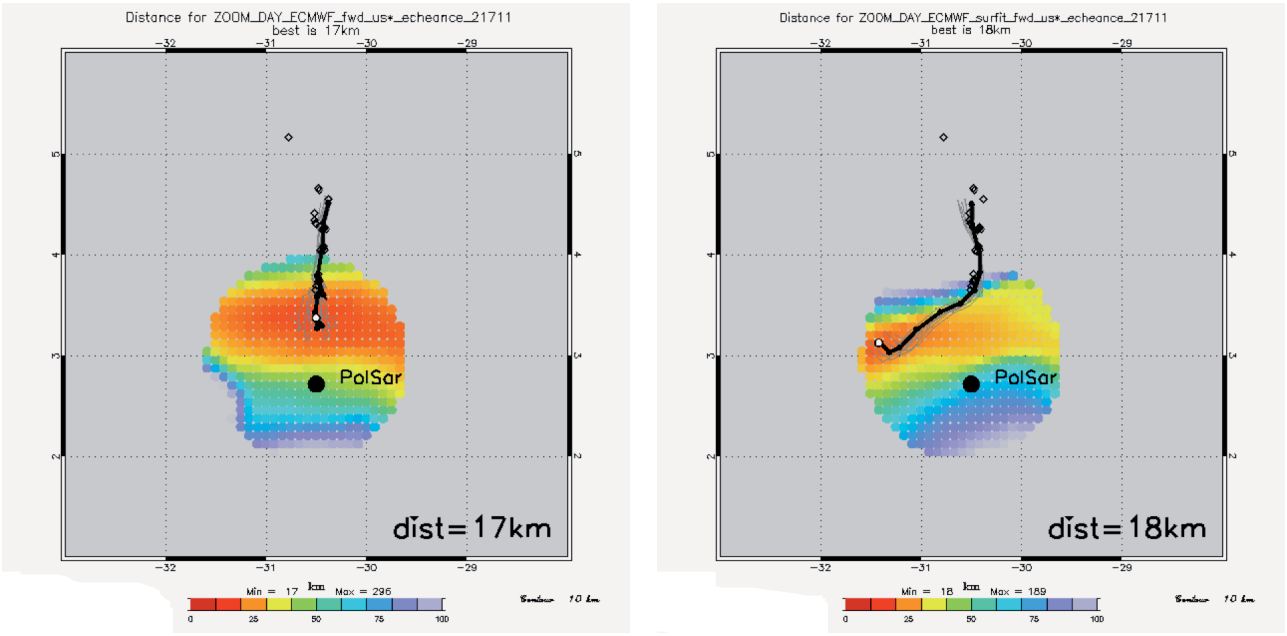

Figure 48 Mean distance repartition for ZOOM1 (with a 0.7 velocity scale) on the left, for ZOOM1 data fitted (with a 0.7 velocity scale) on the right.

If we select instead all the debris positions, or other model background velocity fields, the data fitting results are quite similar: the preferred crash position is to be found in a SW-NE oriented region in the northwest quadrant of the ACARS circle (Figure 49 right panel).

If we consider the minimum of all estimated distances, which is obtained without data fitting (Figure 49, left panel), the crash zone is found just north of LKP at about 27 nautical miles (this is not unlike the crash zone estimated from objective analysis). This would suggest a crash zone within a zonal band about 20-40 nautical miles north of LKP, and perhaps to the west, that is around 3°N 31°10'W.

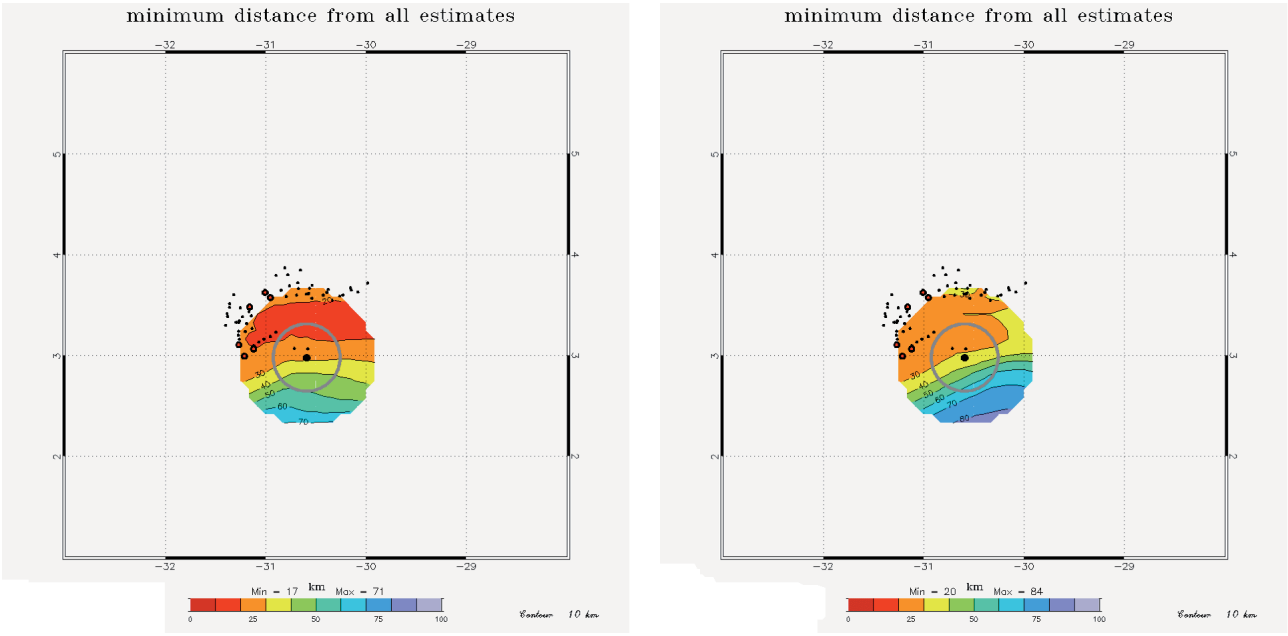

Figure 49 Distribution of the minimum mean distances of all the estimates, from ZOOM1, ZOOM2, PSY4[20] and Surcouf, with and without data fitting on the left, with data fitting only on the right. Red bullets (and little black points) are backtracked positions from VTP (and other debris) obtained with MOTHY (see discussion pages 90 and 91) and with varying immersions (100% and 90% immersion for VTP). The light grey circle is 20 nm from LKP.

Let us now examine the backward trajectories for the six selected debris or bodies (U, S1, BB, G2, E1 and 3Z) for PSY2AVG data fitted. Figure 50 shows the crash points are to the west-northwest of LKP as expected with the actual data fitting (see above). However, backtrack positions for particles recovered on June 5, 6 or 7 respectively are found more and more further west: there is no convergence of the backtracked trajectories.

[20] PSY4 is a new version of PSY2 (but in development phase)

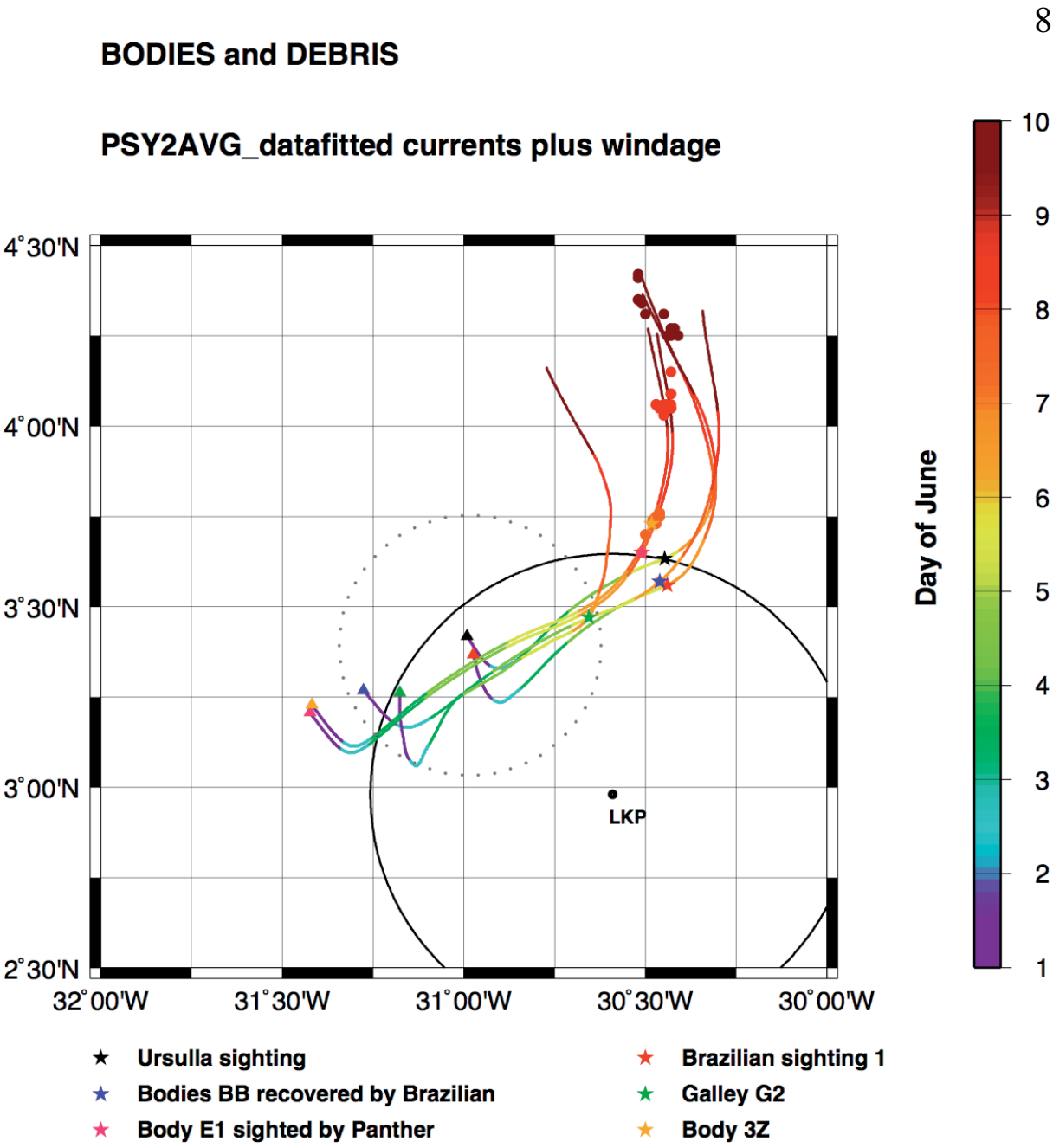

Figure 50 Backtracked positions (using Mercator PSY2AVG data fitted model) for six debris or bodies found over the period June 5 to June 7 2009 (Ursulla and S1 on June 5, BB and G2 on June 6, E1 and 3Z on June 7). No windage on Ursulla and the bodies, 1% and 2.5% on sighting 1 and Galley G2 respectively. The 40 km radius dotted circle gives the estimated standard error on a backtracked point for June 1 at 2h (see Appendix 6 for details).

Discussion

Integration scheme

In this study integration is done with a simple Euler scheme, which may call for caution. However a 4th order Runge-Kutta algorithm (Burden & Faires, 1985) has been compared (using the ZOOM2 velocity field) and gives an order of 1 km difference on the trajectories after 10 days of integration, which is negligible compared to other errors.

Comparison of model velocities to data

Figures 51 to 57 give, for each model, an overview of the fit (or misfit) of the various integrated trajectories (initialized on June 1 0h and at the corresponding buoy position) with the actual buoy trajectories. Of course for models assimilating part of the buoy current data, the comparison can be misleading (see also Figure 31 showing the fit with the objectively analysed field). Distance errors with the buoy trajectories are quantified in Appendix 6.

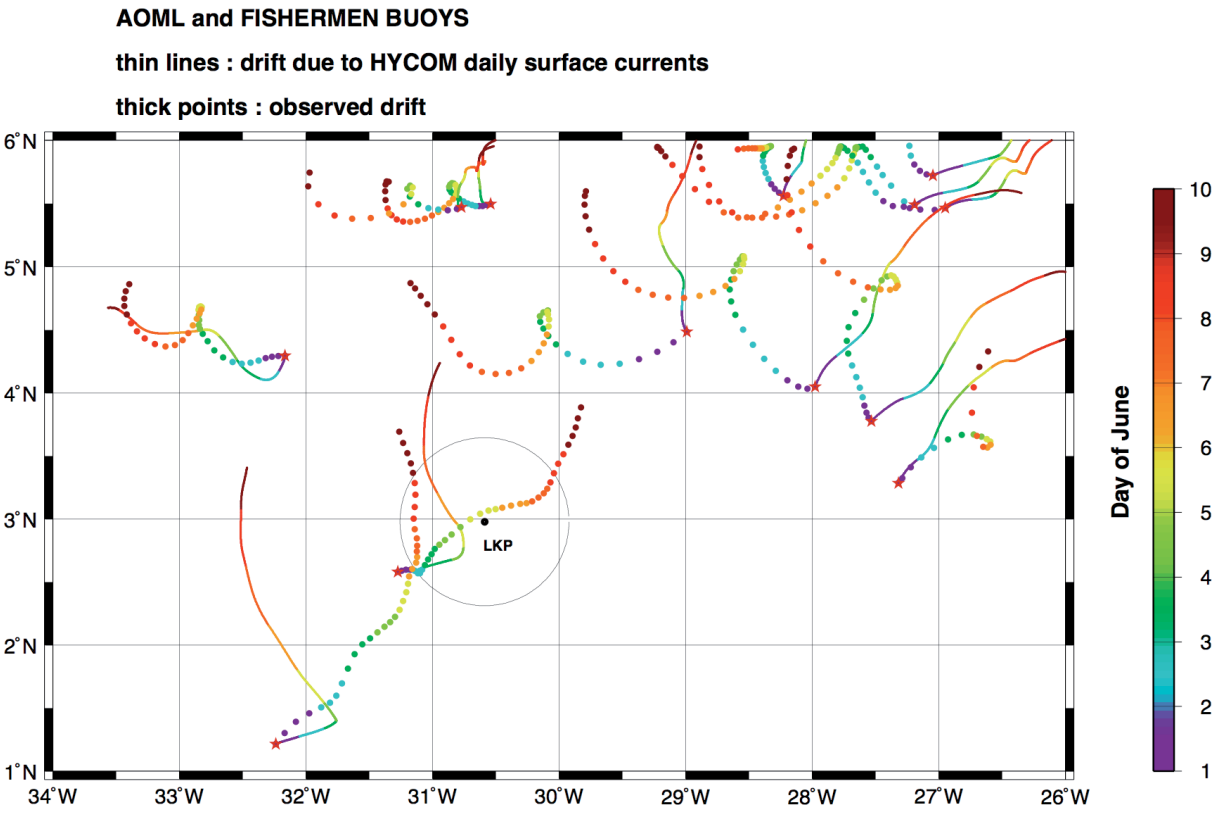

Figure 51 HYCOM model trajectories (forward) compared with real trajectories (one dot every 6h).

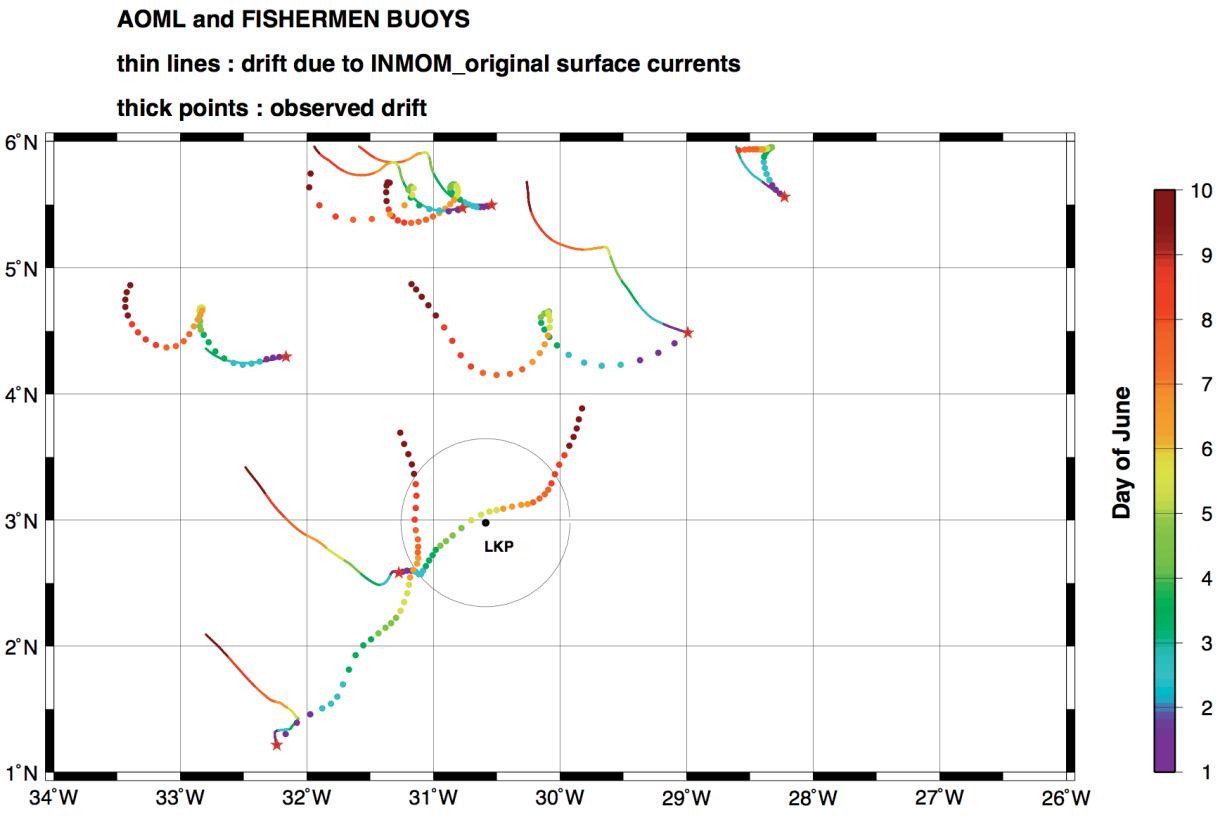

Figure 52 INMOM Original model trajectories (forward) compared with real trajectories (one dot every 6h).

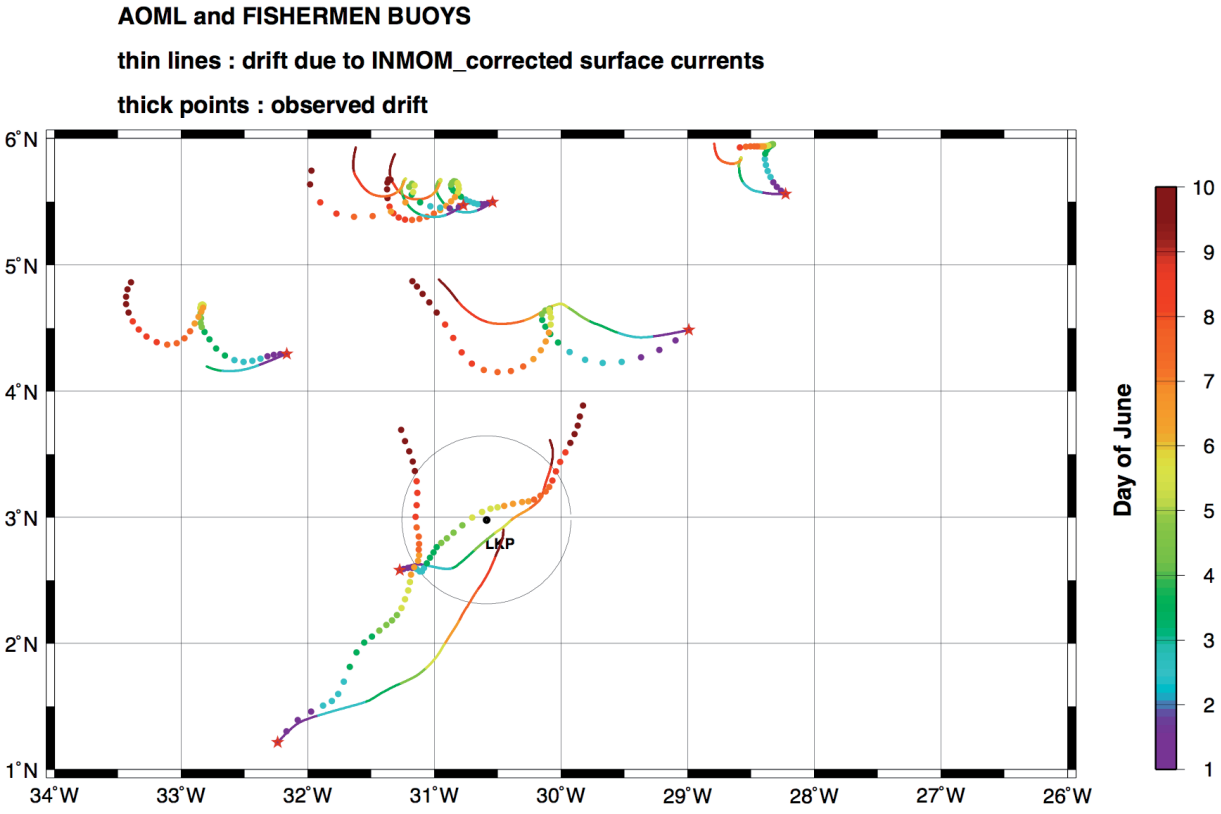

Figure 53 INMOM Corrected model trajectories (forward) compared with real trajectories (one dot every 6h).

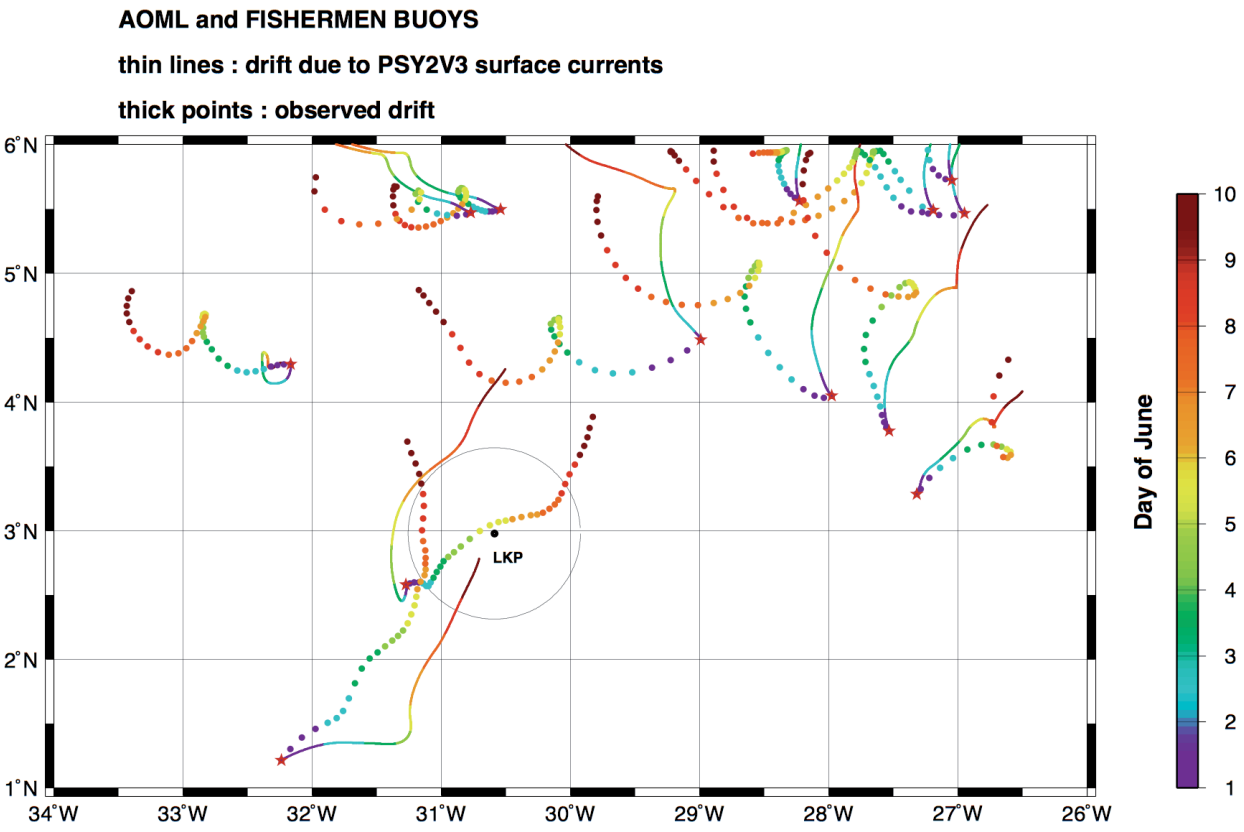

Figure 54 PSY2V3 model trajectories (forward) compared with real trajectories (one dot every 6h).

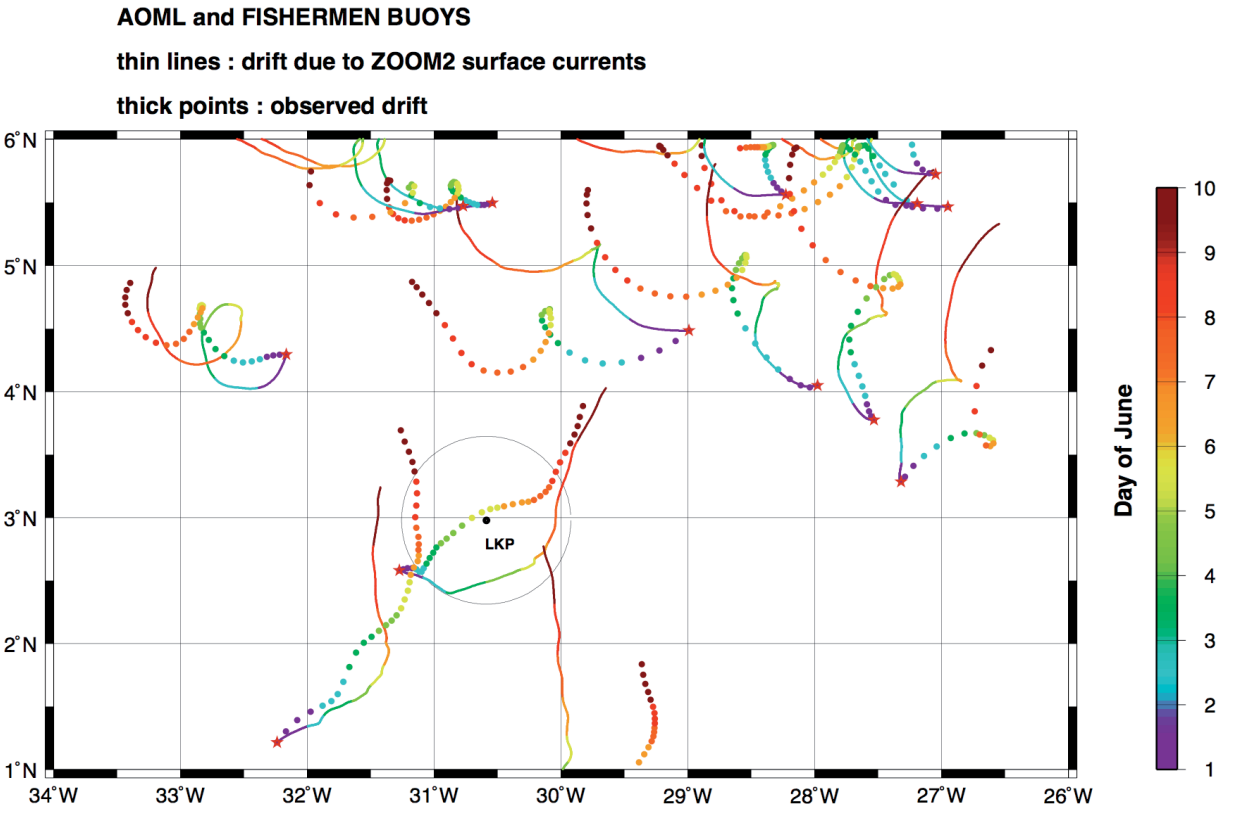

Figure 55 ZOOM2 model trajectories (forward) compared with real trajectories (one dot every 6h).

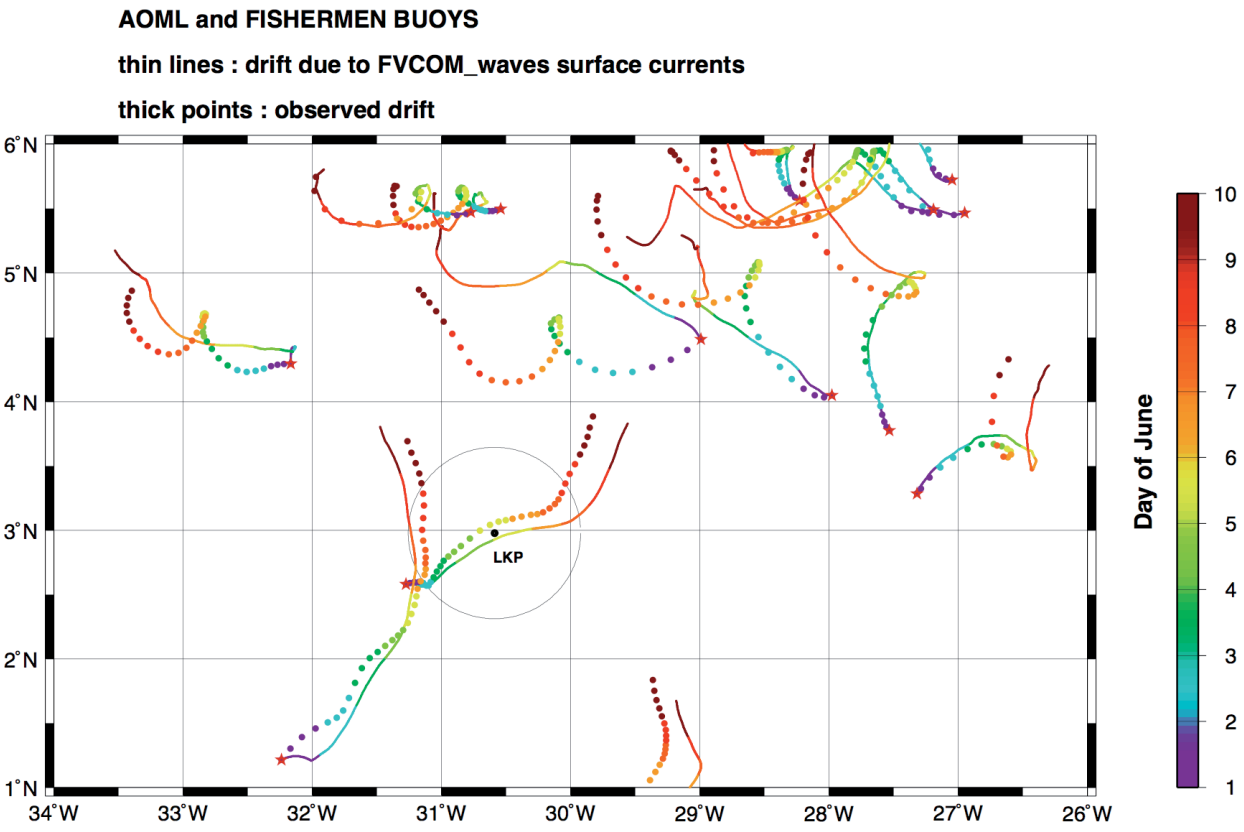

Figure 56 FVCOMW model trajectories (forward) compared with real trajectories (one dot every 6h).

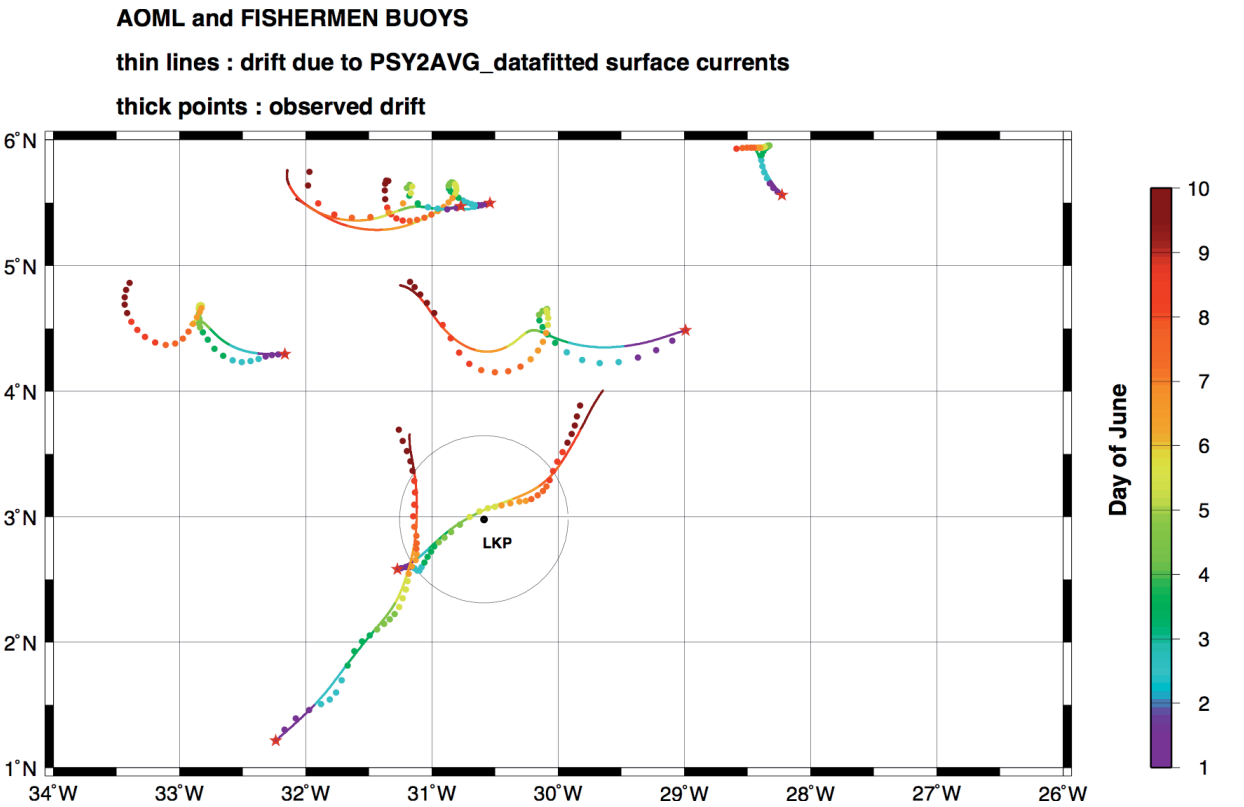

Figure 57 PSY2AVG data fitted model trajectories (forward) compared with real trajectories (one dot every 6h)

Limits of predictability (or sensitivity to initial conditions)

To understand this effect, let us compare oceanic tidal motions with lower frequency and highly energetic transient motions that are ubiquitous in the world ocean. The energy of these transient motions is much larger than that of the mean (so called general) ocean circulation (zero frequency or practically defined as a few year average).

Oceanic tidal currents have a line spectrum (that is, very narrow bands at a few well defined frequencies), whence a very good predictability. But the amplitude of tidal motion over the deep ocean is of the order of 1 cm s^{-1} (or 1 km day^{-1}). A particle will thus oscillate back and forth, tracing a small tidal ellipse. These ellipses are well determined and vary little over spatial distance, because of the very large tidal wave length. Tidal currents are thus unimportant in our case.

On the contrary, lower frequency transient motions are much more energetic, of the order of 10 cm s^{-1} to 100 cm s^{-1} (or 10 to 100 km day^{-1}) near the ocean surface, in particular. Particle drifts are mainly caused by these motions because of their high velocity and their low frequency. Mesoscale (as they are also called) motions have a wide spectrum, and decorrelate fast in time and space. Lagrangian (that is following a particle) velocities decorrelate in O(10 days) and over O(100 km) in space.

Such a fast decorrelation implies a very low predictability: let us assume we measure (with some error) an initial state and that we use a (realistic) numerical model to predict the future states. In the atmosphere, the time necessary for a doubling of the errors (between model output and observations) is of the order of a few days with present weather forecasting models (this is an exponential growth). In the ocean we do not know yet, but we may take something like 20 days (order of the decorrelation time mentioned above).

In consequence, if at t=0, model velocities are 50% erroneous, one can expect they will be 100% erroneous after 20 days. In our specific problem, we know the first debris positions only after 5 days. Thus, numerical models will give us reliable results only if the initial state is known accurately enough. Of course the same phenomenon will occur if we go backward (instead of forward). To quantify the models, we have thus compared the (forward) model integrations with the buoy trajectories over 10 days.

In fact, if we do not have data close enough (in time and space) to constrain the model where and when one wants to predict the circulation (in a deterministic way), it is useless to consider the output circulation from a numerical model (even the best one) to predict the actual circulation, because of this sensitivity to initial conditions. That is the reason why all the models used in our study do assimilate data (T and S profiles, sea surface height). Only FVCOM assimilates currents (but partially). We have seen however that the errors are still large with most (if not all) of the models used.

Stokes drift

At the sea surface, an integrated non-linear gravity wave effect (namely the Stokes drift) must be added to the model surface current (unless the Stokes drift is included somehow in the model formulation, which is the case for FVCOMW). The classical Stokes drift, corresponding to an approximately sinusoidal surface wave is given as $u_S = \omega\ a^2\ k\ e^{-2kz}$ where k, ω and a are respectively the wave number, angular frequency and wave amplitude (Phillips, 1977, e.g.). With $k= 2\pi/\lambda = 2\pi/100\ m^{-1}$, $\omega = 2\pi/T = 2\pi/8\ s^{-1}$ (because $\omega^2= gk$ over deep water) and a = 1 m, one obtains at z=0 m, $u_S = 4\pi^2\ a^2/\lambda T = 5$ cm s^{-1}. This is not much important but implies a 20 km drift over 5 days.

In fact, new theoretical developments by Rascle et al. (2006) and Rascle and Ardhuin (2009) complexifies the above view: with a regular swell over a calm ocean the Stokes drift would be totally compensated by an opposite current generated by the Coriolis force. On the contrary, with a rough sea (with a fully developed wind wave spectrum and a well mixed turbulent layer), the Coriolis induced current at the surface would be negligible compared to the classical Stokes drift. This latter case is more alike the situation on June 1 and 2.

Surface Stokes drift estimates, shown in Figure 58, are obtained from the Wave Watch III model (IFREMER-SHOM version). If this effect is correctly estimated by the model (which uses ECMWF surface stress), one sees this pushes possible crash points towards the Northeast (of the order of 20 km). As already mentioned, the Argo float surface displacements are assumed to include any Stokes drift since they are immerged near 0.5 m depth. On another hand, if the fishermen buoys are drogued near 10 or 15 m depth, they would include at most one third of the surface Stokes drift. It is difficult to say if this invalidates partly our data analysis: all the comparisons done between Argo float and fishermen buoy surface displacements are satisfying, but we do not measure the surface currents with an accuracy better than a few cms^{-1}.

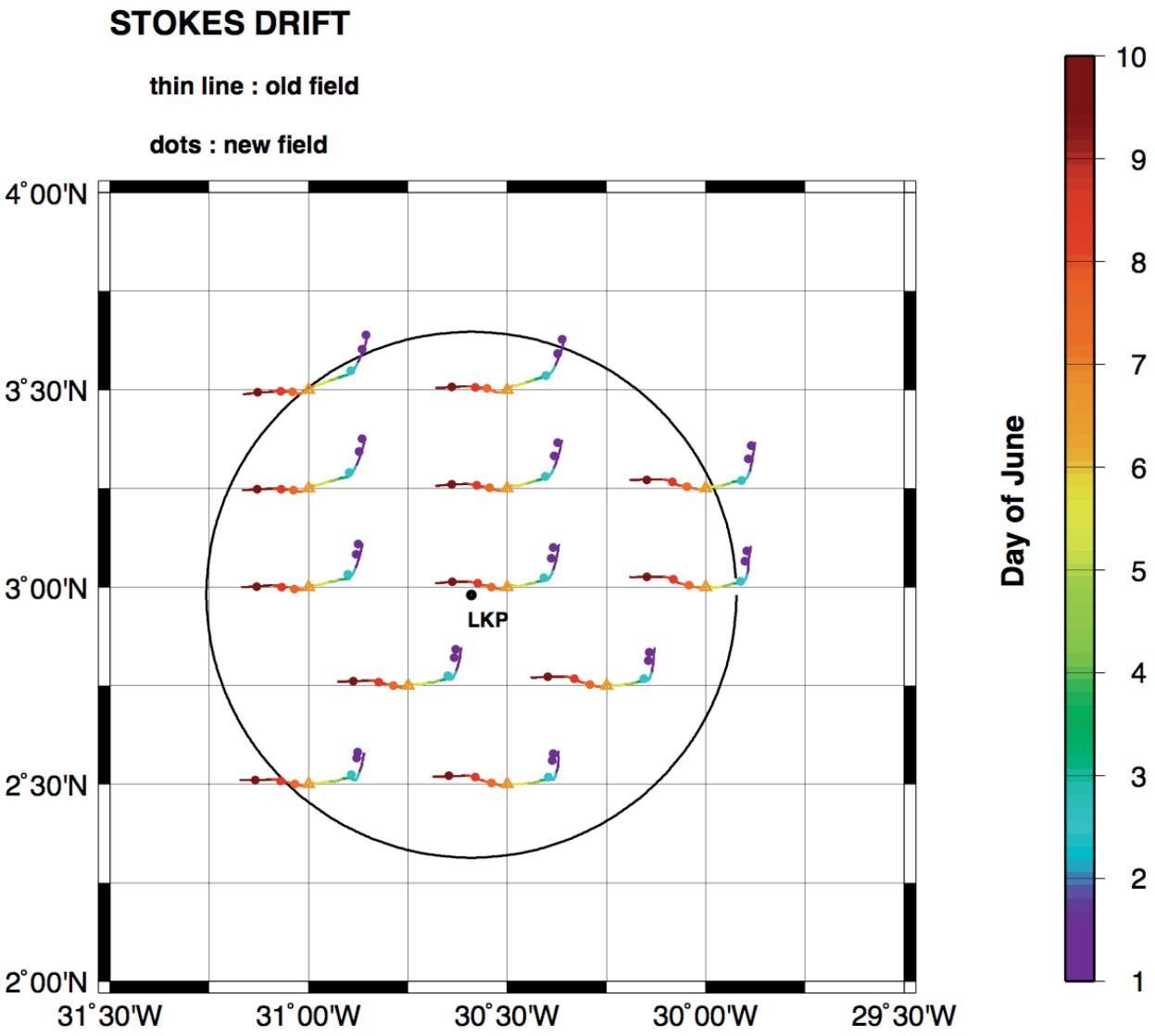

Figure 58 The Stokes drift calculated from Wave Watch III (IFREMER-SHOM version) with 6-hour ECMWF wind stress (triangle is centered on June 6 at 0h).

MOTHY

This is a drift computation (from Météo-France) that uses a given OGCM surface velocity field and adds the wind drag on the emerged part of the objects or bodies[21]. ARPEGE or ECMWF winds were used with different OGCM (PSY2V3, PSY2-REANA, ZOOM1, ZOOM2 or

[21] A more elaborate version uses the given OGCM velocity field at the base of the mixed layer as boundary condition and couples a shallow water model with a 1D model to get the horizontal velocity variation over the mixed layer (the turbulent viscosity K_V increases linearly both from the surface and from the mixed layer depth). See Daniel et al. (2002). However, over our region, results with this version are less reliable than those using directly the model surface velocity.

Surcouf) surface current fields (with a drag coefficient ratio equal to one) and the drifts compared with the two buoy trajectories passing through the ACARS circle. As can be expected, results do not differ significantly from those previously obtained with the different models or analysis considered, which use instead Cersat HR blended wind (see appendix 5). It is the current field that matters (and ZOOM2 got the best score among the OGCMs tested). As an example, the red bullets in Figure 49, give the backtracked positions for the vertical tail fin (or VTP) with an assumed immersion I of 90% or 100%, while the little black points are the possible backtracked positions from U, S1, BB, G2, E1 and 3Z with a few varying immersion rates: with the ZOOM2 model MOTHY gives points north of LKP, while with PSY2-REANA points fall to the west. All results are given in the report of D. Paradis, S. Law-Chune, J. Negre and P. Daniel.

A leeway statistical approach

Up to now, we have considered only a wind drag on the emerged part of an object or body (which causes the slippage relative to the sea surface current[22]). However, if the object is asymmetrical, there will be a "lift" component, perpendicular to the relative wind direction (due to the smallness of current speeds versus wind speeds, absolute and relative wind direction are generally equalled). The drift associated with wind forces on the exposed above-water part of the object is called the leeway. Small objects (typically less than 10 m) are observed to reach terminal velocity in O(10 s) under strong wind conditions (20 m s^{-1}). Infinite acceleration and constant velocity are thus acceptable simplifications (for 1h time steps). Field experiments have determined the relation between the wind speed and the downwind (DWL) and crosswind (CWL) leeway speed components L_d and L_c (Allen, 2005; Breivik & Allen, 2008) for various objects. Linear relations of the form $L_d = a_d\|\mathbf{W}_{10}\|+b_d$ and $L_c = a_c\|\mathbf{W}_{10}\|+b_c$ are well verified (with some scatter). b_d and b_c are small and often neglected. That is what we have done so far for the (down)wind drag.

Rather than forecasting (or backcasting) the "exact" trajectory of an object or body (what we have done so far) MOTHY now calculates a large number N of trajectories (actually N= 480) by perturbing the L_d and L_c coefficients, to account for the observed scatter mentioned (but keeping them constant for each trajectory).

---

[22] We should normally include the Stokes drift in the surface current, but this has not been done here (following Breivik & Allen, 2008).

We have: $\mathbf{x}_n(t_0) - \mathbf{x}(t) = \int_t^{t_0} \left[\mathbf{L}_n(t') + \mathbf{u}_w(t')\right] dt'$ with

$\mathbf{L}_n(t') = a_{d,n}\mathbf{W}_{10}(t') \pm a_{c,n}\mathbf{k} \times \mathbf{W}_{10}(t')$, n=1, …, N.

k is the unit vertical vector, $a_{d,n}=a_d+\varepsilon_n'$, $a_{c,n}=a_c+\varepsilon_n''$ and ε' and ε'' are random samples from a Gaussian distribution. The + (resp. -) sign corresponds to a drift at an angle left (resp. right) of downwind).

Since we do not know if the object or body was drifting to the left or to the right of downwind, the orientation of the ensemble members is distributed equally (but once started to the left, e.g., a member will continue so throughout the simulation).

The 480 MOTHY backtracked particles were started either from the BB or the 3Z body positions, with a_d=1.3% a_c=0.74% and with a scatter implied by a standard error on L_d and L_c of 8.3 cms^{-1} and 6.7 cm s^{-1} (values from Allen, 2005). Figure 59 shows the results for the BB (first two recovered) bodies with ZOOM2 surface currents and ARPEGE or ECMWF winds respectively. Results for the 3Z body are less convincing since most of the particles are found outside of the ACARS circle, but that may be due, in part, to the uncertain latitude of the recovered 3Z position (3.81°N or 3.73°N; the former used here while the latter is used in all the model comparisons).

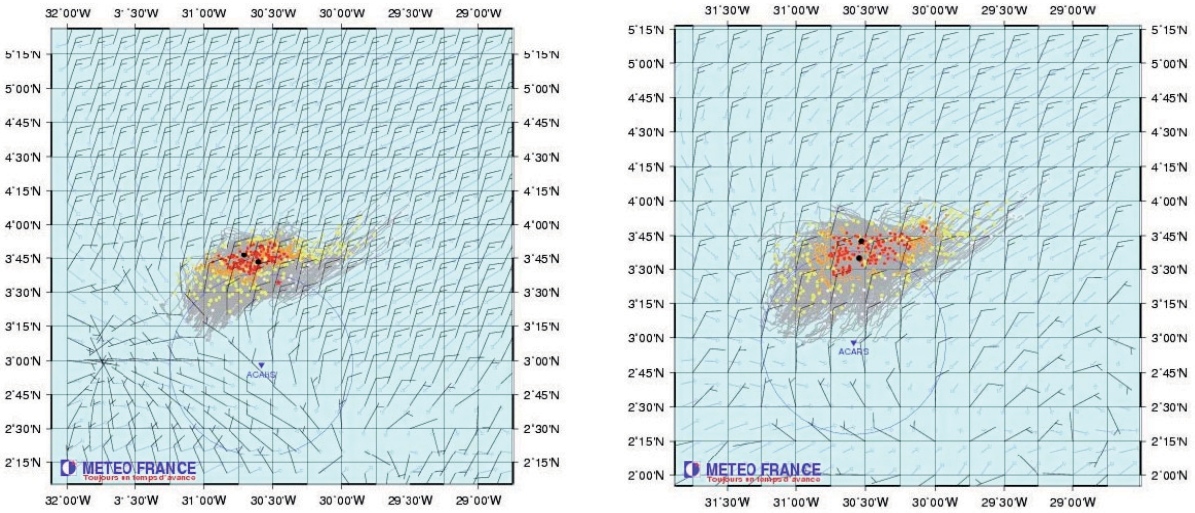

Figure 59 Backtracked particles from BB with ZOOM2 surface currents. ARPEGE winds (left panel) or ECMWF winds (right panel) are used with varying DWL and CWL coefficients. Red, orange and yellow dots represent 50%, 18% and 27% of the particles, thus totalling 95%. The two black dots are the means over left and right of downwind orientations respectively.

Figure 60 shows instead the results for the body 3Z but with PSY2AVG data fitted surface currents.

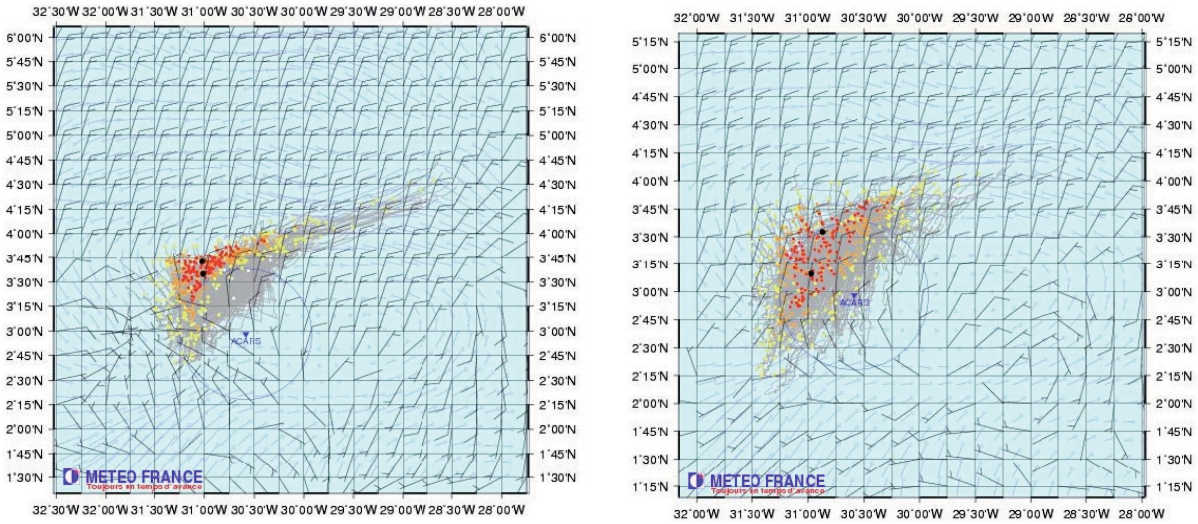

Figure 60 Backtracked particles from 3Z with PSY2AVG data fitted surface currents. ARPEGE winds (left panel) or ECMWF winds (right panel) are used with varying DWL and CWL coefficients. Red, orange and yellow dots represent 50%, 18% and 27% of the particles, thus totalling 95%. The two black dots are the means over left and right of downwind orientations respectively.

It is still not surprising to recover the same regions as with the "deterministic" approach (ZOOM2 versus PSY2AVG data fitted) but these results somehow give an idea of the uncertainty (and size) we must expect for a search area.

Are the a_d and a_c values chosen really relevant for the dead bodies used in this Monte Carlo like simulation? Remember that during the first 24 hours after the accident, bodies are assumed to be fully immerged, thus without any leeway. That almost all the bodies sighted or recovered were found after June 6 flowing consistently northward and not dispersing longitudinally, may not plead for a sensible CWL (unless all bodies behave similarly). Furthermore the experimental basis for estimating deceased persons in water (PIW) leeway coefficients is meagre (Allen & Plourde, 1999). No windage on the bodies until June 7 seems plausible. On June 8 and 9, however, easterly winds strengthened and have possibly pushed the bodies westward (which were then 40% emerged, see Chapter I). This may explain the westward excursion apparent on body positions on June 9 (see Figures 17, 39 or 43 e.g.).

IV Defining the search area

To define a final search area on a statistical basis, we use the average of the six debris or bodies (U, S1, BB, G2, E1 and 3Z) backtracked positions for a given model or analysis (shown in previous Figures) as the estimated wreckage location for that model or analysis. Then using the estimated error after 5 days for each model or analysis, we calculate the weighted mean of these crash points (weights depending on the errors, being smaller with larger errors). We then assume the different crash points are obtained independently which enables us to obtain very simply a 95% confidence area. Details of the procedure will be given below. Figure 61 shows the distribution of the backtracked positions and mean crash points, for each model or analysis selected, together with the 95% confidence area. See also Figure 63 that gives the 95% confidence area superposed over a nicer topography (actually the one surveyed in July and August 2009 by the R/V Pourquoi-Pas).

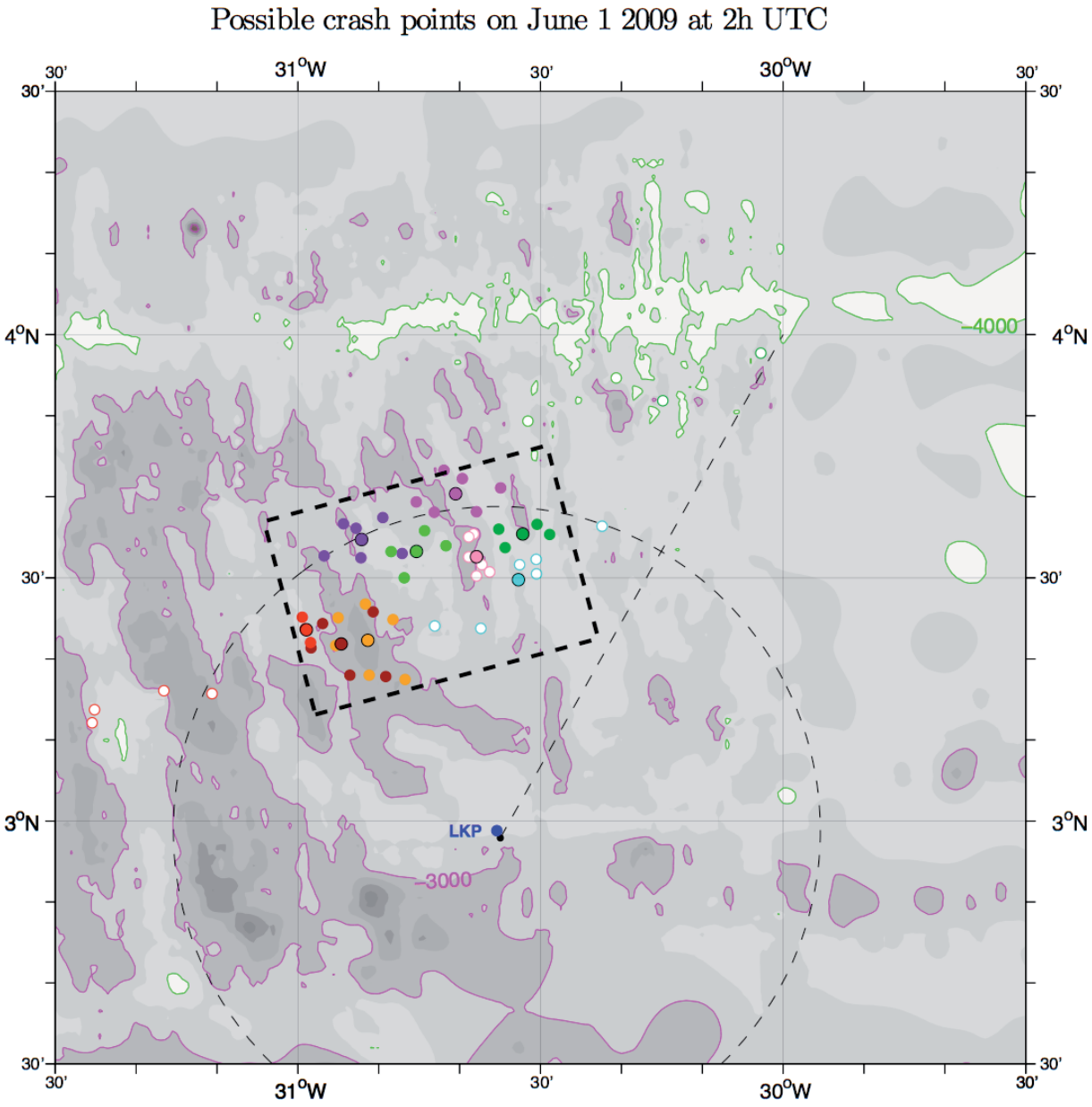

Figure 61 Backtracked positions from the various models selected. Smaller dots give the backtracked positions for the 6 different particles (U, S1, BB, G2, E1 and 3Z) while bigger dots show their mean. PSY2AVG data fitted (only U and S1 are used) points are red, FVCOM ones brawn, FVCOMW orange, ZOOM2 purple, ZOOM2 with Stokes magenta, OI50 green and OI85 dark green (only U, S1, BB and G2 are used with the old analysis). Added on the Figure (but not used for the statistical estimation on the confidence area) are the (new analysis) OI75 points (pink and with the 6 particles). Also shown (but not used for the statistical estimation) INMOMC points (cyan). Red open circles to the west and green open circles to the north-east are the points from PSY2AVG data fitted, OI50 and OI85 considered not realistic to be used in the statistical estimation. Dashed rectangle gives the 95% confidence search zone estimated.

The statistical method

Let us recall first what is a 95% confidence area. This is a **random** domain that contains the crash point with a 95% probability. This means that if a set of measurements were done repeatedly and a confidence region calculated for each set of measurements, then 95 percent of those regions in a long-term relative-frequency sense would include the true wreckage location.

As we have seen, different numerical models and a kinematic analysis have been used to backtrack debris and bodies. We have selected six derelicts sighted or recovered on June 5, 6 and 7 (positions and dates are given in Table 1). So, for each model or analysis (numbered i = 1, …, 7), we have n_i estimates, (x_{ik}, y_{ik}) k = 1, … n_i. Here x and y stand for zonal and meridional distances (since we are close to the equator, we can also approximate one degree of longitude and one degree of latitude both by 111 km) and $n_i = 6$ at most.

First we compute a mean position for each of the seven models selected, as: $\overline{x_i} = \frac{1}{n_i}\sum_{k=1}^{n_i} x_{ik}$ $\overline{y_i} = \frac{1}{n_i}\sum_{k=1}^{n_i} y_{ik}$ i = 1 … 7

We then assume each of these 7 mean positions has a 2D isotropic Gaussian distribution with marginal variance V_i^2 and mean the unknown crash position $\mu = (\mu_x, \mu_y)$. The standard deviations V_i are estimated as the average distance errors to the buoy trajectories after 5 days (for each model) divided by $\sqrt{\frac{\pi}{2}}$, because the distance error is Rayleigh distributed if the position vector error with the buoy corresponding positions is also assumed to be isotropic and Gaussian (see footnote 14 in chapter II about objective analysis). Figures A6_3 and A6_4 in Appendix 6 show the evolution of the distance error.

Table 2 below gives the mean estimated crash positions and the corresponding standard deviations V_i for each of the 7 models selected.

We estimate μ_x and μ_y as the weighted means: $\hat{\mu}_x = \sum_{i=1}^{7} \omega_i \overline{x_i}$, $\hat{\mu}_y = \sum_{i=1}^{7} \omega_i \overline{y_i}$ with $\omega_i = \frac{1/V_i^2}{W}$ and $W = \sum_{i=1}^{7} \frac{1}{V_i^2}$. Assuming mutual independence between the model errors[23] implies that the estimators $\hat{\mu}_x$ and $\hat{\mu}_y$ are Gaussian distributed with mean μ_x and μ_y and the same variance 1/W.

[23] Although this hypothesis is probably false, we assume it because of lack of information about the correlation between the errors.

$\hat{\mu}_x$ and $\hat{\mu}_y$ being also independent, we can determine two confidence intervals I_x and I_y such that Prob $[\mu_x \in I_x] = \beta_1$, Prob $[\mu_y \in I_y] = \beta_2$ with $\beta_1\beta_2 = 0.95$. Thus, we obtain a 95% confidence area.

Using the quantiles of a Normal distribution (Gaussian with mean 0 and variance 1) $q_{(1+\beta 1)/2}$ and $q_{(1+\beta 2)/2}$, we obtain two symmetrical intervals:

$$I_x = \left[\hat{\mu}_x - \frac{q_{(1+\beta_1)/2}}{\sqrt{1/W}}, \hat{\mu}_x + \frac{q_{(1+\beta_1)/2}}{\sqrt{1/W}}\right], \quad I_y = \left[\hat{\mu}_y - \frac{q_{(1+\beta_2)/2}}{\sqrt{1/W}}, \hat{\mu}_y + \frac{q_{(1+\beta_2)/2}}{\sqrt{1/W}}\right].$$

Of course, choosing $\beta_1 = \beta_2 = 0.95^{1/2}$ gives a square zone (with $q_{(1+\beta 1)/2} \approx 2.24$). But we can also choose $\beta_1 \neq \beta_2$ as long as their product is 0.95, giving a rectangle. We can also choose asymmetrical intervals: for example, $I_y = \left[\hat{\mu}_y - \frac{q_{\alpha_2}}{\sqrt{1/W}}, \hat{\mu}_y + \frac{q_{(1-\alpha_1)}}{\sqrt{1/W}}\right]$ with $\alpha_1 + \alpha_2 = 1-\beta_2$.

Actually, in order to minimize the part of the zone outside of the 40 nautical miles ACARS circle, and to cover all the model mean positions, we have chosen $\beta_1 = 0.995^{1/2}$ and $\beta_2 = 0.95/\beta_1$ (recall index 1 stands for x or longitude, index 2 for y or latitude) together with an asymmetrical meridional confidence interval (with $\alpha_1 = 4(1-\beta_2)/5$, $\alpha_2 = (1-\beta_2)/5$). Finally, since all model mean positions are isotropically distributed, we can rotate the zone by 15°, to match the radial direction from LKP.

Details about statistical tests used and alternative results can be found in P. Lezaud's reports.

Lat	Long	Standard deviation	Model
3.579	-30.869	48	ZOOM2
3.673	-30.675	48	ZOOM2+ Stokes
3.364	-30.911	35	FVCOM
3.372	-30.856	35	FVCOMW
3.554	-30.756	20	OI50
3.590	-30.537	20	OI85
3.393	-30.983	40	PSY2AVG data fitted

Table 2 Mean crash positions and estimated standard deviations for the seven models selected.

How did we choose the models

The choice of the models to be kept in the statistical estimation of the search zone was made after many discussions. Basically, all models with estimated standard error less than 50 km were retained, except

INMOMC (40 km standard error) because we considered it would add a position near an already highly constrained one with OI85 (20 km standard error) and we could not exclude a dependence of INMOMC which uses the temporal mean from OI85. Both ZOOM2 and ZOOM2 with Stokes were kept because they sample different positions, and we were not able to decide which was best. FVCOM and FVCOMW giving almost the same positions we could have kept only one of these two. Both were retained however on the prejudice they are dynamically consistent and assimilate current data. Maybe this has constrained too much the estimation in the west where the data fitted PSY2AVG positions is also an attractor. Concerning optimal interpolation, we kept both the old analyses for 50 km and 85 km, to cope for the longitudinal uncertainty, while constraining in fact around the middle zone, near the best estimated positions from the new analysis (e.g. OI75) that was not available yet for this calculation.

A more empirical method

Let us now use only the backtracked positions of the very first debris sighted (actually by the Singaporean merchant ship Ursulla), for each model or analysis and see if we can define a smaller search area.

Our argument is based first on the fact that the earlier the debris is found the better the backtracking should be (the error should be smallest, in a statistical sense).

Secondly, the position relayed by the Ursulla crew on June 5 is north of the first debris found later that day by the Brazilian Navy. This might indicate a southward current which would have moved the debris 8 km to the south in 5 h, thus at ~1 knot. However, at that time and place, the estimated current, well constrained by the buoy data, is only a few cm s^{-1}. This suggests there was a substantial windage effect (not well known) on this debris, while it may be minimal for the debris sighted by Ursulla. This is consistent with the windages that we estimated previously to get the backward trajectories of the different debris and bodies to converge to a small zone. But, of course we cannot exclude some error on the Ursulla position.

Figure 62 shows all the backward Ursulla trajectories (with 0% windage) from the different models used to estimate the search zone (plus INMOMC and HYCOM). Let us discuss briefly these results (this will also give the reader a kind of summary of the work done).

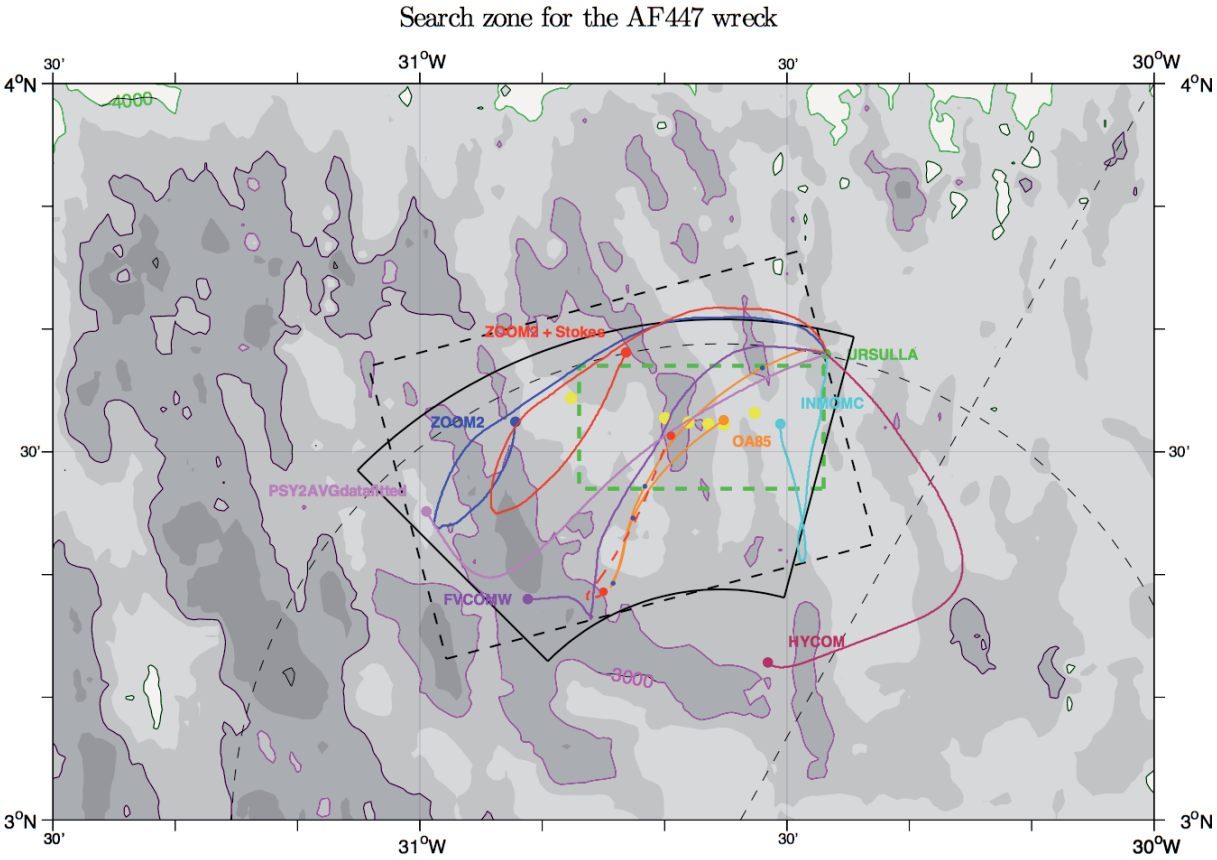

Figure 62 Trajectories backtracked to June 1 2009 2h 15 (date of crash) from the Ursulla position sighted on June 5 at 16h (see text for comments). The yellow dots are the mean crash positions estimated with varying the r_0 parameter of the model covariance function (this is the new analysis with time correlation and more data that is considered here). From west to east, r_0 = 55, 70, 75, 80, 85 and 100 km. The dotted red curve is the backward integration for a hypothetical particle found at 3°18.6'N 30° 45.0'W on June 3 at 0h, using the current field of ZOOM2 with a Stokes drift added (calculated with Wave Watch III). The dashed green rectangle is the provisory search zone given in chapter II.

OBJECTIVE ANALYSIS (of current data)

The new objective analysis of the measured surface (or near surface) currents with r_0=85 km (and a Gaussian time correlation) gives the orange dot (labelled OA85 in the Figure) and the orange backward trajectory. Yellow dots show averages of backtracked positions (from U, BB and G2) for r_0 = 55, 70, 75, 80, 85 and 100 km (West to East). The reconstructed trajectories for r_0 = 70, 75 or 80 km fit almost perfectly the actual buoy trajectories (order of 1 km error after 5 days) which would suggest selecting the corresponding crash points as the more probable. However, the analysis is not well constrained on June 1

and 2 (because the data is far from the region of interest) and we have seen the distance uncertainty can reach 25 km (comparing with an independent model trajectories).

FVCOMW

The predicted Ursulla trajectory (purple) shows a good agreement with OA85 over the period June 3 to June 5. On June 3 at 0h the 2 trajectories are found almost at the same position. However this is not so during June 1 and 2: FVCOM goes to the west while OI85 returns toward the northeast. This discrepancy is easily explained if we look for example at the FVCOMW velocity field on June 1 at 12h (Figure 42). The flow is eastward within the ACARS circle but slightly north of 4°N it is orthogonal to the (cyan and red) buoy westward motions. Probably the flow cannot be so strongly eastward in the northern part of the ACARS circle. This does not reject the FVCOMW solution but casts doubt on it (remember the cyan and red buoy current data are not assimilated by FVCOMW, whereas other current data are).

ZOOM2

The ZOOM2 Ursulla trajectory shows general features similar to OA85 and FVCOMW (at least between June 3 and June 5). However, the model velocity field (Figure 38) is not closer to the measured currents than FVCOMW. Interestingly, if the Stokes drift calculated with Wave Watch III is taken into account, the ZOOM2 Ursulla backtracked position falls close to the green rectangle, but 40 nautical miles away from LKP (which is a bit far). A simulation starting from the mean position on June 3 at 0h as given by FVCOMW and OA85 and integrating backward through the ZOOM2 velocity field with Stokes drift falls quite close to the OA middle points directly on top of a local mountain chain.

PSY2AVG Data fitted

This analysis uses a current field which is an average of 3 current fields from 3 models (not much different between them however) and then adjusts the currents so that they compared satisfactorily to nearby buoy current data and body motions (as given by their recovered positions until June 10 2009). This non academic approach (an average of several model is not a model, stricto sensu) is nevertheless interesting. The backtracked trajectory from Ursulla is roughly consistent with the other approaches with a south-south-eastward current on June 1 2009 which cannot be excluded (by the way this is

intermediate between FVCOM eastward flow and ZOOM2 or OA85 south south-westward flow that same day). What is puzzling in this analysis is the fact that the various backtracked estimates for a few debris and bodies (Figure 50) are scattered over 50 km (whereas if the "model" was consistent they should be found more or less grouped together, let us say within 10 km or so, to cope for reasonable model imperfections).

INMOMC

This model replaces its own mean velocity field over the period June 1 to June 7 by the corresponding mean velocity field from the (old) OI85 in order to give more realistic currents south of 4°N. It finds a crash point near 3°31'N 30°30'W close to OA85, which may give some credit to both models (this does not seem to be a necessary consequence of using the mean OI85 field). If we add the Stokes drift contribution the crash point is now found outside the 95% confidence rectangle, slightly east of the Ursulla sighting (at 42 nm from LKP, not shown on the Figure). We have excluded this last possibility.

HYCOM

This model gives a crash point near 3°15'N 30°30'W, and has been discarded from our analysis, on the basis that the velocity field is not realistic enough and the backtracked debris were scattered over 93 km (Figure 37). However the Ursulla sighting is backtracked not far from our 95% confidence area.

Figure 62 gives the annular sector (20 nm inner and 42 nm outer radii) which envelopes all these estimated crash positions (excluding INMOMC with Stokes and HYCOM). It is pleasing to recover exactly the same region (except for its shape) as the 95% confidence rectangle.

When it comes to define a higher probability zone inside, we can rely only on some prejudices. If we have more faith in the objective analysis we would select a northern region (the dashed green rectangle in Figure 62 may be a possibility). If not, it is difficult to select a smaller zone since model results do differ significantly and their errors are important. However, the western part of the 95% confidence rectangle, apparently a preferred region for the data fitting, could also be a candidate.

Final remarks

All our calculations have been made on the assumption that the plane impacted the sea surface in one piece, rather than breaking up in the air and scattering debris over a large area.

Although we have managed to define a reasonably sized search area, there remain significant discrepancies between the locations predicted by the different approaches.

Buoy data have been invaluable in validating numerical model results and constraining both objective analysis, data-fitting and FVCOM. But we do not know exactly the behaviour of the fishermen buoys and some caution is called for, even if the few inter-comparisons done with ADCP or Argo floats seem satisfying.

Nevertheless, more buoy data, especially during the first two days after the crash, would have given us greater certainty in the accuracy of the flow field reconstructed from the objective analysis.

The ensemble method used to estimate a wreckage zone with the PSY2AVG data fitted velocity, actually gives a preferred region of crash extending to the west of the 95% rectangle and even outside the ACARS circle (but this may be too far).

We have relied on positions of recovered bodies and debris, as well as on simple sightings. There may remain a few errors for some of them.

Assimilating current data into ocean models would improve their skill in simulating the mesoscale ocean circulation, particularly in equatorial regions.

It is possible we have underestimated the wind drag on human bodies. If so, this would push the wreckage area towards the northeast, closer to Ursulla sighting and to the original flight track.

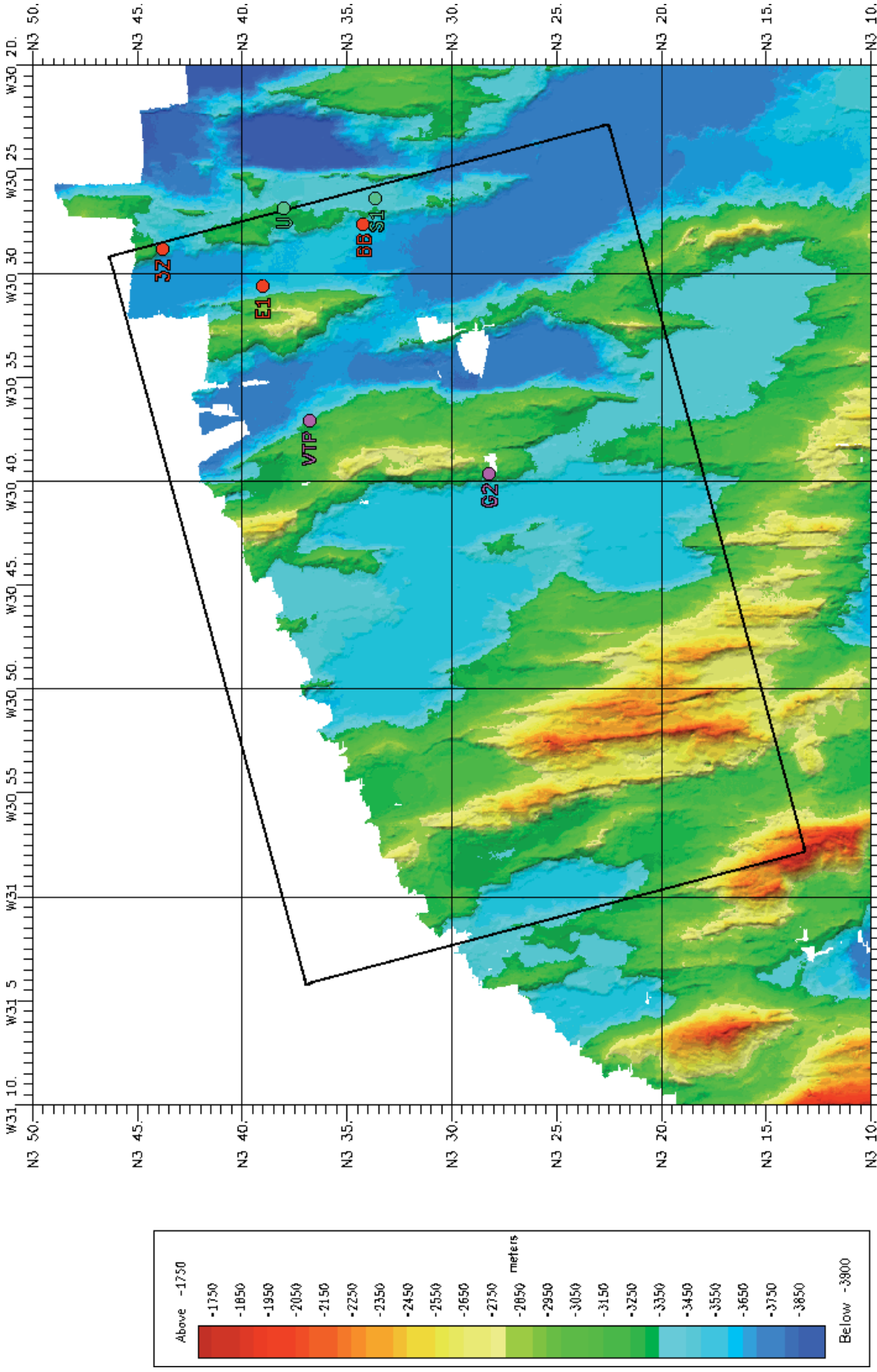

Figure 63 The 95% confidence region estimated through our work. The bathymetry was collected by the Pourquoi-Pas multibeam acoustic sounder in July and August 2009. U and S1 were sighted on June 5, BB, G2 recovered on June 6 and E1, 3Z recovered on June 7.

Appendix 1: ADCP and in-situ data

Some details about ADCP processing

Typically, one raw profile is available every 2 to 3 s. It consists of u, v, $(w_1+w_2)/2$ and w_1-w_2 averaged over 8m and centered at 18.77m, 26.77m, 34.77m, …, 362.77m and 370.77m (w_1 and w_2 are independent estimates of the vertical velocity).

Then an average is done over (disjoint) 2 min periods. A cleaning can now be done : if $|u| > 4$ ms^{-1} or $|v| > 4$ ms^{-1} or $|w_2-w_1| > 0.3$ ms^{-1} or $|\Delta u/\Delta z| > 0.06$ s^{-1} (i.e. a 0.5 ms^{-1} variation over 8m on the vertical), the horizontal current is not preserved. A median test is done after that : for a given profile, the median and the rms deviation ε are estimated from the 30 preceding profiles and the 30 following profiles (thus with 61 profiles, including the one under scrutiny). If the given profile exceeds the median by more than 2.7 ε, it is not preserved (actually, this is done for each level independently and only the concerned levels are flagged).

Finally, an average is done over 2 km (disjoint) segments.

Comparison of buoy data (and objectively analysed field) with ADCP data

Figure A1_1 shows a good agreement between buoy (and objective analysis) velocities and 19 m depth ADCP velocities. However six hours later, ADCP currents were orthogonal to the buoy velocities (Figure A1_2).

This indicates the buoys were not measuring the same currents, possibly because of a vertical shear. This gives some credence in the buoy currents being more alike surface currents, as already implied by the comparison with Argo displacements.

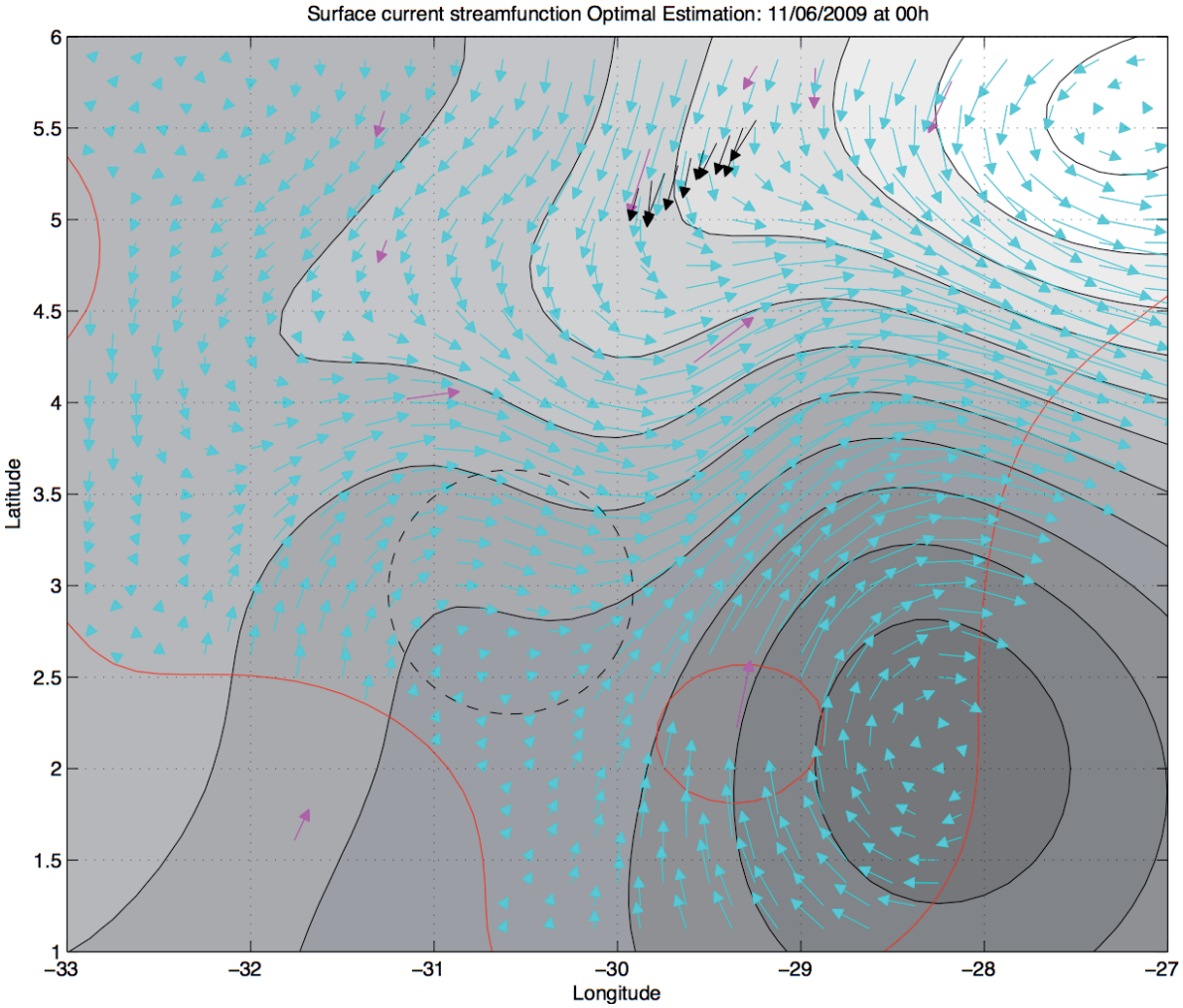

Figure A1_1 ADCP currents at 19 m depth (black) compared with fishermen buoys currents (pink) and the objective analysis velocity field obtained from these buoy data (cyan). ADCP measurements are covering a 4h interval centred June 11 at 0h (date of the analysis).

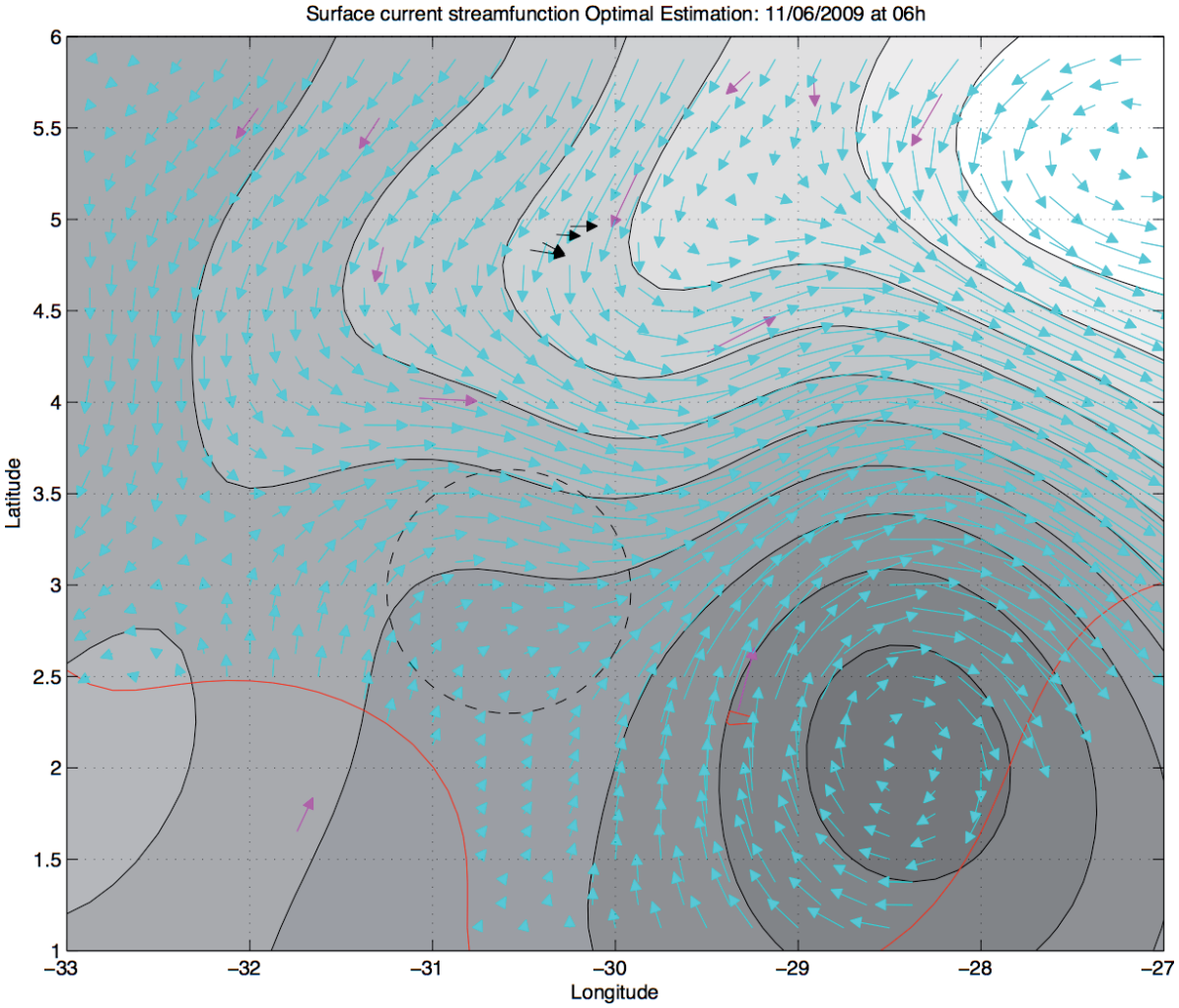

Figure A1_2 ADCP currents at 19 m depth (black) compared with fishermen buoys currents (pink) and the objective analysis velocity field obtained from these buoy data (cyan). ADCP measurements are covering a 4h interval centred June 11 at 6h (date of the analysis).

Appendix 2: PSY2V3 and HYCOM

Model details

NEMO and HYCOM are part of several numerical ocean monitoring and forecasting systems. NEMO is used by Mercator Océan and UK Met Office, and HYCOM by the (US) Navy Research Laboratory (NRL) at the Stennis Space Center and the NERSC. The higher resolution (1/12° horizontal resolution) analyses of PSY2V3 (Mercator Océan) and HYCOM/NCODA (NRL) which are known to be reliable in the Tropical Atlantic Ocean (up to 20% relative error on the near surface current) were naturally chosen to deliver information on the ocean currents at the time of the crash. Although they both operate at the same horizontal resolution, the two systems have made very different technical choices.

Details of the PSY2V3 system

NEMO configuration

The Mercator Océan PSY2V3 setup uses v1.09 of NEMO, with 50 z-levels. Layer thicknesses range from 1 meter (m) at the surface to 450 m at the bottom, with layers less than 2 m thick throughout the upper 10 m, increasing to 10m at 50 m depth and 170 m at 1000 m. Tracers are advected with the TVD (Zalesak, 1979) scheme and momentum by an energy and enstrophy conserving (Madec, 2010). A free surface filtering out the high frequency gravity waves is used (Madec, 2010). A 1.5–order turbulent closure is applied for the vertical mixing (the TKE scheme of Blanke and Delecluse, 1993). An isopycnal Laplacian operator is used for the lateral diffusion of tracers and a horizontal bilaplacian for the lateral diffusion of momentum. Convection is parameterised with enhanced values of vertical diffusivity and viscosity where the stratification is unstable.

The daily atmospheric conditions from ECMWF analyses are transformed into heat fluxes with the CLIO bulk formulae. The momentum fluxes (wind stresses) diagnosed by ECMWF are used directly. Monthly climatological runoffs are prescribed from the database of Dai and Trenberth (2002). Main rivers are spread and coastal runoffs are applied along the coast. The north and south boundaries are buffer zones where temperature and salinity fields are strongly relaxed towards the Levitus monthly climatology. To constrain the Mediterranean water outflow in the Atlantic to the right depth

(around 1000 m), temperature and salinity are restored towards climatology within a zone in the Gulf of Cadiz.

The SAM2 data assimilation method

Data is assimilated using the SAM2 software (Tranchant et al., 2008), which was developed at Mercator Océan and is based on the Singular Evolutive Extended Kalman Filter (SEEK) formulation of Pham (1995) and Brasseur and Verron (2006).

The 3D multivariate background error covariance statistics vary at each analysis via the use of an ensemble of O(250) anomalies. These anomalies (with respect to a running mean) are computed from a long numerical experiment so as to give an estimate of the 7-day scale error in the ocean state at a given period of the year for Temperature T, Salinity S, zonal velocity U, meridional velocity V and Sea-Surface-Height SSH.

The analysis is done at the location of the observations. The first guess at appropriate time (FGAT) approximation is made which means that the model equivalent of the observation is taken at the correct time even if the analysis is delayed. Nearly all the global ocean surface can be analysed once a week thanks to a relatively homogeneous satellite coverage (3 altimeters + Sea-Surface-Temperature SST analysis). The multivariate and multi-data analysis is localised, which means that it is 3D inside a local "bubble" bounded by correlation radii and centred on the analysis point. In the tropical oceans, this zone is several degrees in size.

The errors of the different types of observations are combined with the model error covariances (with the SEEK formulation) in order to obtain the correction or "increment" from the discrepancy (the observation – model misfit). The increment once projected back onto the model space gives an optimal ocean state over all available observations, following the model dynamics and co-variations between the state variables.

The on-track altimeter Sea Level Anomalies (SLA) from AVISO[24] (derived from Jason-1, Jason-2 and Envisat satellites), and the RTG-SST Sea Surface Temperature from NCEP at ½° horizontal resolution, together with the temperature and salinity in situ profiles from Coriolis (IFREMER) are assimilated in this fully multivariate way. The Mean

[24] http://www.aviso.oceanobs.com/en/data/product-information/duacs/

Dynamic Topography derived from observations (Rio and Hernandez, 2004) is used as a reference for the assimilation of SLA.

Details of the HYCOM/NCODA system

This global 1/12° ocean forecasting system is run at NRL Stennis Space Center. It uses 32 vertical hybrid layers. Surface mixing is parameterized with Large et al.'s (1997) K Profile Parameterization (KPP) surface ocean boundary layer model. The surface is forced by 3-hourly wind stress, wind speed, heat flux (using bulk formula) and precipitation from the Navy Operational Global Atmospheric Prediction System (NOGAPS). Runoff from 986 rivers is included as a virtual salinity flux with no mass exchange.

The system assimilates (i) SSH from Envisat, Jason-1 and Jason-2 (ii) SST from all available satellite and in situ sources, (iii) all available in situ temperature and salinity profiles (e.g., Argo, CTDs, moor- ings), and (iv) Special Sensor Microwave/ Imager (SSMI) sea ice concentration. Assimilation is performed using the three-dimensional MultiVariate Optimum Interpolation (MVOI) Navy Coupled Ocean Data Assimilation (NCODA) system (Cummings, 2005). In this scheme, corrections to the model state are obtained by linear combinations of model-observation differences. The MVOI analysis is carried out on 42 z-levels extending from the surface down to 2500 m. The model forecast is interpolated to z-levels before the analysis and the analyzed increments are added to the forecast and interpolated back to the model's hybrid vertical coordinate. More details of the system may be found in Chassignet et al (2009).

Validation against buoys in the equatorial Atlantic

We compared actual trajectories of drifters from the Global Drifter Program (http://www.aoml.noaa.gov/phod/dac/gdp.html) over the equatorial Atlantic to their simulated trajectories as predicted by the operational HYCOM/NOODA and PSY2V3 systems, running in hindcast mode. These drifters are drogued at a depth of 10-15 m and so should not be influenced by Stokes drift.

Study region

The choice of study region was a subjective compromise between choosing a larger area that included more AOML drifters and therefore would provide better statistics, and choosing a smaller area to keep it more homogeneous and more focused on the region of the crash site.

We want the calculation to be relevant to the dynamics of the last known position area during early June. This corresponds to the onset of tropical instability wave season, which typically starts in the equatorial Atlantic in May or June (Weisberg and Weingartner, 1988). So we restricted calculations to drifters within the study region: 10°S to 10°N, 60°W to 0°E, as outlined in Figure A2_2, and to the time period May 1 to June 30, for 5 years (2004 to 2008).

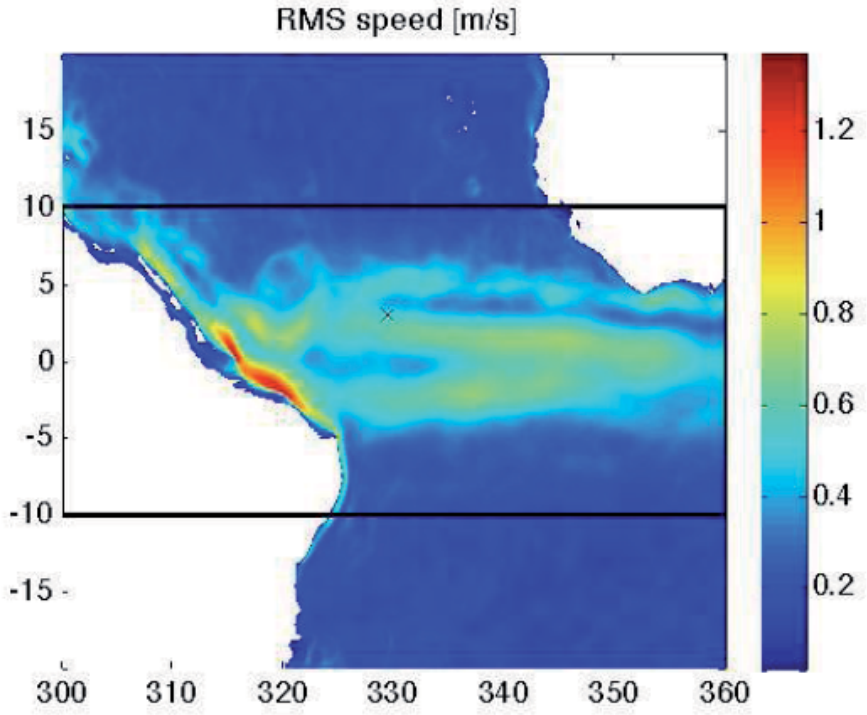

Figure A2_2 Outlined box is the study region. Background colours indicate the root mean square (rms) speed in ms^{-1} found using five years of HYCOM 15 m velocities during the study period. 'X' marks the LKP.

The rms speed has a strong influence on predictability of drifter trajectories (Ozgokmen et al., 2001; Barron et al., 2007). Thus we anticipate that drifters caught in the strong current off the north west corner of Brazil will have worse predictions, while the weaker speeds poleward of 7°N and 4°S will tend to underestimate uncertainty in our statistical model of predictive skill.

Back trajectory methodology

For each drifter in the study region, start at its latest location. Check if location is known n-days earlier, where n is backcast[25] length in days, n = 1, 2, ... 6, or 7. If so, attempt to predict this earlier location using backward integration of HYCOM 15 m daily velocities. Backcast or "prediction" error is the difference between predicted and observed start locations. Starting from the earlier time of last backcast, repeat the above procedure (so backcast trajectories do not overlap, and can be treated as independent).

Statistical Model of Predictive Skill

The predictive skill is summarized in the cumulative density plot of backcast error in Figure A2_3, and the corresponding statistics in Table 2. The 80% percentile of prediction error can be interpreted as the radius of the circle about the predicted back trajectory location that contained 80% of the actual drifter locations. If we only used daily HYCOM and one piece of information (like the Vertical Tail Plane) this is an estimate of the radius of the circle that would have to be searched to locate the actual crash point with 80% probability. The numbers in Table 2 can be read on Figure A2_3. For example, the 5-day forecasts correspond to the cyan line. The cyan line crosses the y-axis value of 80% at about 140km. (see also Table 2).

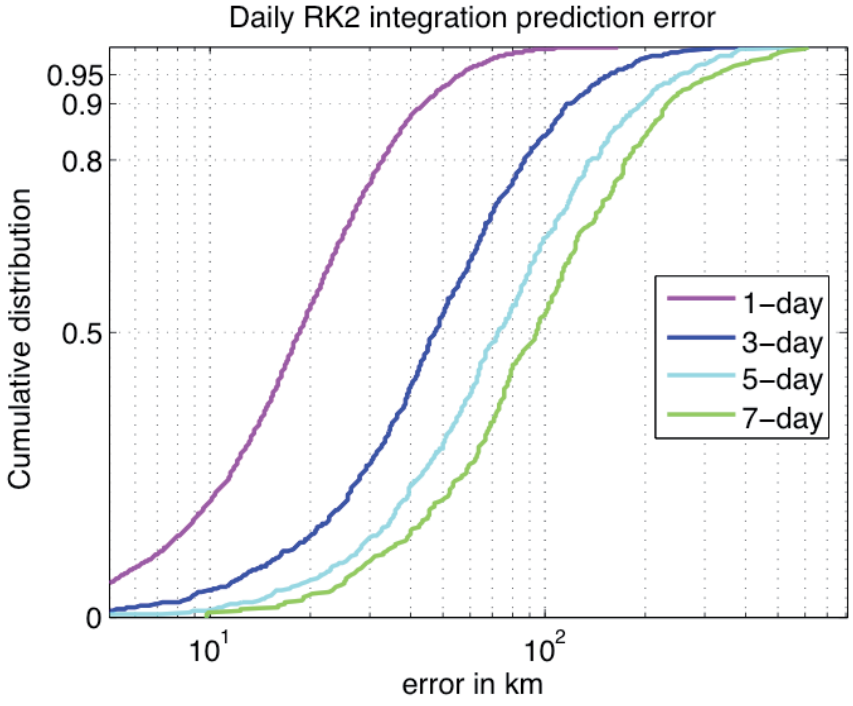

Figure A2_3 Empirical cumulative distribution of backcast errors.

[25] Backcast is a neologism built on forecast

Backcast length [days]	Number of predictions	RMS error [km]	80% quantile [km]
1	3171	29	33
2	1514	55	61
3	948	79	88
4	674	102	114
5	524	125	138
6	394	153	165
7	320	159	176

Table A2 Prediction error for backcasts between 1 day and 7 days for years 2004 through 2008 using HYCOM 15 m velocity.

Comparison of HYCOM and PSY2V3 errors

We now compare the accuracy of the PSY2V3 trajectories to those of HYCOM (Table A3). In general, PSY2V3 trajectories tend to be slightly more accurate, though differences are slight. Further slight improvements in accuracy can be obtained from making an ensemble backcast (HYCOM+PSY2).

Model	Forecast length [days]	Number of predictions	RMS error [km]	80% quantile [km]
HYCOM	3	210	66	81
PSY2	3	210	65	75
HYCOM+PSY2	3	210	57	68
HYCOM	5	114	106	124
PSY2	5	114	100	115
HYCOM+PSY2	5	114	91	116
HYCOM	7	71	134	167
PSY2	7	71	126	149
HYCOM+PSY2	7	71	113	141

Table A3 Like Table A2 but now comparing the back trajectory integrations using daily velocity HYCOM and PSY2 fields, or the average of HYCOM and PSY2.

Validation of PSY2V3 against data near the search zone

Figure A2_4 gives a comparison between ADCP profile #388 and the nearest (in time and space) PSY2V3 velocity profile. Although the Mercator current speed is quite realistic, the meridional component is at odds.

Figure A2_5 shows Mercator PSY2V3 19m depth daily mean currents for June 12 2009 (light grey), fisheries buoys velocities (given at 6h and 18h, whence there are generally two magenta vectors close together), ADCP current vector for station #388 (in blue) and an Argo float surface velocity (in green).

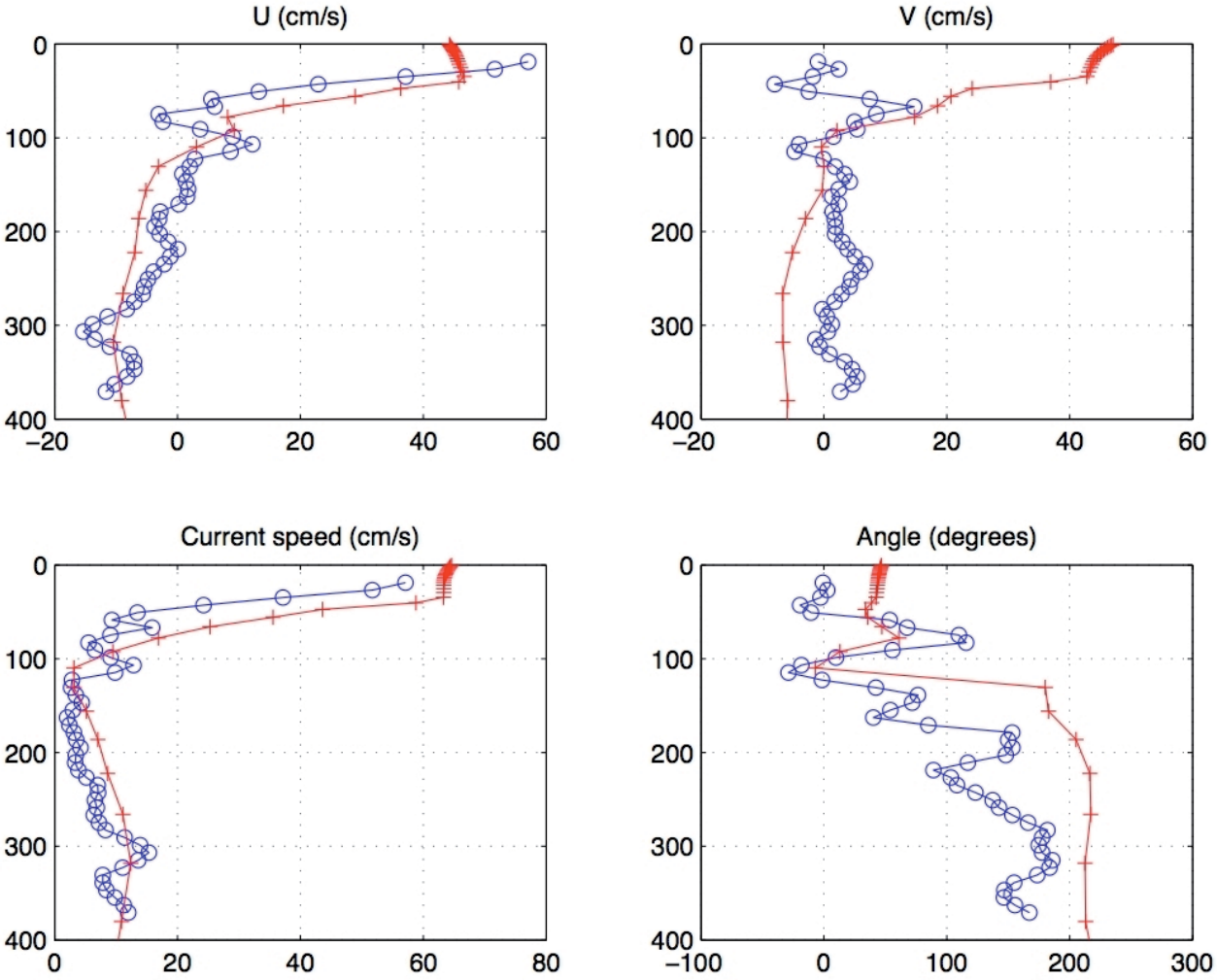

Figure A2_4 ADCP vertical profile at station #388, compared with the nearest time and space Mercator PSY2V3 profile (in red).

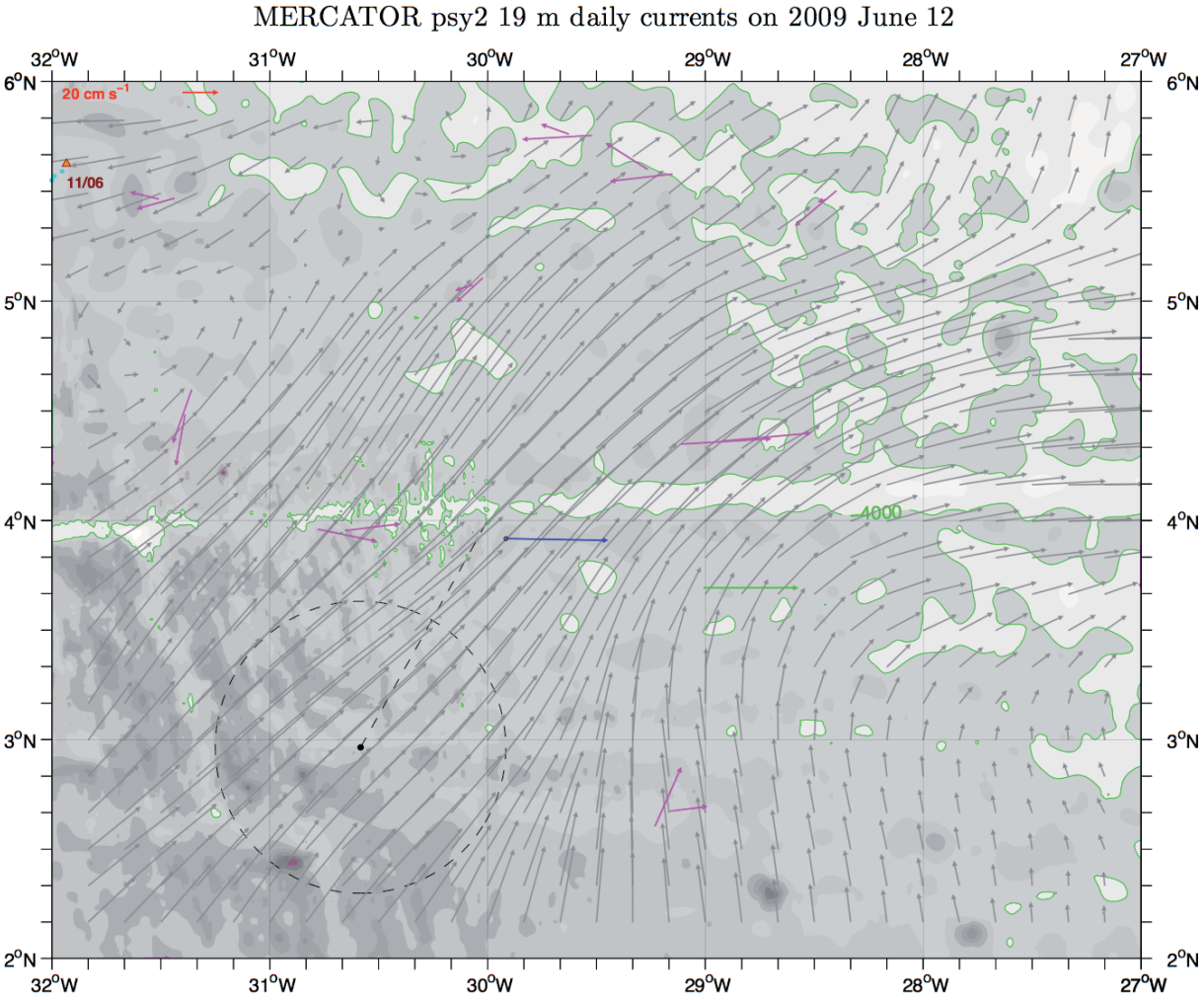

Figure A2_5 Superimposed on the Mercator PSY2V3 mean daily 19m depth velocity field for June 12 2009, the fishermen' buoy velocities (in magenta, at 6h and 18h), Argo float # 3900692 surface (roughly 1m depth) velocity near 18h on June 11 (in green), and ADCP station #388 velocity vector at 19m depth on June 12 at 8h (in blue)

Appendix 3: PSY2-REANA and ZOOM

PSY2-REANA : The reanalysis

The Mercator Océan modelling experimental strategy was to optimize the PSY2 real time analysis and forecasting system in hindcast mode and to perform a PSY2 reanalysis (hereafter called PSY2-REANA) of the whole Tropical and North Atlantic domain for May and June 2009. Compared to real time PSY2V3 new in situ data and delayed mode quality checked in situ and satellite data were assimilated. The data assimilation time frame was also shortened from 7 to 5 days, in order to increase the weighting of the satellite SST data.

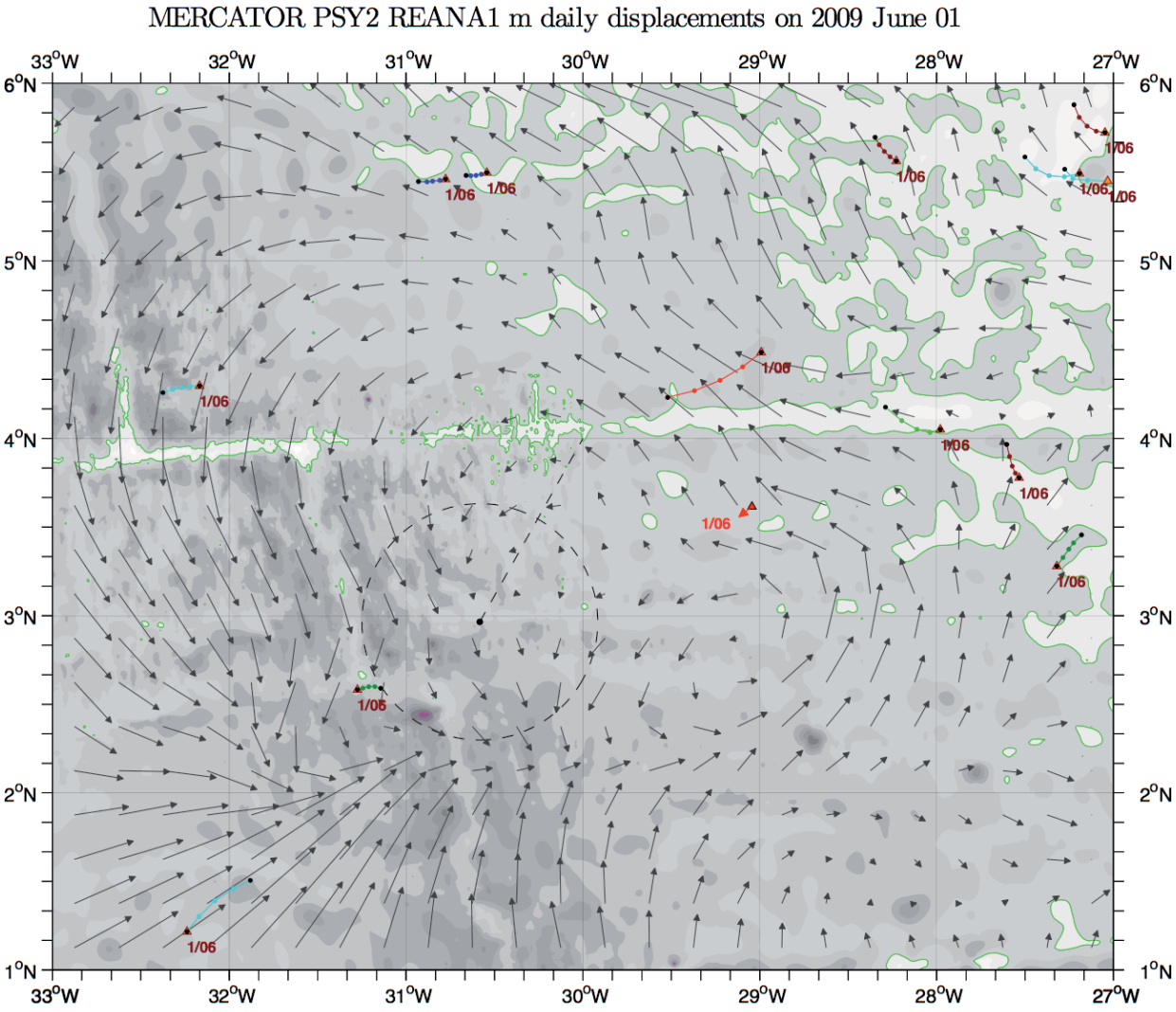

Figure A3_1 The daily velocity field of PSY2-REANA on June 1 2009. Vectors give equivalent 24h displacements and buoy trajectories are shown over the 24h period between 0h and 24h on June 1 2009.

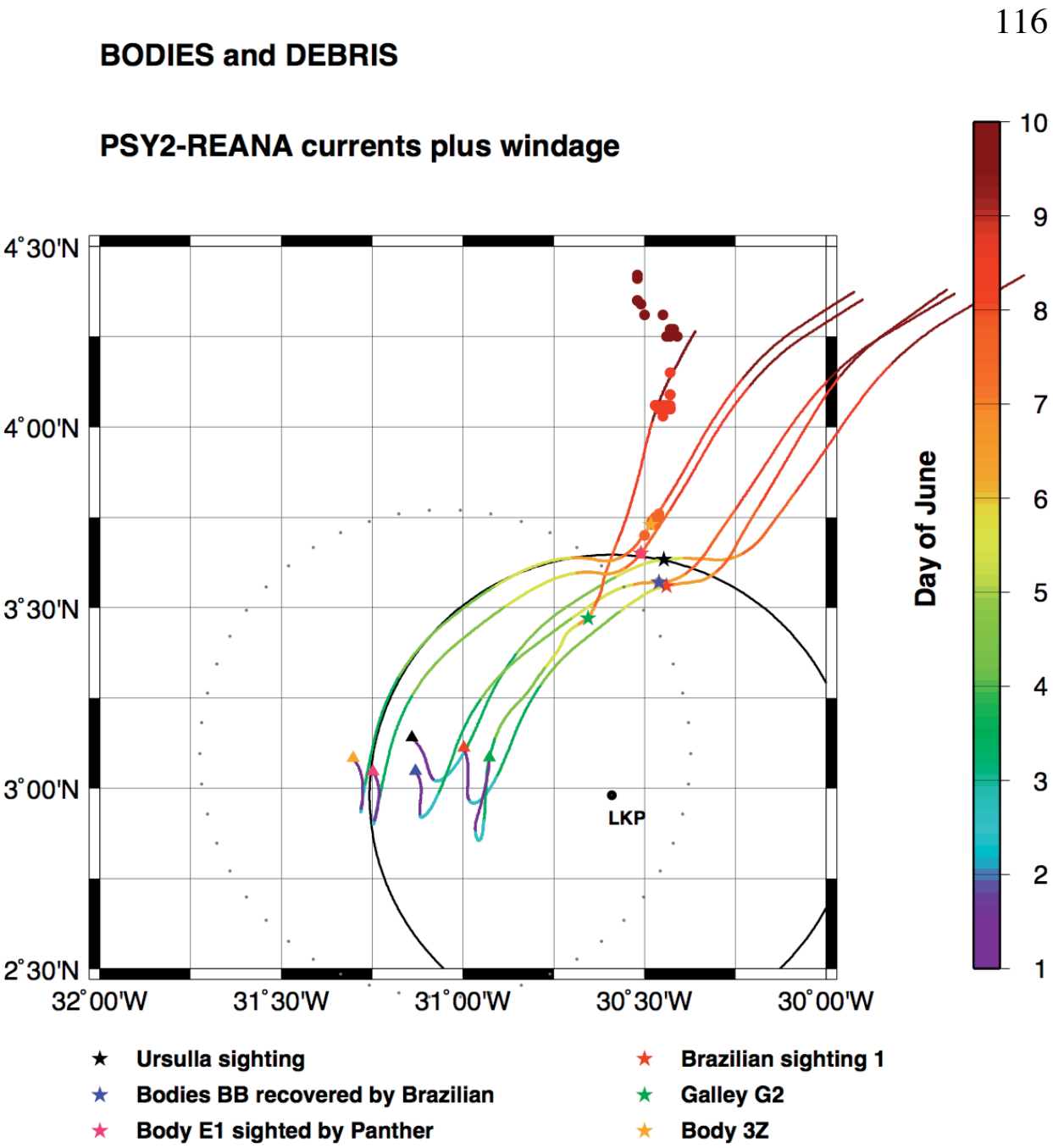

Figure A3_2 Backtracked positions with Mercator PSY2-REANA for six debris or bodies found over the period June 5 to June 7 2009 (Ursulla and S1 on June 5, BB and G2 on June 6, E1 and 3Z on June 7). No windage on Ursulla and the bodies, 1% and 2.5% on sighting 1 and Galley G2 respectively. The 75 km radius dotted circle gives the standard error on a backtracked point for June 1 at 2h.

Validation of ZOOM2 against data near the search zone

The refined version of Mercator (ZOOM2) does compare better with data at a few positions but at some others still disagrees. Figures A3_3 and A3_4 (similar to Figures A2_4 and A2_5) show the corresponding results for ZOOM2.

Figure A3_5 compares the surface displacements from PSY2V3 (green) and ZOOM2 (pink) with corresponding Argo surface displacements. It can be checked ZOOM2 is generally better (but a notable exception is June 1). The velocity field in the background is from ZOOM2 at the time of the Argo float surfacing (see B. Blanke's report).

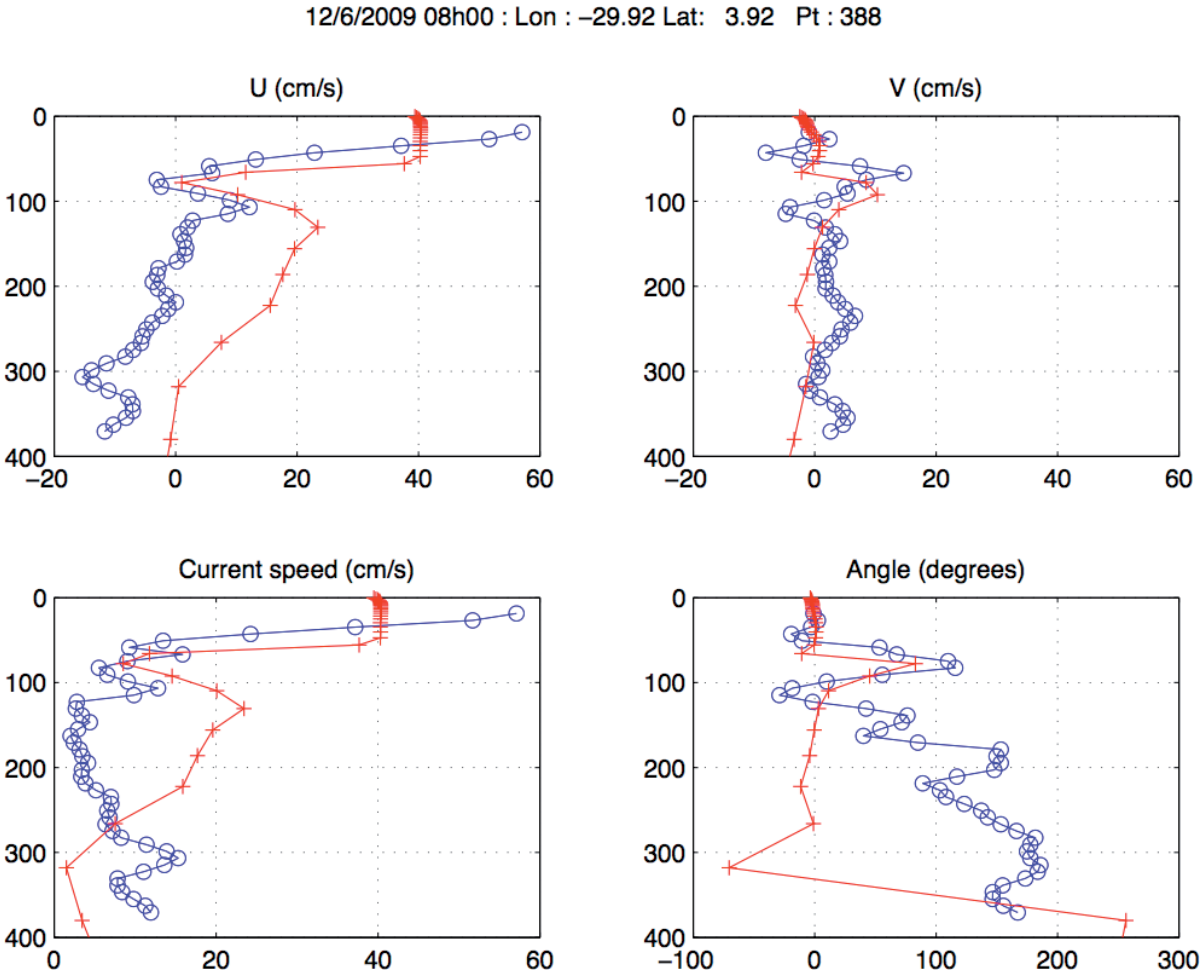

Figure A3_3 ADCP vertical profile at station #388, compared with the nearest time and space Mercator ZOOM2 profile (in red).

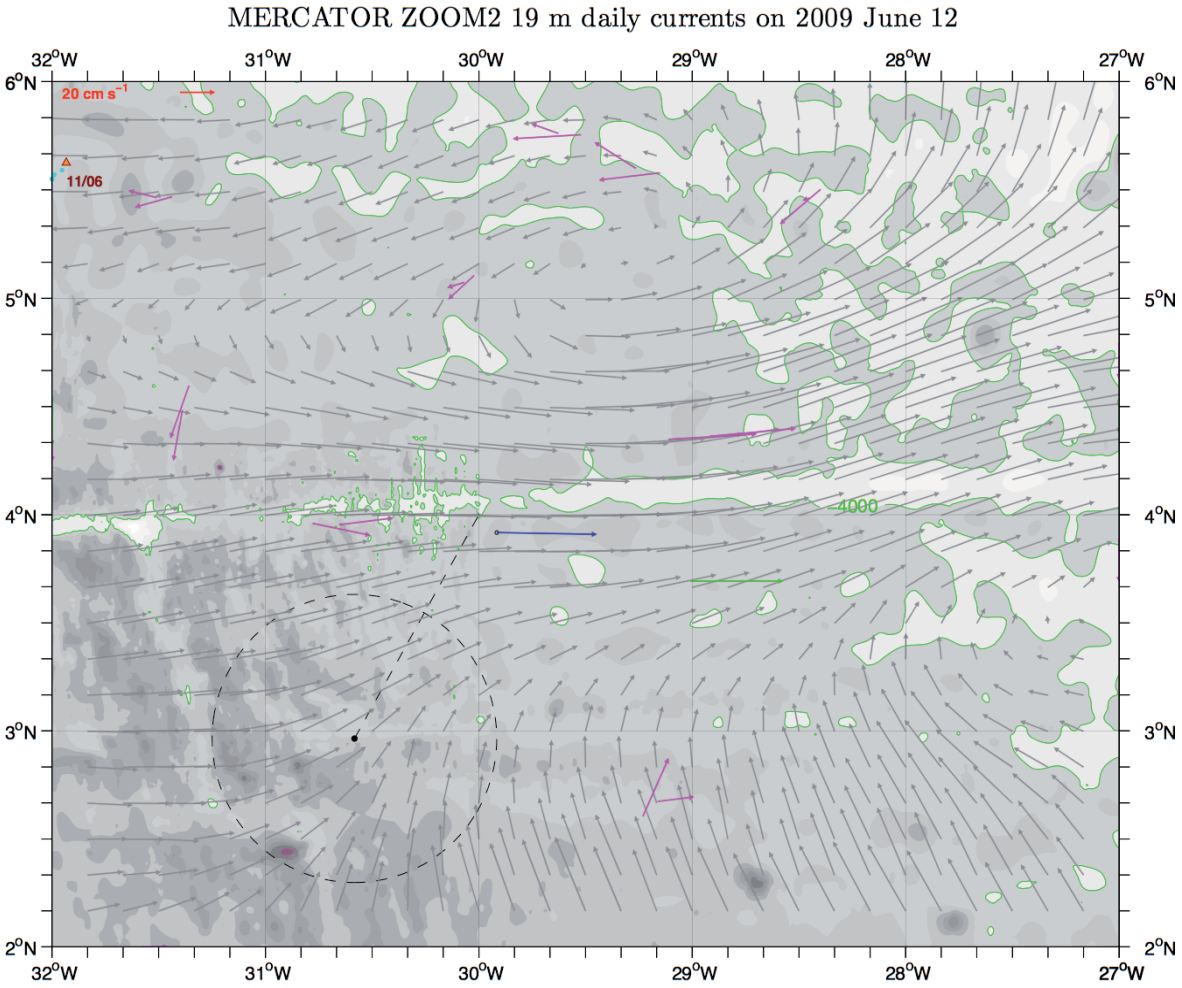

Figure A3_4 Superimposed on the Mercator ZOOM2 mean daily 19m depth velocity field for June 12 2009, the fishermen' buoy velocities (in magenta, at 6h and 18h), Argo float # 3900692 surface (roughly 1m depth) velocity near 18h on June 11 (in green), and ADCP station #388 velocity vector at 19m depth on June 12 at 8h (in blue).

Although ZOOM2 is far from reproducing precisely the near surface daily currents around the ACARS area and over the first days of June 2009, it is a sensible improvement compared to the operational PSY2V3. This is quantified in Appendix 6: the forecast error decreases from 100 km to 60 km after 5 days (almost a factor 2). We have not compared the other model outputs to the same ADCP profiles. This may have been valuable only for models having a better score than ZOOM2. INMOMC and FVCOMW are the only candidates (with forecast errors of 50 and 45 km respectively, see Appendix 6). Unfortunately the velocity fields on the vertical from these two models were not provided preventing such a comparison.

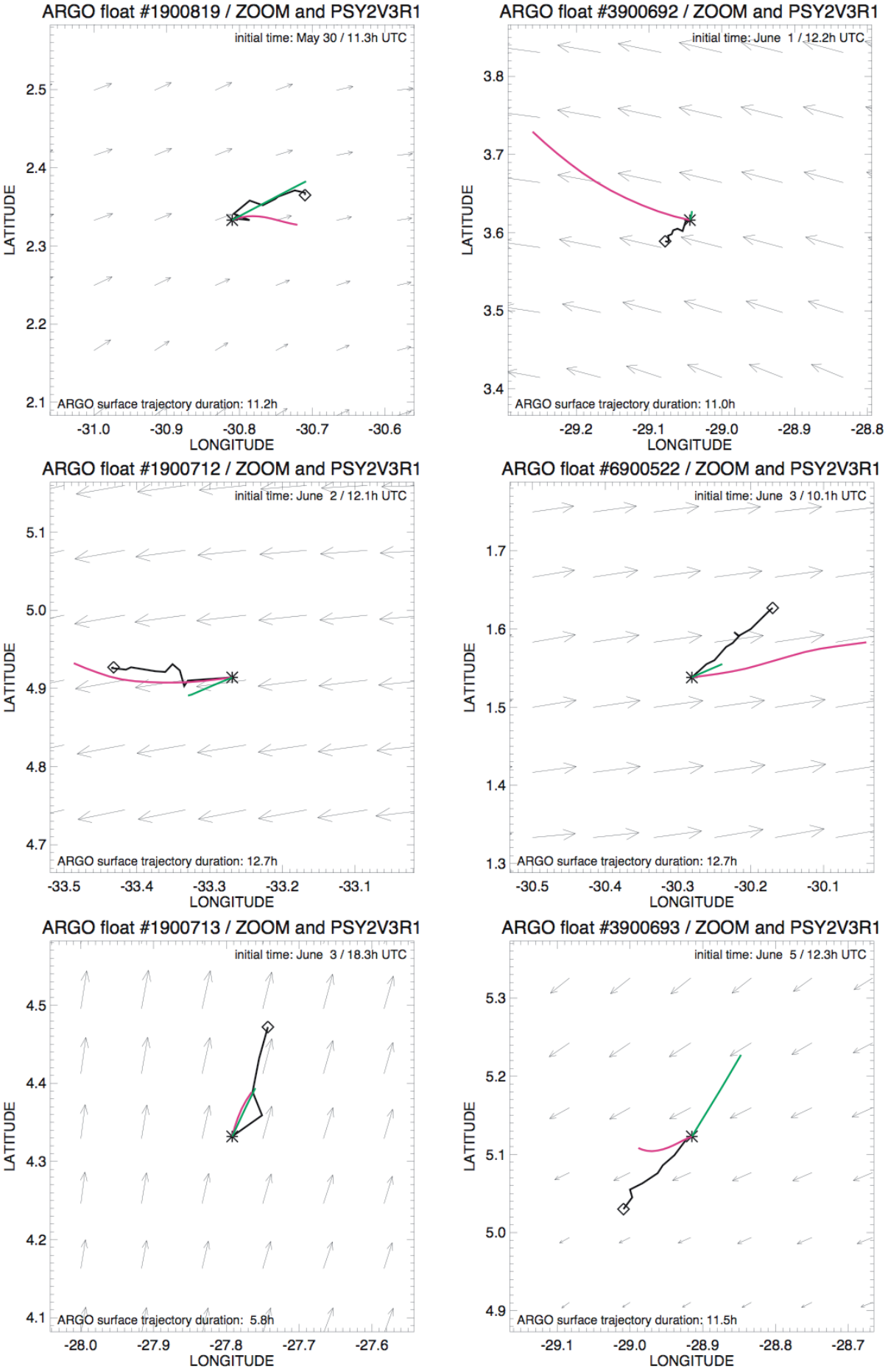

Figure A3_5 PSY2V3 (green) and ZOOM2 (magenta) integrated surface trajectories corresponding to Argo displacements (black).

Appendix 4: The Surcouf model (CLS)

Surface currents are estimated from satellite-derived surface topography and wind stress using a physically based statistical model calibrated by 15 m drogued drifters. The model assumes a surface layer dominated by steady geostrophic and Ekman dynamics (Lagerloef et al., 1999).

The "geostrophic" part

The geostrophic part of the current (u_g,v_g) is obtained from the altimetry maps of SSH (see chapter I) distributed by AVISO:

$$u_g = -\frac{g}{f}\frac{\partial h}{\partial y} \quad , \quad v_g = \frac{g}{f}\frac{\partial h}{\partial x}$$

These maps of SSH (or absolute dynamic topography h) are obtained as the sum of SLA (or h') and an estimate of the Mean Dynamic Topography MDT (or <h>) computed separately (Rio & Hernandez, 2004; Rio et al, 2005): h = h'+<h>.

In the equatorial band, an approximation is done to handle the equatorial singularity (f=0 right at the equator). We use the equatorial approximation:

$$u_g = -F(\varphi)\frac{g}{f}\frac{\partial(h)}{\partial y} - [1-F(\varphi)]\frac{g}{\beta}\frac{\partial^2(h)}{\partial y^2}$$

$$v_g = F(\varphi)\frac{g}{f}\frac{\partial(h)}{\partial x}$$

with

$$F(\varphi) = 1 - \exp[-(\frac{\varphi}{2.2})^2]$$

$$f = 2\Omega\sin\varphi$$

$$\beta = \frac{2\Omega}{R_T}\cos\varphi$$

Thus, "geostrophy" varies smoothly from a β plane formulation at the equator to an f plane in latitudes φ greater than 5°, the transition occurring near 2-3°latitude (Lagerloef et al., 1999)

In this computation however, altimetric heights are filtered twice. This results in a downgraded estimate of the ocean surface current. A specific work has therefore been carried out to improve the Surcouf currents in the area of interest for the BEA investigation**:**

- Only the variable part of the current (u'_g,v'_g) is computed from the altimetric Sea Level Anomalies h' using the equatorial approximation.

- An improved mean current ($<u_g>$,$<v_g>$) has been computed by averaging the geostrophic component of the velocity data measured in the area by drifting buoys from 1993 to 2008. The resulting mean currents are plotted on Figure A4_1 (right). They differ significantly from the mean currents computed using the equatorial approximation from the Rio et al (2005) MDT (left plot on Figure A4_1).

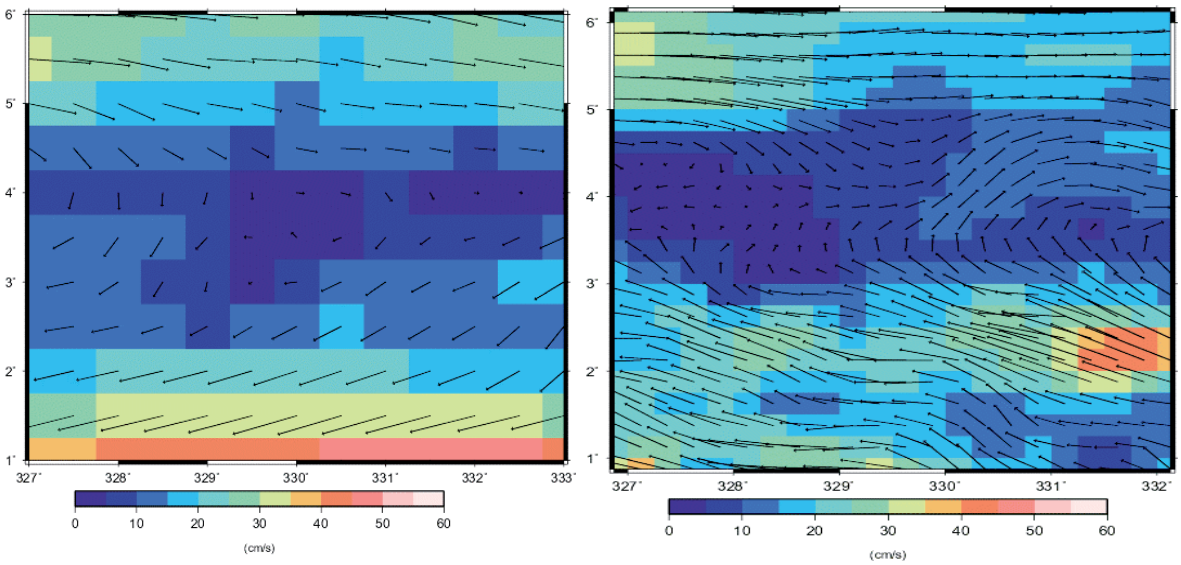

Figure A4_1: Mean velocity field computed using the classical equatorial approximation (left) and new mean field computed for the BEA study using the velocity information from drifting buoy velocities (right).

The Ekman part

Maps of Ekman currents $\mathbf{u}_{Ek}$ are computed from the 6-hourly wind stress fields $\boldsymbol{\tau}$ from ECMWF using the following simple 2-parameter model: $\mathbf{u}_{Ek} = A \cdot \exp(-i\theta) \cdot \boldsymbol{\tau}$

The parameters A and θ have been obtained by least square fit between $\mathbf{u}_{Ek}$ and $\boldsymbol{\tau}$. To estimate $\mathbf{u}_{Ek}$ we have analyzed 15m-drogued drifting buoy velocities that have been collected in 2009 in the framework of the international Global Drifter Program (GDP), quality-controlled and distributed by the AOML center. Absolute altimetric velocities were interpolated along the drifting buoy trajectories and subtracted from the buoy velocities. The residual ageostrophic current was further filtered using a 30h to 20 days band pass filter to focus on

the frequencies where the coherency between the wind stress and the Ekman currents is maximal (Rio and Hernandez, 2003).

Wind stress values from the ERA Interim reanalysis were then interpolated along the drifting buoy trajectories and also band-pass filtered. A least square fit was finally performed between $\mathbf{u}_{Ek}$ and $\boldsymbol{\tau}$ so as to obtain the A and θ parameters by latitudinal bands and by month. The resulting parameters are plotted on figure A4_2.

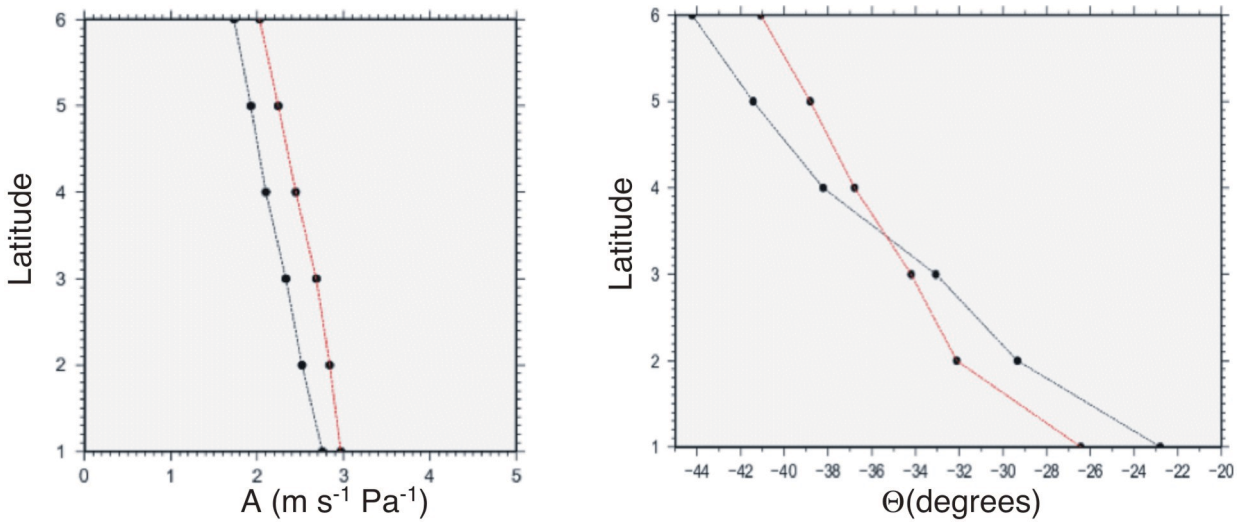

Figure A4_2: Amplitude A (left panel) and phase (positive, if to right of the wind) θ (right panel) parameters of the Ekman model used in the computation of the Surcouf currents. Parameters are displayed by latitude (ranging between 1° and 6°) for May 2009 (black) and June 2009 (red).

The total surface current

Then Ekman currents are estimated and added to the "geostrophic" currents to obtain an estimate of the total surface currents.

Figure A4_3 shows the Surcouf currents on June 1 2009 at 12h and Figure A4_4 compares the forward trajectories with the buoy trajectories. Although the trajectories integrated over a week show some skill to approximate the drifter actual trajectories, Surcouf miss completely the inertial oscillations (which is easily understood because it has no time acceleration). The mean distance error after 5 days (see Appendix 6) is 75 km, giving a 60 km marginal standard error, which is comparable to OGCM ones.

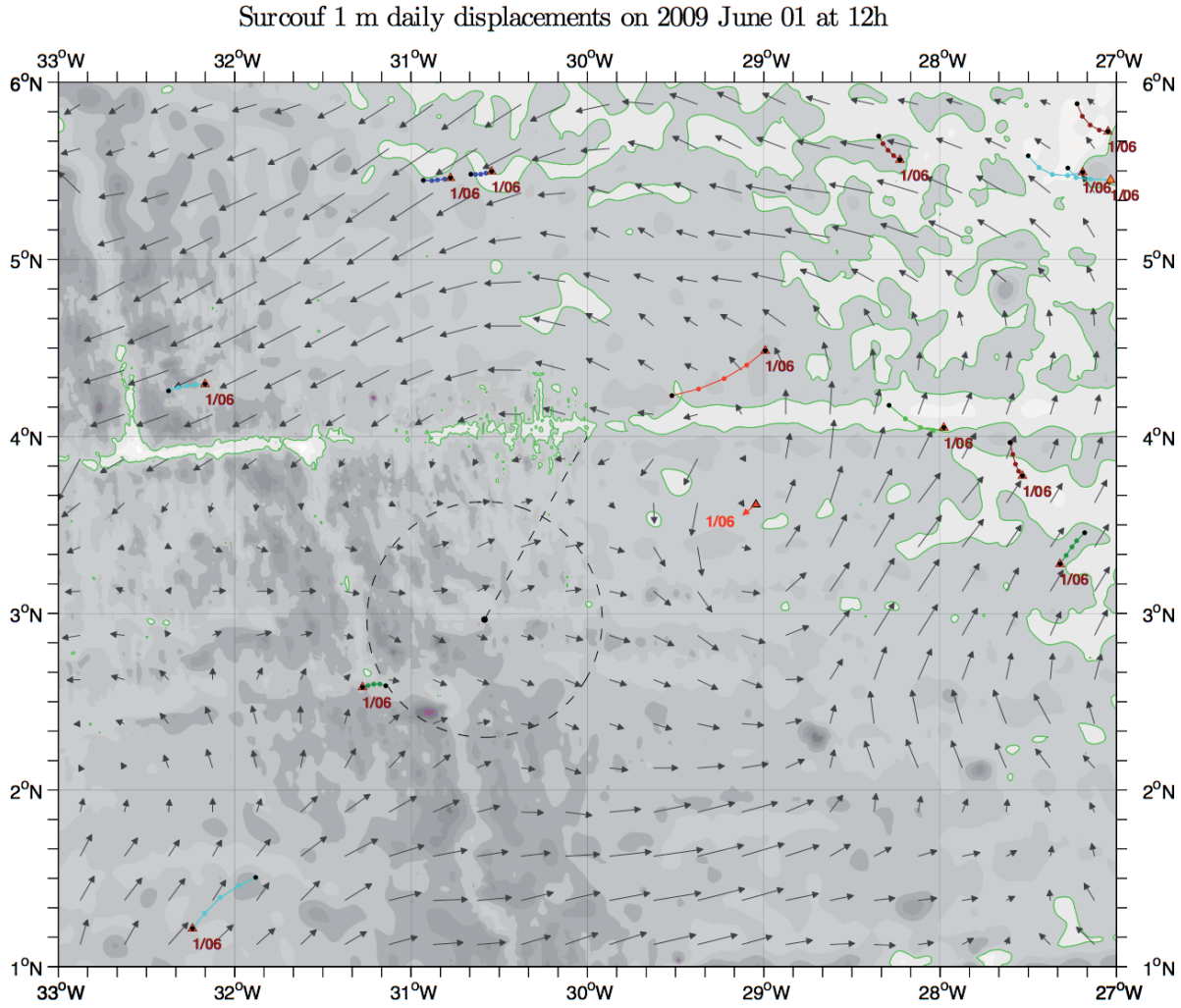

Figure A4_3 The near-surface velocity field from Surcouf, around 15 m depth on June 1 2009 at 12h. Vectors give equivalent 24h displacements and buoy trajectories are shown over the 24h period between 0h and 24h on June 1 2009.

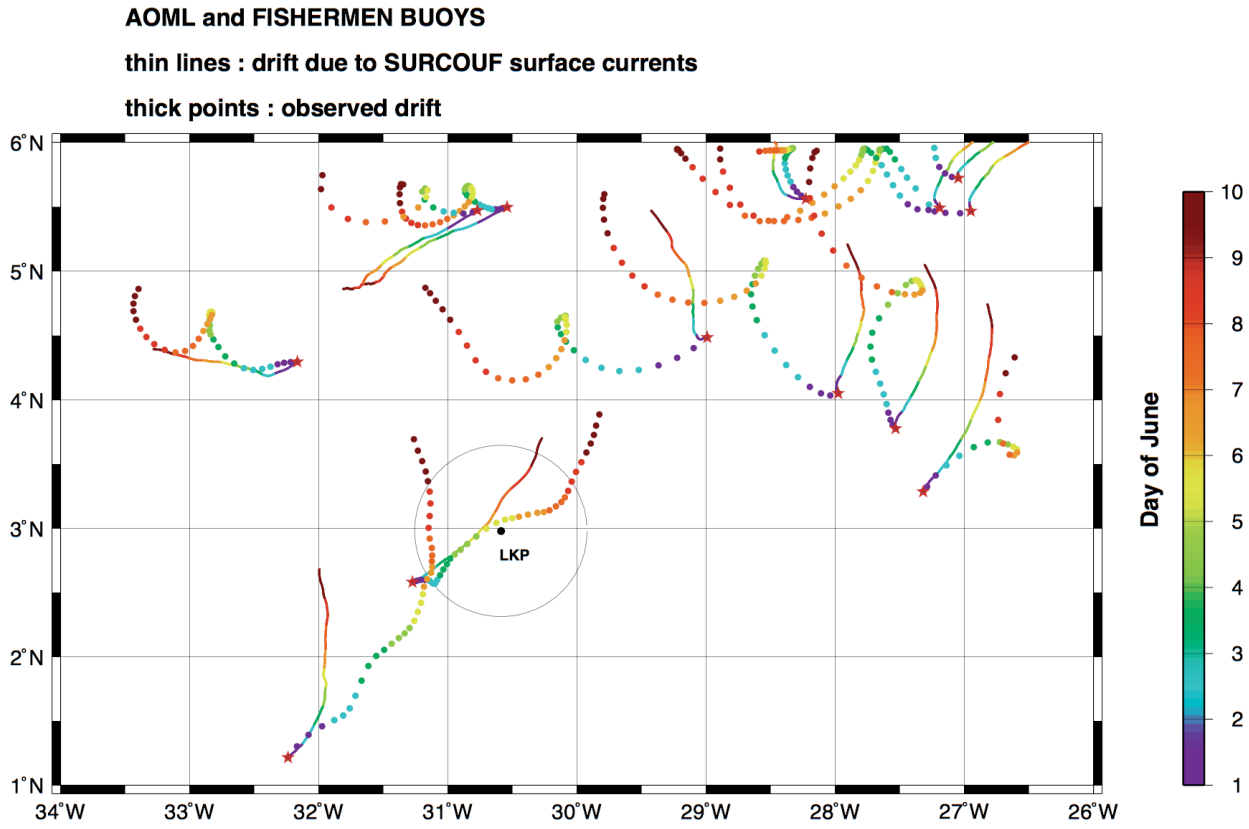

Figure A4_4 Surcouf model trajectories (forward) compared with real trajectories (one dot every 6h).

Appendix 5: Windage effects

Figure A5_1 shows the effect of a 1% wind drag, assuming null sea surface currents. The orange triangles are centred at initial positions on June 6 at 0h. Near 3°30'N 30°30'W the displacement induced for a floating object is 10 nm east-north-eastward if integrated back to June 1 at 2h.

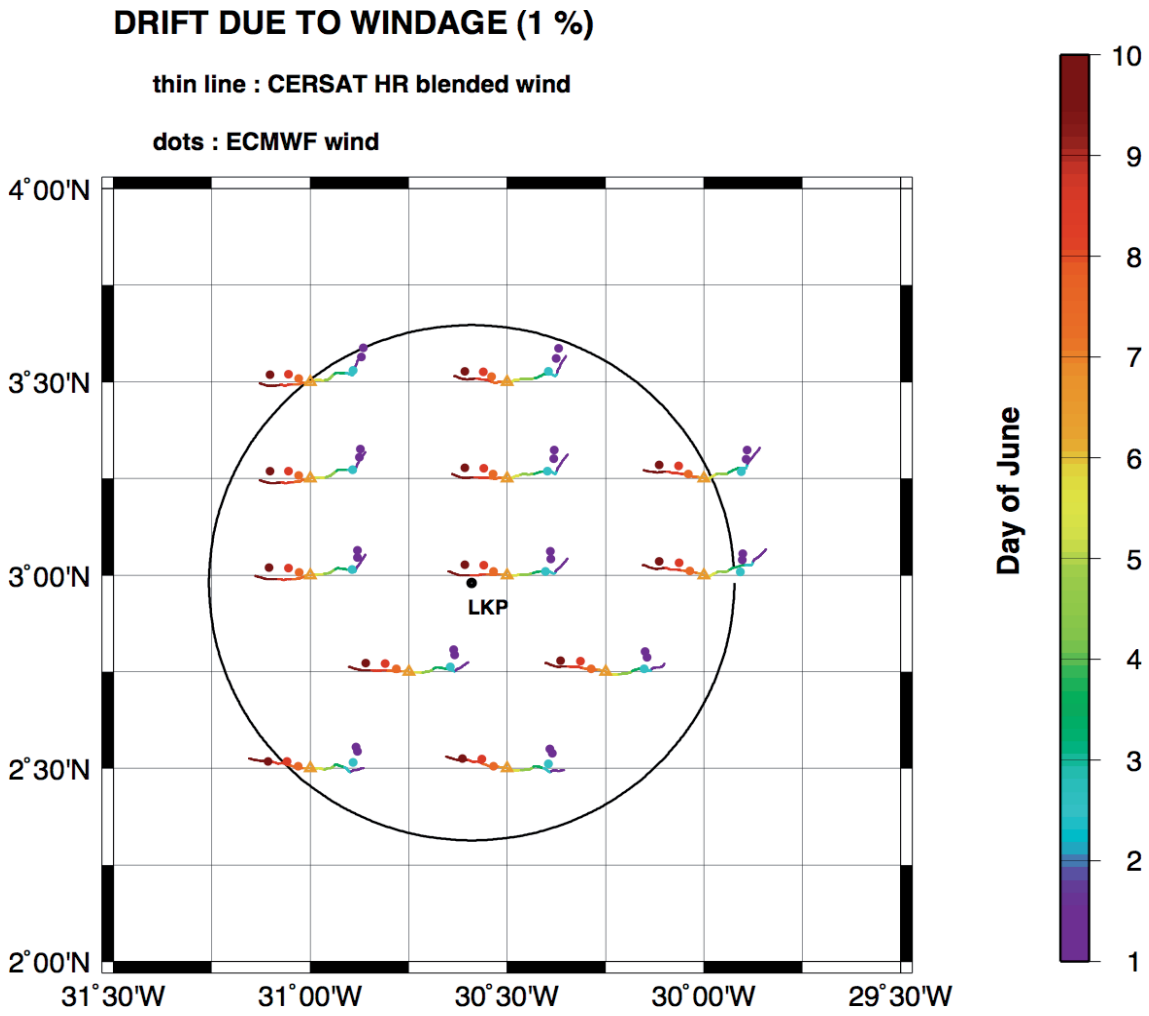

Figure A5_1 This is the drift that would be induced by a 1% windage on a zero surface current field.

Whether one uses ECMWF or Cersat HR Blended, makes almost no difference. Now, Figure A5_2 shows the effect of varying the drag coefficient α. Plots like this one were used to select the α values suitable for the different bodies or debris: with backtracked positions inside the ACARS circle, one could keep 2.5% or 3% for G2, 0 or 0.5% for BB, 1% for S1, 2% for S2 and 0% for U. On this example, the zone of reasonable convergence is actually quite close to the Ursulla

sighting. Note that 2.75% for G2 (which corresponds more closely to the 2.85% value estimated for G2 in chapter I), 2.3% for S2 and 0.5% for BB would fit even better. The latter α value would indicate there was some wind drag on the bodies, even before June 7.

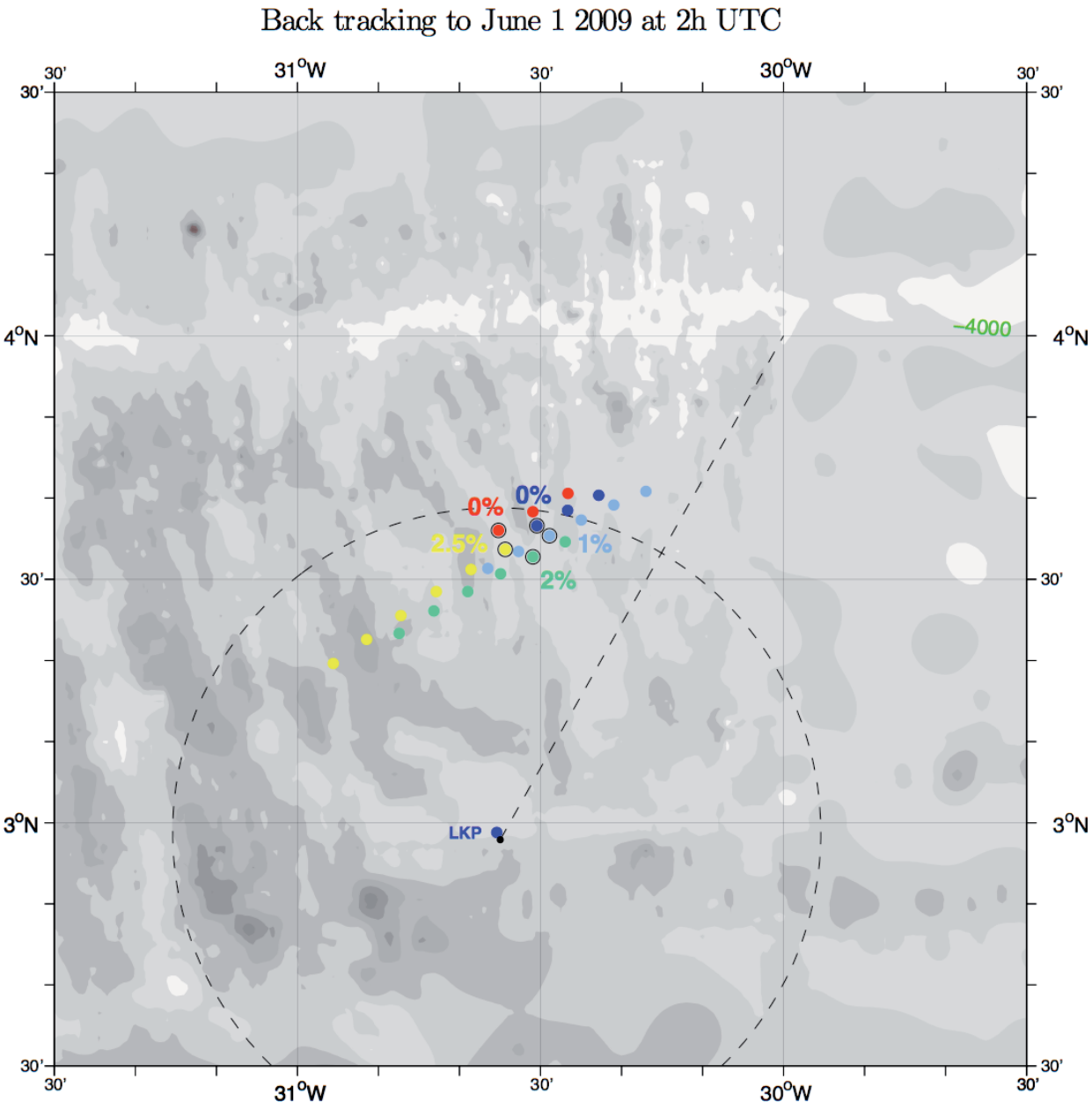

Figure A5_2 North-eastward shifts of the backtracked positions for U (blue), S1 (light blue), S2 (green), G2 (yellow), and BB (red) with increasing windages (0%, 0.5%, …, 2.5%). Simulations are done with the old OI85 field (no time correlation). Bigger dots indicate the selected points (with the percent windage): 0% for U and BB, 1% for S1, 2% for S2 and 2.5% for G2. Of course the α coefficients so selected are approximate (within ± 0.25% at least).

Appendix 6: Objective analysis and models errors

Objective analysis trajectory error

We estimate the distance error between a true particle trajectory and a trajectory integrated in a field optimally estimated from a few current measurements, by assuming the true velocity field is a given model field (here Mercator PSY2V3). The estimated velocity field is obtained exactly as if we had a few real current measurements at some positions, but now the data are model currents at these given positions.

We have done that with the very positions where the real buoy trajectories were found at a given time (thus the mse maps are exactly the same for the model and the real field reconstructions).

First we have compared the psy2v3 trajectories with the buoy trajectories, that is we plot on figure A6_1 top panel the distance between the two as a function of time. This gives us the error of the model trajectories: order of 100 km after 5 days. On the same Figure dashed lines show the distance between the reconstructed trajectories and the buoy ones. The error of the reconstructed trajectories is quite similar, however this does not tell us if the model and reconstructed trajectories are close to each other.

This is actually the case, as shown in the bottom panel of the Figure. Here we have plotted the distance between the model and the reconstructed trajectories, for the same trajectories as in the top panel. From this plot we would infer a 25 km error after 5 days.

We may wonder whether the reconstructed trajectories are too close to the positions of the observations generated in the model. Since the model trajectories are departing rapidly from the real ones this is probably not a problem, except perhaps for one or two days after the initial time.

To solve this point, let us start four trajectories from four points surrounding the zone where the first derelicts were first found, and let us plot the distance between the model and reconstructed trajectories, integrated backward (this is actually what we are interested in, since we know only the positions of the objects or bodies found and we want to go backward in time). The result is shown in the middle panel of the Figure, and shows the same 5 km day^{-1} increase in the distance (the

initial positions are: 3.5N 30.8W, 3.5N 30.2W, 3.8N 30.8W and 3.8N 30.2W, and the backward integration is done from June 6 at 12h until June 1 at 2h).

A similar test compares the distribution of the crash points backtracked from all the bodies (Figures A6_2a and A6_2b). Distance between the two CP clusters (backtracked from all June 6 and 7 bodies) is 20 km.

Conclusion: we assume a 25 km error after 5 days for the trajectories integrated in the optimally estimated velocity field (this is four times smaller than the error in Mercator PSY2V3). This error is equal to the one-dimensional (or marginal) standard deviation multiplied by $\sqrt{\frac{\pi}{2}}$. Whence the 20 km value used in Table 2 (Chapter IV).

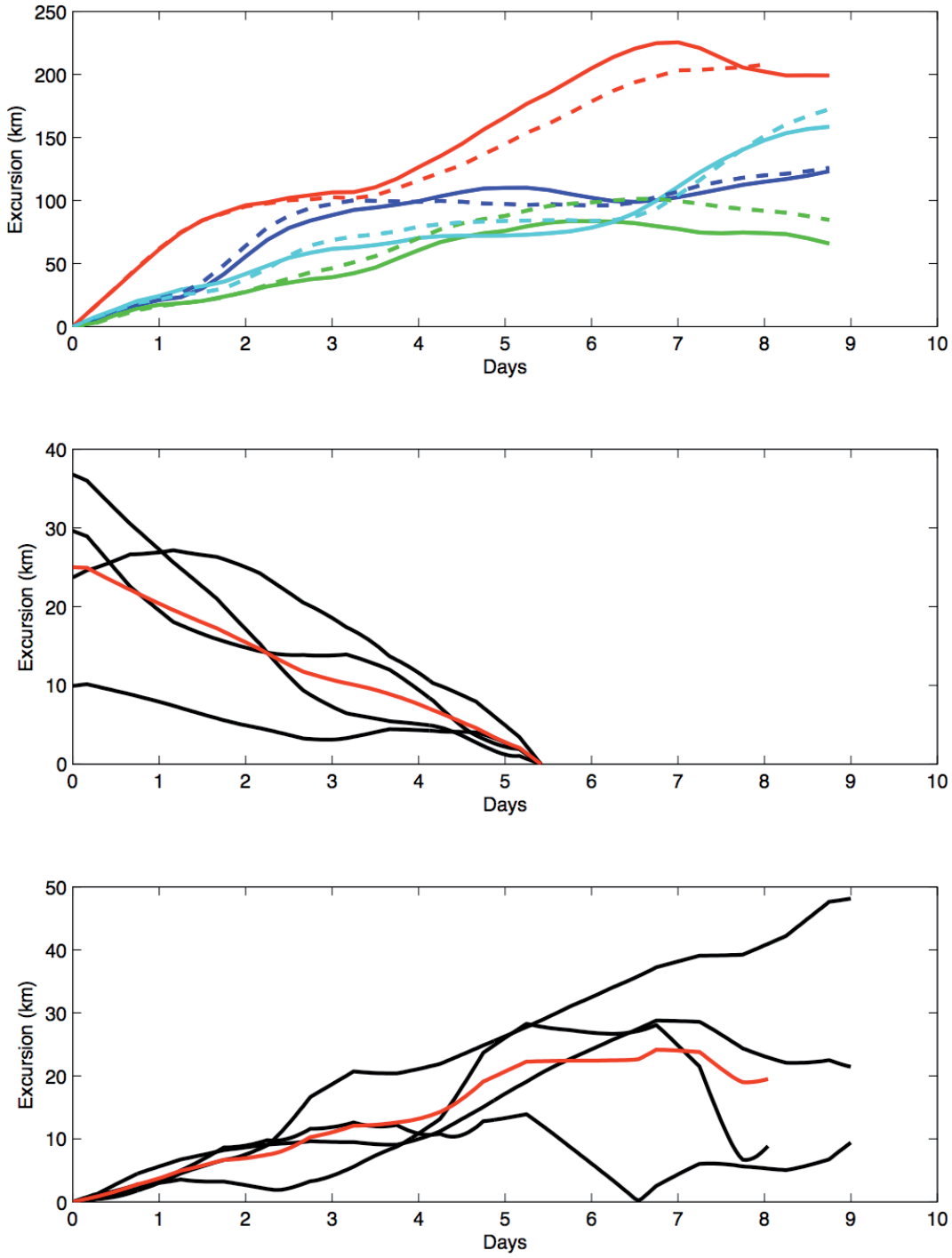

Figure A6_1

Top panel: distance between buoy and Mercator PSY2V3 trajectories (full lines) and between buoy and (model) reconstructed trajectories (dashed lines). Buoy #27045 (red), #246 (green), #92 (cyan), #42 (blue).

Middle panel: distance between model and reconstructed backward trajectories launched on June 6 at 12h at four different positions (see text for details).

Bottom panel: distance between model and reconstructed forward trajectories launched on June 1 at 0h.

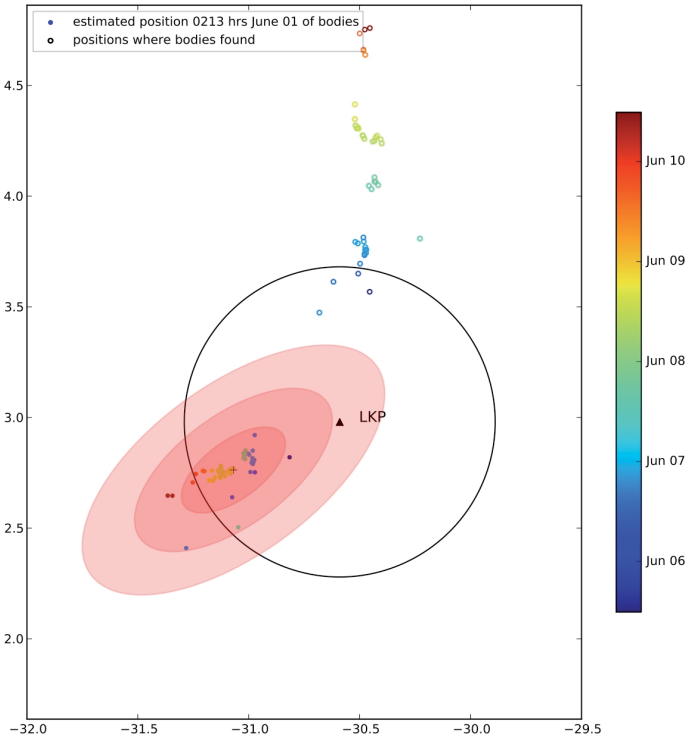

Figure A6_2a Distribution of the crash positions from the bodies recovered and backtracked in the Mercator PSY2V3 velocity field. The 0.5, 0.8 and 0.9 probability ellipses are drawn.

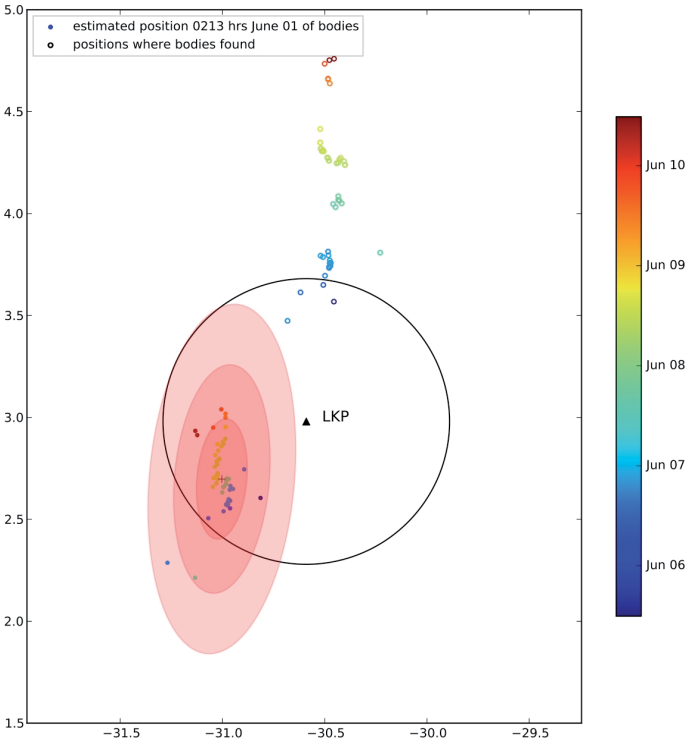

Figure A6_2b Distribution of the crash points obtained from backtracking the bodies positions, in the Mercator PSY2V3 reconstructed velocity field by optimal interpolation on sampled velocity vectors at the corresponding buoy positions.

Model trajectory errors

We present here the distance between simulated and actual trajectories for the four fishermen buoys (#42 blue, #92 cyan, #246 green and #27045 red) which more or less were surrounding the crash zone between June 1 and June 9 2009. The average distance is given by the black curve and time origin is June 1 at 0h. We chose the average distance after 5 days (i.e. on June 6 at 0h) as a measure of the model error. We have already said this error is equal to the one-dimensional (or marginal) standard deviation multiplied by $\sqrt{\frac{\pi}{2}}$. The standard deviations are used in the statistical estimation of the search zone (Chapter IV).

For models (FVCOM and the models data fitted) which assimilate part or all of these four buoy measured currents, we need to be more careful, since buoy trajectories may not be independent of the modelled ones.

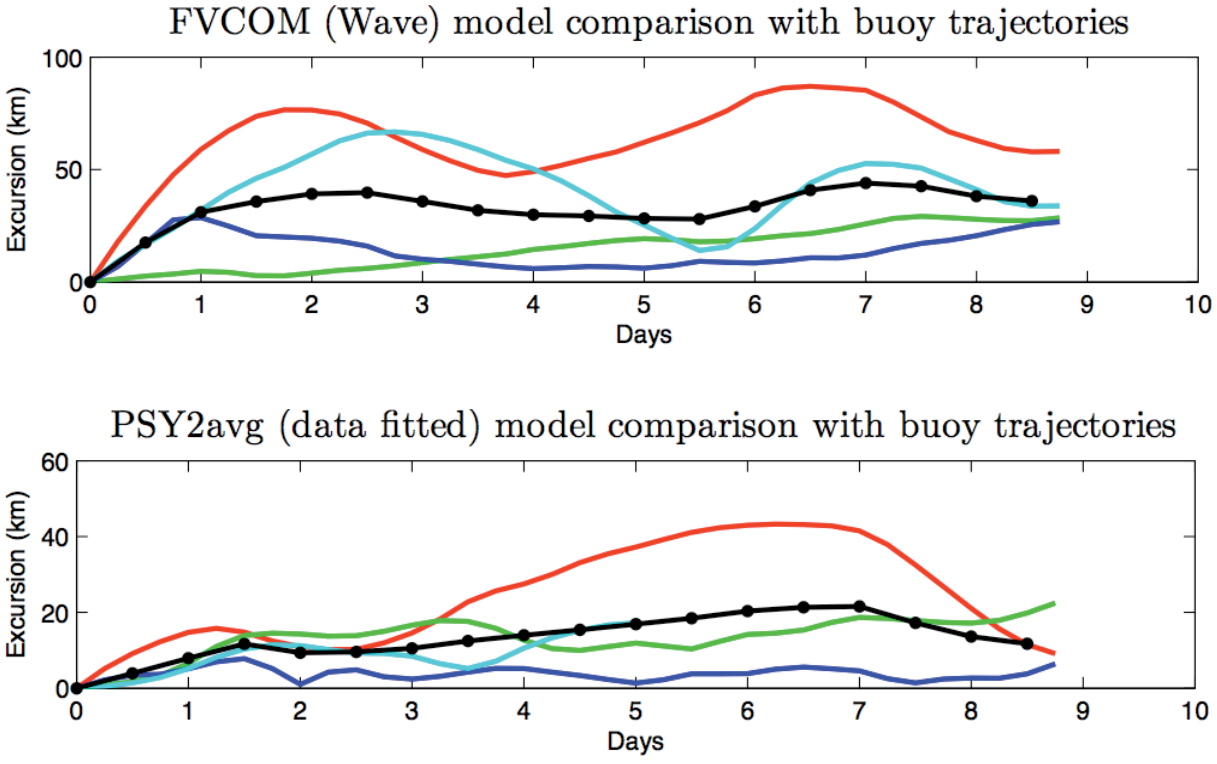

Figure A6_3 Distance between simulated and real trajectories from buoys 42 (blue), 92(cyan), 246(green) and 27045 (red). Average(black). Beware: vertical scale varies between plots. Day 0 corresponds to June 1 2009.

For FVCOM (with wave interactions or without, this incurs no clear difference on the errors), the two buoys #92 and #27045 are not assimilated. We thus naturally chose (see Figure A6_3 upper panel) the mean of the errors with these two buoys: 44 km (whence a 35 km marginal standard error).

With data fitting it is more difficult to give an undisputable error estimate, since all buoy currents are accounted for in the fit. On Figure A6_3 lower panel, the average distance error given by the black curve is 17 km, but does not represent the true error away from the trajectories. Since PSY2AVG has a 100 km distance error (PSY2V3 a 106 km and PSY2-REANA a 94 km error), we arbitrarily divided by two the error for the data fitted model: 50 km (whence a 40 km marginal standard error).

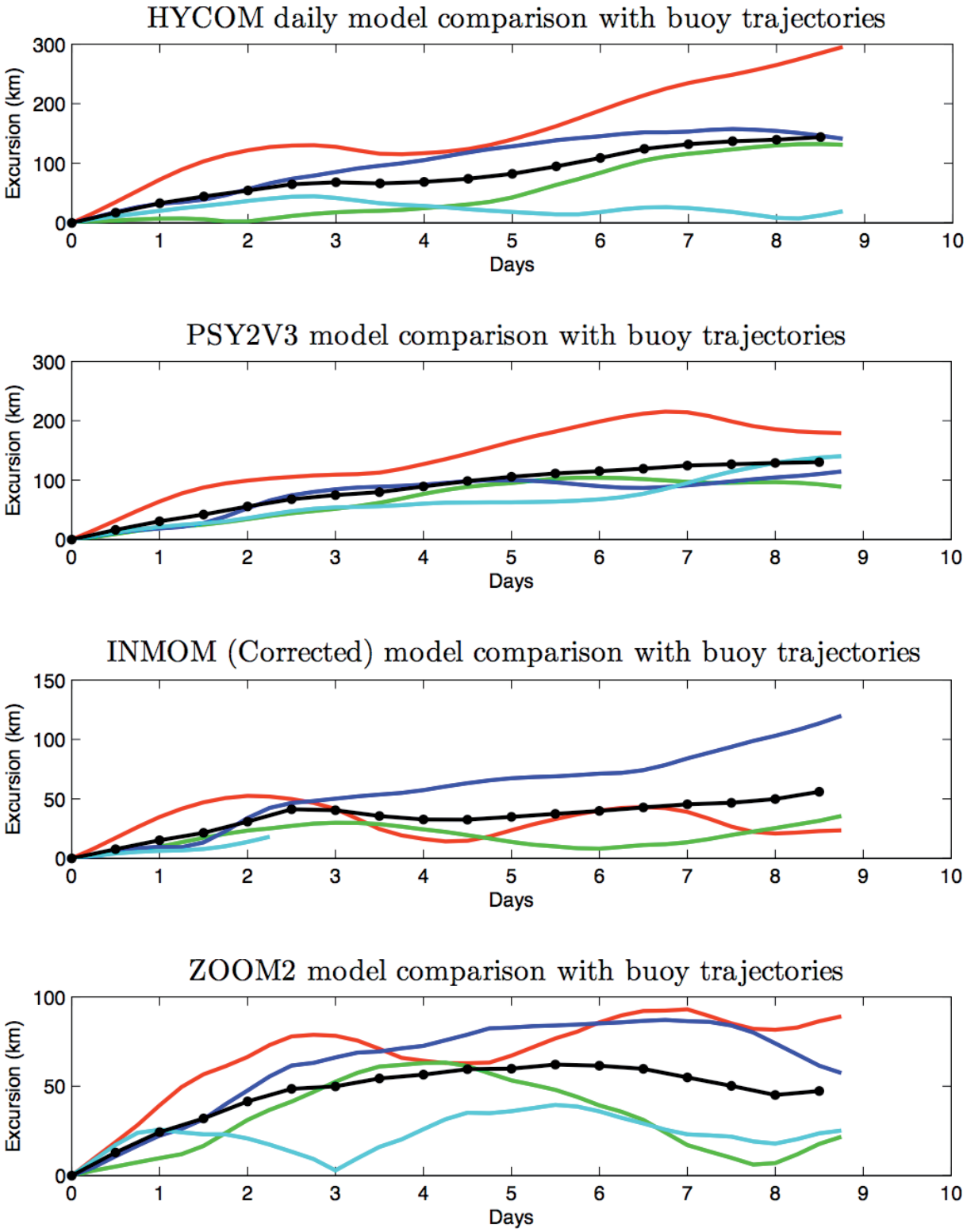

Figure A6_4 Distance between simulated and real trajectories from buoys 42 (blue), 92(cyan), 246(green) and 27045 (red). Average(black). Beware: vertical scale varies between plots.

Appendix 7: a SAR detected pollution spot

On June 2 2009 at 8h16, a possible pollution spot was detected near 30°30.5'W 2°43.4N by the synthetic aperture radar (SAR) on board the COSMO SkyMed 1 satellite. Figure A7_1 below shows the cusp shaped spot detected, which does not have the characteristic elongated form of an oil spill coming from a ship. CLS and CEDRE experts were not able to understand its origin. Report by G. Hajduch, P. Lozach & F. Collard gives other SAR images with well-identified signatures from ship tracks and oil spills.

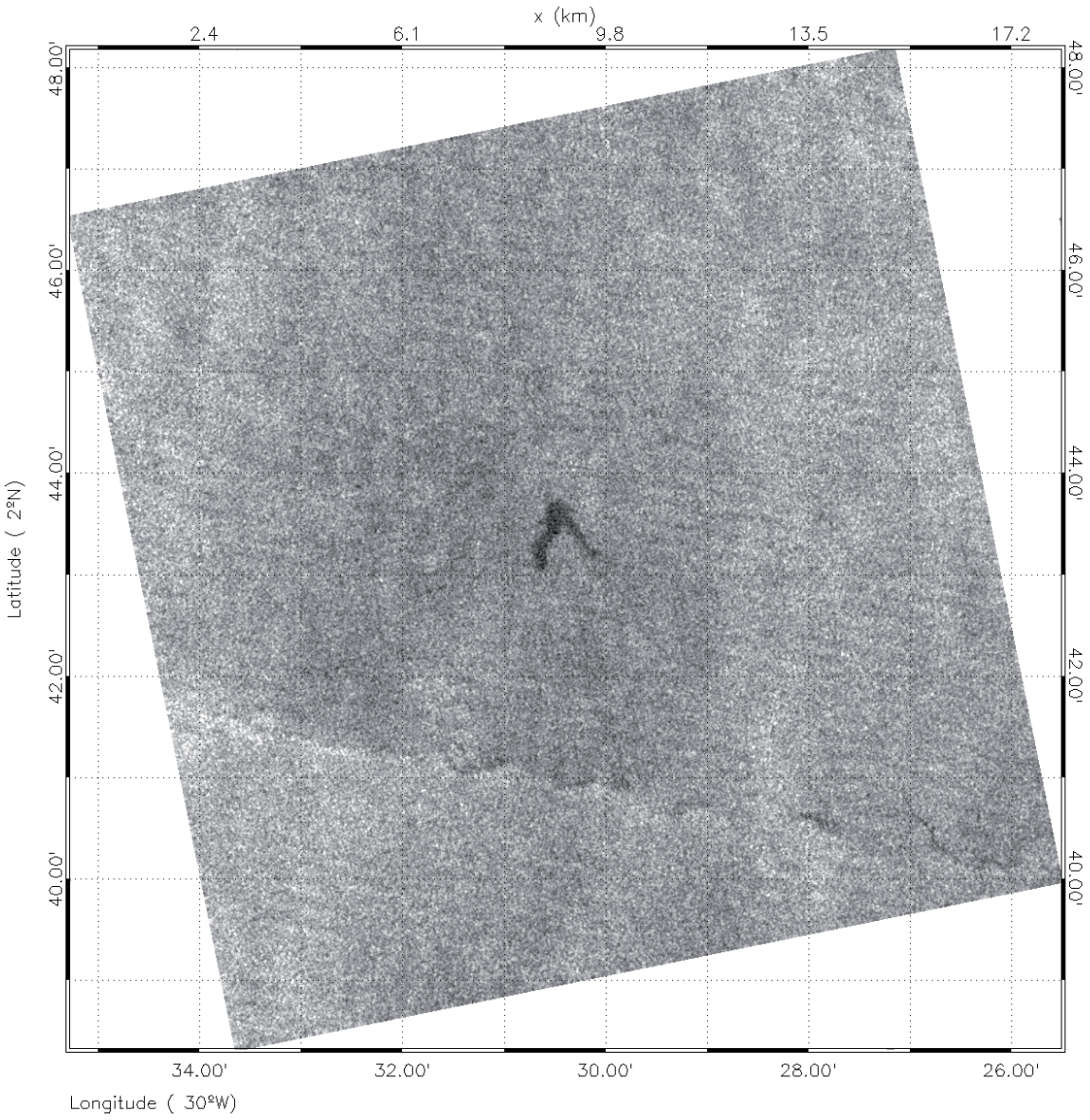

Figure A7_1 Cusp-shaped pollution spot seen on a COSMO SkyMed SAR image (on June 2 2009 at 8h16). A 330 m wavelength swell (propagating southward) is also visible (the SAR resolution is 30 m).

We have seen in chapter II (section on particle trajectories), that the back track (to June 1 at 2h15) of this pollution spot falls (within one or two kilometres) under the plane flight line roughly 10 nautical miles south southwest of LKP (one minute of flight time). This prompted us to check if such a spot could correspond to some kerosene (aviation fuel) released by the plane.

Within a few minutes after release, kerosene spreads on the sea surface as a very thin layer of the order of 1 μm (actually between 0.05 and 5 μm; the uncertainty is large). After 30 hours kerosene will have evaporated and dispersed[26] almost completely: with an initial amount of 50 m^3 there would remain (with a 10 knots wind) roughly 0.5 m^3 for a SAR detection. The estimated area of the spot on Figure A7_1 is approximately 0.5 km^2 and that would correspond to a layer 1μm thick at most. Knowing that some 43 000 kg of kerosene were still in the plane tanks after its 3h 40 mn flight (Rio to LKP), thus roughly 54 m^3 (kerosene density is 0.8 kg dm^{-3}), it is not impossible that this pollution spot may be the remnant of a kerosene release by the plane (be it voluntary or not). Of course it is difficult to tell which quantity is precisely involved (it may vary between 3 m^3 and the whole 54 m^3).

A last point concerns the wind drag on the spot as a whole: generally, 3% to 4% of the wind speed is assumed for oil (CEDRE, 2004). On Figures 25 and 27 we took 0% and 2% respectively (kerosene is light and volatile and has possibly a smaller wind drag than oil). The greater the windage the nearer the back tracked position to LKP since winds were northerly, but the nearest to the plane track is obtained with a 2% wind drag (whence our choice). Over only 30h we could expect a small distance between positions estimated with a 1% drag difference: there is however a 5 km distance (slanted in a SW-NE direction, see Figure A5_2) because the wind was strong then.

We have been unable, however, to relate this pollution spot to any impact point of the plane as determined from the debris and bodies found and the velocity fields estimated (whatever the methods).

But, all our calculations, are based on the assumption that the plane hit the sea surface intact (following BEA expertise of the recovered plane remains).

---

[26] breaking waves can drive small droplets into the water column. This process is called dispersion (Lehr & al., 2002)

References

Allen, A. A. (2005) Leeway divergence. Report CG-D-05-05, US Coast Guard Research and Development Center.

Allen, A. A. and J. V. Plourde (1999) Review of Leeway: Field experiments and implementation. Report CG-D-05-05, US Coast Guard Research and Development Center.

Arhan M. and A. Colin de Verdière (1985) Dynamics of eddy motions in the Eastern North Atlantic, *Journal of Physical Oceanography*, vol.15, n°2, 153-170.

Barron C. N., L. F. Smedstad, J. M. Dastugue and O.M. Smedstad (2007) Evaluation of ocean models using observed and simulated drifter trajectories: Impact of sea surface height on synthetic profiles for data assimilation, *Journal of Geophysical Research*, vol. 112, C07019, doi:10.1029/2006JC003982.

Blanke B. and P. Delecluse (1993) Variability of the tropical Atlantic-Ocean simulated by a general-circulation model with 2 different mixed-layer physics. *Journal of Physical Oceanography*, 23(7):1363–1388.

Bleck R., C. Rooth, D. M. Hu, and L. T. Smith (1992) Salinity-driven thermocline transients in a wind-forced and thermohaline-forced isopycnic coordinate model of the North-Atlantic. *Journal of Physical Oceanography*, 22(12):1486–1505.

Bleck R. (2002) An oceanic general circulation model framed in hybrid isopycnic-Cartesian coordinates. *Ocean Modelling*, 4(1):55–88.

Bomford G. (1971) Geodesy, Oxford University Press.

Boyd E. (1935) The growth of the surface area of the human body. University of Minnesota press.

Brasseur P. and J. Verron (2006) The SEEK filter method for data assimilation in oceanography: a synthesis. *Ocean Dynamics*, 56(5-6):650–661.

Breivik O. and Allen A. A. (2008) An operational search and rescue model for the Norwegian sea and the North sea. *Journal of Marine Systems*, 69 : 99-113.

Bretherton F. P., R. E. Davis and C. B. Fandry (1976) A technique for objective analysis and design of oceanographic experiments applied to MODE-73, *Deep-Sea Research*, vol.23, 559-582.

Bryan K. (1969) A numerical method for the study of the circulation of the world ocean. *Journal of computational physics* 4:347–376.

Burden R. L. & J. D. Faires (1985) Numerical analysis, Prindle Weber & Schmidt publishers.

Campin J. M., A. Adcroft, C. Hill, and J. Marshall (2004). Conservation of properties in a free-surface model. *Ocean Modelling*, 6(3-4):221–244.

CEDRE (2004) L'observation aérienne des pollutions pétrolières en mer.

Chassignet E. P. , H. E. Hurlburt, O. M. Smedstad, G. R. Halliwell, P. J. Hogan, A. J. Wallcraft, R. Baraille, and R. Bleck (2007). The HYCOM (HYbrid Coordinate Ocean Model) data assimilative system. *Journal of Marine Systems*, 65(1-4):60–83.

Chassignet E. P., H. E. Hurlburt, E. Metzger, O. M. Smedstad, J. Cummings, G. Halliwell, R. Bleck, R. Baraille, A. Wallcraft, C. Lozano, H. Tolman, A. Srinivasan, S. Hankin, P. Cornillon, R. Weisberg, A. Barth, R. He, F. Werner and E. J. Wilkin (2009) US GODAE: Global ocean prediction with the HYbrid Coordinate Ocean Model (HYCOM). *Oceanography*, 22(2):64–75.

Chorin A. J. and J. E. Marsden (1993) A mathematical introduction to fluid mechanics, Springer Verlag.

Colin de Verdière A. (1986) The estimation of heat and potential vorticity balance: applications to the Tourbillon array, *Deep-Sea Research*, vol.33, n°3, 277-303.

Cummings J. A. (2005) Operational multivariate ocean data assimilation. *Quarterly Journal of the Royal Meteorological Society*, 131(613):3583–3604.

Dai A. and K. E. Trenberth (2002) Estimates of freshwater discharge from continents: Latitudinal and seasonal variations. *Journal of Hydrometeorology*, 3(6):660–687.

Daniel P. (2004) MOTHY documentation technique. Météo-France.

Daniel P., G. Jan, F. Cabioch, Y. Landau and E. Loiseau (2002). Drift Modeling of cargo containers, *Spill Science & Technonoly Bulletin*, vol. 7, n° 5-6, 279-288

Davidson P. A. (2004) Turbulence. Oxford University Press, 657 pp.

Davis R. E. and W. Zenk (2001) Subsurface Lagrangian observations during the 1990s. In Ocean circulation and Climate, Academic press, 123-139.

Davis R. E., D. C. Webb, L. A. Regier and J. Dufour (1992) The autonomous Lagrangian circulation explorer (ALACE), *Journal of Atmospheric and Oceanic Technology*, vol. 9, n°3, 264-285.

Drévillon M., R. Bourdallé-Badie, C. Derval, Y. Drillet, J.-M. Lellouche, E. Remy, B. Tranchant, M. Benkiran, E. Greiner, S. Guinehut, N. Verbrugge, G. Garric, C. E. Testut, M. Laborie, L. Nouel, P. Bahurel, C. Bricaud, L. Crosnier, E. Dombrowsky, E. Durand, N. Ferry, F. Hernandez, O. Le Galloudec, F. Messal, and L. Parent (2008) The GODAE/Mercator-Ocean global ocean forecasting system: results, applications and prospects. *Journal of Operational Oceanography*, 1(1):51–57.

Dombrowsky E., L. Bertino, G. B. Brassington, E. P. Chassignet, F. Davidson, H. E. Hurlburt, M. Kamachi, T. Lee, M. J. Martin, S. Mei, and M. Tonani (2009) GODAE systems in operation. *Oceanography*, 22(3):80–95.

Feller W. (1968 & 1971) An introduction to probability theory and its applications, vol. 1 & 2, John Wiley & Sons.

Gill A. (1982) Atmosphere-Ocean Dynamics, volume 30 of *International Geophysics Series*. Academic Press, London. 662 + xv pp.

Griffies S. M. (2004) Fundamentals of Ocean Climate Models. Princeton University Press, Princeton, New Jersey.

Griffies S. M., M. J. Harrison, R. C. Pacanowski, and A. Rosati (2004) *A Technical Guide to MOM4*. NOAA/Geophysical Fluid Dynamics Laboratory, Princeton, USA.

Haidvogel D. B., H. Arango, W. P. Budgell, B. D. Cornuelle, E. Curchitser, E. Di Lorenzo, K. Fennel, W. R. Geyer, A. J. Hermann, L. Lanerolle, J. Levin, J. C. McWilliams, A. J. Miller, A. M. Moore, T. M. Powell, A. F. Shchepetkin, C. R. Sherwood, R. P. Signell, J. C. Warner, and J. Wilkin (2008) Ocean forecasting in terrain-following coordinates: Formulation and skill assessment of the regional ocean modeling system. *Journal of Computational Physics*, 227(7):3595–3624.

Hallberg R. W. (2009). HIM: The Hallberg Isopycnal Model. http://www.gfdl.noaa.gov/him-the-hallberg-isopycnal-model

Henssge C. (1988). The rectal temperature time of death nomogram. *Forensic science international*, vol. 38, 209-236.

Hernandez F., L. Bertino, G. Brassington, E. Chassignet, J. Cummings, F. Davidson, M. Drévillon, G. Garric, M. Kamachi, J. M. Lellouche, R. Mahdon, M. J. Martin, A. Ratsimandresy, and C. Regnier (2009) Validation and intercomparison studies within GODAE. *Oceanography*, 22(3):128–143.

Hurlburt H. E., G. B. Brassington, Y. Drillet, M. Kamachi, M. Benkiran, R. Bourdallé-Badie, E. P. Chassignet, G. A. Jacobs, O. Le Galloudec, J. M. Lellouche, E. J. Metzger, P. R. Oke, T. F. Pugh, A. Schiller, O. M. Smedstad, B. Tranchant, H. Tsujino, N. Usui, and A. J. Wallcraft (2009) High-resolution global and basin-scale ocean analyses and forecasts. *Oceanography*, 22(3):110–127.

Lagerloef G., G. Mitchum, R. Lukas and P. Niiler (1999) Tropical Pacific near-surface currents estimated from altimeter, wind and drifter data. *Journal of Geophysical Research*, vol. 104, C10, 23313-23326.

Lehr W., R. Jones, M. Evans, D. Simecek-Beatty and R. Overstreet (2002) Revisions of the ADIOS oil Spill model. *Environmental Modelling & Software*, 17: 191-199.

Leonard B. (1979) Stable and accurate convective modeling procedure based on quadratic upstream interpolation. *Computer Methods In Applied Mechanics and Engineering*, 19(1):59–98.

Leonard B. (1991) The ULTIMATE conservative difference scheme applied to unsteady one-dimensional advection. *Computer Methods In Applied Mechanics and Engineering*, 88(1):17–74.

Madec G. (2010) NEMO ocean engine. Laboratoire d'Océanographie Dynamique et de Climatologie/Institut Pierre-Simon Laplace

Marchuk G.I. (1968) Some application of the splitting-up methods to the solution of mathematical physics problems. Applik. Mat., V. 13, No. 2.

Marchuk G.I. (1988) Splitting-up methods (Nauka, Moscow).

Marchuk G. I., A. S. Rusakov, V. B. Zalesny, and N. A. Diansky (2005) Splitting numerical technique with application to the high resolution simulation of the indian ocean circulation. *Pure and Applied Geophysics*, 162(8-9):1407–1429.

Marshall J., A. Adcroft, C. Hill, L. Perelman, and C. Heisey (1997) A finite-volume, incompressible Navier Stokes model for studies of the ocean on parallel computers. *Journal of Geophysical Research*, 102(C3):5753–5766.

Mood A. M., F. A. Graybill and D. C. Boes (1974) Introduction to the theory of statistics, Mc Graw-Hill.

Niiler P. P.(2001) The world ocean surface circulation, in Ocean circulation and Climate, Academic Press, 193-204.

Niiler P. P., A. S. Sybrandy, K. Bi, P. M. Poulain and D. Bitterman (1995) Measurements of the water-following capability of Holey-sock and TRISTAR drifters, *Deep-Sea Research*, vol. 42, 1951-1964.

Ollitrault M., G. Loaëc and C. Dumortier (1994) MARVOR: a multicycle RAFOS float, *Sea Technology*, vol.35, n°2, 39-44.

Özkögmen T. M., L. J. Piterbarg, A. J. Mariano and E. H. Ryan (2001) Predictability of drifter trajectories in the tropical Pacific ocean. *Journal of Physical Oceanography*, vol. 31, 2691-2720.

Park J. J., K. Kim and W. R. Crawford (2004) Inertial currents estimated from surface trajectories of Argo floats, *Geophysical Research Letters*, vol. 31, L13307, doi:10.1029/2004GL020191.

Pham D. T., J. Verron, and M. C. Roubaud (1998) A singular evolutive extended Kalman filter for data assimilation in oceanography. *Journal of Marine Systems*, 16(3-4):323–340.

Phillips O. M. (1977) The dynamics of the upper ocean, Cambridge University Press.

Pietrzak J., J. B. Jakobson, H. Burchard, H. J. Vested, and O. Petersen (2002). A three-dimensional hydrostatic model for coastal and ocean modelling using a generalised topography following co-ordinate system. *Ocean Modelling*, 4(2):173–205.

Rascle N., F. Ardhuin and E. A. Terray (2006) Drift and mixing under the ocean surface. A coherent one-dimensional description with application to

unstratified conditions. *Journal of Geophysical Research*, vol. 111, C03016, doi:10.1029/2005JC003004.

Rascle N. and F. Ardhuin (2009) Drift and mixing under the ocean surface revisited. Stratified conditions and model-data comparisons. *Journal of Geophysical Research*, vol. 114, C02016, doi:10.1029/2007JC004466.

Rio M.-H. and F. Hernandez (2003) High-frequency response of wind-driven currents measured by drifting buoys and altimetry over the world ocean. *Journal of Geophysical Research*, vol. 108 (C8), 3283, doi:10.1029/2002JC001655.

Rio M.-H. and F. Hernandez (2004) A mean dynamic topography computed over the world ocean from altimetry, in situ measurements, and a geoid model. *Journal of Geophysical Research*, vol. 109, C12032, doi:10.1029/2003JC002226.

Rio M.-H., P. Schaeffer, F. Hernandez and J.-M. Lemoine (2005) The estimation of the ocean Mean Dynamic Topography through the combination of altimetric data, in-situ measurements and GRACE geoid : from the global to regional studies. Proceeding from the GOCINA international workshop, Luxembourg.

Rossby T., D. Dorson and J. Fontaine (1986) The RAFOS system, *Journal of Atmospheric and Oceanic Technology*, vol. 3, n°4, 672-679.

Rossby T. and D. Webb (1970) Observing abyssal motion by tracking Swallow floats in the SOFAR channel, *Deep-Sea Research*, vol. 17, n°2, 359-365.

Sendroy J. and H. Collison (1966). Determination of human body volume from height and weight. *Journal of physiology*, vol. 21, n°1

Shchepetkin A. F. and J. C. McWilliams (2003). A method for computing horizontal pressure-gradient force in an oceanic model with a nonaligned vertical coordinate. *Journal of Geophysical Research*, 108(C3), 3090, doi:10.1029/2001JC001047.

Smith R. and P. Gent (2004) Reference Manual for the Parallel Ocean Program (POP). Technical Report LAUR-02-2484, Los Alamos.

Stewart R. (1985) Methods of satellite oceanography. University of California Press.

Tranchant B., C.-E. Testut, L. Renault, N. Ferry, F. Birol, and P. Brasseur (2008) Expected impact of the future SMOS and Aquarius Ocean surface salinity missions in the Mercator Ocean operational systems: New perspectives to monitor ocean circulation. *Remote Sensing of Environment*, 112(4):1476–1487.

Weisberg R. H. and T. J. Weingartner (1988) Instability waves in the equatorial Atlantic. *Journal of Physical Oceanography*, vol.18, 1641-1657.

Zalesak S. T. (1979) Fully multidimensional flux-corrected transport algorithms for fluids. *Journal of Computational Physics*, 31(3):335–362.

Individual reports given to BEA

Bentamy A. & D. Croizé-Fillon (2010) Enhancement of surface wind fields. ReportBlendedWind_2_BEA.pdf

Blanke B. (2010) Argo floats and Mercator simulations PSY2V3R1 and PSY4V1R2: a brief comparison plus comparison with simulation ZOOM_PSY2-T04. blanke_BEA_final_report.pdf

Chen C. & R. Limeburner (2010) FVCOM modeling estimation of the location of Air France 447. FVCOM_AF447_Jan20.doc

Diansky N., A. Lukianov, A. Ganshin, A. Gusev, O. Nikitin & V. Gruzinov (2010) Simulation of drifter and body trajectories. polarfondation_INMOM_Result.doc

Drévillon M., S. Cailleau, E. Durand, E. Greiner, S. Law Chune, J.M. Lellouche & G. Reffray (2010) A strategy for producing refined currents in the equatorial Atlantic in the context of the search of the AF447 wreckage. Drevillon_et_al_Mercator_Ocean_report.doc

Greiner E. (2010) BEA report on AF447. BEA_report_V2_20100119.pdf

Hajduch G., Lozach P., Collard F. (2009) Enquête vol AF447: Rapport d'analyse d'images CSK. CLS-DAR-NT-0907-026-Ed1Rev2_BEA_AF447_part1.doc & CLS-DAR-NT-0907-026-Ed1Rev2_BEA_AF447_part2.doc

Hunout J.C. & F. Lefèvre (2009) Delivery and expertise of oceanographic products and services for the AF447 investigation: In situ data. CLS-DOS-NT-09-322_BEA_CLS_In_Situ_Data.pdf

Lezaud P. (2010) Statistical methodology to determine the search zone. Search_Zone_report_303.pdf

Météo-France (2009) Comparaison des vents à 10m QuikScat et des analyses du CEP. 091012_Compar_Vents_QuikScat-ECMWF.pdf

Météo-France (2010) Rapport d'étude de situation météo-nautique. 20090601AF447V2.pdf

Ollitrault M. (2010) Search of the crash position of the Rio-Paris AF447 Airbus. AF447_IFREMER_Report_ter_2.pdf

Paradis D., S. Law-Chune, J. Negre & P. Daniel (2010) Météo-France drift study to estimate the AF447 crash area. 100610_MeteoFrance_report.doc

Payan C. (2009) ARPEGE re-analysis for the BEA. Arpegeanalysis_bea.pdf

Scott R., G. Nurser & P. Challenor (2010) Accuracy of 15m drifter trajectory predictions using HYCOM: final report from NOCS. Report-nocs-jan15.pdf

Glossary

ACARS Aircraft Communication Addressing and Reporting System
ADCP Acoustic Doppler Current Profiler
AMSR-E Advanced Microwave Scanning Radiometer for Earth
AOML Atlantic Oceanographic and Meteorological Laboratories
AVHRR Advanced Very High Resolution Radiometer
AVISO Archiving, Validation and Interpretation of Satellite Oceanographic data.
AWACS Airborne Warning and Control System
BEA Bureau d'Enquêtes et d'Analyses pour la sécurité de l'aviation civile.
CEDRE Centre de Documentation, de Recherche et d'Expérimentation sur les pollutions accidentelles des eaux
CLIO Coupled Large-scale Ice Ocean
CLS Collecte et Localisation par Satellite
CNRS Centre National de la Recherche Scientifique
CORE Common Ocean-ice Reference Experiments
COSMO COnstellation of Satellites for the Mediterranean basin Observation
CSIRO Commonwealth Scientific and Research Organization
ECMWF European Center for Medium range Weather Prediction
EKE Eddy Kinetic Energy
EM Electro Magnetic
ENAC Ecole Nationale de l'Aviation Civile
FVCOM Finite-Volume Community Ocean Model
GODAE Global Ocean Data Assimilation Experiment
HIM Hallberg Isopycnal Model
HYCOM HYbrid Coordinate Ocean Model
IFREMER Institut Français de Recherche pour l'Exploitation de la Mer
IMT Institut de Mathématiques de Toulouse
INMOM Institute of Numerical Mathematics Ocean Model
INMRAS Institute of Numerical Mathematics Russian Academy of Sciences
IR Infra-Red
KPP K Profile Parameterisation
LKP Last Known Position

MICOM Miami Isopycnic Coordinate Ocean Model
MITGCM Massachussetts Institute of Technology General Circulation Model
MOM Modular Ocean Model
MOTHY Modèle Océanique de Transport d'HYdrocarbures
NCEP National Center for Environmental Prediction
NCODA Navy Coupled Data Assimilation
NCOM Navy Coastal Ocean Model
NEMO Nucleus for European Modelling of the Ocean
NERSC Nansen Environment and Remote Sensing Center
NOAA National Oceanic and Atmospheric Administration
NOC National Oceanographic Center
NOGAPS Navy Operational Global Atmospheric Prediction System
NRL Navy Research Laboratory
OA Objective Analysis
OGCM Ocean General Circulation Model
OE Optimal Estimation
OI Optimal Interpolation
POP Parallel Ocean Program
REMSS REMote Sensing Systems
RSMAS Rosenstiel School of Marien and Atmospheric Science
SAR Synthetic Aperture Radar
SHOM Service Hydrographique et Océanographique de la Marine
SIO Scripps Institution of Oceanography
SLA Sea Level Anomaly
SSH Sea Surface Height
SSMI Special Sensor Microwave Imager
SST Sea Surface Temperature
SVP Surface Velocity Program
TKE Turbulent Kinetic Energy
TMI Tropical rainfall measuring mission Microwave Imager
TVD Total Variance Dissipation
UBO Université de Bretagne Occidentale
UMASSD University of Massachusetts Dartmouth
UTC Universal Time coordinated
WHOI Woods Hole Oceanographic Institution
WRF Weather Research and Forecast

Acknowledgements

This work would not have been possible without the help and advice of many colleagues, in particular C. Kermabon (IFREMER), T. Reynaud (IFREMER), J.P. Rannou (ALTRAN), D. Croizé-Fillon (IFREMER), A. Bentamy (IFREMER), A. Colin de Verdière (UBO), V. Thierry (IFREMER), P. Lherminier (IFREMER), F. Ardhuin (SHOM), E. Durand (Mercator-Océan), M.H. Rio (CLS), B. Guéguen (Genavir), M. Pazos (NOAA), J.M. Lellouche (Mercator-Océan), G. Reffray (Mercator-Océan), S. Guinehut (CLS), S. Cailleau (Mercator-Océan), D. Delaitre (BEA), B. Cappelle (Météo-France), P. Daniel (Météo-France), J. Nègre (Météo-France), C. Payan (Météo-France), S. Law Chune (Mercator-Océan), E. Chassignet (RSMAS), E. Blockley (UK MO), G. Gao (UMass), Q. Xu (UMass), J. Qi (UMass), P. Xue (UMass), Z. Lai (UMass), L. Zhao (UMass), H. Lin (UMass) and of course without the many discussions we had in the “Comité de dérive” then in the “Drift group”.

BEA has supported work done by G. Nurser and Robert Scott in NOC (UK), N. Dyansky in RAC (Russia), R. Limeburner and C. Chen in WHOI and UMass (USA), M. Drévillon and E. Greiner at Mercator-Océan (France), F. Lefèvre and G. Hajduch in CLS (France).

M. Ollitrault is much grateful to IFREMER which let him work on a full time basis.

Special thanks and appreciation is given to Sébastien Travadel (BEA) who coordinated the various modeler’s efforts into a cohesive one, and brought them back on a focused track when the results diverged.

We also thank the BEA for sharing its knowledge and giving hospitality for the many meetings we had in Le Bourget headquarters.

Last but not least, we are very grateful to the following scientists who accepted to review a first version of this report: Carl Wunsch (MIT, USA), Peter Niiler (SIO, USA), Laurent Bertino (NERSC, Norway), Gilles Reverdin (CNRS, France), Valérie Quiniou (Total) and Fraser Davidson (Fisheries and Ocean, Canada).